Floating to Floating Installation of a Full 15 MW Wind Turbine on a Tension Leg Platform with a Semi-Submersible Crane Vessel

A Parametric Sensitivity Study

Q. van Suijlen

Delft University of Technology
Heerema Engineering Solutions

Floating to Floating Installation of a Full 15 MW Wind Turbine on a Tension Leg Platform with a Semi-Submersible Crane Vessel

A Parametric Sensitivity Study

by

Q. van Suijlen

ODE MSc Thesis OE54035
Offshore and Dredging Engineering

to obtain the degree of Master of Science
at the Delft University of Technology
to be defended publicly on Tuesday May 4, 2023 at 3:00 PM.

Student number:	4384466	
Thesis Committee:	Dr.-Ing. S. Schreier,	TU Delft, Chairman and Daily supervisor
	Dr. ir. L. Pahlavan,	TU Delft
	Dr. D. Fiscaletti,	TU Delft
	ir. H. Smienk,	Heerema Engineering Solutions
	ir. R.A. Weegenaar,	Heerema Engineering Solutions
	Dr. P. Liu,	Intecsea

This thesis is confidential and cannot be made public until May 4th, 2025.

An electronic version of this thesis is available at `http://repository.tudelft.nl/`.

Cover Photo: ”Heerema’s Sleipnir installing the DOT pilot turbine with their novel RNA method”,
courtesy of Heerema.

Abstract

The increased consciousness of the negative impact of human-induced climate change has resulted in rapid developments within the offshore wind industry. With Wind Turbine Generators (WTGs) becoming increasingly larger and available shallow water sites becoming scarcer, new offshore wind solutions must be developed to accomplish the goals set by today's policymakers. The new deep water sites available for offshore wind are not applicable for the current benchmark of monopiles and jack-up vessels. New state-of-the-art applications, such as Floating Offshore Wind (FOW), come into play in the global offshore wind market. To meet this demand, Heerema is developing installation methodologies for floating to floating installation applications. One of these methodologies is the RNA+ method (Rotor Nacelle Assembly + Tower), lifting a fully assembled WTG module in one lift from the vessel deck on top of its foundation to limit the number of critical lifts. Operability studies are required to examine whether such an operation is feasible. As the FOW industry is the new kid on the block, little is known about FOW's configuration and other influences. Therefore, this research aims to determine the effect of design parameters of the three key components of an offshore floating to floating installation on its operability. These key components are the WTG, floater, and installation vessel. For this research, the IEA 15 MW reference turbine with an altered tower, a Tension Leg Platform (TLP) provided by Intecsea, and Heerema's Semi-Submersible Crane Vessel (SSCV) Sleipnir were used as WTG, floater, and installation vessel respectively.

A numerical base case model containing these key parameters was built to address the influence of the design parameters. This base case models the free-hanging stage of a full WTG module suspended in the SSCV's crane 3 m above the TLP in a water depth of 150 m. The numerical model was analyzed in the Frequency Domain (FD), considering only first-order effects. With respect to this base case, all parameter variations were compared. To Asses the operability, the limiting wave height, H_{lim}, was set to 2 m. Resulting in a maximum $H_s T_p^2$ limit of 120 ms^2. A mean JONSWAP spectrum was used as wave spectrum.

The results show that this installation method is sensitive to long wave periods (> 8 s). The clearance between the nacelle and crane boom is deemed the most governing limiting criterion. The secondary governing limits are the relative vertical motion between the tower bottom and TLP top and the side-lead angle of the crane hoist wire. Design parameters that influence the static clearance between the nacelle and crane boom have the most impact on the total operability. With the current design parameters world's largest SSCV has a limited operability for installing the modified version of the IEA 15 MW reference turbine with a single crane lift. Alterations to increase its crane boom reach and clearance are needed to perform this single lift installation. The WTG's hub height and nacelle casing size limit the operability significantly. Furthermore, due to its relatively small size, stability, and stiffness in heave direction, the TLP hardly affected the operability with the used configuration.

Preface

Dear Reader,

This thesis before you has been written to fulfill the Master Offshore and Dredging Engineering at Delft University of Technology, in collaboration with Heerema Engineering Solutions and Intecsea. This thesis focuses on the floating installation of floating offshore wind turbines. It was an insightful and educational process that helped me evolve into my role as a future engineer. Many have helped me complete this task. I want to express my appreciation towards those who helped me to complete this work of science.

First of all, Sebastian, your thorough feedback and involvement throughout this research were of great help to me. Our weekly meetings were concise and effective. They helped me to stay on track and to focus on the details without losing sight of the bigger picture. Pooria and Daniele, I would like to thank you for your time and contribution in the final part of this research.

Robert, your guidance has been a valuable asset to the success of this process. It helped me to put sometimes abstract problems into tangible, real-life applications. Also, language and jargon-wise, you were of great help. Henk, your support in getting me up to speed on the subject and your fresh view on my results contributed greatly. Ping, thank you for your enthusiasm, insights and for connecting me with HES. Martijn, your help with developing the TLP is much appreciated. Furthermore, I want to give credit to everyone at HES for their receptiveness and assistance.

Additionally, I would like to thank my friends and family for their support during this process. Especially my Dad, Jeroen, for proofreading this document from a non-engineering point of view. Last but not least, Ockje, for your encouragement and optimism during this quest and for getting the ball rolling that resulted in me ending up at HES.

Enjoy!

Quint van Suijlen
Delft, April 2023

Nomenclature

Abbreviations and Acronyms

CAPEX	Capital Expenditures
CoB	Center of Buoyancy
CoG	Center of Gravity
CoV	Center of Volume
DAF	Dynamic Amplification Factor
DNV	Det Norske Veritas
DOF	Degree(s) of Freedom
EoM	Equation of Motion
FD	Frequency Domain
FEM	Finite Element Method
FOW	Floating Offshore Wind
FOWT	Floating Offshore Wind Turbine
GBF	Gravity Based Foundations
GDF	Geographic Data File
HCG	Horizontal Center of Gravity
HES	Heerema Engineering Solutions
HLV	Heavy Lift Vessels
HMC	Heerema Marine Contractors
IEA	International Energy Agency
JONSWAP	Joint North Sea Wave Project
LCOE	Levelized Cost of Energy
MBL	Minimal Breaking Load
MSL	Mean Sea Level
NREL	National Renewable Energy Laboratory
OWT	Offshore Wind Turbine
POI	Point of Interest
PS	Port Side
PSD	Power Spectral Density
RAO	Response Amplitude Operator
RNA	Rotor Nacelle Assembly
RNA+	Rotor Nacelle Assembly + Tower
SB	Starboard
SMPM	Single Most Probable Maximum
SSA	Significant Single Amplitude
SSCV	Semi Submersible Crane Vessel
SSD	Significant Double Amplitude
SWL	Safe Working Load
TD	Time Domain
TLP	Tension Leg Platform
TRL	Technology Readiness Level
UM	Universal Model
VCG	Vertical Center of Gravity
WTG	Wind Turbine Generator

Symbols

A_{wl}	$[m^2]$	Waterline surface
$F_{pertendon}$	$[kN]$	Force per tendon
F_b	$[kN]$	Buoyancy Force
F_g	$[kN]$	Force of Gravity
F_s	$[kN]$	Spring Force
F_t	$[kN]$	Total Tendon Force
g	$[\frac{m}{s^2}]$	gravitational acceleration
H_{max}	$[m]$	Maximum wave Height
H_s	$[m]$	Significant Wave Height
I_A	$[m^4]$	Area moment of inertia
J_{ij}	$[tm^2]$	Mass Moment of Inertia
k_{hyd}	$[\frac{kN}{m}]$	Hydro-static stiffness
$k_{m_{ij}}$	$[\frac{kN}{m}]$	Mooring stiffness
L_0	$[m]$	Initial tendon length
L_{total}	$[m]$	Total Stretched Tendon Length
m	$[t]$	mass in metric tonnes
$r_{m,ii}$	$[m]$	Radius of Gyration
r_1	$[m]$	Inner Cylinder Radius
r_2	$[m]$	Outer Cylinder Radius
T_n	$[s]$	Natural period
T_p	$[s]$	Wave Peak period
δL	$[m]$	Tendon elongation
ε	$[°]$	Wave direction
θ	$[°]$	Angle between mooring lines and positive Z= axis
∇	$[m^3]$	Displacement
ρ_w	$[\frac{t}{m^3}]$	Sea Water Density
ω_n	$[\frac{rad}{s}]$	Natural frequency

Units

t	Metric Tonnes
m	meter
s	second
N	Newton
rad	radian
W	watt

Contents

1

Introduction

Climate change is a global concern and is an item on the agenda for many people, organizations, and governments. The last four decades have all been successively warmer than any decade that preceded it since 1850 [1]. The increase in global surface temperature since 1850–1900 is assessed to be 1.1°C [2]. The annual average rate of sea level rise almost tripled from 1.3 mm/year to 3.7 mm/year between 1901-1971 and 2006-2018 [1]. The United Nations (UN) established global climate change conferences with corresponding agreements to limit human impact on climate change. The most known is the 2015 Paris agreement, which mandates limiting the global temperature rise to preferably 1.5°C this century with respect to pre-industrial levels [3]. The most recent one is the 2021 Glasgow agreement. This Glasgow agreement calls for reducing global carbon dioxide emissions with 45% by 2030 and net zero by 2050, with respect to the 2010 levels [4]. If the world continues on its current path, this 45% reduction will occur around 2050, and the net zero in 2100 [2]. So measures have to be taken to comply with this global goal.

Focussing on the subject of electricity generation in 2050, the global energy demand is expected to double [5]. Det Norske Veritas (DNV) made a prediction for the world grid-connected electricity generation per power station type, see Figure 1.1. It can be seen that the electricity production of oil and mainly coal-fired electricity generators will not only decrease with respect to (w.r.t.) the other power station types but also in absolute proved PWh/y. It decreases from roughly 10 PWh/y to about 2.7 PWh/y. The most growth in this electricity generation in the coming years is expected for solar and wind energy. In 2050 83% of the electric power is predicted to be renewable based, fossil fuels will only generate 12% of the electricity, and nuclear energy contributes with 5% [5]. This was 26%, 64% and 10% in 2019 respectively [6]. Of this 83% renewable energy generation, 33% of grid-connected electricity supply will be wind-based: 20% onshore, 11% bottom fixed offshore wind, and 3% of the energy generation in 2050 will be floating offshore wind based, being 300 GW of installed power [5, 7], see Figure 1.1.

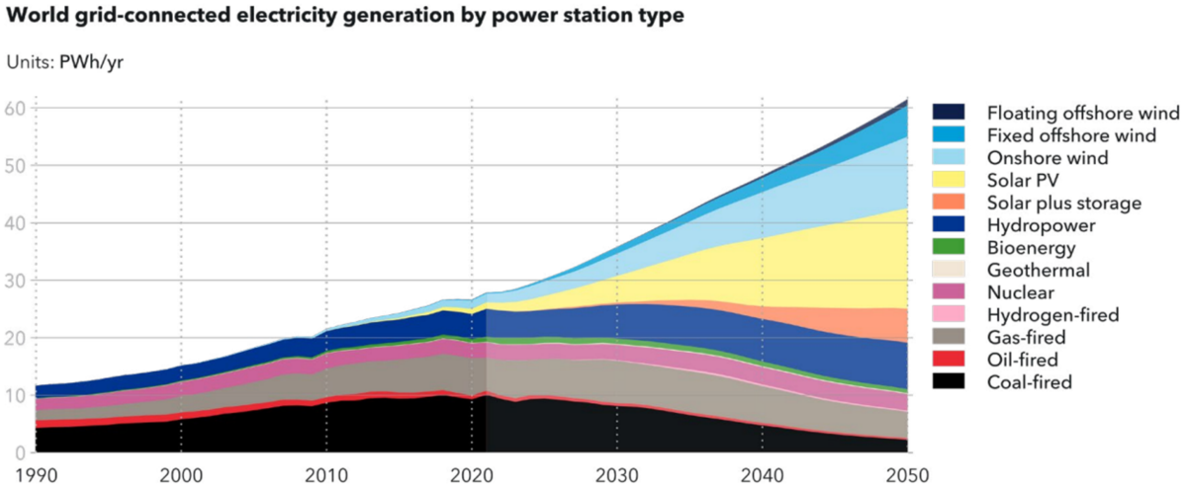

Figure 1.1: Electricity generation per power station type [5]

One contribution to reaching the UN's goal set in Glasgow is to utilize new renewable offshore wind energy. The vast majority of current offshore wind farms are in shallow waters with less than 50 m water depth, close to shore and bottom fixed [8]. Limited suitable shallow water locations with sufficient wind are still available for offshore wind [8]. 80% of offshore wind energy is available at sites with water depths over 60 m [9]. The current bottom-founded foundations such as Monopiles, Jackets, and Gravity Based Foundations (GBFs) are optimal for water depths up to 40 m, 70 m, and 30 m, respectively [10]. The new generation of 'Beyond XXL' Monopiles will suit water depths up to 65 m [11]. Because shallow water sites under 60 m become scarce, have less available wind energy than deeper sites, and are not suited for the next generation of bottom-fixed foundations, FOW is an addition to the future of offshore wind energy in general. It is expected to be 15% of the total offshore wind capacity by 2050 [5]. To meet the UN's resolution of the Glasgow summit deeper water sites will have to be utilized with renewable energy sources such as FOW farms. In 2012 the average offshore wind farm's water depth was 22 m, and the distance to shore 29 km. This is projected to be up to 215 m water depth and 200 km distance to shore in the near future [12].

One of the governments investing in offshore wind farms is the Scottish government. It auctioned 8,600 km² of seabed rights to offshore wind developers for a total of 25 GW of offshore wind power, of which 15GW will be utilized with floating wind [13]. This will result in 750-1000 floating WTGs depending on the size, 15-20 MW respectively. The French government aims for 40 GW of offshore wind by 2050. Of the 3.5 GW already auctioned, 500 MW is set out for floating wind [14]. The Dutch Government presented the ambition to have 70 GW of offshore wind capacity installed in 2050. No distinction between fixed and floating wind was given [15].

To let these plans see the light of day these WTGs have to be installed. The installation costs of a 5.5 MW turbine are 7.6% and 8.2% of the Capital Expenditures (CAPEX) for bottom fixed and floating wind, respectively [16]. Installation is considered a main critical stage in the life cycle of a WTG [10]. With the rapidly growing sizes of WTGs, contractors have more difficulties installing these large structures, reaching the limits of existing installation vessels [17]. Specialized installation vessels have limited availability and high day rates [10]. The operability window of this installation process is an interesting topic to asses. The main causes of delay in offshore wind turbine construction projects are in-port planning, unfinished previous offshore tasks, and weather or vessel related [18]. Floating offshore wind gives a new dimension to the offshore installation process, with the possibility of full onshore assembly or floater movements while performing an offshore installation on site.

Currently, Offshore Wind Turbines (OWTs) installation is mainly conducted with Jack-Up vessels [10]. For floating wind, this type of vessel is unsuitable as the water depth is beyond the reach of the legs of a jack-up. Currently, most floating farm pilots are assembled in port and towed to their final location. Port assembly and tow-out is considered in these FOW projects because it is seen as an easy and straightforward option, and no heavy lift vessels are needed [8, 10]. However, future port logistics are not considered in these assessments. It is predicted that with the current developments and port characteristics, ports will become the bottleneck in most floating offshore wind projects [19, 20]. This is because of limited port availability and (storage) size. A benefit of floating to floating assembly on site is that partly assembled configurations can be stored at an offshore site, and not all parts have to be funneled through one port. Manufacturers of floaters can directly deliver the floater on-site. Instead of shipping it from the manufacturing port to the assembly port, where it needs to be processed again.

Coming back to the offshore on-site installation of FOWTs, the current configuration with jack-ups and monopiles standing on and being fixed in the seabed, there are hardly any wave-induced motions on the vessel and foundation. This leads to high operability during the installation of these OWTs, as the OWT is only encountered by wind- and crane motions. For the installation of FOWTs, floating vessels are to be used. Both the floating installation vessels and the floating foundations bring new aspects to the installation equation. Most floating installation vessels are not yet fitted for WTG installations, as their main objective is to install offshore wind foundations or oil and gas structures. Some developments have been made regarding the floating to floating installation of WTGs. Heerema, for instance, started their novel Rotor Nacelle Assembly (RNA) installation method for Arcadis Ost in the Baltic Sea in late 2022 [21]. With floating to floating WTG installation being a novelty in the industry, few vessels are suited for this method [10]. Current vessels must be innovated, and new vessels are designed to fulfill this need for floating-to-floating installation. The three main parts of this installation method are the WTG, floater, and installation asset. Separate models and designs exist for these main parts, but an integrated design does not. Research on whether the floating to floating installation is operationally feasible is needed before this can be implemented in real-life applications. Therefore, assessing the operability of this new floating to floating WTG installation method is an interesting query to research.

1.1. Heerema Engineering Solutions

Heerema Engineering Solutions (HES) is the newest member of the Heerema Group. HES is an independent engineering consultancy offering engineering solutions for the offshore renewable industry, from early-phase development to offshore execution. The Heerema group exploits the world's two largest Semi-Submersible Crane Vessels, the Sleipnir, and the Thialf. The Sleipnir has a Safe Working Load (SWL) of 20,000 t. This is 14,200 t for the Thialf. Another SSCV Balder (SWL 6,300 t) and the mono-hull Aegir (SWL 5,000 t) complete their fleet of Heavy Lift Vessels (HLV). In the past, Heerema focused on the floating installation of heavy oil and gas modules. Heerema has a vast track record installing Tension Leg Platforms (TLPs) for the oil and gas industry. With these huge SSCVs at their disposal, they are now looking into using them for floating installation for offshore wind. Heerema started their novel Rotor Nacelle Assembly (RNA) installation campaign for Arcadis Ost in the Baltic Sea in late 2022 [21]. With this RNA installation method first the tower is installed on the foundation, then the RNA module is assembled on deck on top of a dummy tower. Finally, the whole RNA is lifted and installed on top of the tower. The next step in their installation innovation is the RNA+ installation method. The plus indicated the installation of the RNA module plus tower. So the whole RNA, including the tower, will be assembled on deck and with a single lift placed on top of the foundation. Research regarding the feasibility of this new floating to floating RNA+ method is needed. Therefore, this thesis will focus on the floating to floating RNA+ installation, a single lift installation of a full WTG, on top of a floater. For this thesis, HES provided a detailed model of SSCV Sleipnir. Figure 1.2 shows the Sleipnir installing a 2.75 pilot WTG.

Figure 1.2: Heerema's Sleipnir installing the pilot 2.75 MW WTG for the FOX project, Courtesy of Heerema

1.2. Floating wind

FOW is a new chapter in the offshore wind business. The first real-life floating wind installation steps started in 2009 [22] with more rapid developments in the last three years. Most of the currently installed floaters are part of a pilot. Currently, more farms are under construction and will be fully commissioned in 2023 [22]

To put that in perspective, in 2023, 0.5% of the installed capacity offshore wind will be caused by floating wind. This shows that offshore floating wind is still in its infancy but has a high potential for further development. In context with bottom fixed offshore wind, the first fixed offshore wind farm was the Vinderby farm in Denmark, constructed in 1991. Consisting of eleven 450 kW WTGs in 4 m water depth, accumulating shy of 5 MW of installed power [23]. Since then, bottom fixed wind has come a long way. In the coming years, FOW is expected to grow substantially and gain a global market share in offshore wind-generated electricity of 15% in 2050 [5]. An overview of the growth in coming decades is given in Figure 1.3.

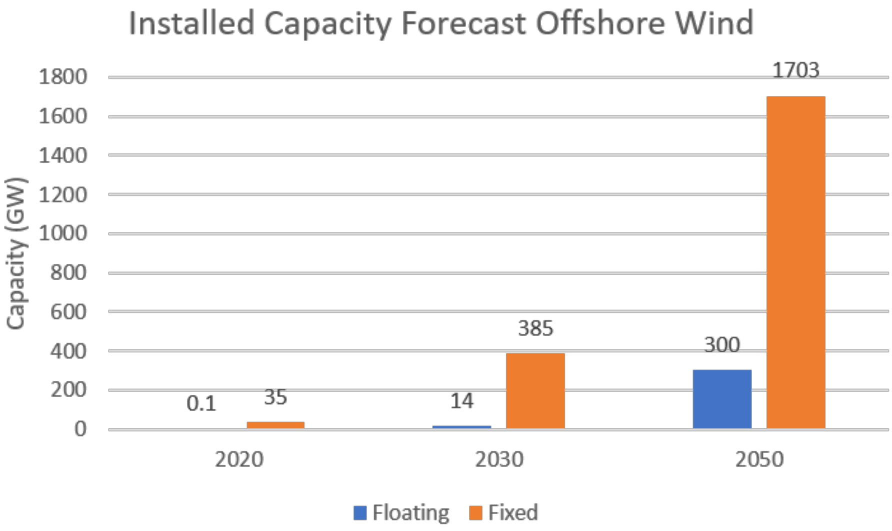

Figure 1.3: Forecast for installed floating versus fixed offshore wind [5]

Fixed offshore wind being the benchmark in OWTs design, currently has a large lead w.r.t. FOW. The vast majority of OWT manufacturers have their manufacturing process designed for fixed wind, as it is a proven design. The same applies to foundation manufacturers and installation entities. Also, existing and outdated fixed wind infrastructure can be refitted with new higher-rated turbines [24]. On the other hand, FOW is still in its infancy, with few proven concepts ready for manufacturing and operation. The developments in FOW for designs to be ready for manufacturing and operation are expected in the coming years [8, 10]. The current developments regarding FOW up to 2050 pave the way for its development to 2100 and beyond.

The predicted growth shown for FOW in Figure 1.3 means that if only 15 MW WTGs are used, 20,000 FOWTs have to be installed in the coming 30 years. In 2021 2,827 OWTs were installed with a total of 15.7 GW, and an average of 5.5 MW per turbine [25]. The installed capacity in the preceding three years was just shy of one-third of the 2021 levels, around 5.2 GW per year [25]. This jump in installed capacity in 2021 is mainly driven by innovation in the Chinese market. Last year 45 of the total 53 new wind farms were installed in Chinese waters, adding 12.7 GW of capacity to the global offshore wind capacity [25]. With the current installation pace, the expected offshore wind capacity growth will not succeed in the given time frame. To realize this goal, FOW installation must be innovated to meet policymakers' demands.

Both the floating and fixed wind capacity will grow significantly over the coming 28 years, as seen in Figure 1.3. As stated before, 80% of Europe's energy potential is at a location with a water depth deeper than 60 m [9]. Also, many offshore structures for both the oil and gas industry and other renewable projects are already in place in these waters. A visualization of these aspects is given in Figure 1.4

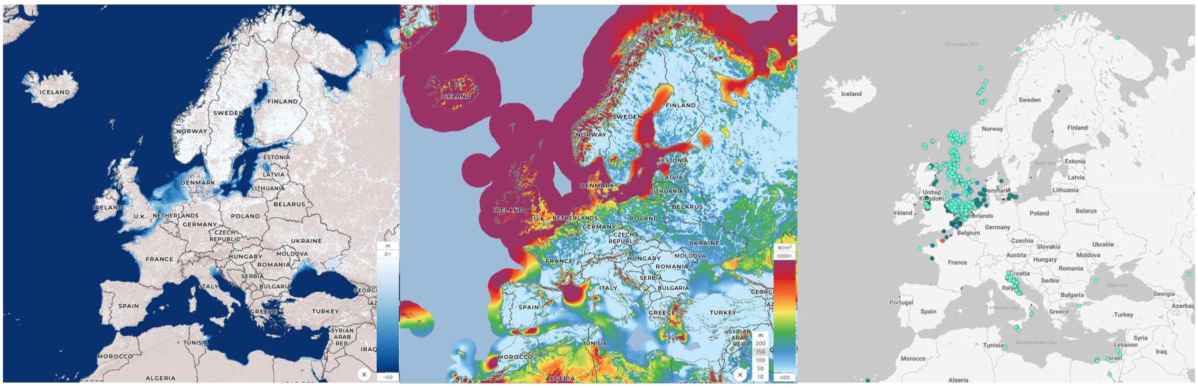

(a) (b) (c)

Figure 1.4: Bathymetry in m [legend range -60 to 0 m] [26] Mean Wind Power density at 150 m height in $\frac{W}{m^2}$ [legend range 400 to 1000+ $\frac{W}{m^2}$] [26] Structures currently build, constructed and planned [27]; in European waters

Hywind Scotland, a floating wind farm in operation since 2017, achieved the highest average capacity of all offshore farms in the United Kingdom (UK) [7]. Next to the fact that shallow water sites are becoming scarcer, the energy generation of floating wind farms could be better than that of fixed farms. Currently, the Levelized Cost of Energy (LCOE) of fixed offshore wind in 2020 was 56 USD/MWh. For FOW, this is much higher at 222 USD/MWh [5]. By 2050 these are expected to lower to 31 and 43 USD/MWh. This drop of 179 USD/MWh is mainly due to non-turbine costs, being the floater design and installation costs. With the proper investments and innovation, the LCOE of FOW will thus be lower than the current cost for fixed offshore wind.

The three main floating wind foundation principles are a Spar-buoy (Spar), a Semi-submersible (Semi-sub), and a Tension Leg Platform (TLP) shown in Figure 1.5. A fourth principle exists, being a barge foundation. However, this principle is not considered because of its poor hydrodynamic behavior in moderate and harsh weather conditions [22].

Figure 1.5: The three floater foundation concepts. Spar-buoy (Spar), Semi-submersible (Semi-Sub) and Tension Leg Platform (TLP) [28]

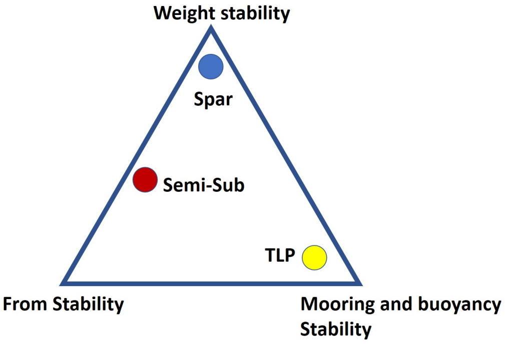

Figure 1.6: stabilization principle per floater type. Adapted from [29]

The three floaters have different stabilization principles, as shown in Figure 1.6 and described in the paragraphs below.

Spar-Buoy A Spar is a ballast-stabilized structure that relies on having a high center of buoyancy and a low center of gravity, see Figure 1.7. This floating principle uses the coupling between the buoyancy force, F_b, and the gravity force, F_g, to create a restoring moment, as shown in Figure 1.8. Because of the low center of gravity, most spars need a large draft of >100m during installation and operation [8].

Semi-Submersible A Semi-Sub is a form-stabilized structure with a relatively big water plane area. It remains stable due to the shift in buoyancy between its legs, see Figure 1.8. For a Semi-Sub to maintain its stability, a large structure is needed [30]. This results in the Semi-Sub having the highest average weight but the lowest draft requirements of the three principles [8].

Tension Leg Platform A TLP is a very buoyant structure anchored to the seabed with tensioned mooring lines (tendons). A Free Body Diagram (FBD) of the static forces is given in Figure 1.7. Stability is obtained due to the tension in the tendons resulting in a tendon-induced restoring moment, see Figure 1.8. This tension stability and its limited draft result in a smaller and thus lighter structure [8]. Furthermore, compared to the other floaters' limited platform motions are expected, engendering in lower structural loading on the tower and blades. This results in the need for less stiff and thus lighter WTG towers [31].

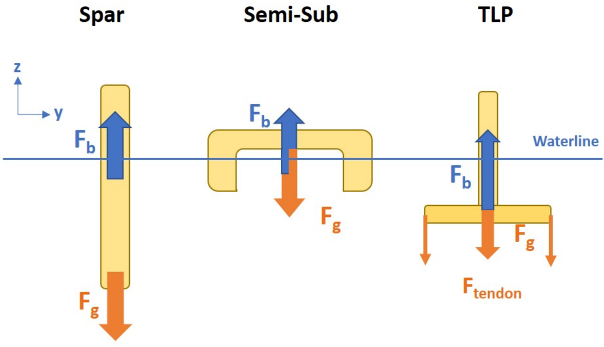

Figure 1.7: Floating principle Floaters

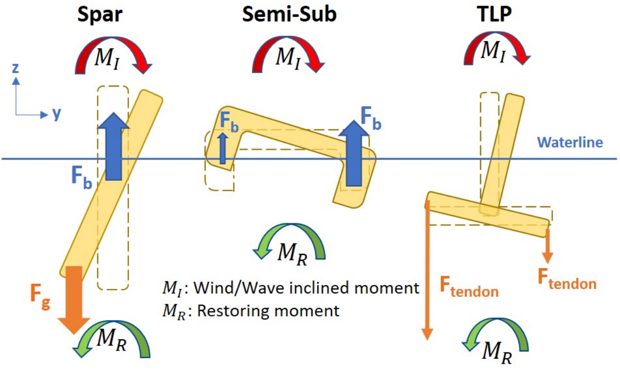

Figure 1.8: Restoring moment per floater type

For this research, a TLP is chosen. From a floating to floating installation on-site point of view, the TLP is the most interesting floater type to consider. For a SPAR, the floating to floating installation must occur in sheltered waters due to its motion behavior [10]. As the final location is often not sheltered, an additional tow to its final destination is needed. A Semi-Sub is best suited for a port assembly and Tow-out due to its free-floating stability and size [8]. A TLP is relatively smaller in size and has the least motion in heave compared to the other floater types [8]. Therefore, a TLP is assessed for this research. Below, some background information and elaboration regarding the choice for the TLP is given.

1.2.1. TLP

As described above, a TLP is a very buoyant structure. For most offshore and marine structures, their structural mass and displacement in tonnes are equal, as the buoyancy force equals the gravitational force. For a TLP, this is not the case. Its stability comes from the tensions in the tendons. This tendon force, in combination with its gravitational force, equals the buoyancy force. The tendons of a TLP are very stiff, and thus a TLP will not move significantly in heave direction. Therefore, looking at the static case, its displacement will not vary due to installing a WTG on top of it. Because of this 'constant' buoyancy force, the WTG's added weight must be accounted for by the tendons. The design tension for a FOW TLP is designed for its installed state. Therefore, the tendons must account for the lack of top weight in its uninstalled state. The tension in the tendons before the WTG is installed is called the pre-tension. The installation of the WTG will lead to a reduction in pre-tension equal to the weight of the WTG. For an overview see Subsection 3.2.4.

1.2.2. Wind Turbine Generator

The capacity of WTGs and their size is estimated to grow significantly in the coming years. The estimate by the International Energy Agency (IEA) can be seen in Figure 1.9

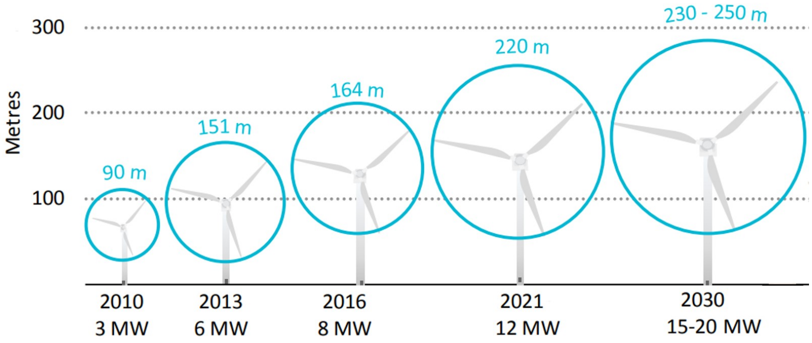

Figure 1.9: IEA's 2019 prediction for WTG capacity and size growth, Altered from [32]

A task force of the IEA has designed a reference turbine to accommodate offshore wind developers with a publicly available benchmark for advancement in offshore wind development. This reference turbine bridges the gap between the industry and academics and offers an entry point for educational purposes [33]. As WTGs with 15 MW capacity and over are expected to be manufactured and installed in the near future, this 15 MW Reference turbine is chosen for this study.

There are three types of WTG tower designs, soft-soft, soft-stiff, and stiff-stiff. The terms soft and stiff represent the value of the first natural frequency of the towers. To avoid resonance, the natural frequency of the towers should be outside the wind and wave spectrum peak frequencies. Furthermore, their natural frequency should be outside the bandwidth of the 1P and 3P frequencies. The 1P frequency is the rotational speed of the turbine, the frequency of a full rotation of all the blades. The 3P frequency is the single-blade passing frequency and equals three times the 1P frequency. For a soft-stiff tower, its natural frequency lies between the 1P and 3P frequencies. A soft-soft tower has its first natural frequency below the 1P frequency. For a stiff-stiff tower it lies above the 3P frequency. An overview of this is given in Figure 1.10

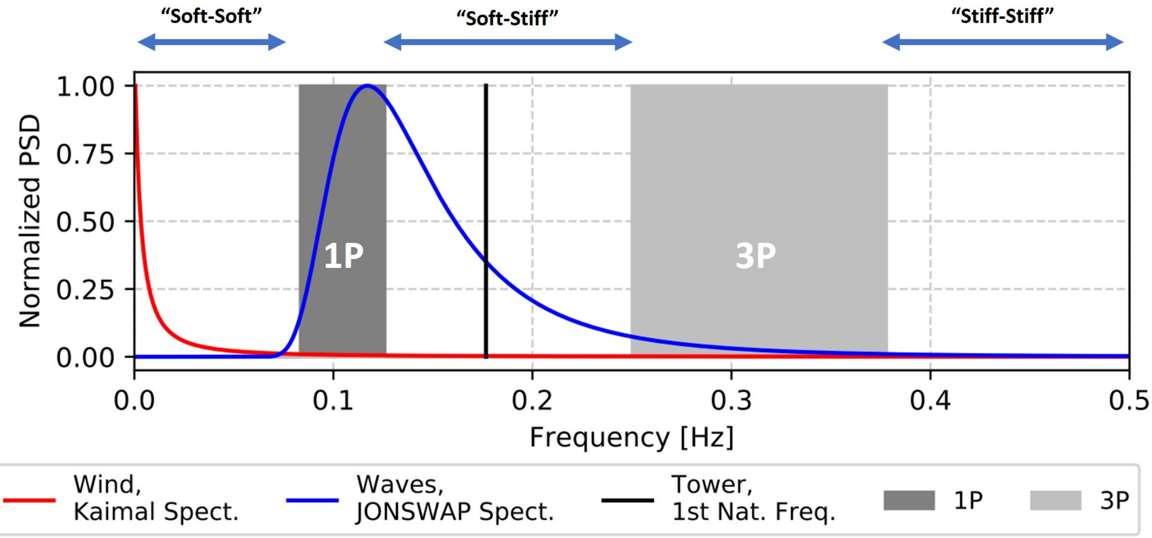

Figure 1.10: Stiffness definitions for WTG towers frequencies w.r.t. wind/wave spectra and 1P/3P frequencies relative to normalize power spectral density (PSD). Altered from [33]

The red line shows the Kaimal wind spectrum and its corresponding peak frequency. The blue line shows the ocean wave frequencies of a JONSWAP spectrum. The dark grey block on the left shows the range of the 1P frequency. The block on the right denotes the range of 3P frequencies. For fixed offshore wind, mainly soft-stiff towers are used. However, for some floating configurations, these are not sufficient due to platform motions, and more rigid stiff-stiff towers are needed [33].

1.3. Problem statement

FOW is a novelty market, ready for innovation and other new designs. Because of this novelty, most components of FOW are designed with respect to known fixed wind designs and are not yet connected to the other FOW designs. Gearboxes, for instance, may suffer from problems due to floater motions. Design or installation choices influence the total outcome of a FOW Design. For example, a TLP has lesser platform motions [34, 35] with respect to other floater types. Because of this motion behavior, less structural loading is transferred from a TLP to the WTG tower [31]. Therefore, a lighter soft-stiff tower can be used for a TLP. For the IEA reference turbine, using a soft-stiff tower results in a 403 t weight reduction with respect to the stiff-stiff tower [33]. Less structural weight of the WTG tower could lead to other possibilities in the installation process. The installation location and methodology of a FOWT could influence the design of the TLP. For the TLP specially designed by Intecsea for this research, a TLP for Tow-Out installation is 325 t heavier than the one for on-site installation. These are some examples of design/installation choices that influence the overall outcome of the development of FOWTs. Nevertheless, which component of FOWT designs becomes the leading factor in the installation and design process is yet to be resolved. Does the WTG determine the design of the floater, the other way around, or does the installation asset control the outcome of the integrated design? These design choices together contribute to the expected drop in LCOE of FOW. A higher operability results in fewer vessel days needed, leading to lower installation costs and, thus, a lower LCOE.

Therefore, the following research question is formulated:

”What is the influence of the design parameters of a WTG, TLP, and iguration on the operability of a floating to floating single lift installation of a 15MW WTG on a TLP with an SSCV?”

1.4. Research scope

The main objective of this research is to conduct a sensitivity study on the influence of FOW design parameters with respect to the operability of the installation process. In this research, the floating to floating installation of the IEA 15 MW reference turbine [33] with an altered tower on top of a TLP with Heerema’s SSCV Sleipnir is assessed. This analysis is done in the frequency domain (FD) and considers only first-order effects. As multiple simulations with varying parameters are assessed rather than one specific configuration, the FD is chosen. The TLP is pre-installed, and the WTG is fully assembled and suspended in the crane with the bottom of the tower 3 m above the TLP. This 3 m clearance is set by DNV [36] to be the margin between the underside of the lifted object and any other previously installed structure(s) during lifting. The full RNA+ installation sequence is as follows: First, the RNA+ module is assembled on deck. Next, the module is lifted off the deck and aligned with the foundation. During this stage, all clearances between the load and other objects need to stay above 3 m. This aligned stage 3 m above the foundation is called the Free Hanging stage. Then the set-down sequence begins, where the module first contacts the mating tool and later the foundation itself. This sequence consists of multiple Pre-tension stages that embody transferring the WTG loads from the crane to the foundation. In practice, when the WTG and TLP are lined up and vertically 3 m apart in its free-hanging stage, the ”set-down sequence” begins. If the conditions are favorable, the set-down can begin from this point. Thus, if there is no operability in the free-hanging stage, the set-down sequence cannot succeed. Therefore, the free-hanging stage with a clearance of 3 m is chosen for this research. The set-down of the WTG on top of the TLP itself is not considered. Furthermore, this study does not assess whether the alterations to the WTG/TLP are feasible for their operational state.

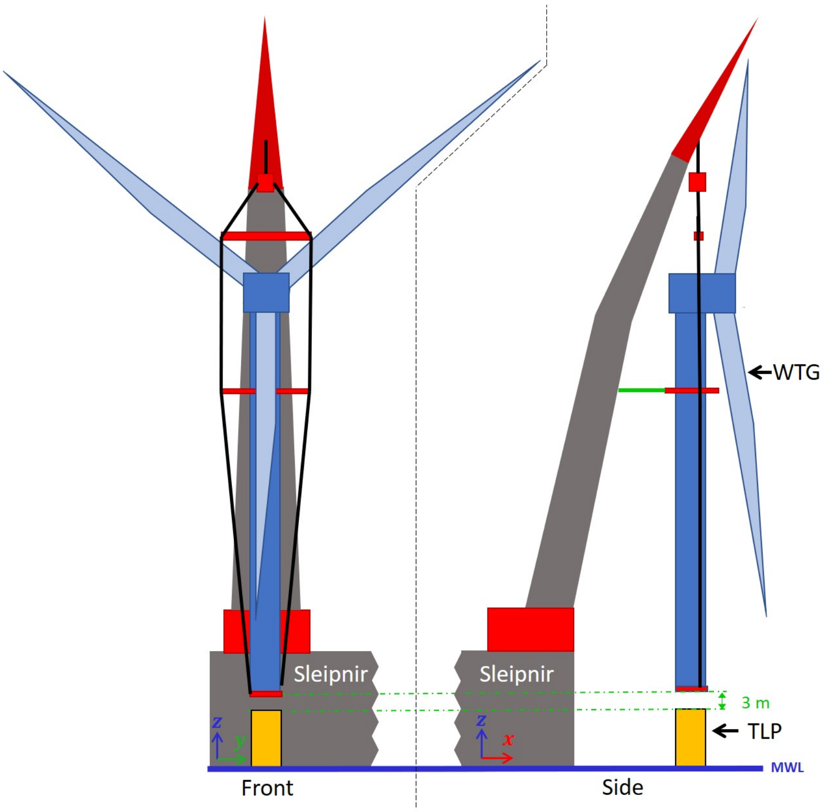

Figure 1.11: Visualization of scope, front and side view

1.5. Thesis structure

This thesis consists of 6 chapters. This first chapter contains the introduction. Chapter 2 gives the theoretical background for this thesis. Single and multi-body Equations Of Motion (EOMs) in the FD and Response Amplitude Operators (RAOs) are deducted, and the interpretation and aspects of operability are given. In Chapter 3, the setup of the base case model, the relevant parameters, and used software packages are discussed. The variations of these parameters with respect to the base case are presented in Chapter 4. The results of the change in operability due to these variations are discussed in Chapter 5. Chapter 6 contains the conclusion and recommendations of this thesis. An overview of the structure of this research is given in Figure 1.12.

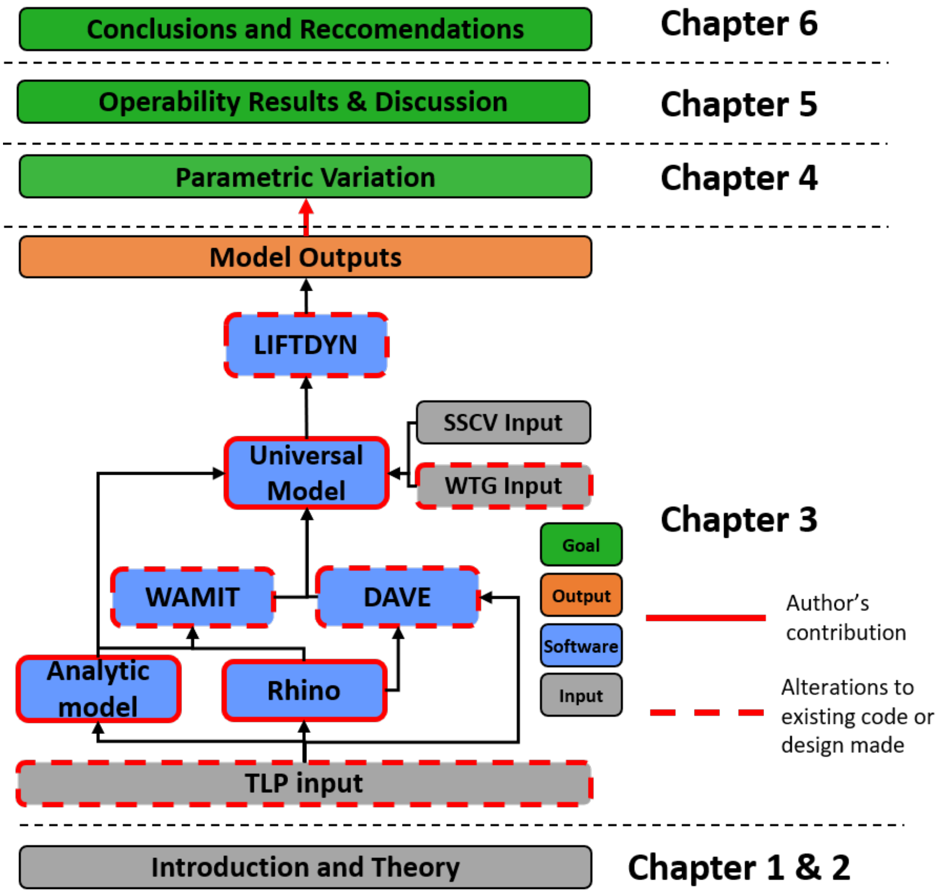

Figure 1.12: Thesis structure

2

Theory

In this Chapter, the theoretical background for the model is presented. The single- and multi-body Equations of Motion (EoM) are discussed. Furthermore, the definition and approach for operability are discussed.

2.1. Equations of motion

2.1.1. Single Body

The EoM, Equation 2.1, for a dynamic system with a single Degree of Freedom (DOF) x, expresses the dynamic force equilibrium of the inertia-, damping- and restoring forces on the left-hand side. An external force F_{ex} on the system completes the equation on the right-hand side. The inertia forces are the product of the mass m and the acceleration $\ddot{x}$. The damping term is expressed as the damping coefficient b times the velocity $\dot{x}$. The restoring force is given by the spring stiffness c and the displacement x of the body.

$$m \cdot \ddot{x}(t) + b \cdot \dot{x}(t) + c \cdot x(t) = F_{\text{ext}}(t) \tag{2.1}$$

For a body with 6 DOF, the scalar displacement x is replaced by the vector of the displacements $\vec{\xi}$, shown in Equation 2.2

$$\vec{\xi} = \begin{bmatrix} x \\ y \\ z \\ \varphi \\ \theta \\ \psi \end{bmatrix} = \begin{bmatrix} Surge \\ Sway \\ Heave \\ Roll \\ Pitch \\ Yaw \end{bmatrix} \tag{2.2}$$

The scalar parameters of mass m, damping coefficient b, and spring stiffness c then become 6x6 matrices being the: mass matrix **M**, damping matrix **B**, and stiffness matrix **C**, respectively. On the right-hand side of the equation, the force F_{ex} also becomes a vector with length 6. For bodies exposed to waves, the force vector $\vec{F_{wave}}$ is distinguished from the external force vector to accommodate for wave-induced forces acting on the system.

$$(\mathbf{M}) \cdot \ddot{\vec{\xi}}(t) + (\mathbf{B}) \cdot \dot{\vec{\xi}}(t) + (\mathbf{C}) \cdot \vec{\xi}(t) = \vec{F}_{\text{wave}}(t) + \vec{F}_{\text{ext}}(t) \tag{2.3}$$

For a floating body of arbitrary shape, the mass matrix **M** given in Equation 2.4 contains the dry mass m and moments of inertia J_{xx}, J_{yy}, and J_{zz} on the main diagonal as well as the full matrix of added mass coefficients a_{ij}, representing the hydrodynamic force in direction i due to motion in direction j with i,j = [1...6].

$$\mathbf{M} = \begin{bmatrix} m + a_{11} & a_{12} & a_{13} & a_{14} & a_{15} & a_{16} \\ a_{21} & m + a_{22} & a_{23} & a_{24} & a_{25} & a_{26} \\ a_{31} & a_{32} & m + a_{33} & a_{34} & a_{35} & a_{36} \\ a_{41} & a_{42} & a_{43} & J_{xx} + a_{44} & a_{45} & a_{46} \\ a_{51} & a_{52} & a_{53} & a_{54} & J_{yy} + a_{55} & a_{56} \\ a_{61} & a_{62} & a_{63} & a_{64} & a_{65} & J_{zz} + a_{66} \end{bmatrix} \tag{2.4}$$

The damping matrix **B** for a floating body of arbitrary shape is given in Equation 2.5. Damping coefficients b_{ij}, representing the hydrodynamic damping force in direction i due to motion in direction j with i,j = [1...6].

$$\mathbf{B} = \begin{bmatrix} b_{11} & b_{12} & b_{13} & b_{14} & b_{15} & b_{16} \\ b_{21} & b_{22} & b_{23} & b_{24} & b_{25} & b_{26} \\ b_{31} & b_{32} & b_{33} & b_{34} & b_{35} & b_{36} \\ b_{41} & b_{42} & b_{43} & b_{44} & b_{45} & b_{46} \\ b_{51} & b_{52} & b_{53} & b_{54} & b_{55} & b_{56} \\ b_{61} & b_{62} & b_{63} & b_{64} & b_{65} & b_{66} \end{bmatrix} \tag{2.5}$$

Spring matrix **C** for a moored structure consists of two submatrices being $\mathbf{K}_{moor}$ and $\mathbf{K}_{hyd}$.

$$\mathbf{C} = \mathbf{K}_{moor} + \mathbf{K}_{hyd} \tag{2.6}$$

$\mathbf{K}_{moor}$ contains the spring values induced by the mooring system on the floating body. On the diagonal, the spring values for the 6 DOF are shown. The mooring spring coefficients $k_{m_{ij}}$ show the coupling for spring coefficients in direction i due to motion in direction j with i,j = [1...6]

$$\mathbf{K}_{moor} = \begin{bmatrix} k_{m,11} & 0 & 0 & 0 & k_{m,15} & 0 \\ 0 & k_{m,22} & 0 & k_{m,24} & 0 & 0 \\ 0 & 0 & k_{m,33} & 0 & 0 & 0 \\ 0 & k_{m,42} & 0 & k_{m,44} & 0 & 0 \\ k_{m,51} & 0 & 0 & 0 & k_{m,55} & 0 \\ 0 & 0 & 0 & 0 & 0 & k_{m,66} \end{bmatrix} \tag{2.7}$$

$\mathbf{K}_{hyd}$ denotes the hydrostatic stiffness of a floating body. It can be seen that this stiffness applies to DOFs heave, roll, and pitch. There is a coupling between heave and pitch for asymmetrical bodies where the Center of Flotation (CoF) and Center of Buoyancy (CoB) are not aligned.

$$\mathbf{K}_{\text{hyd}} = \begin{bmatrix} 0 & 0 & 0 & 0 & 0 & 0 \\ 0 & 0 & 0 & 0 & 0 & 0 \\ 0 & 0 & \rho\cdot g\cdot A_{WL} & 0 & -\rho\cdot g\cdot A_{WL}\cdot(CoF-CoB) & 0 \\ 0 & 0 & 0 & \rho g\nabla\cdot GMT & 0 & 0 \\ 0 & 0 & -\rho\cdot g\cdot A_{WL}\cdot(CoF-CoB) & 0 & \rho g\nabla\cdot GML & 0 \\ 0 & 0 & 0 & 0 & 0 & 0 \end{bmatrix} \tag{2.8}$$

Where A_{wl} is the water-plane area. GMT and GML are the transverse and longitudinal metacentric heights, respectively.

The Time Domain (TD) EoM is then converted to a Frequency Domain (FD) EoM using Equation 2.9 and Equation 2.10

$$\begin{aligned} \vec{\xi}(t) &= \hat{\chi}_a(\omega)\cdot\sin(\omega t+\varepsilon) \\ \dot{\vec{\xi}}(t) &= \omega\cdot\hat{\chi}_a(\omega)\cdot\cos(\omega t+\varepsilon) \\ \ddot{\vec{\xi}}(t) &= -\omega^2\cdot\hat{\chi}_a(\omega)\cdot\sin(\omega t+\varepsilon) \end{aligned} \tag{2.9}$$

$$\begin{aligned} \vec{F}_{\text{wave}}(t) &= \vec{F}_a(\omega)\sin(\omega\cdot t+\varepsilon_F(\omega)) \\ \vec{F}_{\text{ext}}(t) &= 0 \end{aligned} \tag{2.10}$$

This results in the following FD EOM:

$$\left[-(\mathbf{M})\omega^2 + (\mathbf{B})i\omega + (\mathbf{C})\right]\cdot\hat{\chi}_a(\omega) = \vec{F}_{\text{a}} \tag{2.11}$$

2.1.2. Multi body EOMs

In this research, three bodies with 6 DOF and one with 3 DOF are used, resulting in a total of 21 DOF. The first three bodies subjected to 6 DOF are the Vessel, TLP, and RNA+ module. The 6 DOF being surge (x), sway (y), heave (z), roll (φ), pitch (θ) and yaw (ψ). The Crane-Block is considered a point mass and can only move in surge (x), sway (y), and heave (z) direction.

With 21 DOF Equation 2.11 becomes:

$$\left[-(\mathbf{M}_{i,j})\omega^2 + (\mathbf{B}_{i,j})i\omega + (\mathbf{C}_{i,j})\right] \cdot \hat{\chi}_{a,j}(\omega) = \vec{F}_{\mathrm{a,j}} \tag{2.12}$$

Where:

$\mathbf{M}_{i,j}$ = 21 x 21 Mass and Added Mass Matrix [1]

$\mathbf{B}_{i,j}$ = 21 x 21 damping matrix [2]

$\mathbf{K}_{i,j}$ = 21 x 21 stiffness matrix

$\mathbf{F}_{a,j}$ = 21 row vector containing the forces and moment in direction j

$\hat{\chi}_{a,j}(\omega)$ = 21 row displacement vector

With displacement vector $\hat{\chi}_{a,j}(\omega)$ defined as:

$$\left[\hat{\chi}_{a,j}\right]^T = \left[\begin{array}{cccccccccc} x_1 & y_1 & z_1 & \phi_1 & \theta_1 & \psi_1 & x_2 & y_2 & \dots & \psi_i \end{array}\right] \quad \text{for: } i = 1, \dots 4 \tag{2.13}$$

Where:

x_i = translation of body i in global $x-$ direction

y_i = translation of body i in global $y-$ direction

z_i = translation of body i in global $z-$ direction

ϕ_i = rotation of body i about global $x-$ axis [3]

θ_i = rotation of body i about global $y-$ axis [3]

ψ_i = rotation of body i about global $z-$ axis [3]

Mass and Added Mass Matrix

The 21 x 21 Mass and Added Mass matrix is defined as follows:

$$\mathbf{M}_{i,j} = \begin{bmatrix} (m_1 + a_{1,1}) & a_{1,2} & \dots & a_{1,j} \\ a_{2,1} & (m_2 + a_{2,2}) & \dots & a_{2,j} \\ \vdots & \vdots & \ddots & \vdots \\ a_{i,1} & a_{i,2} & \cdots & (J_{zz,5} + a_{i,j}) \end{bmatrix} \quad \text{for: } i,j = 1, \dots 21 \tag{2.14}$$

Where:

m_i = the mass of the body

$a_{i,j}$ = the added mass coefficient of the body [1]

$J_{i,j}$ = the mass moment of inertia of a body

---

[1] Only bodies immersed in water have added mass properties, being the Vessel and TLP

[2] Only bodies immersed in water have damping properties, being the Vessel and TLP. Minimum damping in the model is accounted equal to 1.5% of the critical damping, which is the standard approach in Liftdyn

[3] The crane block is restricted in all rotational DOF, resulting in $\phi_i = \theta_1 = \psi_i = 0$

Damping Matrix

The 21 x 21 Damping matrix is defined as follows:

$$\mathbf{B}_{i,j} = \begin{bmatrix} (b_{1,1} + b_{\text{visc}}) & b_{1,2} & \cdots & b_{1,j} \\ b_{2,1} & (b_{2,2} + b_{\text{visc}}) & \cdots & b_{2,j} \\ \vdots & \vdots & \ddots & \vdots \\ b_{i,1} & b_{i,2} & \cdots & (b_{i,j} + b_{\text{visc}}) \end{bmatrix} \quad \text{for: } i,j = 1, \ldots 21 \tag{2.15}$$

Where:

b = Wave radiation damping

b_{visc} = Viscose damping

Stiffness Matrix

The 21 x 21 Stiffness matrix is defined as follows:

$$\mathbf{C}_{i,j} = \begin{bmatrix} k_{1,1} & k_{1,2} & \cdots & k_{1,j} \\ k_{2,1} & k_{2,2} & \cdots & k_{2,j} \\ \vdots & \vdots & \ddots & \vdots \\ k_{i,1} & k_{i,2} & \cdots & k_{i,j} \end{bmatrix} \quad \text{for: } i,j = 1, \ldots 21 \tag{2.16}$$

Where: k = Spring coefficients shown in Equation 2.6. A specification of these coefficients for the TLP is given in Subsection 3.2.7.

2.2. Response Amplitude Operator

A Response Amplitude Operator (RAO) is a transfer function used to determine the effect of a wave with wave elevation ζ_a on the amplitude of a motion of a floating body, w.r.t. different wave frequencies. Due to the assumption of harmonic excitation forces, RAOs are frequency dependent. An RAO can be defined for each given location or internal force of a floating structure. By assuming Equation 2.13 is harmonic, an RAO is described as:

$$RAO(\omega, \varepsilon) = \left|\hat{\chi}_a \cdot \zeta_a^{-1}\right| = \left|F_a(\omega, \varepsilon) \cdot \left[-(\mathbf{M})\omega^2 + (\mathbf{B})i\omega + (\mathbf{C})\right]^{-1}\right| \tag{2.17}$$

Where:

ω= the wave frequency

ε = wave direction

ζ_a = wave amplitude

2.3. Wave Spectrum

The wave spectrum for this research is a JONSWAP spectrum with a peakedness factor γ of 3.3. This is the spreading for a mean JONSWAP spectrum [36]. The mean JONSWAP spectrum is defined as follows [37]:

$$S_\zeta(\omega) = \frac{320 \cdot {H_s}^2}{{T_p}^4} \cdot \omega^{-5} \cdot \exp\left\{\frac{-1950}{{T_p}^4} \cdot \omega^{-4}\right\} \cdot \gamma^{\exp\left\{-\left(\frac{\frac{\omega}{\omega_p} - 1}{\sigma\sqrt{2}}\right)^2\right\}} \tag{2.18}$$

With:

ω_p = the circular frequency at spectral peak, $\frac{2\pi}{T_p}$

σ = a step function of ω: if $\omega < \omega_p$; σ = 0.07

if $\omega > \omega_p$; σ = 0.09

The Theoretical relations of the characteristic periods are given as [37]:

$$T_{mo1} = 1.073 \cdot T_{m02} = 0.834 \cdot T_p \tag{2.19}$$

2.4. Response Spectrum

When the wave spectrum, $S_\zeta(\omega)$, and RAO of a body are derived. One can calculate the response per DOF of the said body to the used wave spectrum, see Equation 2.20.

$$S_\zeta(\omega) \cdot RAO^2\,(\omega) = S_{resp}(\omega) \tag{2.20}$$

The response spectrum defines how a body responds when it is subjected to a given wave spectrum. A visualization of the response spectrum for a given wave spectrum and motion RAO is shown in Figure 2.1. This response can be subjected to operational limits to determine the operability.

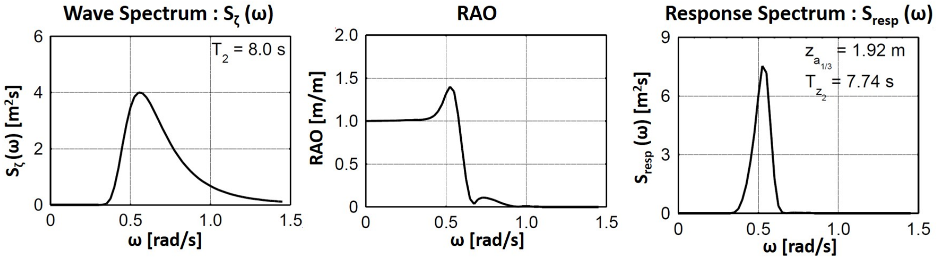

Figure 2.1: Visualization of creating response spectrum, altered from [38]

2.5. Operability

2.5.1. Definition

The term operability in this thesis is defined as an indication of the maximum sea state in which an offshore operation can be performed without exceeding pre-defined limiting criteria. It is presented as an operability curve indicating the maximum allowable wave height H_s as a function of the peak period T_p of a standard theoretical wave spectrum. This is Heerema's definition of operability, used in their assessments of offshore activities [39]. Operability is often confused with workability. Workability indicates the resulting duration of the operation itself, with a given site and time-specific weather data, as a fraction of the actual duration, including the waiting on weather. So where workability evaluates a specific short-term location- and time frame for an offshore operation, operability assesses the possibility of this operation from a broader perspective. An example of a H_s-T_p curve for three different operational limits, with corresponding wave scatter diagram, is given in Figure 2.2. Operations can be executed if their H_s-T_p values are below the indicated lines.

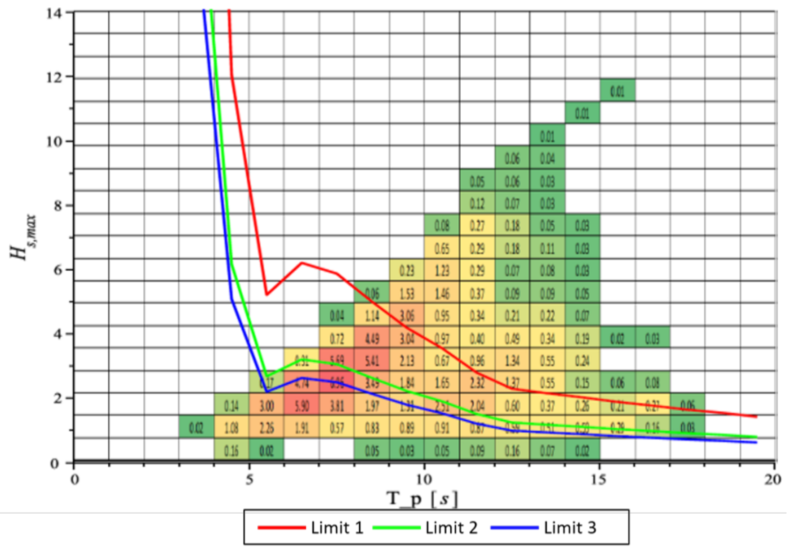

Figure 2.2: Example of a H_s-T_p curve for three operational limits, with corresponding wave scatter diagram. Altered from [40]

2.5.2. Considered Sea-States

To get a representation of the waves in a spectrum in the design stage of an offshore installation, DNV defined a range to consider wind and swell-dominated areas within the wave spectrum depending on H_s. These considered sea states for this study are defined by DNV as follows: The H_s - T_p combinations for the H_{s-lim} are based on these three curves:

$$\begin{aligned} H_s &= T_p^2/13 && \text{for } Tp < \sqrt{13 * H_{s-Lim}} \\ H_s &= H_{s-Lim} && \text{for } \sqrt{13 * H_{s-Lim}} < T_p < \sqrt{30 * H_{s-Lim}} \\ H_s T_p^2 &= H_{s-Lim} * \sqrt{30 * H_{s-Lim}}^2 = 30 * H_{s-Lim}^2 && \text{for } Tp > \sqrt{30 * H_{s-Lim}} \end{aligned} \tag{2.21}$$

The first two curves cover wind-developing wave spectra for H_{s-lim} according to Section 3.4.11.5 in [36]. Based on the wave-breaking limit, the first curve physically represents the maximum H_s for a range of periods up to $T_p^3/13$. The second curve covers the range of periods where an H_{s-lim} can occur in a wind-developing sea state. The third curve covers longer wave periods representative of swell sea states up to T_p equal to 15 s considering an $H_s T_p^2$ equal to $30H_{s-Lim}^2$. A visualization of these curves is given in Figure 2.3

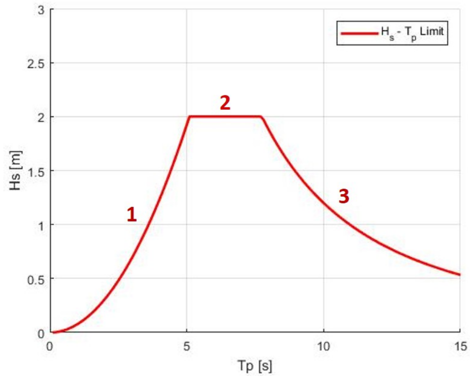

Figure 2.3: Visualization of Equation 2.21

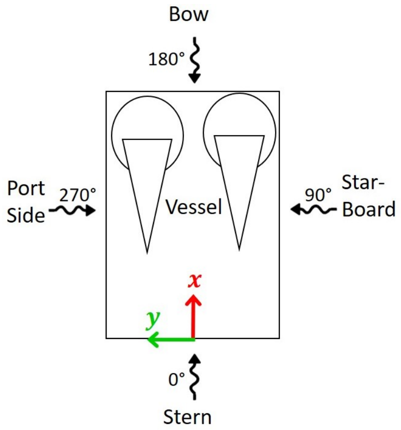

Figure 2.4: Vessel coordinate system and wave direction definition

For all considered sea states, the wave spreading factor of n = 10 is used when spreading is modeled as cos^n. This value should be representative for both high wind sea-states (upper bound) as well as swell sea-states (lower bound) according to Section 3.5.8.7 in [41]. All possible wave directions with a bin of 15 deg are checked in this research. The definition of wave directions is given in Figure 2.4.

2.5.3. Determination - Most probable maximum

The 3-hour Single Most Probable Maximum (3h SMPM) values for this research are used for the limiting criteria. Assuming a Rayleigh distribution, the MPM can be determined using the following:

$$MPM = \sigma \sqrt{\frac{1}{2} \ln \left(\frac{T_{duration}}{T_{m02}} \right)} \tag{2.22}$$

With σ being the Root Mean Square (RMS) of the water surface elevation. and defined as [37]:

$$\sigma = \sqrt{m_0} \tag{2.23}$$

With m_0 being the 0^{th} spectral moment, and is equal to the area under the spectrum. It can be derived with:

$$m_n = \int_0^\infty \omega^n S_\zeta(\omega) d\omega \quad \text{for: } n = 0, 1, 2 \ldots \tag{2.24}$$

To determine the MPM for the the significant wave amplitude ζ_{a_s}, σ in Equation 2.22 is exchanged with:

$$\zeta_{a_s} = 2 \cdot \sqrt{m_0} = SSA = \frac{H_s}{2} \tag{2.25}$$

Where SSA is the Significant Single Amplitude, being the significant wave amplitude. The Significant Double Amplitude (SDA) is equal to the Significant wave height H_s, which is two times the SSA.

For a 3 h storm and a mean JONSWAP spectrum H_{max} is defined as [37]:

$$H_{max} = 1.86 \cdot H_s \tag{2.26}$$

So Equation 2.26 becomes:

$$SSA_{max} = \zeta_{a_{max}} = \frac{H_{max}}{2} = \frac{1.86}{2} \cdot H_s \tag{2.27}$$

2.5.4. Significant Response and operability

Provided that the wave spectrum is defined using H_s, The SDA instead of the SSA should be considered. The significant double response $\vec{\chi_s}\left(\omega_p, \vec{\varepsilon}\right)$ is then determines as follows:

$$\hat{\chi_s}\left(\omega_p, \hat{\varepsilon}\right) = 4 \cdot \sqrt{\int_0^\infty \{RAO(\omega, \vec{\epsilon})\}^2 \cdot S_\zeta\left(\omega, \omega_p\right) \cdot d\omega} \tag{2.28}$$

Given the maximum allowable SDA, the maximum allowable wave height $H_{s\ max}$ can be determined by dividing the maximum allowable value by the response to a unity wave:

$$H_{s,\ max}\left(\omega_p, \vec{\varepsilon}\right) = \frac{SDA_{max}}{\vec{\chi_s}\left(\omega_p, \vec{\varepsilon}\right)} \tag{2.29}$$

3

Model Setup

This chapter discusses the configuration and assembly of the whole model. The model consists of three main bodies: The TLP, the WTG, and the installation vessel. Below, the configuration of these bodies and their integration is discussed. The model is built in the python environment Universal Model (UM). This is a software package where one can model bodies and lines with their physical properties. It gives a visualization of the coded model to perform numerical and visual checks. Furthermore, it provides a uniform model that can be exported to most known formats, data types, or software tools such as OrcaFlex and LiftDyn. This universality between programs allows checking different model steps independent from the program. It also gives the opportunity to add unforeseen model steps during the modeling process. The goal of this model is to generate an input file for LiftDyn. With LiftDyn, an FD analysis can be conducted to get the desired operability curves.

3.1. Model Setup

Intecsea provided the TLP used in this model. It is a non-existing floater, using basic floater principles, and is scaled to be used for a 15 MW WTG. The IEA 15 MW reference turbine [33] with an altered tower is used for this model. This WTG is a non-existing turbine designed for use in academic research with publicly available data. The installation vessel is Heerema's Sleipnir, currently the world's largest SSCV, with the highest Safe Working Load (SWL) [42].

3.1.1. Modeling Methodology

In Figure 3.1 a visualization of the methodology of the model configuration is given. Table 3.1 gives a more detailed description of the in and outputs for the used software.

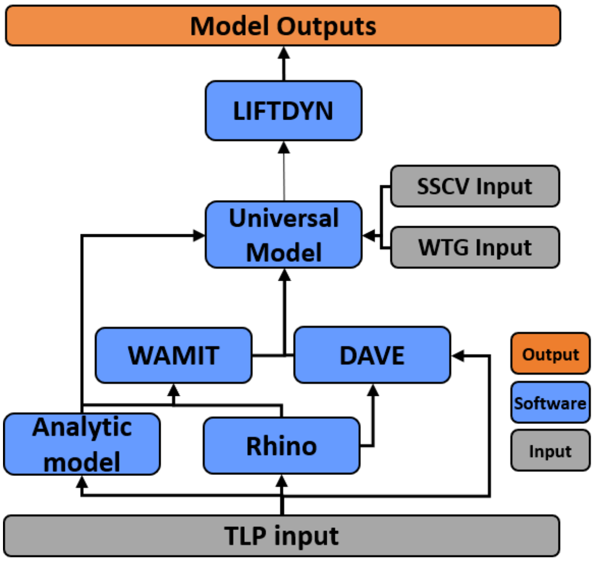

Figure 3.1: Methodology flow chart

Table 3.1: Methodology overview

Input →	Method →	Output
- Geometry - Mass and COGs - Mooring (line) configuration	**Analytic model**	- Mass distribution - Radii of gyration, mass inertia moments - Hydrostatics - Mooring line tension
- Geometry - Mass and VCG - Outputs Analytic model	**Rhino** [43]	- Mass distribution - Radii of gyration and mass moments - Hydrostatics - .GDF mesh for WAMIT - .obj file for Carene Table and visualization in UM
- .GDF mesh - Hydrostatics	**WAMIT** [44]	- Force RAOs - .out file → export to OrcaFlex - .hyd file, hydrodynamic properties → export to Universal model
- .obj file - Mass & COG	**DAVE** [45]	- Carene Table
- Geometry and POIs - Mass and COGs - Mooring (line) configuration - .obj files (visualization) - Constraints - Carene Table - .hyd file - Sleipnir model - Parametric variations	**Universal Model**	- Solved Hydrostatics - Visualisation of all model dimensions, properties, and inputs - Local and global positions - Constraints - Cable tension - .inp file → Export to LiftDyn
- .hyd file - .inp file - Wave spectrum - Limiting criteria	**LiftDyn**	- Model checks - (eigen) Mode shapes - Static response - RAOs - Significant motion Responses - Operability curves (H_s-T_p curve)
- LiftDyn outputs	**Post Process**	- Effects and sensitivities of parametric variations on operability

3.1.2. Modeling Software

In this subsection, the used software programs and their applications are presented.

WAMIT

WAMIT [44] is a software program to determine wave-induced motions and loads of offshore structures in waves. It was developed within the Massachusetts Institute of Technology (MIT), hence the name WaveAnalysisMIT (WAMIT). For this model, it was used to determine the added mass and radiation damping of the TLP in waves. With these force RAOs, a hydrodynamic database file (.hyd) can be made. This hyd file contains the data in a particular order so it can be exported to LiftDyn. WAMIT uses a 3D panel method based on the boundary integral equation method, and potential flow theory [46]. The boundary value problems are solved using Green's theorem, resulting in integral equations for diffraction and radiation velocity potentials.

An alternative for WAMIT is OrcaWave, developed by Orcina ltd. [47]. It uses the same potential flow principles as WAMIT and is created as an addition to Orcina's dynamic marine analysis software OrcaFlex [48]. WAMIT is chosen over OrcaWave as the digital infrastructure between WAMIT and LiftDyn is already established, such that WAMIT outputs can be used almost directly as LiftDyn inputs.

LiftDyn

LiftDyn is a Heerema computer program designed to model and solve general linear hydrodynamic problems in the frequency domain. It can solve systems consisting of rigid bodies connected to the earth or each other by dampers, springs, and or hinges. The body could have frequency-dependent damping, mass, and exciting forces resulting in an RAO or frequency-dependent system response.

The resulting RAO can be post-processed to a velocity, acceleration, or motion RAO at any relevant point relative to any other point. A generated RAO can be used to provide the significant response in a specific sea state. Furthermore, limiting criteria can be defined to acquire operability curves indicating the maximum allowable wave height (H_s) as a function of the spectral period (T_P). It can also be used to check mode shapes of the bodies to give an overview of the sensitivity of the relevant motions of the body. Also, statics responses and load cases are assessed to see if the computed bodies are in static equilibrium. Liftdyn is validated by, among other things, conducting scale model tests with a Sleipnir model at the Maritime Research Institute Netherlands (MARIN) [49]. One validation result for the Surge RAO is shown in Figure 3.2.

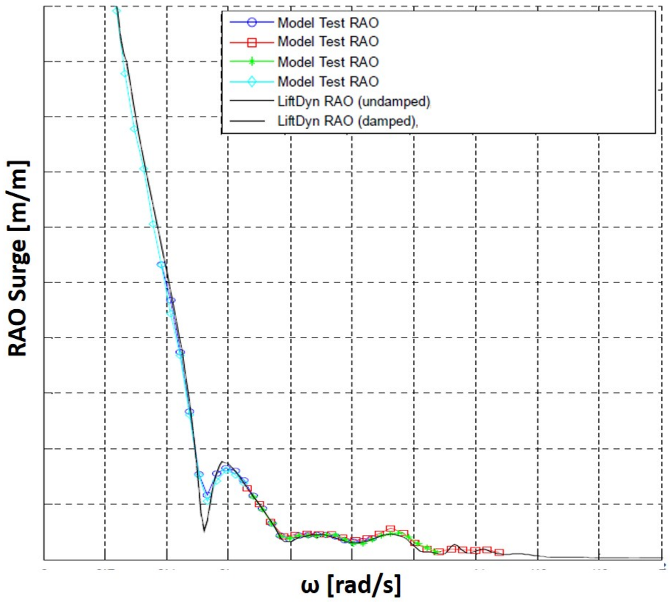

Figure 3.2: LiftDyn validation for Sleipnir in Surge direction with multiple wave conditions [49]

OrcaFlex is known for its dynamic analyzing power for multi-body dynamics in the time domain. It also has the capability to solve these problems in the frequency domain. LiftDyn is chosen over OrcaFlex because of its specification for the used vessel, its available engineering support within HES, and its availability without a license.

Universal Model

Universal Model is a Python environment that provides a uniform format for (offshore) engineering models and is developed within Heerema. It creates a visual interpretation of models for engineers to design and analyze operations more efficiently. It provides a universal model description containing physical objects/bodies, their physical connections, relative positions, and physical properties. It is a front for multiple other software packages, and as its name implies, it is meant to be universal for importing and exporting between multiple existing software packages. For instance, the statics of a system can be solved with its internal static solver, OrcaFlex' static solver, or Heerema's Advanced Generic Equilibrium Solver(AGES). The build models can be exported as inputs for OrcaFlex, LiftDyn, and aNySIM. It is compatible with most python packages, has a Graphical User Interface (GUI), and contains a database with standard elements and vessel assets.

Design Analysis Visualization Engineering (DAVE) [45] was developed by Ruben de Bruin, who also developed UM. In essence, it is the further developed and non-Heerema-orientated version of UM, with some added functionalities, and it uses its integrated static solver. This model uses DAVE to obtain a carene table of the TLP hull. UM is chosen to model the main model over DAVE because of the available Sleipnir model in UM and its linked output to LiftDyn.

Rhinoceros 3D

Rhinoceros 3D (Rhino) [43] is a computer-aided design (CAD). It uses curves and surfaces to model objects in 3D. Furthermore, it can calculate hydrostatics and volume properties for solids and surfaces. Furthermore, the Center of Volume (CoV), Center of Buoyancy (CoB), and Area and Volume moments of inertia can be determined. This research uses it to model the different aspects of the TLP in 3D and to check the analytic approach regarding the volume moments of inertia, CoG, CoV, CoB, and the effect of varying parameter properties. Multiple CAD programs are available these days. Some focus on structural aspects, others on machining, but most have the same basic capabilities. Rhino is chosen because of its availability and its focus on hydrostatic properties.

3.2. Tension Leg Platform

This Section discusses the configuration and assembly of the TLP model. First, an overview of the input parameters is given. Second, the mass distribution and hydrostatics of the TLP are discussed. Third, the modeling of the mooring configuration is presented. Finally, an overview and model checks of the TLP model as a whole are presented.

3.2.1. Input

Intecsea provided two types of TLPs. One made for a tow-out assembly method and one for an onsite installation assembly. For this research, the onsite assembly is used. Per TLP, the different masses and corresponding Vertical Centers of Gravity (VCG), geometry, and mooring parameters are given. See Table 3.2. Also, 3D models of the TLPs were provided, shown in Figure 3.3.

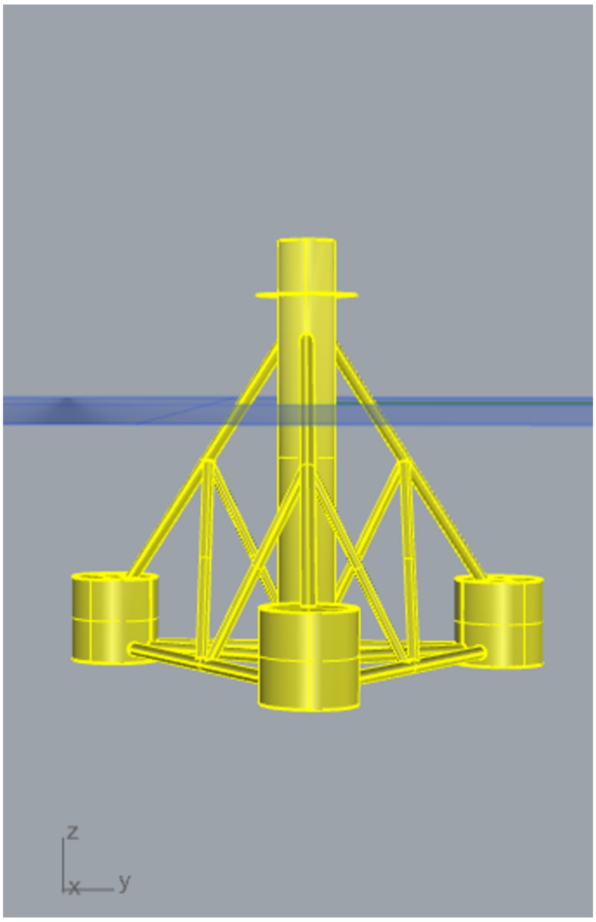

Figure 3.3: 3D view of provided TLPs

Table 3.2: Input parameters TLP Intecsea per assembly method

Overview of TLPs	**Assembly on site**	
Mass and disp.	**Mass [t]**	**VCG [m]**
Overall mass	7388	44.9
Nacelle mass	1017	179.5
Tower mass	860	94.3
Tether system load	2685	6.0
Hull mass	2826	18.5
Center column disp.	1932	18.8
Outer columns disp.	4528	6.0
Trusses disp.	928	8.0
Overall disp.	7388	9.8
Geometry		**[m]**
Overall draft - installed		37.5
Overall draft - free-floating		10.0
Center column diameter		8.0
Center column depth		60.0
Outer column diameter		12.5
Outer column depth		12.0
Hub height		142.0
Outer column offset		32.0
Mooring tether parameters		
Chain Type	Stud-less	
Grade	R4	**[mm]**
Diameter in mm		130

3.2.2. Mass distribution

With the geometry, draft, mass, and CoG known, the next things needed for the TLP model are its gyration radii. Therefore, its mass distribution is needed. The 3D model was assessed using both the CAD program Rhino [43] and an analytic approach. As Rhino is a free-form surface modeler, the 3D model consists of only surfaces with identical thicknesses. This is not the case for the final model. Therefore, the model was split into sections: the center column, outer columns, and trusses. The center column was split into four subsections. The wall thickness of the outer columns and bottom part of the center column was provided by Intecsea as 0.03 m. This is to withstand the water pressure at the given draft. The top Section of the center column has a provided thickness of 0.06 m to endure the bending moment generated by the tower. The intermediate sections are modeled as 0.04 m and 0.05 m, respectively. The wall thickness of the trusses is set to 1 inch, 0.0254 m. An overview of the mentioned dimensions is given in Figure 3.4 and Table 3.3. The Vertical center of gravity can be determined by the sum product of the masses per object with their vertical centroid coordinate, divided by the sum of all masses, see below:

$$VCG = \frac{\sum_{i=1}(m_i\ z_i)}{\sum_{i=1} m_i} \tag{3.1}$$

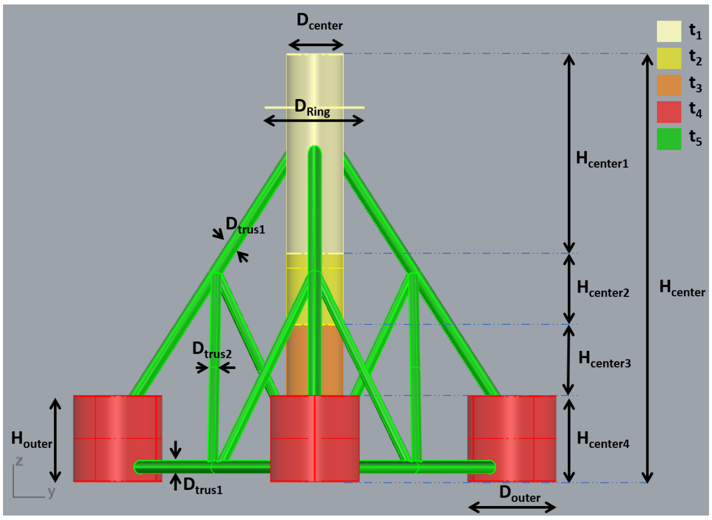

Figure 3.4: Dimensions TLP

Table 3.3: TLP Dimensions

Dimensions TLP		
		[m]
Center column diameter	D_{center}	8.00
Outer column diameter	D_{outer}	12.5
Height center column	H_{Center}	60.0
Height center column 1	$H_{Center1}$	28.0
Height center column 2	$H_{Center2}$	10.0
Height center column 3	$H_{Center3}$	10.0
Height center column 4	$H_{Center4}$	12.0
Wall thickness 1	t_1	0.0600
Wall thickness 2	t_2	0.0500
Wall thickness 3	t_3	0.0400
Wall thickness 4	t_4	0.0300
Wall thickness 5	t_5	0.0254
Outer trusses diameter	D_{trus1}	1.825
Inner trusses diameter	D_{trus2}	1.40

With the dimensions mentioned above in place and with steel with a density, ρ_{steel}, of 7.85 $\frac{t}{m^3}$, the total mass and VCG were 1701 t and 20.45 m, respectively. Structures of this size need internal braces in the center and outer columns. This internal structure should, according to Intecsea, have a density between 0.15-0.2 $\frac{t}{m^3}$. To get to the desired mass and VCG as described in Table 3.2, this internal structure density was iteratively found at 0.152 $\frac{t}{m^3}$. A detailed overview of the model parameters is given in Section A.1. The mass added by the internal structure was modeled as extra wall thickness in both the 3D and the analytic approach. With the mass distribution determined, the radii of gyration and corresponding mass moments of inertia can be calculated.

Radii of Gyration

The radius of gyration is defined as: ”the distance from an axis at which the mass of a body may be assumed to be concentrated and at which the moment of inertia will be equal to the moment of inertia of the actual mass about the axis, equal to the square root of the quotient of the moment of inertia and the mass.” [50] and can be determined with Equation 3.2.

$$r_{m,ii} = \sqrt{\frac{J_{m,ii}}{m}} \qquad i = x; y; z \tag{3.2}$$

Where J_m is the mass moment of inertia for the given axis in $[tm^2]$, and m is the mass of the TLP in $[t]$

To calculate the TLP's mass moments of inertia, the center-, outer columns, and trusses will be assessed as thick-walled cylinders. The top and bottom plates of all columns and the ring will be modeled as solid discs.

For thick-walled cylinders, the mass moments of inertia are as follows. The coordinate system and definitions of variables are given in Figure 3.5

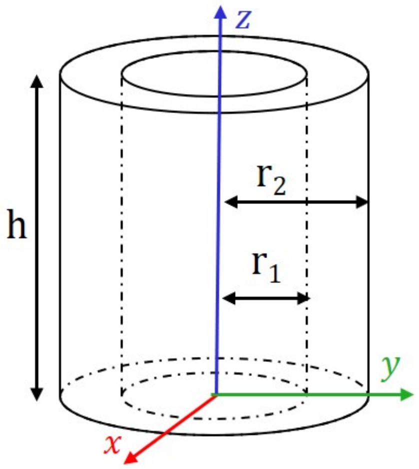

Figure 3.5: Coordinate system mas moment of inertia for a cylinder and disc

$$J_{m,xx} = \frac{1}{12}m(3(r_1^2 + r_2^2) + h^2) \tag{3.3}$$

$$J_{m,yy} = J_{m,xx} \tag{3.4}$$

$$J_{m,zz} = \frac{1}{2}m(r_1^2 + r_2^2) \tag{3.5}$$

For a disc, r_1 is zero, so the moments of inertia can be calculated as:

$$J_{m,xx} = \frac{1}{12}m(3r_2^2 + h^2) \tag{3.6}$$

$$J_{m,yy} = J_{m,xx} \tag{3.7}$$

$$J_{m,zz} = \frac{1}{2}mr_2^2 \tag{3.8}$$

With the use of Steiner's Theorem, seen in Equation 3.9, the mass moments of inertia along the axis of the different bodies can be transposed to a parallel axis at the origin of the model. Being in the middle of the center column at the water line.

$$J'_{m,ii} = J_{m,ii} + md^2 \tag{3.9}$$

Where d is the distance in meters between the two corresponding parallel axes.

The mass moments of inertia found are then compared to the volume moments of inertia generated by Rhino. The mass and volume radii of gyration, $r_{m,ii}$ and $r_{V,ii}$ as mass equals the object's volume times its density. See Equation 3.10

$$r_{V,ii} = \sqrt{\frac{J_{V,ii}}{V}} = \sqrt{\frac{J_{V,ii} * \rho_{st}}{V * \rho_{st}}} = \sqrt{\frac{J_{m,ii}}{m}} = r_{m,ii} \qquad i = x; y; z \tag{3.10}$$

The calculated mass moments of inertia and the volume moments of inertia, converted to mass moment of inertia, generated by Rhino are shown in Table 3.4

Table 3.4: Mass moments of inertia and radii of gyration analytic vs. Rhino

	Analytic	Rhino	Difference	
J_{xx}	2.63E+06	2.65E+06	0.57%	tm^2
J_{yy}	2.63E+06	2.65E+06	0.57%	tm^2
J_{zz}	1.42E+06	1.42E+06	0.10%	tm^2
r_{xx}	30.53	30.58	0.17%	m
r_{yy}	30.53	30.58	0.17%	m
r_{zz}	22.43	22.42	0.06%	m

It can be seen that the analytic and Rhino results are in line with each other. In the analytic approach, all members are considered walled cylinders. Whereas in the rhino model, the beginning and end of these cylinders are slightly different in shape and form. This could explain the slight difference in found values. Because the Rhino model is more detailed than the analytical model, the Rhino values are chosen for the TLP model.

3.2.3. Hydrostatics

The input data showed a free-floating draft of 10 m. After configuring the model in UM, a draft of 9.97 m was found. Corresponding with the given rounded draft. Then the hydrostatics of the floater will be determined for the free-floating situation at a 10 m draft. The metacentric height (GM) is an indication of the stability of the vessel and can be determined with Equation 3.11

$$GM = KB + BM - KG \tag{3.11}$$

Where KB is the distance in meters between the keel and center of buoyancy, KG is the distance between the keel and VCG. A visualization is given in Figure 3.6. BM is the distance between the CoB and Meta-center of the TLP and can be determined by dividing the transverse Area moment I_A by the displacement, ∇, of the vessel.

$$BM = \frac{I_A}{\nabla} \tag{3.12}$$

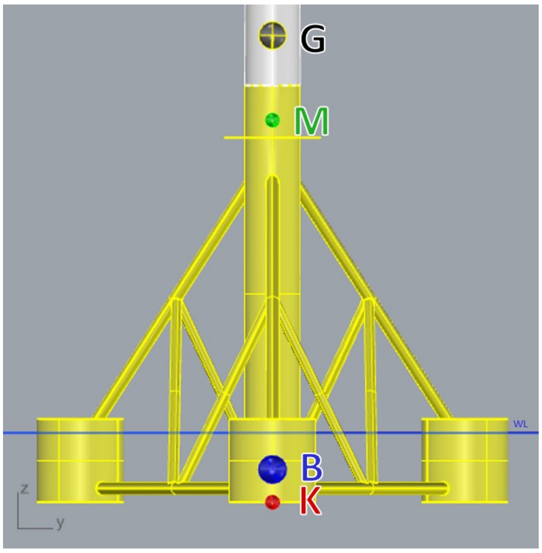

Figure 3.6: Visualization geometric height inputs

Table 3.5: Hydrostatic properties TLP onsite Free Floating with RNA+ installed

	Analytic	Rhino	WAMIT	
VCG	57.18	57.21	57.18*	m
∇	4762	4773	4751	m^3
A_{wl}	429.3	429.3	428.5	m^2
I_A	1.93E+05	1.93E+05	-	m^4
BM	40.62	40.53	40.65	m
KB	4.34	4.70	4.71	m
KG	67.18	67.21	67.18	m
GM	-22.21	-21.98	-21.82	m

*analytic input as WAMIT doesn't calculate COG

It can be seen that the GM is negative for the onsite TLP in its free-floating installed phase. This means that the system is not stable in this case.

For the tow-out TLP, a positive GM is found. See Table 3.6

Table 3.6: GM calculation value for onsite and tow-out TLP

	On-Site	**Tow-Out**	
I_A	1.93E+05	5.35E+05	m^4
∇	4773	4998	m^3
BM	40.53	106.98	m
KG	67.21	63.69	m
KB	4.7	4.2	m
GM	-21.98	47.49	m

3.2.4. Mooring

For the mooring of the TLP, the parameters in Table 3.7 are given. The Tether system load given is for the situation with the RNA+ module installed. As described in Subsection 1.2.1, this tether system load is the resultant of the Buoyancy and Gravitational forces. See Equation 3.15. As the system should be in equilibrium, when removing the RNA+ module, the difference in mass should be countered with a difference in tether system load, the extra pre-tension. In Table 3.8, an overview of the forces acting upon the whole structure is given. Figure 3.7 shows the Free Body Diagram (FBD) of the TLP and the definition of tendon angle θ.

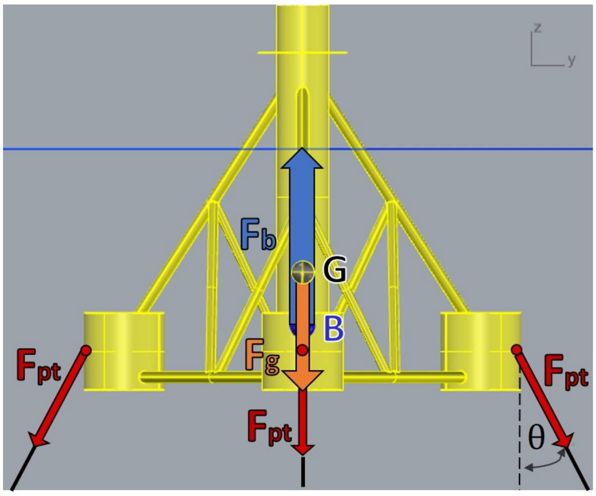

Figure 3.7: Free Body Diagram TLP

Gravitational Force: $$F_g = m\ g \tag{3.13}$$

Buoyancy Force: $$F_b = \nabla\ \rho_{water}\ g \tag{3.14}$$

Total Tendon Force: $$F_t = F_b - F_g \tag{3.15}$$

The Force per tendon can be calculated with:

Force per Tendon: $$F_{pt} = \frac{F_t}{No.Tendons\ cos(\theta)} \tag{3.16}$$

Table 3.7: Mooring input parameters

Mooring tether parameters		
Tether system load	2,685	t
No. Tendons	6	-
Chain Type	Stud-less	-
Grade	R4	-
angle θ	15	°
Diameter in mm	130	mm
EA	1.44E+06	kN

Table 3.8: Static Forces acting upon system

Forces	**With RNA+**	**Without RNA+**	
F_g	4.61E+04	2.77E+04	kN
F_b	7.25E+04	7.25E+04	kN
F_t	2.63E+04	4.48E+04	kN
$\sum F$	0	0	kN
F_{pt}	4.54E+03	7.72E+03	kN

The mooring chains are modeled as a linear spring. With a given extensional stiffness (EA), Tension per tendon, and the stretched length, the spring's unstretched length and, thus, stiffness (K) can be calculated.

$$F_{pt} = K_I \, \Delta L \tag{3.17}$$

$$K_I = \frac{EA}{L_0} \tag{3.18}$$

$$L_0 = L_{total} - \Delta L \tag{3.19}$$

These equations can be substituted and rewritten as:

$$\Delta L = \frac{F_{pt} \, L_{total}}{EA + F_{pt}} \tag{3.20}$$

For the given situation, the linear elongation of the mooring line can be determined with the EA in Table 3.7, force per tendon determined with Equation 3.16 and the known total length of the tendon, due to the desired draft and mooring line angle. The results per load case are shown in Table 3.9. In this calculation the hydrostatics stiffness of the floater is neglected as it is 0.04% of the mooring line stiffness.

Table 3.9: Mooring line elongation and lengths for linear spring

	With RNA+	**Without RNA+**	
ΔL	0.385	0.653	m
L_{total}	122.680	122.680	m
L_0	122.295	122.027	m

A TLP, due to its stiff tendons, is restrained in heave motion [51]. Because of the linear approach of the mooring lines and how they are implemented in the final FD model as springs with stiffness and given pre-tension, the expected elongation is in the order of mm. This limited extension is due to the force needed to elongate the tendons being much higher than the difference in gravity force. Therefore the draft is kept at 37.5 m, and the lines are modeled so that the total elongated length stays the same for all cases.

3.2.5. WAMIT

Mesh Convergence

To determine the first-order Added Mass, Radiation Damping, and wave force excitation WAMIT uses a Geographic Data File(GDF) as input. It contains all the coordinates of the nodes of a Mesh and consists of the underwater body of the TLP. Different mesh configurations are made to determine the number of panels for a valid WAMIT analysis. Because only the first-order properties of the TLP are determined in WAMIT, it is chosen to assess the structure as four cylinders without all the smaller trusses. It is presumed this is justified because of their relatively small diameter with respect to the center and outer columns. Therefore, their effect is expected to be negligible for the first-order properties.

Furthermore, running the model in WAMIT with the trusses it is expected to lead to 'noise' in the output and non-linear effects. This will be checked later on. The analysis then has to be compensated for the missing displacement. This can be done by extracting this data from WAMIT and converting it into a .hyd file. Using Rhino, seven different GDFs are made with 599, 972, 1903, 2091, 3321, 6388, and 13050 panels, respectively. The finer the mesh, the more exact the data, but the longer the computation time. In Figure 3.9, the radiation damping in surge-surge direction is shown for all meshes. In Table 3.10, the displacement and difference for the cylindrical model, B11 at $\omega = 1.35$ and the difference with the B11 of the finest mesh, and the calculation time per WAMIT run are given per mesh. For this instance, the mesh with 3321 panels differs by 0.17% in volume and 1.6% in radiation damping with the TLP and finest mesh. On the other hand, it can be seen that the computation time for this mesh is significantly lower than for the two finer meshes. In Section A.2, an overview of the Added

Masses and radiation damping per mode per mesh is given. With visual comparison and differences less than 2% in the peak values and significantly less computation time, the mesh with 3321 panels is chosen for the continuation of this model step. The mesh is shown in Figure 3.8.

Table 3.10: Mesh convergence for volume and B11 damping at 1.4 $rads^{-}1$

Mesh	$\nabla[m^3]$	Difference	B11 at peak $[\frac{kNs}{m}]$	Difference	Calculation Time [h:m:s]
TLP	6302.8	-	-	-	-
N= 599	6214.1	1.43%	407.9	23.7%	00:00:02
N= 972	6267.6	0.56%	460.3	9.6%	00:00:07
N= 1903	6281.3	0.34%	482.3	4.6%	00:00:39
N= 2091	6285.1	0.28%	485.9	3.8%	00:00:49
N= 3321	6292.3	0.17%	495.6	1.8%	00:03:04
N= 6388	6292.5	0.16%	503.3	0.3%	00:25:47
N= 13050	6297.9	0.08%	504.56	-	03:19:12

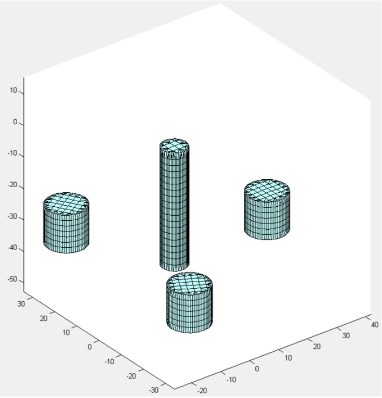

Figure 3.8: Mesh with N= 3321

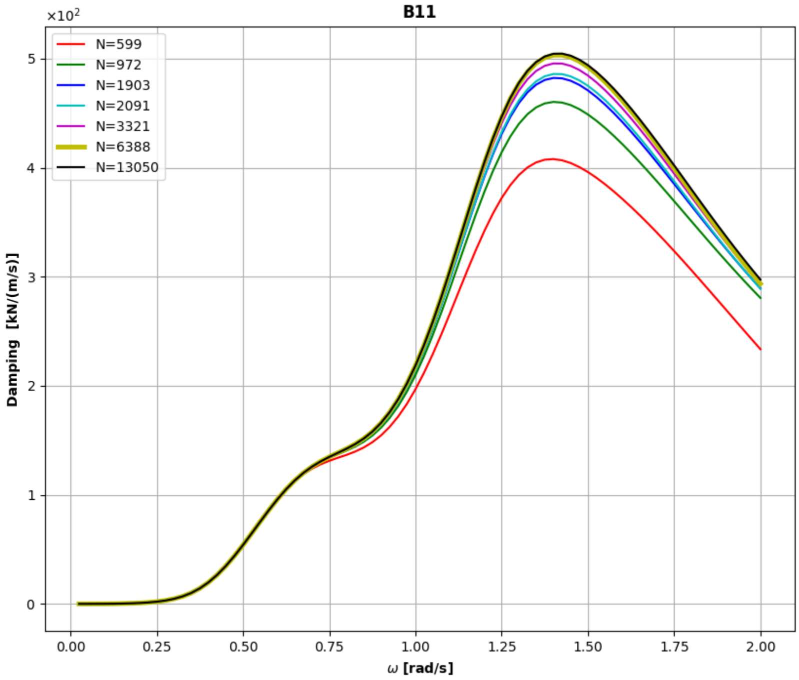

Figure 3.9: Mesh convergence for B11 Damping

WAMIT mesh 2

To check if the assumption that the trusses have negligible influence on the first-order properties, a check is done with three model meshes including the trusses. The added mass for heave and radiation damping for roll are given in Figure 3.10 and 3.11, respectively. All plots are given in Section A.2.

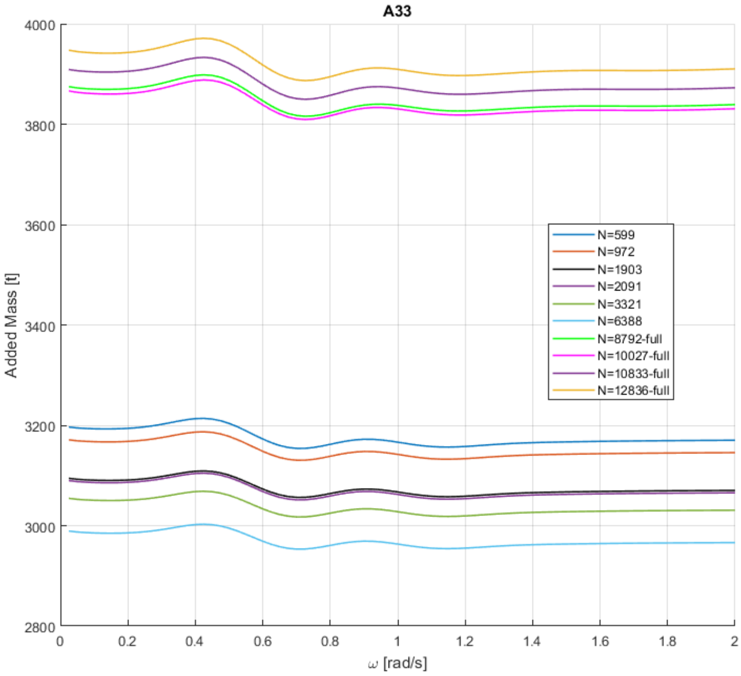

Figure 3.10: Added mass in Heave direction. Stripped vs. Full structures

In Figure 3.10, two groups of added mass plots can be seen. The top group is the added mass for the meshes, including the trusses, and the bottom group is for those without the trusses. It can be seen that the added mass for the case with and without trusses differs by around 15% depending on the different meshes. This indicates that with respect to the added mass, the trusses can not be neglected in the WAMIT run.

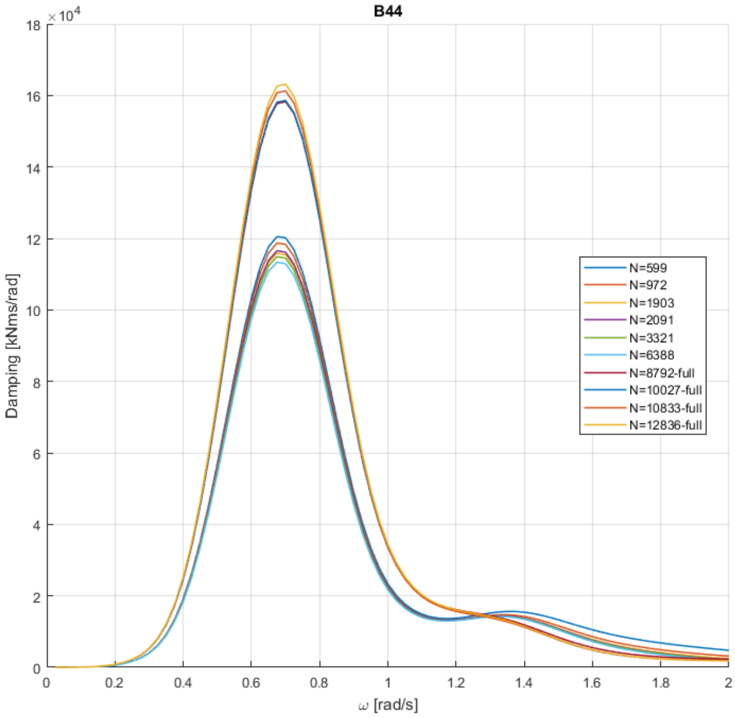

Figure 3.11: Radiation Damping in heave direction. Stripped vs. Full structures

In Figure 3.11, two groups of signals can be seen. The top one with its peak around 16 $\frac{kNms}{rad}$ being of the meshes, including the trusses. The group with its peak around 12 $\frac{kNms}{rad}$ the meshes without trusses. It can be seen that for the damping in roll direction, the increase in damping between the stripped and full configuration is around 33%. Both the difference in added mass and radiation damping indicate that the model can not be modeled as four cylinders, the stripped situation. The problem of the significantly longer computation time, roughly 3 minutes versus 3 hours, is not a problem for future computation time, as the hyd file has to be made once. Furthermore, the expected noise or disturbances in the found data did not occur, the absolute data is different, and the overall trend of the plots is similar. Therefore, a mesh with trusses is used for the WAMIT analyses.

For the meshes with trusses, a second mesh convergence is done. An overview can be seen in Section A.3. With the previous convergence, more panels meant a more 'precise' model, but this is not the case with these meshes. The meshes with n=12836, 10833, and 8792 seem like meshes with a large number of panels. However, most panels are placed within the trusses, and the outer columns are meshes just like the mesh with N= 972 panels from previous analyses. This is because the mesh function in Rhino very precisely meshed the connection points of the trusses with each other with the smallest panel length of 0.001 m. With very rough meshed main columns and very fine meshed trusses, the model was a bit in dis-balance. The trend seen in the convergence of the added mass in the stripped situation, the finer the mesh, the lower the added mass, is reversed in this new convergence analysis. Therefore, two new meshes were made where this minimum panel length was set to 0.5 m. The same meshing configurations for the main columns were chosen as those of the N=3221 and N=2091. The panels on the trusses were meshes such that their panel size matched the panel size of the vertical sides of the main columns. The mesh with N=12825 is shown in Figure 3.12

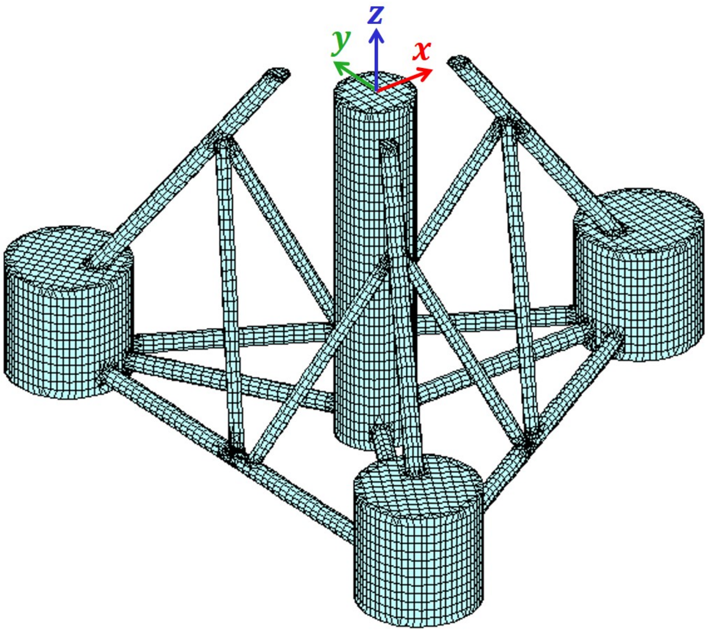

Figure 3.12: Mesh N=12825

An overview of the values for the meshed and full TLP are given in Table 3.11

	Full WAMIT Mesh	Full TLP	Diff.	
A_{wl}	59.7	60.1	0.6%	m^2
∇	7299.4	7344.1	0.6%	m^3
KB	9.99	10.0	0.1%	m

Table 3.11: Final WAMIT inputs

With this mesh and settings shown in Section A.8, WAMIT is run. WAMIT's .1 output files contain the non-dimensional added mass, $\bar{A}_{ij}$, and radiation damping $\bar{B}_{ij}$ [46]. To convert these into dimensional values, the following formula is used:

$$\bar{A}_{ij} = \frac{A_{ij}}{\rho L^k}, \quad \bar{B}_{ij} = \frac{B_{ij}}{\rho L^k \omega} \tag{3.21}$$

Where L is a length scale factor defined in the GDF file. This factor is 1. k is dependent on the different assessed modes. As L is equal to 1, these are irrelevant for this configuration. With the Wam2dat function, this conversion uses ρ_w and the frequencies for which the non-dimensional values are deducted. This function then creates the .hyd file, which is readable by LiftDyn. The calculated hydrodynamics properties will be generated for the given draft of the TLP. This Wam2dat function is checked with an independent self-made python function, giving the same results for added mass and damping.

Carene Tabel

For the hydrostatics per draft, Universal Model needs a Carene table. A Carene Table contains the mass, displacement, water-plane area, CoB, Center of Flotation (CoF), and the distance between the keel and the metacentric height (KM) of the TLP per given draft interval. For the construction of the table, this draft interval is chosen at 0.1m, as it is expected that the TLP will stay at its designed draft, and smaller intervals lead to more computation time later in the process. As inputs for this table, an object file (.obj), its mass, and CoG are needed. The object file is a mesh created in Rhino from the whole TLP structure, including its trusses. Then all the DoFs of the TLP are fixed except the heave direction, which is lowered in the water with the draft intervals steps until fully submerged. The hydrostatic properties are calculated per draft interval using Equation 3.11. An overview of the non-zero values in the Carene table and their analytic counterpart for a draft of 37.5 m is given in Table 3.12

Table 3.12: Hydrostatic properties TLP, Carene vs. Analytic

	Analytic	**Carene**	**Diff.**	**Unit**
Draft	37.5	37.5		m
Mass	2826	2826		t
∇	7207.80	7207.77	0.00%	m^3
A_{wl}	60.09	59.56	-0.88%	m^2
VCB	10.00	10.08	0.84%	m
KM	10.10	10.18	0.82%	m
GM	-8.40	-8.32	-1.00%	m

The difference in A_{wl} and thus the KM, Equation 3.11, could be due to the fact that the cross-sectional area of the trusses is under-designed in the .obj file or over-estimated in the analytic approach. With a difference of 0.8-0.9%, this is acceptable for this order of magnitude.

3.2.6. TLP modeling in UM

With all the hydrostatics properties from the carene table, the hydrodynamic properties in the hyd file, the mesh as an obj file, tendon tension and properties, and the geometry, a model in Universal Model can be made. Universal model gives a visualization of the model and all its properties. Local and global position, parent-child relations, mass and inertia properties, hydrostatics, and static state forces of the TLP body, POIs, and tendons can be checked.

Static equilibrium, mooring lines

The analytic static equilibrium shown in Table 3.8 is now compared with the results from the statics solver of Univeral model. This comparison can be seen in Table 3.13

Table 3.13: Mooring line tension per tendon for installed TLP with and without RNA+ on top

Tension	**With RNA+**	**Without RNA+**	**Unit**
Analytic per tendon	4544.84	7721.99	kN
Line 1A	4544.92	7722.02	kN
Line 1B	4544.92	7722.02	kN
Line 2A	4544.50	7721.78	kN
Line 2B	4544.50	7721.78	kN
Line 3A	4544.91	7722.01	kN
Line 3B	4544.91	7722.01	kN
Total	26339.51	44752.91	kN
Analytic total	26339.85	44753.22	kN
Difference	0.341	0.312	kN

The slight differences between UM's occur because of slight asymmetries in the meshes used to compute the model. As the most significant difference between tendons for the no RNA+ situation is 0.03‰ and 0.007‰ for the total difference between the analytic and UM's approach, these differences are deemed negligible.

3.2.7. TLP modeling in LiftDyn

The un-damped system without excitation is assessed to find the natural frequencies for the 6 DOFS. So Equation 2.11 becomes:

$$\left[\mathbf{C} - \omega^2 \cdot \mathbf{M}\right] \cdot \hat{\chi} = 0 \tag{3.22}$$

The natural frequency ω_n per DOF can be found using the equation below:

$$\omega_{n,ii} = \sqrt{\frac{\mathbf{C}}{\mathbf{M}}} \tag{3.23}$$

The natural period then is:

$$T_{n,ii} = \frac{2\pi}{\omega_{n,ii}} \tag{3.24}$$

The equivalent mooring spring matrix, $\mathbf{K}_{moor_{eq}}$ is shown below [52]:

$$\mathbf{K}_{moor_{eq}} = \begin{bmatrix} k_{m,11} & 0 & 0 & 0 & k_{m,15} & 0 \\ 0 & k_{m,22} & 0 & k_{m,24} & 0 & 0 \\ 0 & 0 & k_{m,33} & 0 & 0 & 0 \\ 0 & k_{m,42} & 0 & k_{m,44} & 0 & 0 \\ k_{m,51} & 0 & 0 & 0 & k_{m,55} & 0 \\ 0 & 0 & 0 & 0 & 0 & k_{m,66} \end{bmatrix} \tag{3.25}$$

The corresponding $k_{m,ii}$ values are deducted in Equation 3.26, for the definition of variables see Figure 3.13 [52].

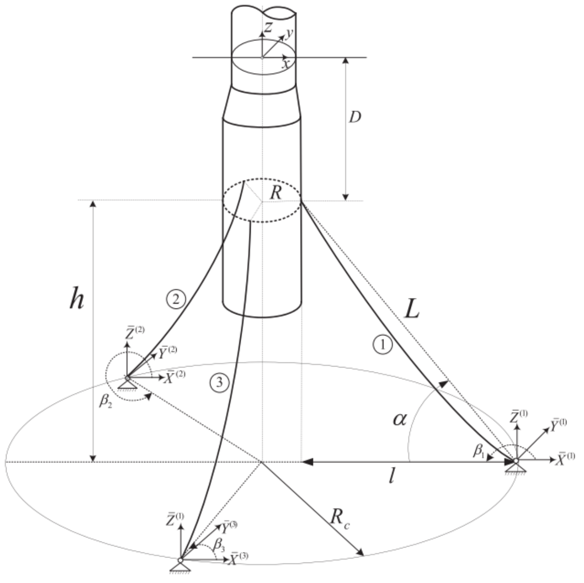

Figure 3.13: Definition of variables of Equation 3.26 [52]

$$\begin{aligned}
k_{m,11} &= 0.5n\left[\frac{T}{L}\left(1+\sin^2\alpha\right)+K_I\cos^2\alpha\right]\\
k_{m,15} &= -n\left[\frac{T}{2L}\left(D+D\sin^2\alpha+R\sin\alpha\cos\alpha\right)\right.\\
&\quad\left.+\frac{K_I}{2}\left(D\cos^2\alpha-R\sin\alpha\cos\alpha\right)\right]\\
k_{m,22} &= k_{m,11}, k_{m,24}=-k_{m,15},\\
k_{m,33} &= n\left[\frac{T}{L}\cos^2\alpha+K_I\sin^2\alpha\right], k_{m,42}=k_{m,24}\\
k_{m,44} &= n\left\{T\left(D\sin\alpha+\frac{1}{2}R\cos\alpha\right)\right.\\
&\quad+0.5\frac{T}{L}\left[(R\cos\alpha+D\sin\alpha)^2+D^2\right]\\
&\quad\left.+0.5K_I(D\cos\alpha-R\sin\alpha)^2\right\}\\
k_{m,51} &= k_{m,15}, k_{m,55}=k_{m,44},\\
k_{m,66} &= n\frac{\mathrm{TR}}{L}(R+L\cos\alpha)
\end{aligned} \tag{3.26}$$

For K_I See Equation 3.17. The hydrostatic spring matrix $\mathbf{K}_{hyd}$ for the TLP is shown below. The corresponding values for the non-zero spring coefficients computed with the values in Table 3.12 are shown in Table 3.14

Table 3.14: Hydrostatic Spring values

DOF	k_{hyd}**[**$kN\ m^-1$**]**
Heave 33	6.04E+02
Roll 44	-6.09E+05
Pitch 55	-6.09E+05

$$\mathbf{K}_{\text{hyd}} = \begin{bmatrix} 0 & 0 & 0 & 0 & 0 & 0\\ 0 & 0 & 0 & 0 & 0 & 0\\ 0 & 0 & \rho\cdot g\cdot A_{WL} & 0 & 0 & 0\\ 0 & 0 & 0 & \rho g\nabla\cdot GM & 0 & 0\\ 0 & 0 & 0 & 0 & \rho g\nabla\cdot GM & 0\\ 0 & 0 & 0 & 0 & 0 & 0 \end{bmatrix} \tag{3.27}$$

$$\mathbf{C} = \mathbf{K}_{moor} + \mathbf{K}_{hyd} \tag{3.28}$$

For the different meshes and DOFs LiftDyn provided the following natural periods.

Table 3.15: Natural frequencies per mesh per DOF

ω_n	**Surge 11**	**Sway 22**	**Heave 33**	**Roll 44**	**Pitch 55**	**Yaw 66**	Unit
Stripped	0.25	0.25	3.47	3.69	3.69	0.51	$[rad\ s^-1]$
Full n10027	0.23	0.23	3.16	3.50	3.50	0.48	$[rad\ s^-1]$
full n 10833	0.23	0.23	3.15	3.49	3.49	0.48	$[rad\ s^-1]$
full n8782	0.23	0.23	3.16	3.49	3.49	0.48	$[rad\ s^-1]$
full n9300	0.23	0.23	3.16	3.50	3.50	0.48	$[rad\ s^-1]$
full n 12825	0.23	0.23	3.17	3.52	3.52	0.48	$[rad\ s^-1]$

For heave using $k_{m,33}$ from Equation 3.26, the following value is found and compared to LiftDyns output for mesh n12825, see Table 3.16

	ω_n	Unit
LiftDyn	3.173	$[rad\ s^-1]$
Analytic	3.179	$[rad\ s^-1]$
Difference	0.17%	

Table 3.16: Natural frequency for Heave, LiftDyn vs. analytical output

With the use of Equation 2.17, LiftDyn generates RAOs. The RAO of Heave and roll for wave direction ε = 45°is shown in Figure 3.14. The RAOs of the other DOFs are shown in Section A.6

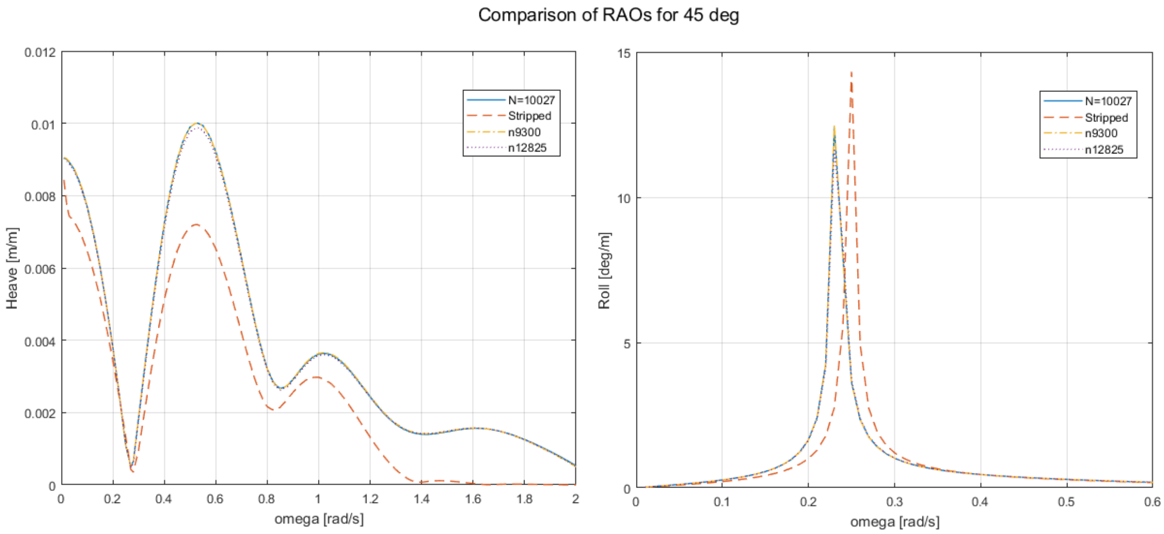

Figure 3.14: RAO for Heave and Roll for ε = 45°

In Figure 3.14, the dashed red line shows the RAO for the mesh without trusses. The three other lines represent the model with trusses. It can be seen that for the model with trusses, the RAOs are pretty much equal. With a significant wave height H_s of 1 m, and using Equation 2.20 this gives the following responses:

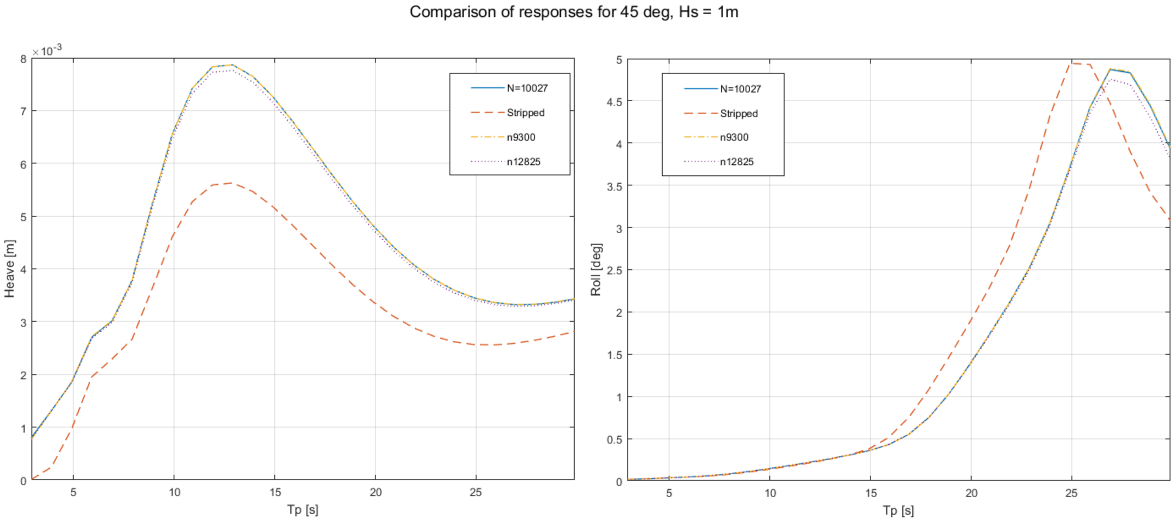

Figure 3.15: Response for Heave and Roll for ε = [45°], H_s = 1 [m], T_p= 3-30 [s]

More responses are shown in Section A.7. Similar to Section A.7, Figure 3.15 shows that the model's response without trusses differs from the model with trusses. Also, the different models with trusses show almost the same response.

3.2.8. Relevant TLP parameters

Parameters relevant to the behavior of the TLP are its mass, the angle of its tendons, and mooring line stiffness. As varying these parameters influences the natural frequencies of the TLP and thus FD behavior, see Equation 3.23.

3.3. Wind Turbine Generator

An International Energy Agency (IEA) task force has designed a reference turbine to accommodate offshore wind developers with a publicly available benchmark for advancing offshore wind development. This reference turbine bridges the gap between the industry and academics and offers an entry point for educational purposes [33]. With its publicly available data, one can look at a universal solution for offshore wind matters instead of running aground on specific confidential industry data. An overview of the relevant parameters for installation is given in Table 3.17. A visualization is displayed in Figure 3.16.

Table 3.17: Specifications of IEA 15 MW reference turbine [33]

Parameter	Value	Unit
Rated power	15	MW
Rotor diameter	240	m
Hub height	150	m
Hub diameter	7.94	m
RNA mass	1017	t
Tower mass 'stiff-stiff' (SPAR, barge, semi-sub)	1263	t
Tower mass 'soft-stiff' (TLP)	860	t
Nacelle mass	821	t
Blade mass	65	t

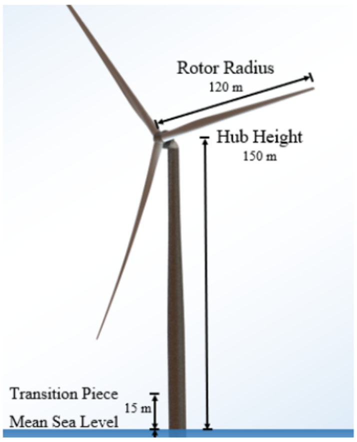

Figure 3.16: Illustration of IEA 15 MW reference turbine [33]

This reference turbine is chosen for this research because of its publicly available data and usage in other academic research. The tower and hub heights of the reference turbine were designed with an air gap of 30 m between the blade tips and MS [33]. The increasing heights of future WTGs could lead to problems in the installation process by HLVs [10]. For this model, it is expected to be the case that clearance between the RNA and the crane boom will be a leading limiting criterion. The IEA report states that: " The 30-m clearance value is not specified in an official standard and offshore wind turbine clearances can vary between 20 m to 30 m " [33, p. 21]. Therefore, the tip clearance used for this model will be 20 m, which results in a hub height of 140 m.

$$H_{hub} = H_{tower} + H_{TLP-top} + 0.5H_{Nacelle} \tag{3.29}$$

Then the total tower height can be determined. See Table 3.18

Heights		
H_{hub}	140	$[m]$
$H_{TLP-top}$	22.5	$[m]$
$H_{nacelle}$	5.5	$[m]$
H_{Tower}	112	$[m]$

Table 3.18: WTG Heights

As the Hub height of the tower is altered, and the TLP is designed for a tower with a bottom diameter of 8 m, The IEA 15MW tower is scaled accordingly. The tower will be modeled as multiple cylinders whit descending wall thickness and outer diameter. The VCG and mass moments of inertia will be determined with Equations: 3.1, 3.3, 3.4, 3.5 respectively. A detailed overview of the tower properties is given in Appendix B. The original NREL tower has a base diameter of 10 m. Intecsea's TLP is designed for a tower with a base diameter of 8 m. The original IEA tower consists of 10 sections, the bottom 9 all have a height of 13 m, and the top one is 5 m, resulting in a tower height of

122 m. The bottom has a wall thickness of 0.041 m, decreasing to 0.024 m at the top. This decrease in wall thickness is not linearly distributed. The outer tower diameter per Section is refitted such that the bottom Section is 8 m in diameter and the top part 6.5 m. The distribution of wall thicknesses of the original tower is distributed over the altered 10 tower sections. As the hub height is lowered by 10 m, all 10 sections are reduced by 1 m in height. Resulting in 9 sections of 12 m and the top Section of 4 m height. The scaled diameter and wall thickness per segment are shown in Figures 3.17 and 3.18.

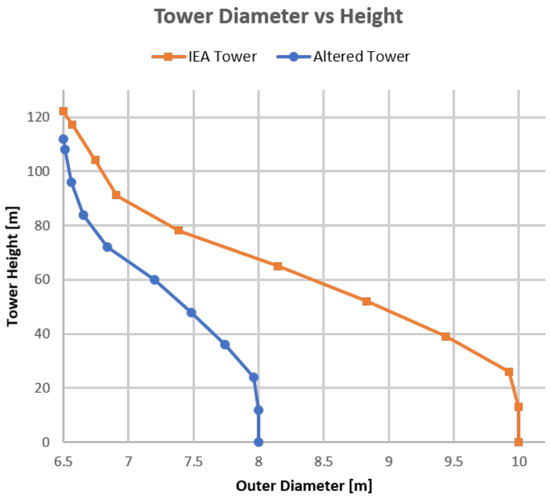

Figure 3.17: Diameter of tower segments w.r.t tower height

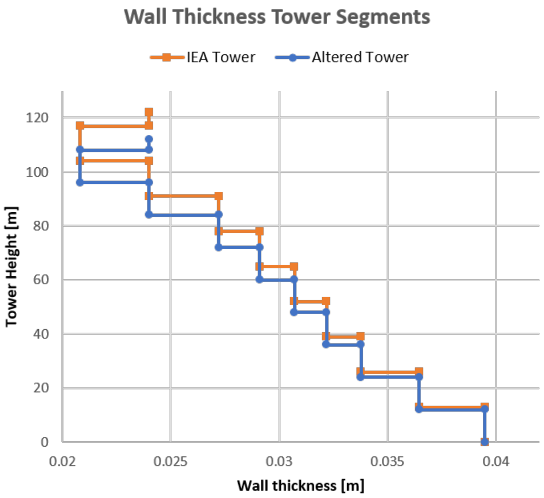

Figure 3.18: Wall thickness of tower segments w.r.t tower height

The outer diameter and height alteration result in a lower tower mass. The mass for the altered tower is 660 t. The nacelle and rotors' mass and inertia properties and geometry are extracted from the IEA report [33] and entered in the UM model. An overview of the Mass and inertia properties of the Tower, Nacelle, and Rotors is given in Table 3.19

Table 3.19: Mass and Inertia properties RNA+

Body	Mass	CoG w.r.t Top tower			Radii of Gyration		
		x	y	z	Rxx	Ryy	Rzz
	[mT]	[m]	[m]	[m]	[m]	[m]	[m]
Tower	660	0	0	-63.8	31.5	31.5	3.74
Rotor	196	10.6	0	5.46	50.4	36	36
NAH	821	5.49	0	3.98	0.683	4.45	2.70

3.3.1. Nacelle Casing

The IEA 15 MW reference turbine report [33] does not mention a nacelle casing. Only the bare construction is modeled. However, this is unlikely to be the case in the actual configuration. Therefore, Points of Interest (POIs) are modeled in such a way that a cube with sides of 12 m. On two heights, Z0 and ZH, 5 POIs per height are modeled at intervals of 1.75 m in the negative x direction, see Figure 3.19. Each POI's static distance with the crane boom will be mapped. The different clearances between the nacelle and crane boom can be determined with this static distance. This way, multiple nacelle casing sizes can be examined per model run. The final POI can be selected in a later stadium without altering the model.

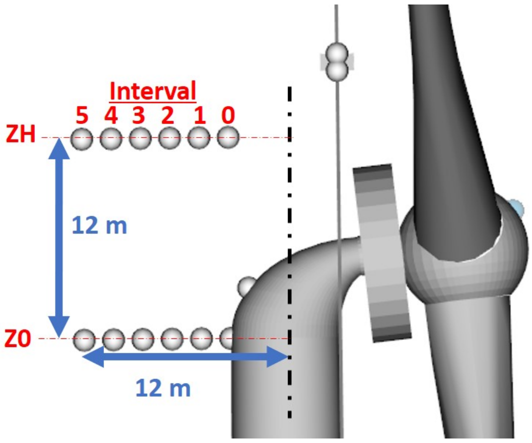

Figure 3.19: Nacelle Casing intervals

3.3.2. Relevant WTG parameters

Relevant parameters regarding the RNA+ configuration are the positions of its CoGs, the hub height, and the masses of the different parts.

3.4. Vessel

For this model, the Sleipnir will be used. The Sleipnir is the world's largest SSCV with a maximum lifting capacity of 20,000 metric tonnes [42]. The vessel is equipped with two cranes of 10,000 metric tonnes lifting capacity each. HES provided a detailed Sleipnir model with all its hydrostatic and hydrodynamic properties. This model is checked with respect to the model tests mentioned in Subsection 3.1.2. It contains the hull with various hydrostatic and dynamic properties for different drafts, ballasting systems, and crane modules. These crane modules have detailed lifting points, crane curves, and rigging configurations. A visualization of the model is given in Figure 3.20.

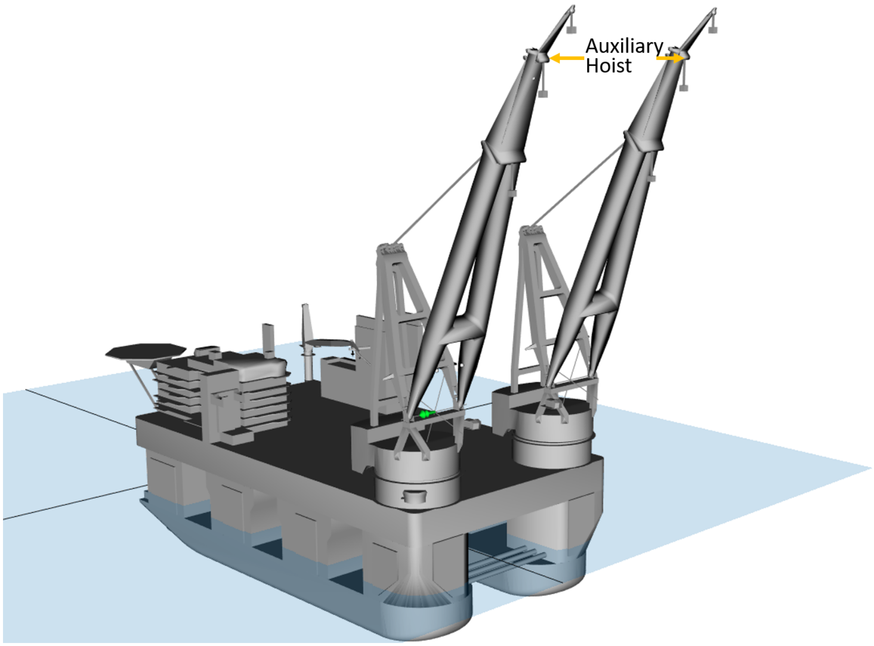

Figure 3.20: Visualization of Sleipnir model, Auxiliary hoist identification

The Auxiliary (Aux) hoist will be used. This Aux hoist has a Safe Working Load (SWL) of 2500 metric tonnes and enough height to install components at the desired hub heights above MSL. In Figure 3.21, the preliminary lifting curves of the Sleipnir are shown. It shows the SWL per boom radius and the corresponding lifting height above the main deck. The maximum boom radius where the 2500 t SWL is applicable is 58 m. See point A in Figure 3.21. This corresponds with a lifting height of around 140 m above the main deck. A draft of 19 m of the Sleipnir results in a lifting height of around 170 m above MSL. A hub height of 140 m gives the maximum amount of clearance between the crane.

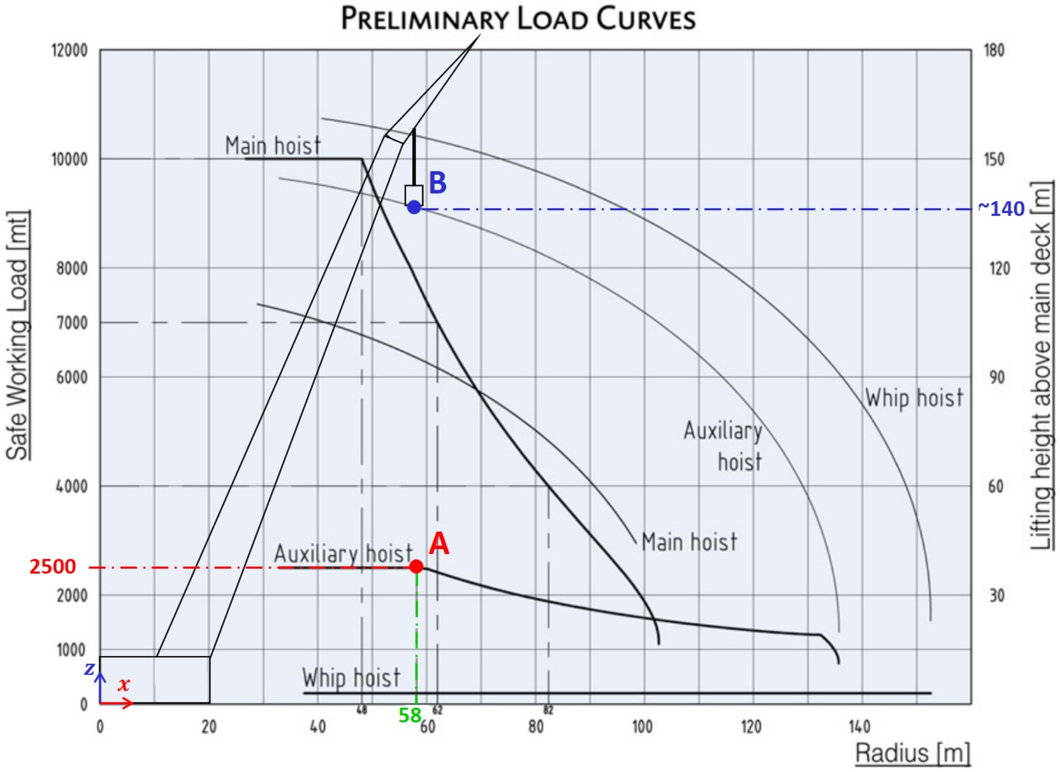

Figure 3.21: Crane Curve Sleipnir. Point A; max crane radius for 2500 SWL. Point B; Corresponding max Aux Block Height w.r.t. main deck height. Altered from [53], crane not to scale

A definition of the crane boom radius, slew, and boom angle for the SB crane is given in Figure 3.22

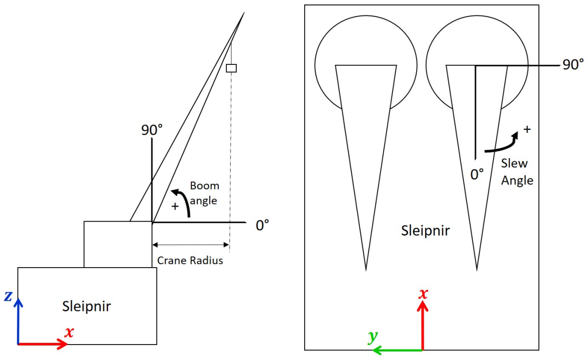

Figure 3.22: Definition of crane boom radius, Slew, and Boom angle Sleipnir

3.4.1. Relevant Vessel parameters

As discussed above, the crane boom radius affects the SWL and lifting height of the crane. Furthermore, the slew angle of the crane could influence the installation process. This is because of different motion behavior coupling, such as roll and pitch. Additionally, the rigging configuration has some relevant parameters to vary; see Subsection 3.5.1.

3.5. Combined model - Base Case

With the separate models of the TLP, WTG, and Vessel in place, a combined model can be made. In Figure 3.23, a visualization of the whole model can be seen. The model is set up in a way that if one varies an input parameter, all bodies change accordingly. The origin is set at the stern of the vessel at the waterline. For this model, the Starboard Crane is chosen. A Base Case for the model is made. This base case is not, per se, the most optimal configuration. It is determined using the standard configuration of the TLP and WTG. Considerations regarding vessel configurations were made during the build.

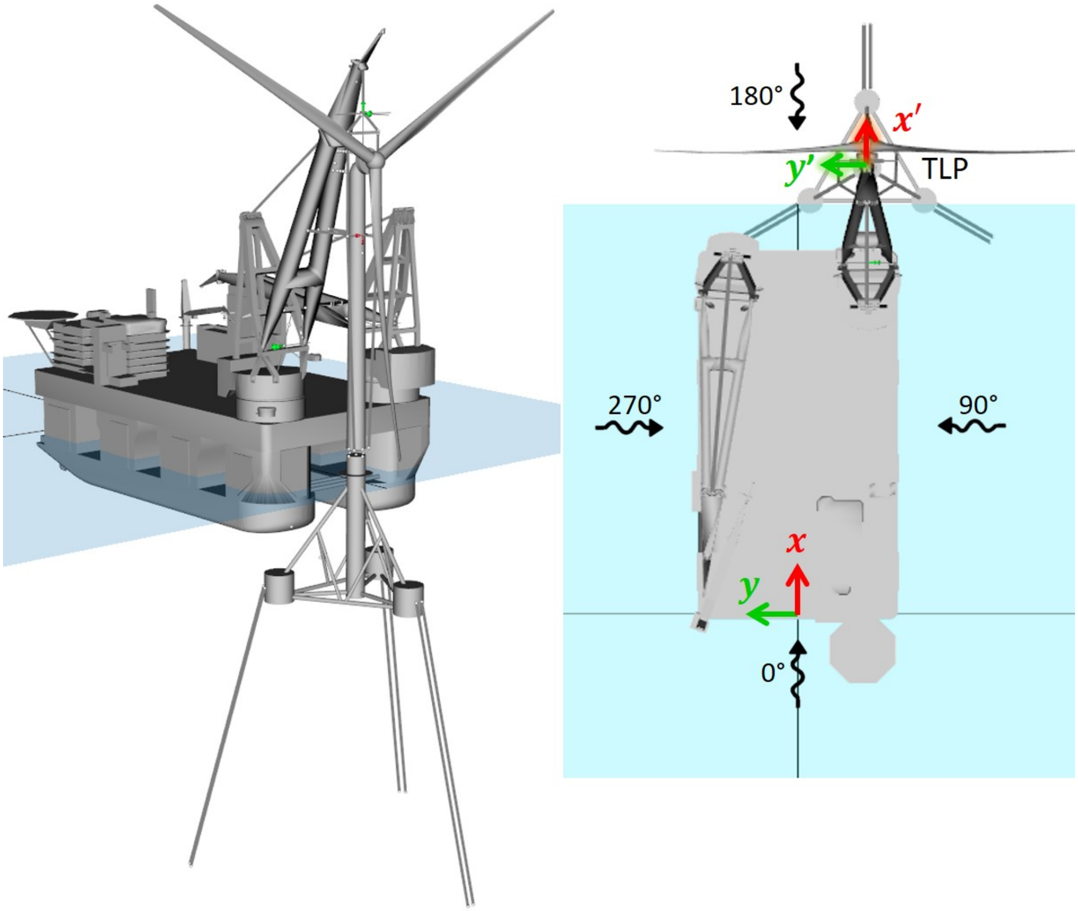

Figure 3.23: Base Case 3D and top view

3.5.1. Rigging

The setup shown in Figure 3.24 is chosen for the rigging. The model calculates the combined CoG of the Tower, Nacelle, Hub (NAH), Rotors, and lifting tools. Then the position of the RNA+ module is set at the exact x and y coordinates as the Aux hoist block. Because of the considerable lifting height, a setup with two lifting tools is chosen. If needed, dampers can be applied to the upper lifting tool. This rigging configuration creates larger clearances between the RNA+ module and the crane boom. Two tugger lines will be attached between the Upper lifting tool and the crane boom. They are modeled horizontally to only alter the movement in the horizontal plane. Diagonal tugger lines are less effective as their tugging capacity alters with $cos^2(\theta_{tug})$, where θ_{tug} is the angle between the horizontal plane and the tugger lines.

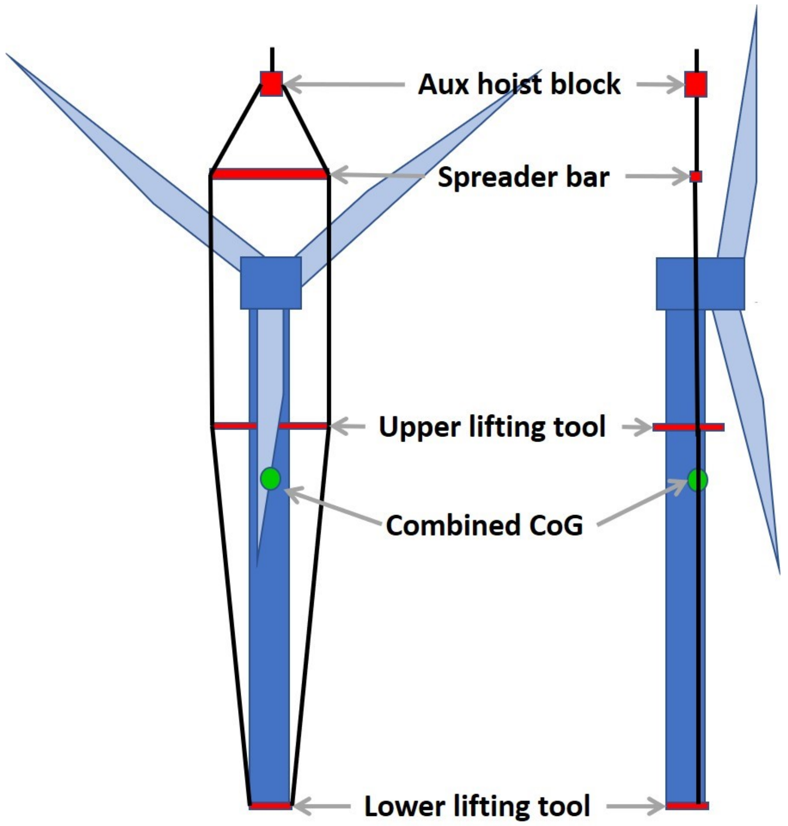

Figure 3.24: Rigging RNA+ front and side view

3.6. Base Case parameters

For the base case, 13 relevant parameters are identified. All parameters will be discussed below. The corresponding base case values per main body are shown inTable 3.20

Table 3.20: Overview of base case parameters

Body	Parameter	Value	Unit	Note
Vessel	Crane Boom Radius	58	$[m]$	
	Slew Angel	180	[°]	
	Tugger Line Damping	15	$[tsm^{-}1]$	
	Tugger Line Angle	15	[°]	
	Upper Lifting Tool Height	7	$[m]$	w.r.t Combined CoG
WTG	Tower Mass	660	$[t]$	
	Nacelle Mass	820.9	$[t]$	
	HCG Nacelle	5.48	$[m]$	w.r.t. top tower
	Hub Height	140	$[m]$	
	VCG Tower	48.72	$[m]$	w.r.t. bottom tower
TLP	TLP Mass	2826	$[t]$	
	Tendon Angle	15	[°]	
	Mooring Line Stifness EA	1.44E+06	$[kN]$	

3.6.1. Vessel

Crane Boom Radius

The clearance between the Nacelle and Crane Boom is expected to be one of the limiting factors for the operability. Therefore the maximum crane boom radius where the Aux Hoist can still lift at its maximum SWL of 2500 t, 58m, is chosen.

Slew Angle

For the Slew Angle, 180° is chosen. This is because all bodies have the same orientation w.r.t the world axis system. After that, variations regarding these orientations can be mapped accordingly.

Tugger Line Damping

For the Tugger Line damping, 15 $[tsm^{-}1]$ is chosen, resulting in a damping of 147.15 $[ts^{-}1]$. This is the standard value for tugger lines used in LiftDyn and Heerema's Sleipnir model.

Tugger line Angle

For the Tugger line angle, 15° is assumed. This is the angle where the tugger lines attach to the middle of the crane boom structure on each side of the crane.

Upper Lifting Tool Height

The upper lifting tool height is set to 7 m above the combined CoG of the RNA+ module and the lifting tools. This is currently the standard distance for the HMC rigging designed for this process.

3.6.2. WTG

For the WTG, the standard nacelle mass and HCG of the nacelle given by IEA are used [33]. The Tower height is altered for the lower hub height, as discussed in Section 3.3 and shown in Table 3.18. The mass and VCG of the tower are scaled accordingly.

Nacelle casing

As discussed in Subsection 3.3.1 the nacelle casing is modeled with multiple POIs. In Figure 3.25, it can be seen that the nacelle casing will collide with the crane boom. The black dashed line is the clearance of 3 m set by DNV [36]. Without the nacelle casing, the closest distance between the crane boom and RNA is 10.7 m.

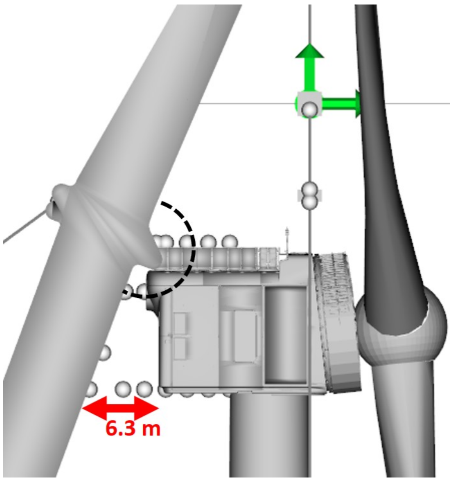

Figure 3.25: Nacelle boom clearance with full nacelle casing

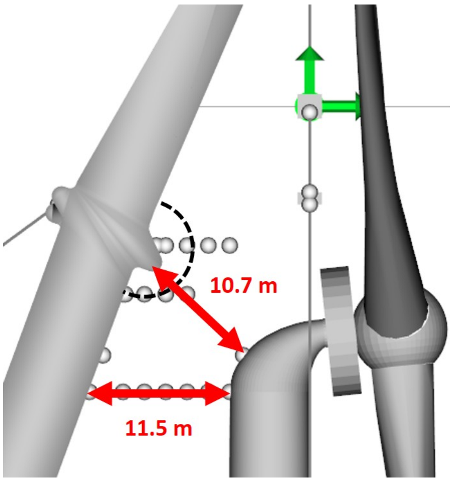

Figure 3.26: Nacelle boom clearance without nacelle casing

The case without the casing is seen as non-realistic, with a clearance of 10.7 and, thus, an operability limit of 7.7 m. This will not represent the actual life application. With the modeled nacelle casing

POIs, those at intervals 0 and 1 are outside the 3 m air gap needed between the crane boom and the nacelle. Interval 0 has a 3 m clearance, whereas int 1 has a 1.3 m clearance. However, interval 0 would imply a nacelle with only a height and no depth in the negative x direction.

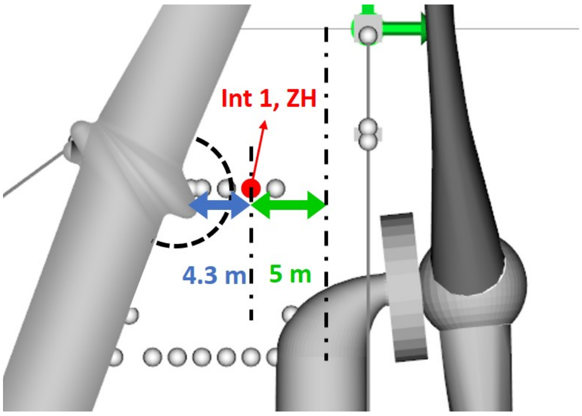

Figure 3.27: Chosen interval for Nacelle Clearance

To approximate a nacelle casing size, interval 1 at height ZH represents the nacelle casing.

3.6.3. TLP

For the TLP, the provided design properties given in Table 3.2 are used for its mass, tendon angle, and mooring line stiffness.

3.7. Modeling

The UM model is set up in a way that it is a function, needing the parameters shown in Table 3.20 as inputs. This is so each parameter variation set can be implemented in one go instead of changing the parameters by hand. The model is built in a way that the RNA+, including lifting tools, is always lifted above its combined CoG, and the distance between the WTG bottom and TLP top is always 3 m. If, for example, the Crane boom radius is altered, the Aux Hoist wire is elongated to compensate for the height difference. The build-up of the model is as follows: First, the vessel is defined, with its stern at the origin, and it is ballasted to the draft of 19 m. Then the Crane module is configured with the input parameters slew- angle and boom radius. The Aux Hoist wire length is set dependent on the crane boom radius. The spreader bar is placed 8 m under the Aux Block. This gives enough space to the rigging wires to not interfere with the RNA+ module. Then the RNA+ module and lifting tools are modeled. Those being the NAH (Nacelle and Hub), Tower, Rotors, Upper- and Lower lifting tools. For this module, the combined CoG is determined. The VCG of the module is determined as a function of the upper lifting tool height, as the placement of the upper lifting tool is determined relative to the combined CoG. With the RNA+ module configured, the nacelle is placed 15 m under the spreader bar to obtain sufficient clearance and maximize the boom clearance. The rigging lines are attached two from the spreader bar to the upper lifting tool and two from the upper to the lower lifting tool. Then the Tugger lines are set up horizontally from the Upper lifting tool to the crane boom with the input parameter for the Tugger line angle. This part of the model is then statically solved using UMs static solver. With the RNA+ module suspended in the vessel's crane in place, the TLP is built. The TLP is placed at the global X and Y coordinates of the WTG tower bottom center and moored to its design draft. The TLP is modeled in this way so that for every variation, the RNA+ module is in its free-hanging stage 3 m above the TLP.

A couple of checks are built to see if all possible variations act accordingly. An overview of values will be calculated and stored in a data file for every run. This data file contains, for instance, all static tensions in all cables. Not only to check if they are as expected but also to see if they may exceed certain limits. Also, the static distance between multiple points is stored. The static distance between the tower bottom and TLP top, the TLP and vessel hull, all nacelle casing intervals, and their corresponding crane-boom clearance POI are stored. Also, the run time per variation is stored to see if the simulation took the expected time. A large variation in simulation time could indicate that something went wrong during the simulation. In addition to this, visual checks of the model in UMs model viewer are done to see and check values and parameters.

For the next step in the LiftDyn simulation POIs need to be identified to map the specific behavior of the model. The model is built so that the RAOs of multiple aspects and objects can be mapped in advance. In LiftDyn, the motion-, velocity-, acceleration- and force RAOs of bodies, POIs, and cables can be determined. Therefore, multiple POIs are identified. As discussed, the Nacelle casing consists of multiple POIs connected to the nacelle. A POI at the WTG tower bottom and TLP top are made. This is to log the relative motions and velocities between the two. The motion RAOs of the CoGs of the Vessel, TLP, and RNA+ module as well as the force RAOs for all rigging cables, are mapped. Furthermore, the Side- and off-lead angles for the Aux Hoist wire are registered.

3.7.1. Model Verification

For the rigging, the static tension in all slings is compared to the expected analytic tension and how the tensions correlate relative to each other. For the base case, the static tension in the aux hoist wire and the total weight of the RNA+ module, including lifting configuration, are compared. The relative difference between the two can be seen in Table 3.21. Furthermore, the tension in the aux hoist wire is compared to that in slings 3 and 4. For the rigging wire definition, see Figure 3.28. It can be seen that the relative difference between the aux hoist wire and slings 3 and 4 equals the weight of the aux hoist block and spreader bar. The mass of these two components is 161 t.

Table 3.21: Tension in Aux Hoist wire compared with total RNA+ and Lifting Configuration weight

	Force	Unit
Aux Hoist Wire	2.11E+04	kN
Weight RNA+ and lifting configuration	2.11E+04	kN
Difference	0.001%	

Table 3.22: Relative tension difference between Aux Hoist Wire compared to Sling 3 and 4

	Force	Unit
Aux Hoist Wire	2.11E+04	kN
Sling 3	9.74E+03	kN
Sling 4	9.74E+03	kN
Combined Slings	1.95E+04	kN
Difference Aux and Slings	1.58E+03	kN
Weight Aux block and Spreader-Bar	1.58E+03	kN
Difference	0.003%	

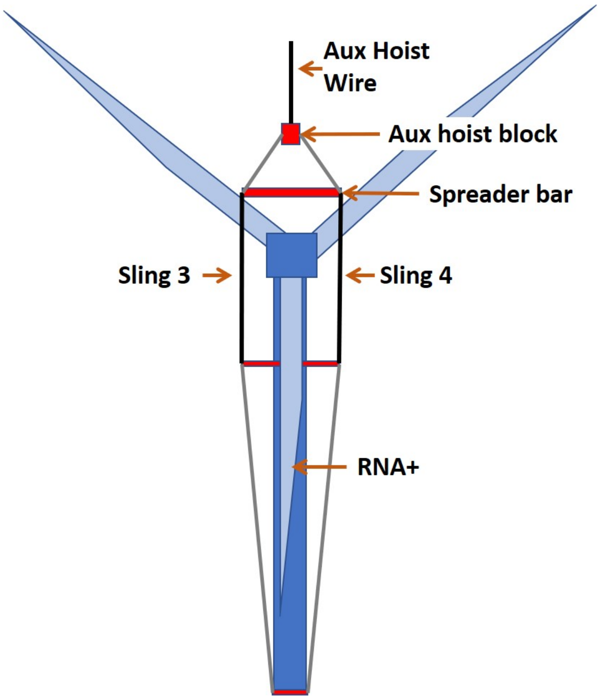

Figure 3.28: Rigging wire definition

The RAOs and corresponding responses to a mean JONSWAP spectrum of the base case model configured with LiftDyn are compared to the RAOs and responses of the model validated with the model test described in Subsection 3.1.2 [49]. As the base case model has an RNA+ module suspended in the crane, its RAOs and responses differ slightly. For all DOF, the ROAs and Responses show similar trends. The comparison of the RAO and response for Surge with wave heading 180° is shown in Figure 3.29

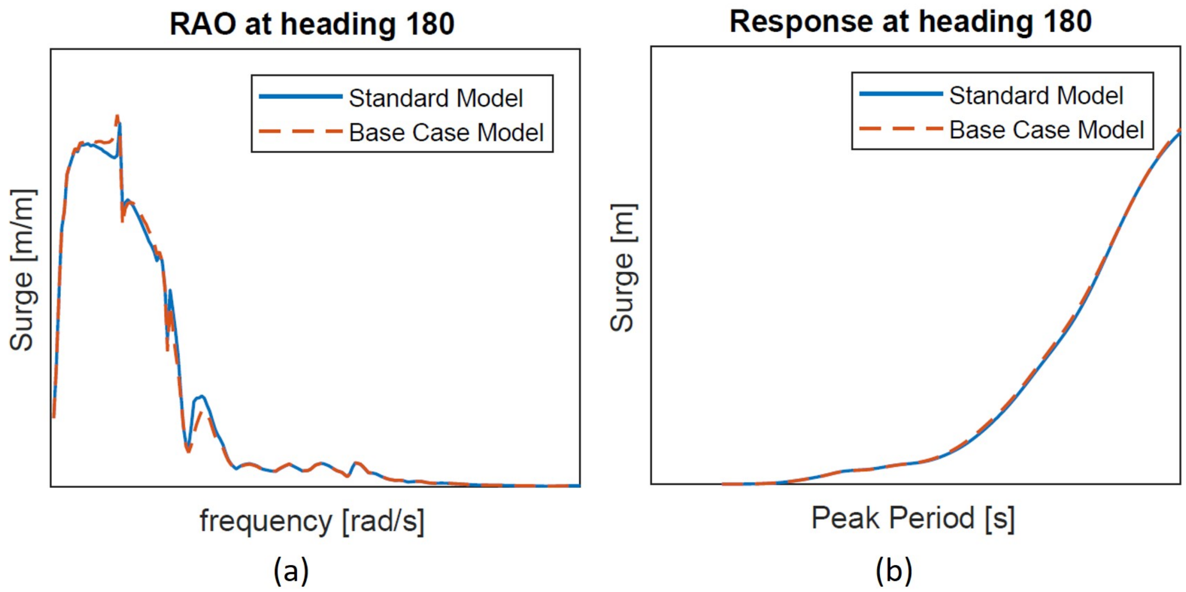

Figure 3.29: RAOs (a) and Responses (b) of validated model compared with base case model

As the total configuration differs slightly in mass and inertia moments, some peaks have a marginally different amplitude but approximately the same frequency. With the visual, static, and hydrodynamic checks in place, the base case can now be subjected to parametric variations.

4

Parametric Variation

This chapter discusses the variation of the 13 base case parameters presented in Section 3.6. In total, there are 27 parameter sets. The first set is the base case, and the other 26 variation sets. For each variation set, one parameter is varied w.r.t. the base case and the set is then completed with the remaining base case settings. Per parameter, two variation steps are identified. Some variations imply real-life applications and other variations vary in range to see the effect of the variation. All variations of the parameters are shown in Table 4.1. An overview of all variation sets is given in Table C.1.

Table 4.1: Base Case Parameters and their two variations

Body	Parameter	Base Case	Var 1	Var 2	Unit	Note
Vessel	Crane Boom Radius	58	40	50	$[m]$	
	Slew Angel	180	135	90	[°]	
	Tugger Line Damping	15	0	30	$[tsm^-1]$	
	Tugger Line Angle	15	0	-25	[°]	
	Upper Lifting Tool Height	7	1	14	$[m]$	w.r.t RNA+ VCG
WTG	Tower Mass	660	860	1060	$[t]$	
	Nacelle Mass	821	621	1021	$[t]$	
	HCG nacelle	5.48	0	-5.48	$[m]$	w.r.t. top tower
	Hub Height	140	130	150	$[m]$	
	VCG Tower	48.72	35	65	$[m]$	w.r.t. bottom tower
TLP	TLP Mass	2826	2402	3250	$[t]$	
	Tendon Angle	15	0	-25	[°]	
	Mooring Line Stiffness EA	1.44E+06	7.72E+05	1.78E+06	$[kN]$	

4.1. Crane Boom Radius

As discussed above, the crane boom radius of 58 m is used in the base case. This is because it is the maximum radius the crane can still lift at its maximum Aux hoist capacity. The minimum radius is 33 m. A smaller radius means a higher total lifting height but also limits the clearance between the boom and the lifted object. To see the relation between the two, the crane boom radius is varied to 40 and 50 m. an impression of the variation is given in Figure 4.1

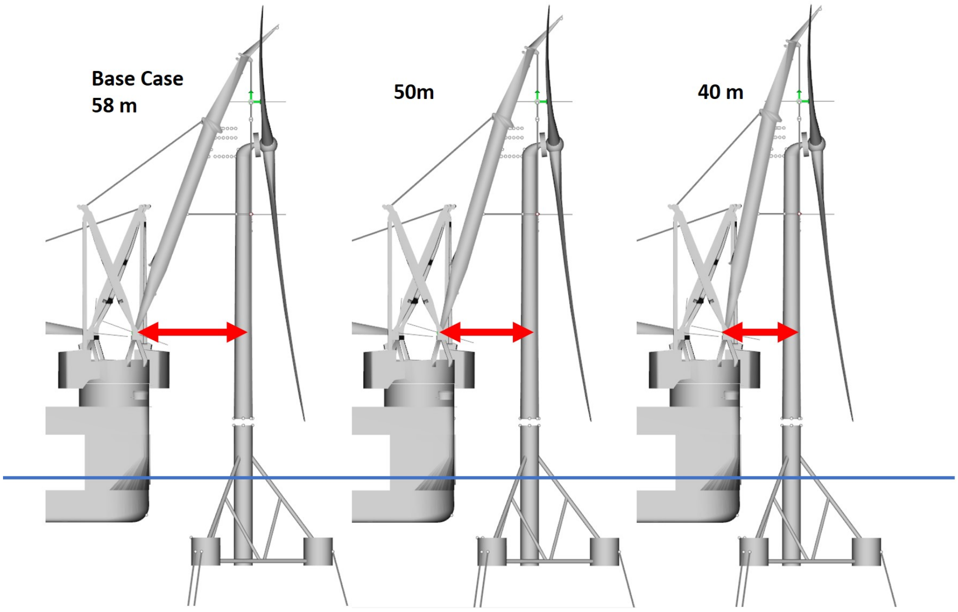

Figure 4.1: Visualization of Boom Radius Variation

As the Boom radius decreases, the lifting height of the crane changes. The Free hanging situation of 3 m above the TLP is maintained for all three cases. Therefore the Aux hoist wire is elongated accordingly with the boom radius variation.

4.2. Slew Angle

The slew angle is varied to 135° and 90°. This is to see the effect of the different vessel motions w.r.t to the WTG and TLP. The variation steps are visualized in Figure 4.2.

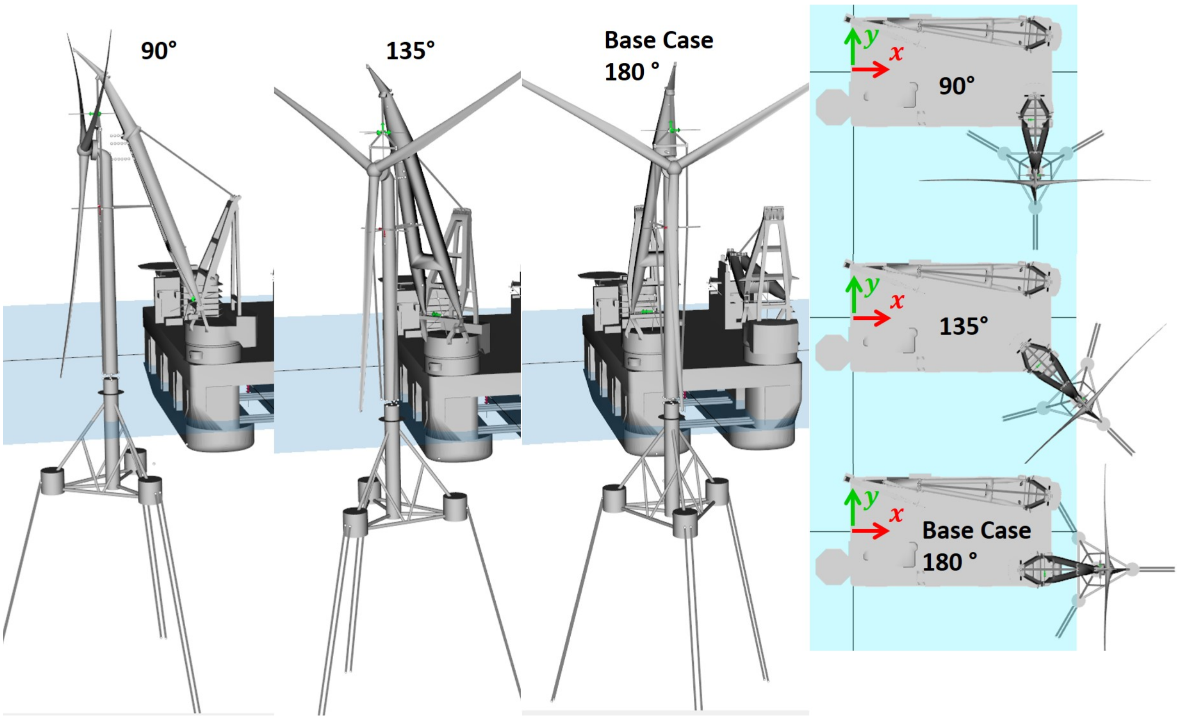

Figure 4.2: Visualization of Slew Angle Variation

For the base case, it is expected that the RNA+ influences the pitch motion of the vessel. To see the relative difference and as the wave directions are considered with a bin of 45°, a slew angle of 90° is chosen to see if this expectation is valid and to see the effect of the WTG on the roll motion. The angle of 135° is chosen as a midway point between 90° and 180°. To keep the clearance between the TLP and vessel hull sufficient, the TLP is rotated with respect to the slew angle. So its X-axis stays orthogonal to the vessel's hull, see Figure 4.6. For slew angles between 90° and 180°, this means its X-axis is in line with the Crane booms X-axis. For slew angles smaller than 90° and larger than 180°, the TLP keeps orthogonal to the ship's hull.

4.3. Tugger Line Damping

For the tugger line damping, the standard Heerema Value of 15 $tsm^{-}1$, being 147.15 $ts^{-}1$, is varied from 0 to 30. This is to model the situation without tugger damping and to see the effect if one would double this damping.

4.4. Tugger Line Angle

For the Tugger Line Angle, a situation with an angle of 0° is considered to see the effect of only tugging forces in the crane booms x direction. Also, the situation with crossed tugger lines is considered. This crossed configuration results in a tugger line angle of - 25°.

4.5. Upper Lifting Tool Height

The Upper lifting tool Height is altered in the following manner. The first alteration is 1 m above the combined RNA+ VCG. For this lifting configuration, the upper lifting tool should stay above the VCG to have a positive moment on the RNA+ module. For the second variation, the base case offset is doubled. This is to see the alteration's effect and keep enough clearance between the upper lifting tool and the blades. The variations steps for the upper lifting tool off-sett are shown in Figure 4.3.

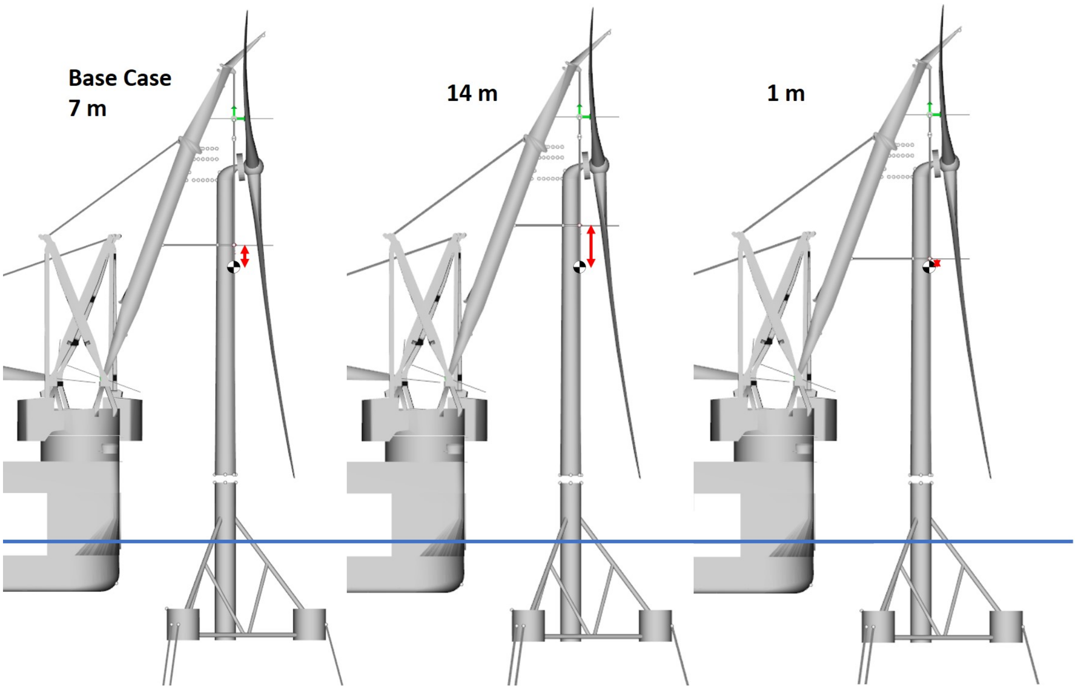

Figure 4.3: Visualization of Upper lifting tool offset variation

4.6. Tower Mass

As the original tower is altered to a weight of 660 t due to diameter and height alterations, the first Tower Mass variation is its original mass of 860 t. This is the tower's mass if the hub height had been 150 m and the outer diameter of the bottom 10 m. As the second variation, the difference in mass between the base case and the first variation is added to this first variation resulting in a mass of 1060 t. A lighter tower is not considered as the current tower already approaches the lightweight application of such towers.

4.7. Nacelle Mass

The nacelle mass is varied with 200 t in both directions. There is little publicly available data regarding specific dimensions and masses of WTG components. The mass calculated for the IEA 15MW turbine is a summation of the needed and used parts of the WTG. It considers only the bare minimum needed components. However, some parts have an estimated or rounded up weight. Therefore, both a 200 t lighter and heavier nacelle will be assessed.

4.8. HCG Nacelle

For the variations, the first situation assessed is where the cog is right above the X-Y center of the tower. The second variation is where the HCG is transferred -5.48 m, the x-distance of the original HCG, over the X-Axis. This variation could model a situation where the RNA+ is rotated 180° around its Z-Axis. The variation of HCG w.r.t. the nacelle is shown in Figure 4.4

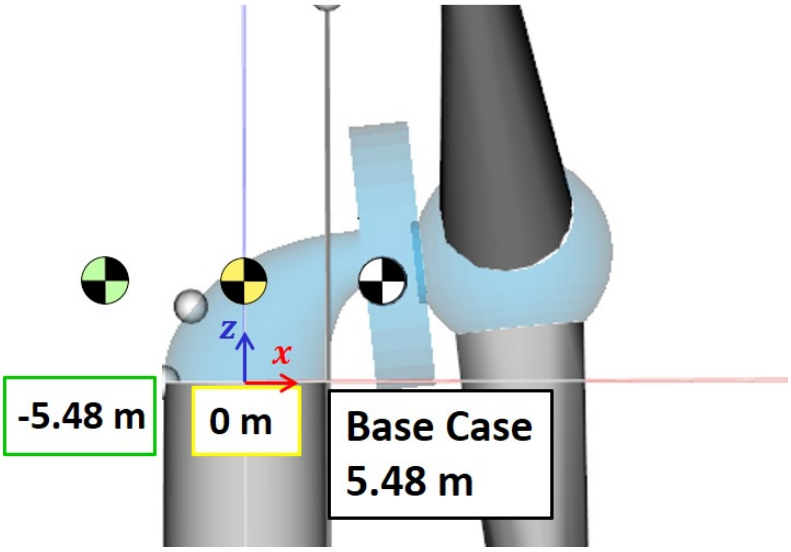

Figure 4.4: Visualization of Nacelle HCG Variation

Direct Drive turbines such as the NREL 15 MW turbine have no gearbox. Therefore its HCG is placed relatively towards its hub, as the weight of a gearbox does not counter the generator's weight located just behind the hub. As the weight of the RNA module is more than 50% of the total weight of the RNA+ and rigging, it significantly affects the combined CoG of the RNA+. As the RNA+ is lifted in line with the combined CoG, an RNA+ with its HCG more backward will result in more clearance between the RNA+ and the crane boom. This process is shown in Figure 4.5. Left the base case situation is shown. The black-white, black-yellow, and black-green circles show the HCG variation of the base case, 0 m and -5.48 m, respectively. The red-white circles show the corresponding combined CoG of the RNA+ module.

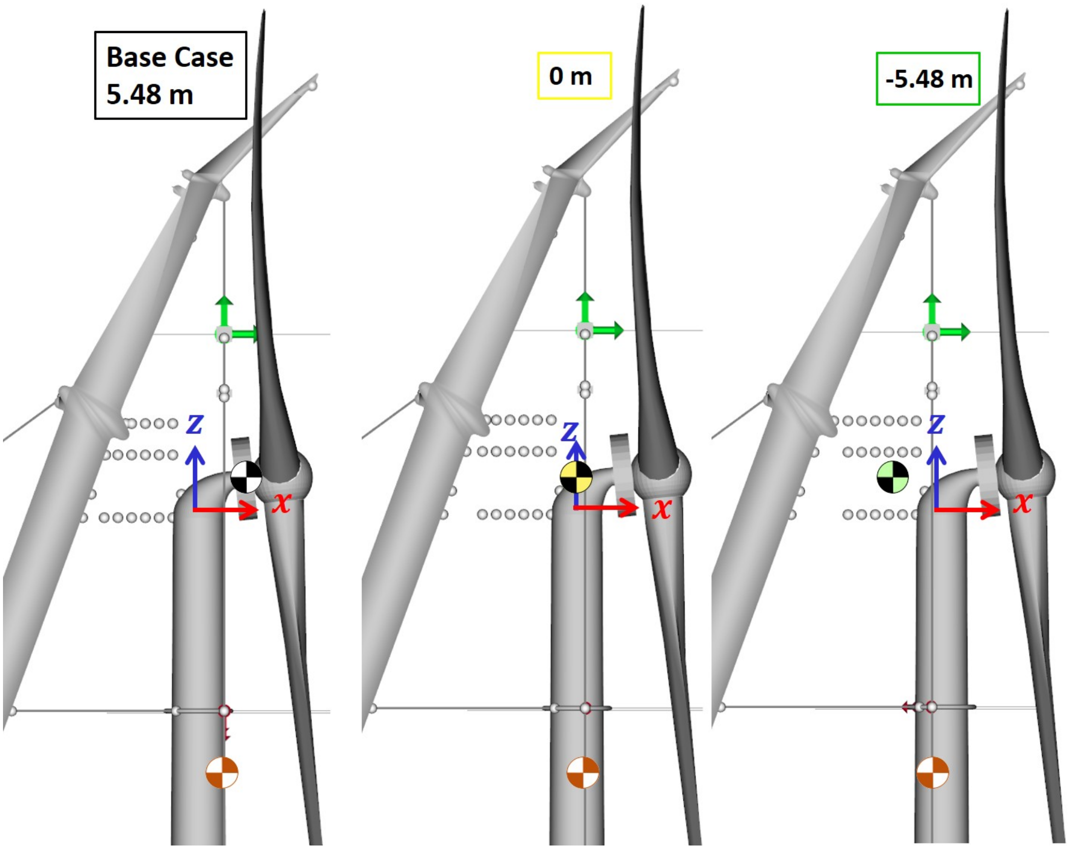

Figure 4.5: Visualization shift in Combined RNA+ CoG

4.9. Hub Height

As the hub height is lowered by 10 m, see Section 3.3. Its original height of 150 m is considered as the first variation. As the hub height of 150 is already expected to cause limitations in the installation process, higher hub heights are not considered. Therefore, a height of 130 m is chosen as the second variation. One thing to note is that the mass and VCG of the altered towers are not compensated for their variation in size. This is to see only the effect of the tower height variation w.r.t. the base case. The mass and VCG of the tower are kept at the same position as those in the base case. This is to keep the variations independent from each other.

4.10. VCG Tower

Variations in sizes, wall thicknesses, or other modifications to the tower could lead to different VCGs of the tower. Also, Different weights of lifting tools used to lift the tower could alter the total combined VCG of the tower. Therefore the VCG is varied. The upper limit is about one-third above the original VCG, being 65 meters. The lower limit is about one-third lower than the original value rounded up to the first multiple of five.

4.11. TLP Mass

As the TLP mass influences its behavior significantly, but also with a realistic point of view, its mass is varied by 15% both ways. TLPs exist in many different forms and shapes. Their mass and tendon tension are dependent on one another. As those aspects lead to the functioning of the TLP's design, its value is varied to see the effect in this specific case. Less mass lead to more tension in the tendons en vice versa.

4.12. Tendon Angle

The Given tendon angle of 15° is designed to also alter horizontal motions of the TLP, for instance, the wind-induced force of the wind on the WTG or wave-induced motions. To see if these horizontal tendon forces influence the installation process, the first variation is set with a tendon angle of 0°. The second variation is 20°.

4.13. Mooring Line Stiffness

Different tendon materials are used as inputs for the variation of the Mooring Line Stiffness. As the original TLP design uses stud-less 0.13 m R4 chains with a Minimum Breaking Load (MBL) of 15.6 MN. with the use of FibreMax' Cable Configurator [54] a Dyneema and carbon tendon with equivalent or more MBL for the cable length of about 120 m are configured. This results in an EA of 7.72E+05 kN and 1.78E+06 for Dyneema and Carbon tendons, respectively.

4.14. Coordinate System

For all variations, the following coordinate system is defined:

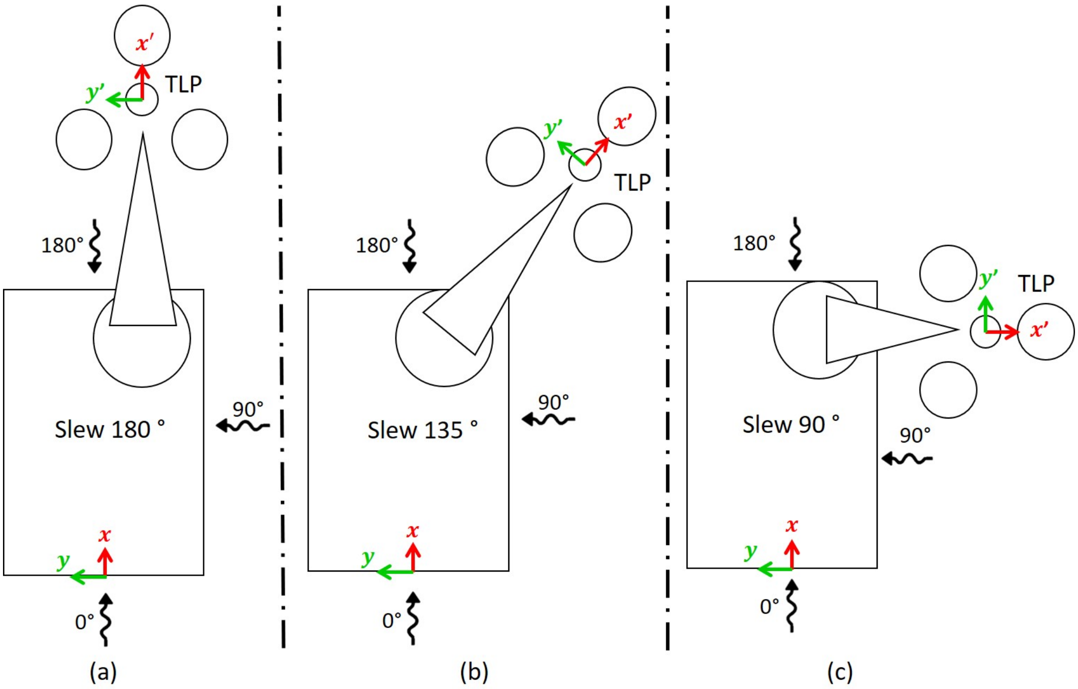

Figure 4.6: Wave Direction and Coordinate system per slew Angle

Waves propagating in global positive x- direction are defined as a wave direction of 0°. Waves propagating in the global positive y-direction are waves with wave direction 90°. As the Slew angle is altered, so is the orientation for the TLP. The alteration for slew angle 135° can be seen in Figure 4.6(b), for slew angle 90° in (c).

5

Operability and Results

This chapter confines how the operability is assessed and how this operability per parameter variation varies. The operability is asses with regard to the 3-hour Single Most Probable Maximum (3h SMPM) limits. Furthermore, the workability of the base case is determined for two example locations.

5.1. Operability

The methodology used in Subsection 3.2.7 to determine the RAOs and responses using Equations 2.17 and 2.20, respectively, can be applied for all model POIs. With these responses, the 3h SMPM responses, see Subsection 2.5.3, per POI RAO can be calculated. These 3h SMPM responses can then be subjected to the operational limits defined below to determine the operability.

5.2. Operational limits

The operational limits shown in Table 5.1 are used for this research. These are the operational limits Heerema uses for the floating to fixed installation of WTGs on monopiles. Instead of the relative horizontal and vertical movement w.r.t. the earth coordinates systems, these motions are now relative to the WTG tower bottom and TLP top.

Table 5.1: Limiting criteria, 3h SMPM

Limiting criteria	**3h SMPM values**	Unit
Nacelle Crane boom clearance		m
Vessel Roll		°
Vessel Pitch		°
Crane Side Lead		°
Crane Off-lead		°
Relative X-Y movement Tower- TLP		m
Relative Z movement Tower- TLP		m
Nacelle Acceleration		m/s^2

5.3. Three Hour Single Most Probable Maximum

With the use of Equations 2.22, 2.25, 2.26, the 3h SMPM for all limiting criteria are determined for a H_s of 2 m and $H_sT_p^2$ of 120 ms^2. The base case's 3h SMPM values are shown in Table 5.2.

Table 5.2: 3h SMPM values for H_s = $2m$ and $H_S T_p^2$ = 120 ms^2, Base Case

Parameter	Base Case	Unit
Vessel Roll		°
Vessel Pitch		°
Sidelead A		°
Offlead A		°
Z tip		m
XY tip		m
Clearance Nacelle		m
Nacelle acceleration		m/s^2
Clearance Nacelle 2		m

For all other variations, these are shown in Table E.1. Their relative difference w.r.t. the base case is shown in Table E.2. It can be seen that the variations in slew angle, offset 14 m for the upper lifting tool, and the VCG 65m of the tower influence the 3h SMPM values with respect to the nacelle clearance and acceleration the most. The case without tugger damping has the most considerable effect on the off-lead and XY tip motion of the tower bottom w.r.t. the TLP top.

5.4. Operability Parametric variation

In this Section, the generated plots operability plots are discussed. LiftDyn determines the operability with the use of Equation 2.29. For the wave direction, ϵ, the range of 0° to 180° in steps of 45° is chosen to assess the operability. Since the vessel has Port-Starboard side symmetry, the effects of waves coming from 225° to 315° are considered equal to their opposite counterpart. As the vessel has no Fore-Aft symmetry, both 0° and 180° are assessed.

A plot for limiting $H_s - T_P$ combinations is made per parameter variation per wave direction. Figure 5.1 shows the operability curve for the Base Case and wave direction 180°.

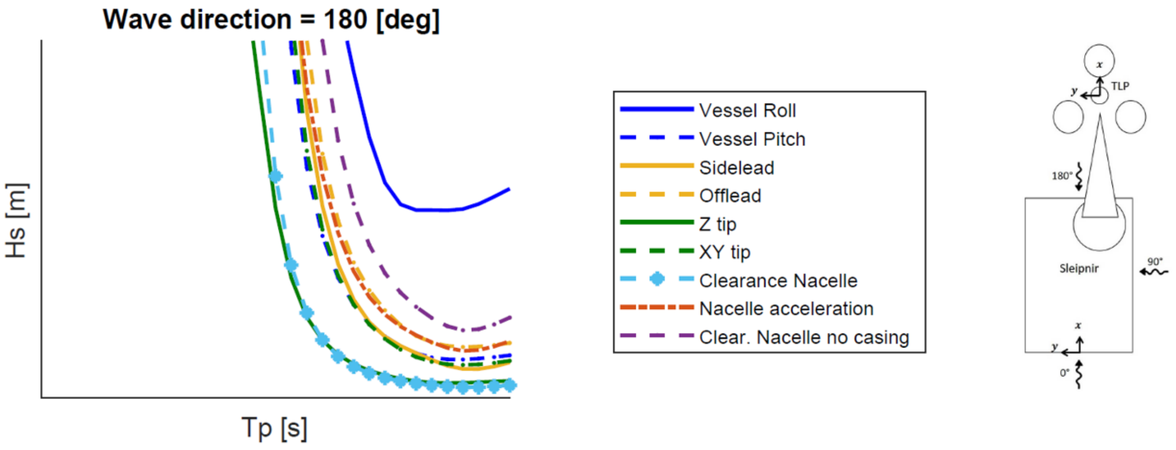

Figure 5.1: Operability curve - base case- all limits - 180°

In Figure 5.1 and all other operability plots: The blue and blue dashed lines show the permissible significant wave height depending on the peak frequency, H_s-T_p curve, for the vessel roll and pitch, respectively. The yellow and yellow dashed lines show the side- and off-lead H_s-T_p curve, respectively. Green is the relative motion in Z-direction between the Tip of the TLP and the bottom of the WTG tower. The green dashed line is the relative motion of these two bodies in the horizontal XY plane. The cyan dashed line with the diamond marker shows the H_s-T_p curve for the clearance between the crane boom and nacelle int 0. The orange dash-dotted line is the H_s-T_p curve for the nacelle acceleration. The purple dashed line is that of the nacelle clearance if no nacelle casing would be considered. This demonstrates the effect that this parameter has on the operability. Finally, the thick red line is the considered wave spectrum, described in Equation 2.21. For this case, it can be seen that for T_p < 9 s, the governing limit is the relative Z tip motion between the tower and TLP. For T_p > 9 s, this becomes the nacelle crane boom clearance. All Operability plots per parameter variation for all limits are shown in Appendix D. In the following subsections, the relevant findings per relevant plot are given

The governing limits are fitted into one minimal operability line to get the total operability per parameter per variation step. They are then grouped per parameter. An example of this grouped operability for the upper lifting tool offset is given in Figure 5.2:

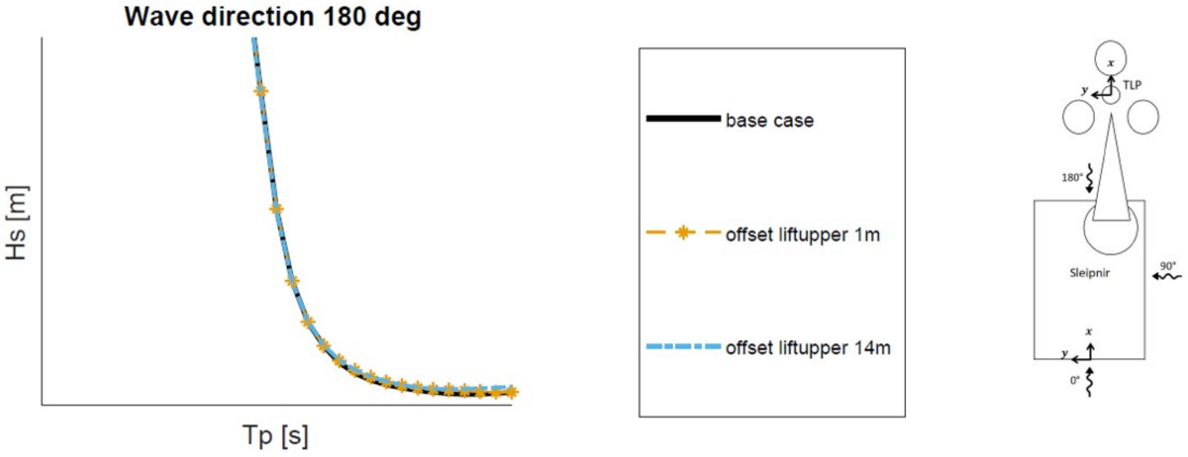

Figure 5.2: Grouped operability Upper Lifting Tool height variation w.r.t. Base Case,180°

Here the grouped operability for the upper lifting tool offset variation is plotted. The black line represents the governing limits for the base case. For this instance, this line follows the relative Z motion between the tower and TLP for T_p < 9 s and the nacelle crane boom clearance for T_p > 9 s shown in Figure 5.1. In this case, the yellow dashed line with an asterisk marker is the governing limit for the first variation, being the offset of 1 m, and the cyan dash-dotted line is the governing limit for the second variation. Again, the thick red line is the considered wave spectrum, described in Equation 2.21. In Figure 5.2, it can be seen that for the second variation, the operability is lower than those of the base case and the first variation. The first variation has a slightly larger operability for T_p>0 w.r.t. the base case.

The total area under the operability- and $H_s - T_P$ limit is calculated to put these differences into perspective. With the use of Matlab's [55] trapz function and InterX' [56] intersection function. The intersecting points between the operability limits and $H_s - T_P$ limit are found with the InterX intersection function and are then used as the lower bound of the integration done with trapz. The upper limit is set to 15, the maximum T_p considered. Both curves are integrated, and the areas are deducted from one another to obtain the area between the operability and $H_s - T_P$ limit, marked in pink in Figure 5.3. With the trapz function with lower bound 0 and upper bound, the total area under the $H_s - T_P$ limit defined in Equation 2.21 is calculated. Then the area between the curves is deducted from this total area to get the total area under both limits, marked in green in Figure 5.3.

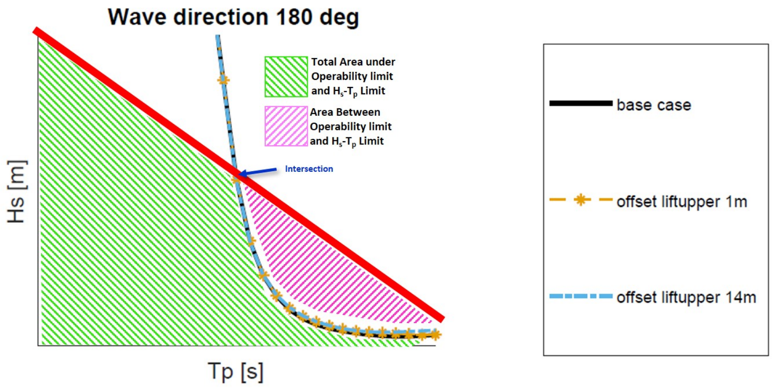

Figure 5.3: Area integration Grouped operability limits

This is done for all three parameter cases. The percentage difference between the areas of the parameter variations and base case is then calculated. For this instance regarding the upper lifting tool offset and wave direction 180°, this results in the following relative differences:

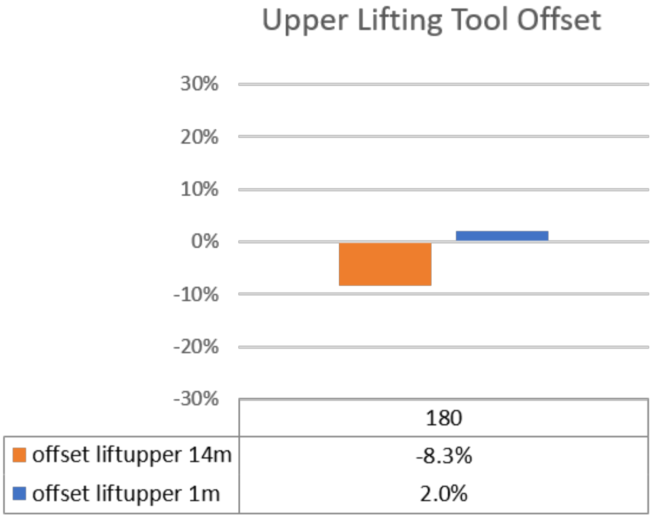

Figure 5.4: Relative difference between the base case and upper lifting tool offset variation

This process is done for the base case, the 13 parameters, and their two variations in the five wave directions. Resulting in 27*5 plots regarding the operability of all operational limits. For the grouped situation, this yields 13*5 plots. This means 200 plots are generated. The effect of the parameter variations w.r.t. the operability per parameter is discussed in the subsections below.

For the digital reader: Each Subsection refers to the corresponding (grouped) operability plots in the Appendix. In the Appendix, each parameter variation has its own page, containing the five subplots per wave direction. On the bottom right, under the legend, ’buttons’ are created to easily browse through the results. These buttons on the Appendix pages link back to the Section where they are discussed. The grouped plots refer to the plots of the parameter variation ones and vice versa.

5.4.1. Base Case

The Operability for the Base Case per operational limit is shown in Section D.1. It can be seen that for all wave directions, the nacelle clearance is the governing limit. For wave direction = 0°, the operability is the highest. For wave directions, 0°, 135°, 180°, the second limit is the relative Z motion between the tower bottom and TLP top. For wave directions 45° and 90°, the second limit is the side lead. For all wave directions, the difference in operability between the situation with and without nacelle casing is significant. Where the first situation has a large impact on the operability, being governing in most situations. The instance without casing for most situations does not even cross the considered sea states line.

The effect on the operability of the clearances of all five intervals can be seen in Figure 5.5. The black line shows the case without nacelle casing and a clearance limit of 7.7 m. The yellow line is the one of interval 0, with a clearance of 3 m. The blue dotted line is the one of interval 1, with a clearance limit of 1.3 m. For all other intervals, the static clearance is smaller than 3 m, and thus the operability is zero. This shows that the chosen interval discussed in Subsection 3.6.2 results in an operability larger than zero.

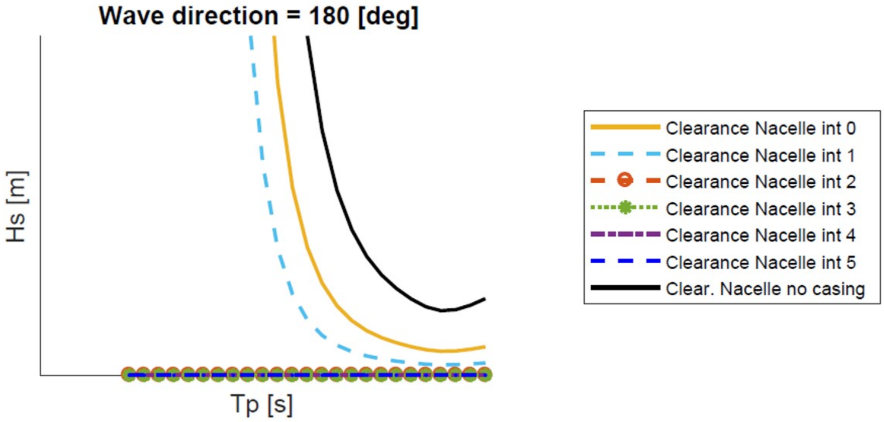

Figure 5.5: Operability for Nacelle Clearance per interval at ZH - Base Case

5.4.2. Boom Radius

For the operability plots of Boom radius 50 [m], see: Section D.2.
For the operability plots of Boom radius 40 [m], see: Section D.3.
For the grouped Boom Radius operability plots see: Section F.1.

In all plots regarding the variation in boom radius, it can be seen that the operability is zero. This is due to the fact that the nacelle clearance is too small, it will even collide with the boom in some sea states. Looking at the other limiting criteria, the Z tip motion and side-lead are the second lowest limits. All limits other than the nacelle boom clearance are very similar for both variations w.r.t. the base case.

5.4.3. Slew Angle

For the operability plots of Slew Angle 135°, see: Section D.4.
For the operability plots of Slew Angle 90°, see: Section D.5.
For the grouped Slew Angle operability plots see: Section F.2.

The grouped operability for the slew angle variation shows that for wave directions 0° and 180°, the operability is lower than that of the base case. In the other directions, this is slightly higher. With the slew angle variation of 90°, the operability is 18.8% higher than that of the base case at 90°. However, this operability is still 8.8% lower than that of the base case with wave direction 0°. Looking at the individual plots per limits; for both slew angle variations, a decrease in nacelle clearance can be seen for wave directions 0° and 180°. The governing limits are the nacelle boom clearance, Z-Tip motion, and Side-lead.

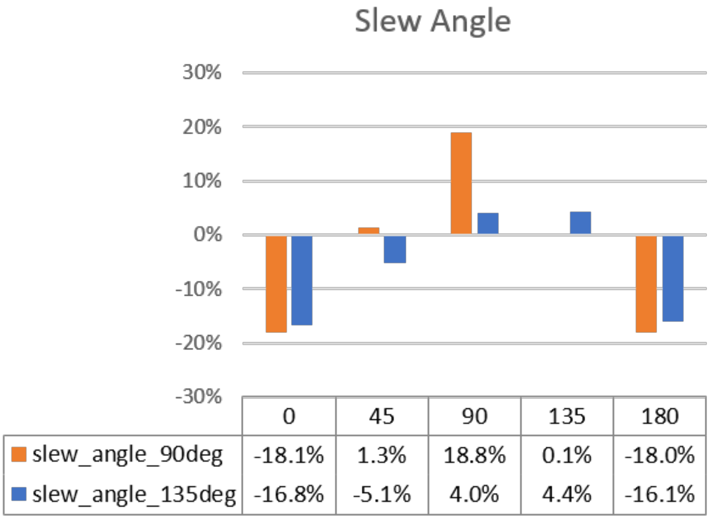

	0	45	90	135	180
🟧 slew_angle_90deg	-18.1%	1.3%	18.8%	0.1%	-18.0%
🟦 slew_angle_135deg	-16.8%	-5.1%	4.0%	4.4%	-16.1%

Figure 5.6: Relative Difference Operability Slew Angle w.r.t. Base Case

5.4.4. Tugger Damping

For the operability plots of Tugger Damping 0 [t*s/m] see: Section D.6.
For the operability plots of Tugger Damping 30 [t*s/m] see: Section D.7.
For the grouped Tugger Damping operability plots see: Section F.3.

The variation in tugger damping shows minimal effect on the operability. For wave directions 0° and 180°, the variation with no damping shows a decrease of about 5%. The situation with more damping shows a slight increase of around 2% in these directions, see Figure 5.7. Again the Nacelle clearance and the Z tip motion are the governing limits. As the tuggers are purely horizontal, the operability of the z-tip motion is not altered. This 5% in- and 2% decrease are due to the effect of the tuggers on the nacelle clearance. As the tugger lines are mostly directed in the global x- direction, their effect is the largest for wave directions 0° and 180°. A significant reduction in off-lead can be seen for the increased damping case for these two wave directions. However, because the off-lead is not near the governing limits, this does not affect the grouped operability. The tugger damping alterations also influence the XY-tip motion.

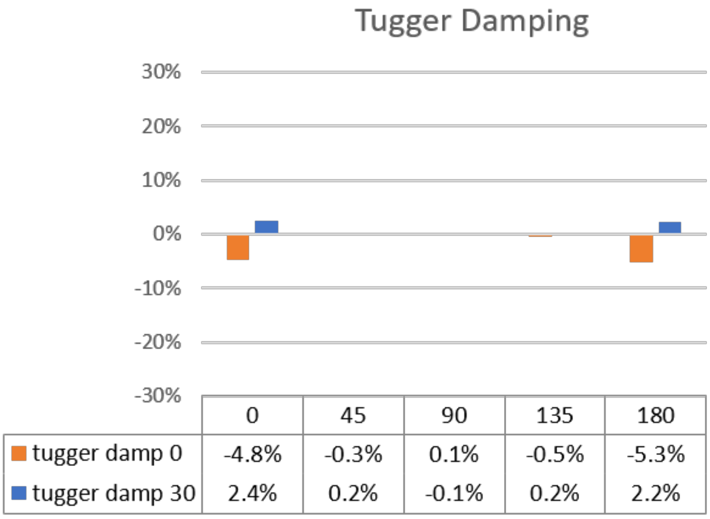

	0	45	90	135	180
🟧 tugger damp 0	-4.8%	-0.3%	0.1%	-0.5%	-5.3%
🟦 tugger damp 30	2.4%	0.2%	-0.1%	0.2%	2.2%

Figure 5.7: Relative Difference Operability Tugger Damping w.r.t. Base Case

5.4.5. Tugger Line Angle

For the operability plots of Tugger Line Angle 0°, see: Section D.8.
For the operability plots of Tugger Line Angle -25°, see: Section D.9.
For the grouped Tugger Line Angle operability plots see: Section F.4.

No major effect on the operability is seen for the variation in the tugger line angle. The nacelle clearance and z-tip motion are the governing limits in most directions. Interesting is to see that for the wave directions other than 0° and 180°, a slight increase in operability can be seen for the case with crossed tugger lines, see Figure 5.8. This could be because the tugging capacity in the global Y-direction is larger than that of the base case. Therefore, the nacelle movement is damped in the global y direction. No significant increase can be seen for the case with a tugger line angle of 0°. Therefore, it can be assumed that for tugger lines to affect both X and Y directions, a larger angle than 15° should be considered, it having a larger Y component.

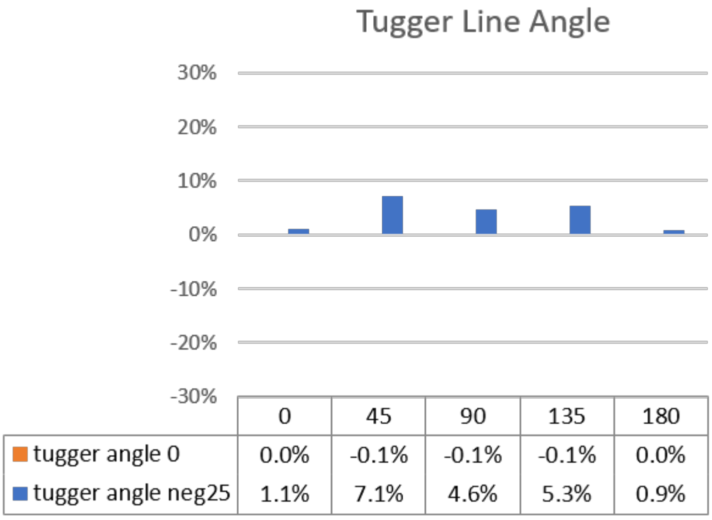

	0	45	90	135	180
🟧 tugger angle 0	0.0%	-0.1%	-0.1%	-0.1%	0.0%
🟦 tugger angle neg25	1.1%	7.1%	4.6%	5.3%	0.9%

Figure 5.8: Relative Difference Operability Tugger Line Angle w.r.t. Base Case

Subsection Upper Lifting Tool Offset For the operability plots of Upper Lifting Tool Offset 1 [m], see: Section D.10.
For the operability plots of Upper Lifting Tool Offset 14 [m], see: Section D.11.
For the grouped Upper Lifting Tool Offset operability plots, see: Section F.5.

The first variation of the upper lifting tool offset of 1 m shows increased operability in all directions. The plots in Section D.10 show that this variation positively influences the nacelle boom clearance. It also affects the side lead limit in a positive manner, leading to higher operability. It can also be seen that the XY-tip movement becomes more limiting. However, this decrease in operability regarding the XY-tip movement does not become a governing limit. These are still the nacelle boom clearance and Z-tip motion. For the 14m variation, the opposite can be seen. The operability regarding the nacelle clearance and side lead decreases, and the XY-tip motion limit becomes less limiting.

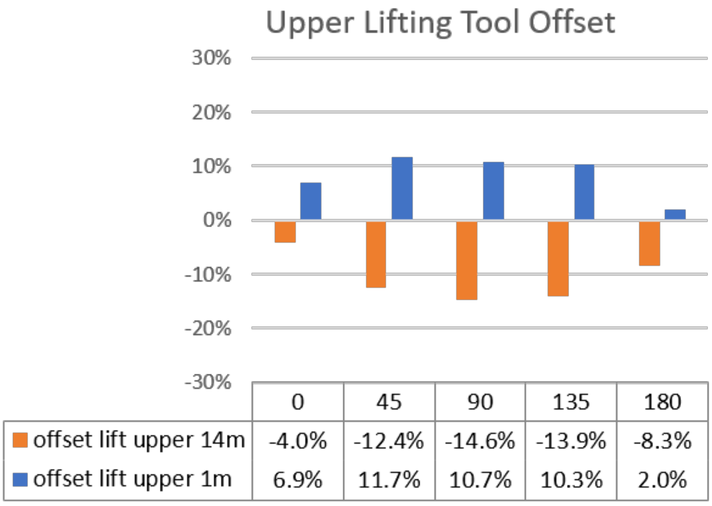

	0	45	90	135	180
🟧 offset lift upper 14m	-4.0%	-12.4%	-14.6%	-13.9%	-8.3%
🟦 offset lift upper 1m	6.9%	11.7%	10.7%	10.3%	2.0%

Figure 5.9: Relative Difference Operability Upper Lifting Tool Offset w.r.t. Base Case

5.4.6. Tower Mass

For the operability plots of Tower Mass 860 [t], see: Section D.12.
For the operability plots of Tower Mass 1060 [t], see: Section D.13.
For the grouped Tower Mass operability plots see: Section F.6.

In Figure 5.10, it can be seen that an increase in operability can be seen for both tower mass variations. For both cases, this is due to the fact that this increase in mass widens the nacelle boom clearance. This is because the RNA+ module is lifted above its combined CoG. When the tower increases in mass, the HCG moves toward the tower's center. This is visualized in Figure 4.5. For the 860 t increase, the HCG moves -0.3 m in the global x position, which is -0.56 m for the 1060 t case. These shifts in HCG can be seen in the clearance of the nacelle. Where the base case this limit is 1.3 m, these are 1.6 m and 1.9 m for the 860 t and 1060 t variations, respectively. This higher boundary lead to a higher operability. Also, this increase in mass limits the total RNA+ movement in the global Y-direction, as the side-lead becomes less limiting in all cases.

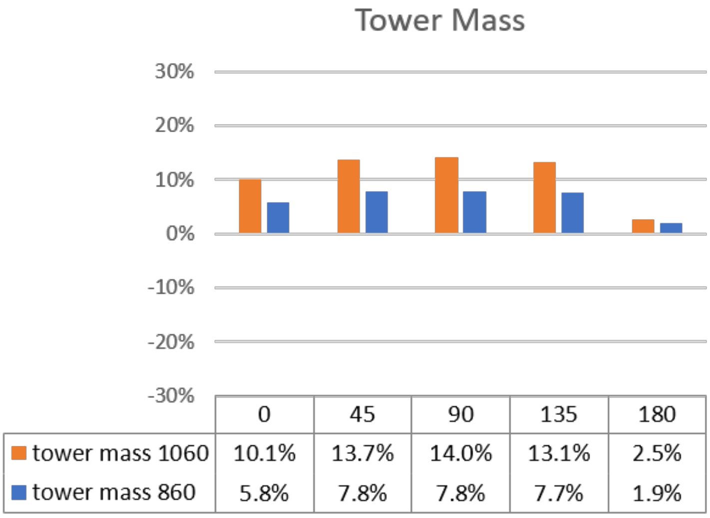

	0	45	90	135	180
🟧 tower mass 1060	10.1%	13.7%	14.0%	13.1%	2.5%
🟦 tower mass 860	5.8%	7.8%	7.8%	7.7%	1.9%

Figure 5.10: Relative Difference Operability Tower Mass w.r.t. Base Case

5.4.7. Nacelle Mass

For the operability plots of nacelle Mass 620 [t], see: Section D.14.
For the operability plots of nacelle Mass 1020 [t], see: Section D.15.
For the grouped Nacelle Mass operability plots see: Section F.7.

Similar behavior as the tower mass variation can be seen with the variation in nacelle mass. The only difference is that the nacelle is located on the positive X-axis w.r.t. the combined RNA+ CoG. Therefore, a reduction in mass moves the combined HCG in negative X-direction. An increase in mass results in the combined HCG moving in positive X-direction. The move of HCG in the X-direction are -0.24 m and 0.20 m for the 620.9 t and 1020.9 t, respectively. This results in the nacelle clearance limits of 1.5 m and 1.1 m. This variation in limit boundaries results in the following shift in operability per wave direction:

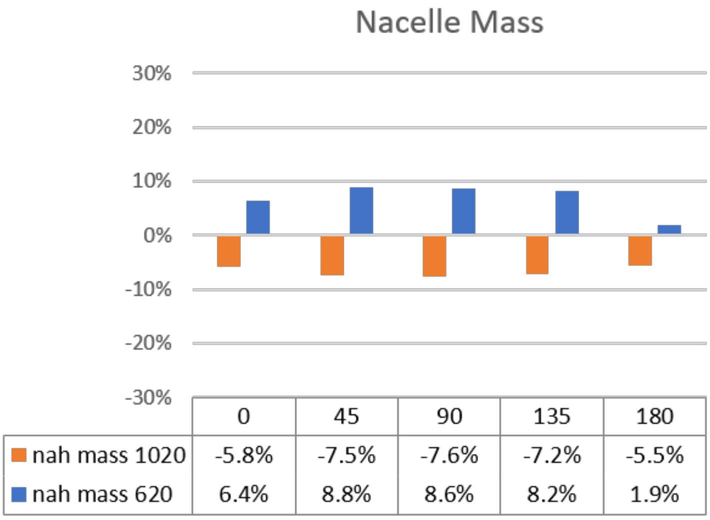

	0	45	90	135	180
🟧 nah mass 1020	-5.8%	-7.5%	-7.6%	-7.2%	-5.5%
🟦 nah mass 620	6.4%	8.8%	8.6%	8.2%	1.9%

Figure 5.11: Relative Difference Operability Nacelle Mass w.r.t. Base Case

5.4.8. Nacelle HCG

For the operability plots of Nacelle HCG 0 [m], see: Section D.16.
For the operability plots of Nacelle HCG 5.48 [m], see: Section D.17.

For the grouped Nacelle HCG operability plots see: Section F.8.
By shifting the HCG of the nacelle, the HCG of the RNA+ module shift accordingly. The shift to a nacelle HCG of 0 m, located at the center line of the tower, results in a reduction of 2.3 m for the combined HCG, leading to a clearance limit of 3.6 m. The shift to a nacelle HCG of -5.48 m results in a reduction of 4.5 m for the combined HCG, enlarging the clearance limit to 5.8 m. For all wave directions, it can be seen that the increase in operability is equal for the two variations, see Figure 5.12

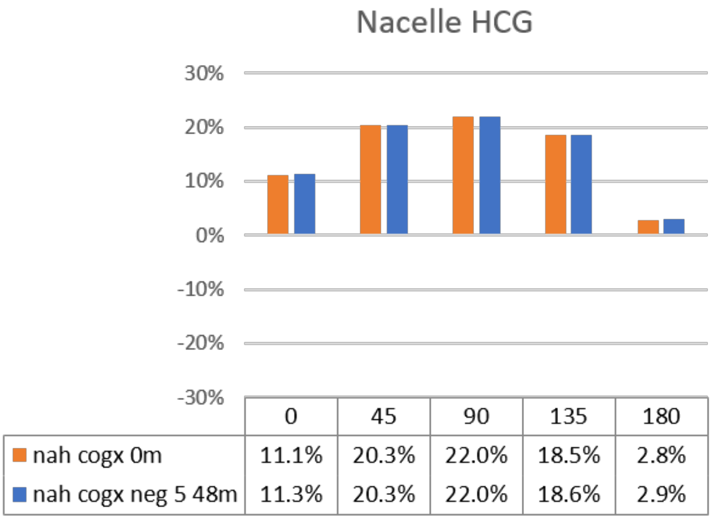

	0	45	90	135	180
🟧 nah cogx 0m	11.1%	20.3%	22.0%	18.5%	2.8%
🟦 nah cogx neg 5 48m	11.3%	20.3%	22.0%	18.6%	2.9%

Figure 5.12: Relative Difference Operability Nacelle HCG w.r.t. Base Case

This equality is due to the fact that because of the increase of the nacelle clearance limit boundary, the nacelle clearance becomes a non-governing limit for these variations. Now the relative Z-tip motion, for wave directions 0°, 135° & 180°, and side-lead, for wave directions 45° & 90° become governing. Again it can be seen that the operability increases as the nacelle clearance limit boundary increases due to moving the combined RNA+ HCG in negative global X-Direction. As the current nacelle clearance interval for the base case is chosen according to Figure 3.19, with this boundary increase, the nacelle casing size could also be increased, resulting in a lower limit boundary.

5.4.9. Hub Height

For the operability plots of Hub Height 130 [m], see: Section D.18.
For the operability plots of Hub Height 150 [m], see: Section D.19.
For the grouped Hub Height operability plots see: Section F.9.

With the original NREL 15 MW hub height variation, the operability becomes zero as the static nacelle boom clearance becomes smaller than 3 m. For the hub height o 130 m, an increase in operability can be observed, see Figure 5.13

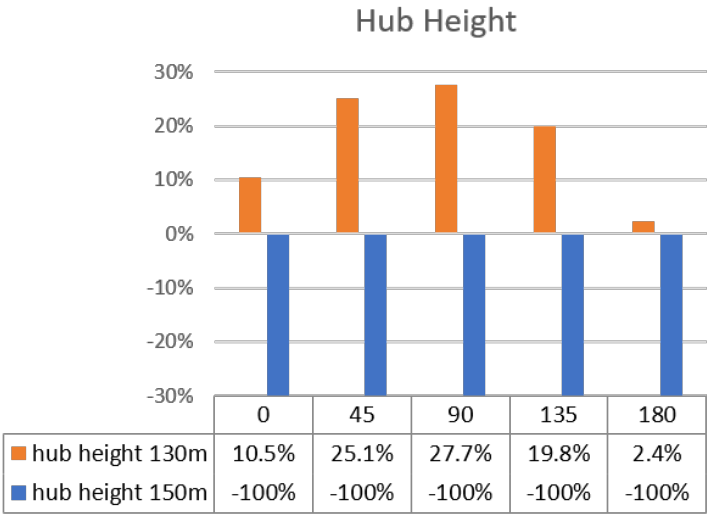

	0	45	90	135	180
🟧 hub height 130m	10.5%	25.1%	27.7%	19.8%	2.4%
🟦 hub height 150m	-100%	-100%	-100%	-100%	-100%

Figure 5.13: Relative Difference Operability Hub Height w.r.t. Base Case

For the 130 m hub height, an increase in operability for all wave directions can be perceived. This is mainly due to the shift in the nacelle clearance limit boundary from 1.3 m to 5 m. Therefore, the relative Z-tip motion, for wave directions 0°, 135° & 180°, and side-lead, for wave directions 45° & 90° become governing.

5.4.10. Tower VCG

For the operability plots of Tower VCG 35 [m], see: Section D.20.
For the operability plots of Tower VCG 65 [m], see: Section D.21.
For the grouped Tower VCG operability plots see: Section F.10.

By varying the VCG of the tower, the combined VCG of the RNA+ module also varies. The tower variation to 35 m results in a 4.8 m lower combined VCG. The 65 m tower VCG variation has a 5.7 m higher combined VCG as outcome. Because the Upper Lifting Tool's vertical position is 7 m above the combined RNA+ VCG, its global position varies with the above height variations. Similar to the Upper lifting tool variations, see Figure 5.4.5, the case with a lower global upper lifting tool height results in a higher operability.

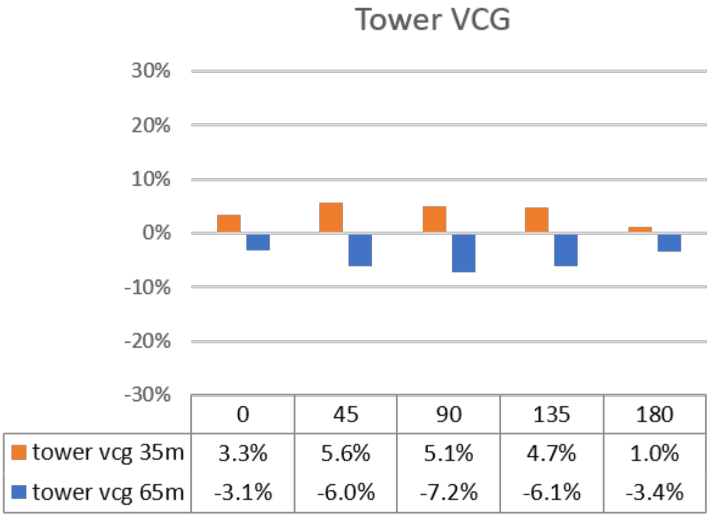

	0	45	90	135	180
🟧 tower vcg 35m	3.3%	5.6%	5.1%	4.7%	1.0%
🟦 tower vcg 65m	-3.1%	-6.0%	-7.2%	-6.1%	-3.4%

Figure 5.14: Relative Difference Operability Tower VCG w.r.t. Base Case

5.4.11. TLP Mass, Tendon Angle, and Mooring Line Stiffness

For the operability plots of Parameter	See:
TLP Mass 2402 [t]	Section D.22
TLP Mass 3249 [t]	Section D.23
Grouped Operability TLP Mass	Section F.11
Tendon Angle 0°	Section D.24
Tendon Angle 20°	Section D.25
Grouped Operability Tendon Angle	Section F.12
Mooring Line Stiffness 772e3 [kN]	Section D.26
Mooring Line Stiffness 178e4 [kN]	Section D.27
Grouped Operability Mooring line stiffness	Section F.13

As the governing operability limits nacelle clearance and side-lead are TLP independent, variations toward the TLP do not influence the operability in those cases. The relative Z-tip, however, is dependent on the TLP. Nevertheless, as the TLP has no significant heave motion in all variation steps, neither loss nor gain of operability is witnessed.

5.5. Model alterations

The above operability results show that sequentially the Nacelle Clearance, Z-tip motion, and Side-lead angle are the governing limits for the presented parametric variations. Without altering the design of the TLP and WTG, one could look at the following matters to influence these limits.

For the Z-Tip motion, one could look at different slew angles. The SB crane is located at 33.75 m from the roll axis. Therefore the amplitude of the roll-induced crane and, thus, the RNA+ heave motion is more extensive than for a case where the crane tip would be located above the roll axis. A model configuration is made where the slew angle is altered to 217.5°. Resulting in the tower bottom being straight above the roll axis. This alteration also has a reduction of distance between the tower and the vessel's pitch axis as a result. For pitch, a similar approach can be configured. However, as the pitch axis of the vessel is 'out of reach' for the SB crane, a configuration where the slew angle is minimal and the clearance between the vessel and TLP is still sufficient. This results in a slew angle of 55°. Another approach could be to rotate the RNA+ 180° along its Z-axis. This results in a slightly smaller static distance between the nacelle and crane boom but eliminates the nacelle casing size as a limiting parameter. Below, these variations are elaborated.

5.5.1. Slew angle Alteration

A visualization of the slew angle alteration is given in Figure 5.15

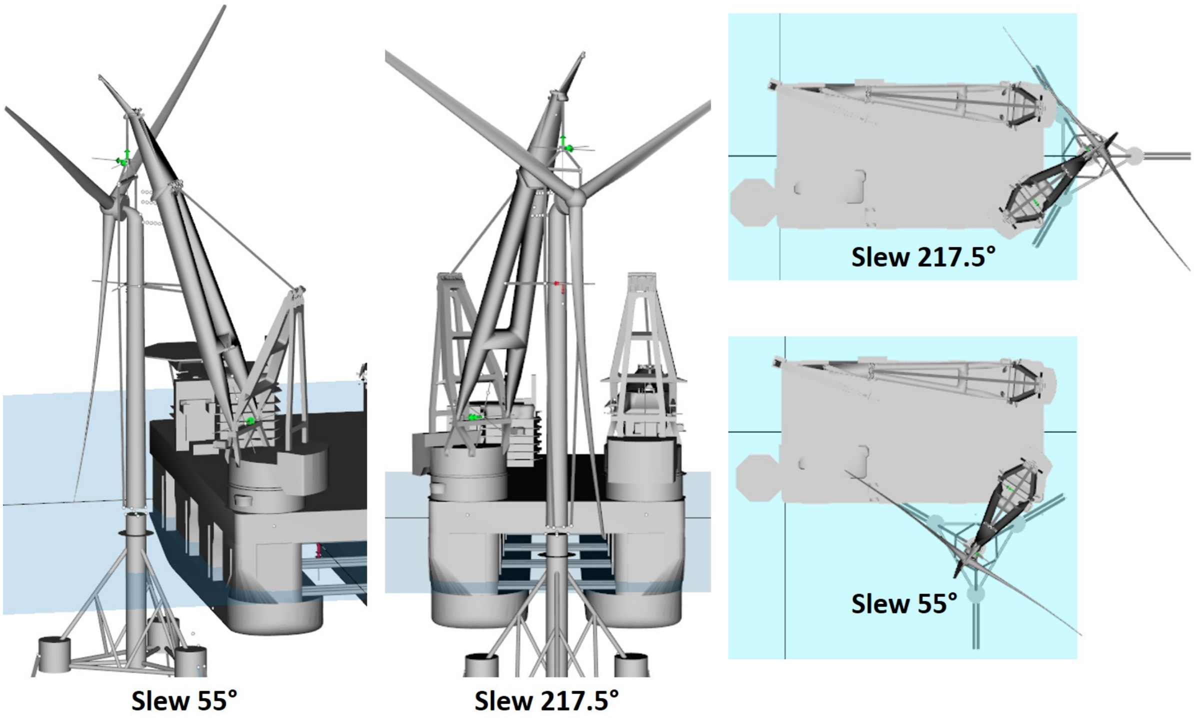

Figure 5.15: Slew Angle variations for 55° and 217.5°

For the operability plots of Slew Angle 55° see: Section D.28.
For the operability plots of Slew Angle 217.5°, see: Section D.29.
For the grouped Slew Angle Alteration operability plots see: Section F.14.

In the plots regarding the slew angle of 217.5°, the relative z-tip motion is decreased for all wave directions. With this alteration, the side lead replaced the Z-tip motion as the second governing limit. For the 55° alteration, the same can be seen. For wave directions 0° and 180°, a decrease in operability can be seen for both alterations. For directions 45° and 90°, a slight increase in operability is seen.

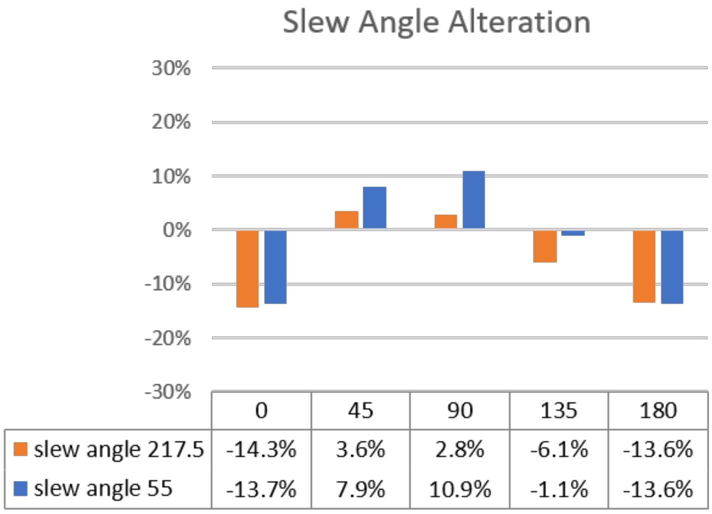

	0	45	90	135	180
🟧 slew angle 217.5	-14.3%	3.6%	2.8%	-6.1%	-13.6%
🟦 slew angle 55	-13.7%	7.9%	10.9%	-1.1%	-13.6%

Figure 5.16: Relative Difference Operability Slew Angle Alteration w.r.t. Base Case

5.5.2. Rotated RNA+

Figure 5.17 shows the reversed RNA+ configuration. With this variation, the nacelle casing does not directly influence the nacelle boom clearance. It is assumed that the tugger lines do not interfere with the down-facing blade for this variation, which is not the case in the real-life application.

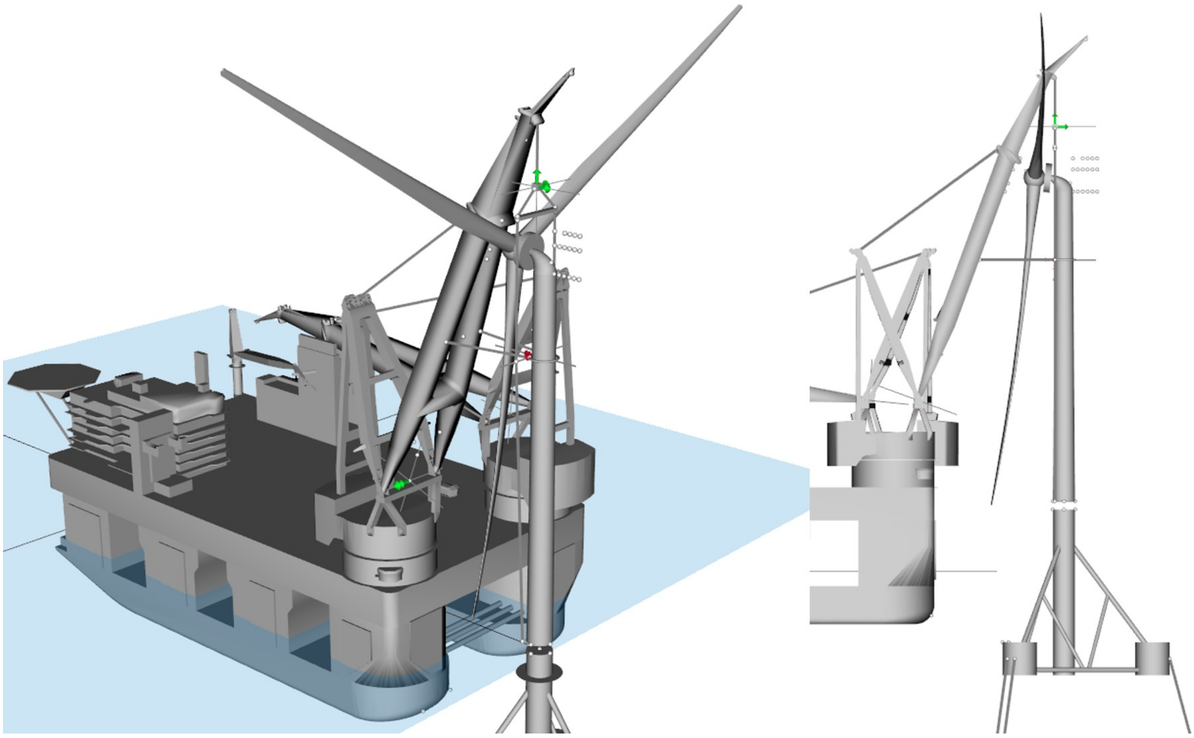

Figure 5.17: Reversed Tower Visualization

For the operability plots of Rotated RNA+ see: Section D.30.
For the grouped Rotated RNA+ operability plots see: Section F.15.

The nacelle crane boom limit boundary for the reversed RNA+ case is 1.1 m, 0.2 m smaller than the base case limit. This results in a slight decrease in operability for all wave directions, see Figure 5.18.

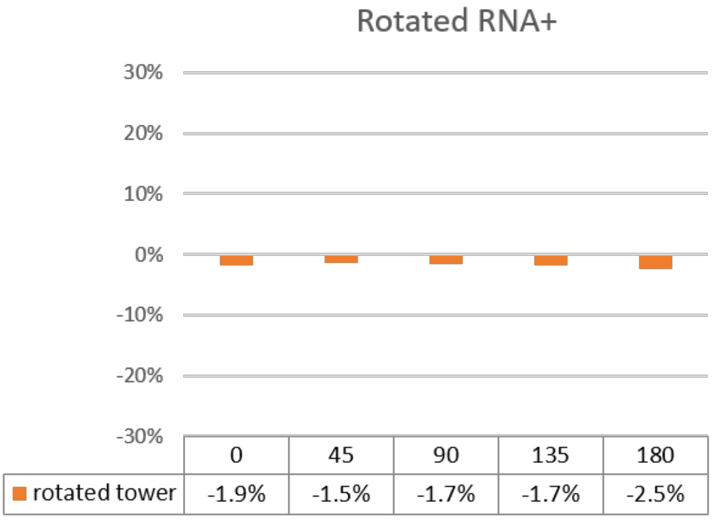

Figure 5.18: Relative Difference Operability Rotated RNA+ w.r.t. Base Case

All other limiting criteria show the same operability w.r.t. base case operability. One thing to note is that when the nacelle casing size is increased, its HCG moves along with this enlargement. This results in the total combined HCG moving in the negative x-axis of RNA+, leading to a shift of the lifting points and a smaller clearance between the nacelle and crane boom.

5.6. Workability

In this section, the workability of the base case is assessed. This is to demonstrate how the derived operabilities comply with specific locations and environments. Two locations with different environmental conditions are selected.

5.6.1. Defnition

The workability, W, of an offshore operation in an environment, can be evaluated with the scatter diagram approach. This approach represents the workability as the sum of the occurrence of H_s-T_p combinations that are below the operability curves of $H_{s,max}$ for a given location-specific scatter diagram P.

$$W = 100\% \cdot \sum_{T_p=0}^{T_{p,max}} \sum_{H_s=0}^{H_{s,\max}(T_p)} [P] \tag{5.1}$$

The scatter diagram, P, contains the occurrence of H_s-T_p combinations for a specific location for a given time frame.

5.6.2. Locations and environmental data

As the operability embodies the possible H_s-T_p combinations where the installation is operable, one can look at the workability on a specific location in a specific time frame. The workability of the base case is examined for two locations as an example. The First location is in the North Atlantic Ocean just west of New York City near the US east coast, the second one is located north of Germany in the Baltic Sea. Both locations are shown in Figure 5.19.

(a) (b)

Figure 5.19: Locations used for workability assessment, US East Coast (a), Baltic Sea (b)

In Figure 5.20 the environmental sea data for an entire year is shown. The figures denote the wave height combined with its direction and the occurrence of this combination.

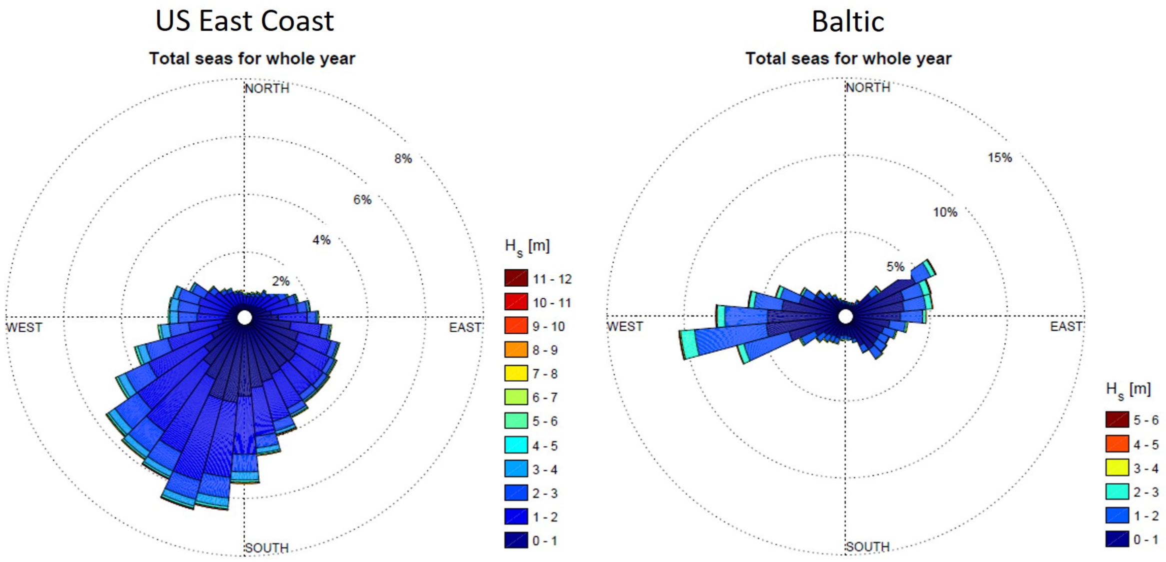

(a) (b)

Figure 5.20: Total seas for a whole year for US east coast (a) and Baltic (b)

With this environmental data, and the occurrence of the H_s-T_p combinations the overall workable time frame for each location can be assessed. For each time frame of a month the total workability for the set $H_{s,lim}$ of 2 m and $H_sT_p^2$ limit of 120 ms^2 can be calculated, see Figure 5.21.

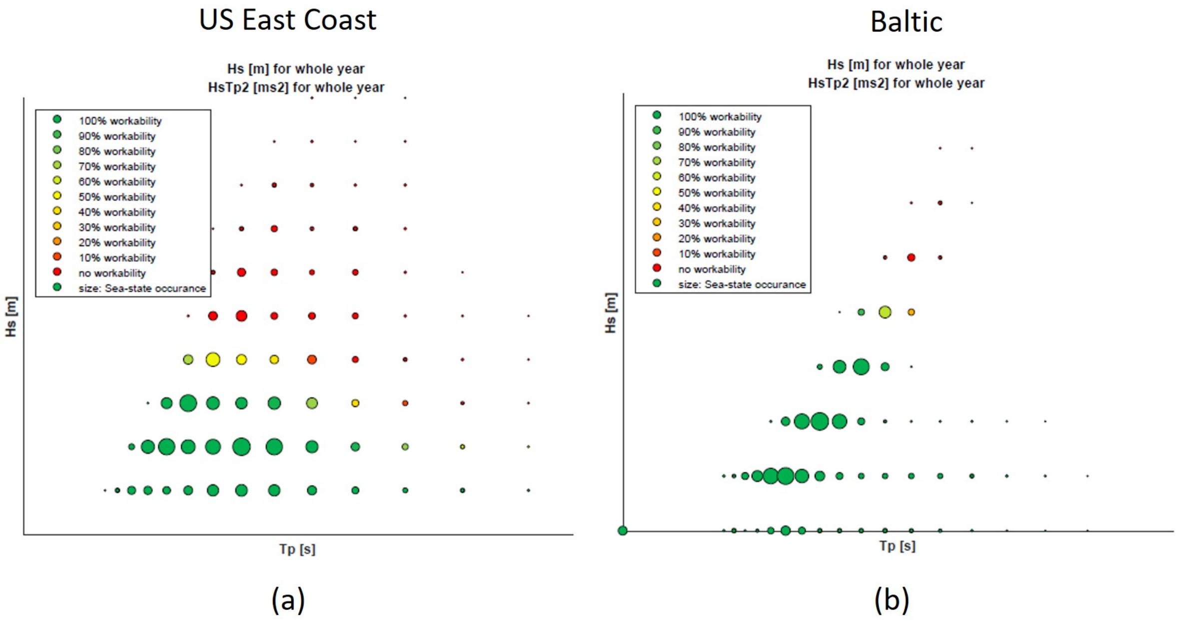

Figure 5.21: H_s-T_p combinations combined with occurance

Figure 5.21 shows that for the Baltic Sea, most wave occurrences are below a H_s of 2 m and a T_p of 6. The plot for the US East Coast shows that in this spectrum waves with a T_p between 4 and 11 seconds occur. So both wind and swell waves occur. The all-year workability for the US East Coast where the $H_{s,lim}$ of 2 m and $H_sT_p^2$ limit of 120 ms^2 are not exceeded is found to be 75%, this is 94% for the Baltic Sea. This yearly workability then can be deducted into monthly and quarterly workability, see Figure 5.22. For both locations, July is the most workable month.

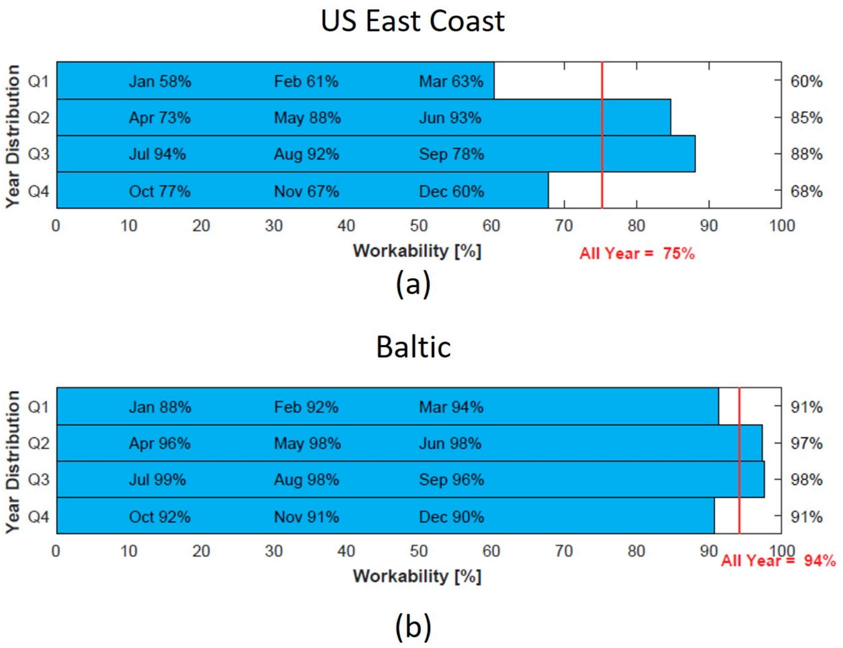

Figure 5.22: Workability per time period, Month, Quarter, Year for fixed heading. US East Coast (a) and Baltic (b)

5.6.3. Governing Limits

The nacelle clearance, side-lead, and Z-tip motion are now subjected to these environments. The total workability per month per limit is calculated. Table 5.3 shows the monthly and annual operability per governing limit for the US East Coast. Table 5.4 shows this for the Baltic Sea location.

Table 5.3: Periodic workability per governing limit, US East Coast

	US East Coast												
Limit	**Jan**	**Feb**	**Mar**	**Apr**	**May**	**Jun**	**Jul**	**Aug**	**Sep**	**Oct**	**Nov**	**Dec**	**Avg**
Nacelle Clearance	41	38	34	39	54	65	70	59	40	42	42	39	46.9
Sidelead	55	53	50	58	76	83	87	79	56	61	60	55	64.4
Z-Tip	61	61	60	69	86	92	93	89	69	74	69	63	73.8
Combined	40	53	50	58	76	83	87	79	56	61	60	55	63.2

Table 5.4: Periodic workability per governing limit, Baltic Sea

	Baltic Sea												
Limit	**Jan**	**Feb**	**Mar**	**Apr**	**May**	**Jun**	**Jul**	**Aug**	**Sep**	**Oct**	**Nov**	**Dec**	**Avg**
Nacelle Clearance	99	99	100	99	100	100	100	100	100	100	99	99	99.6
Sidelead	99	99	100	100	100	100	100	100	100	100	100	100	99.8
Z-Tip	99	99	100	100	100	100	100	100	100	100	99	99	99.7
Combined	98	99	100	100	100	100	100	100	100	100	100	100	99.8

For the US East Coast, July has the highest, and January has the lowest combined workability. For the Baltic Sea area, a very high workability can be seen. This is because the operation is sensitive to swell waves, which have a very low probability of occurrence in this area. The corresponding limiting H_s-T_p occurrences for the governing limits and the workability per wave heading for these months are shown in Appendix G.

5.7. Discussion of Modeling Choices

The numerical model created in this study and the corresponding results provide valuable insights into the different aspects of the floating to floating installation of the IEA 15 MW reference turbine. It provides a tool with interchangeable building blocks to assess the design parameters of FOW installations. However, modeling choices were made to get a working model with preferable simulation times. Choices that contain assumptions or alterations w.r.t the real-life application. This section discusses these choices and their effect on the results of this study.

5.7.1. Vessel

The choice of vessel significantly influences the model. As its dimensions and hydrodynamic behavior impact the outcome of the operability study. On the one hand, these 'physical' boundaries narrow the modeling choices. On the other hand, as the vessel is the world's largest SSCV and SSCVs show great stability w.r.t. monohull vessels [57], the choice for this vessel embodies realistic and favorable conditions for FOWT installation.

5.7.2. TLP

The choice for the TLP, because of its size, shape, and behavior, resulted in it having minor effects on the operability. Other floater types or even other TLPs could lead to different outcomes. Furthermore, the anchoring of the TLP to the seabed is modeled as point connections. This type of connection could influence the behavior of the mooring lines. Modeling these anchor points as mass-spring-damper systems would resolve this.

5.7.3. WTG

The alterations made to the WTG and choice of nacelle casing size also impacted the outcome of this study. As the static clearance between the nacelle and crane boom is governing in this model, and the hub height and nacelle casing are directly correlated with this clearance. If no nacelle casing had been chosen, the nacelle crane boom clearance would not have become the governing limit for all alterations. This embodies the importance of these parameters but also their influence.

5.7.4. Domain

The decision to use FD instead of TD impacts the model results significantly. The advantages of FD over TD are that because FD only solves a system of algebraic equations, it is much more time efficient than solving a significant number of iterations over discrete time steps. The disadvantages of FD are that it requires a linear system, and multiple approximations have to be made, such as linear wave theory and small angle approximations. Furthermore, no transient effects are implemented. This could lead to results differing from practice. As this parametric sensitivity study is set up to get an overview of multiple parameters in multiple conditions instead of a detailed analysis of one specific case, FD is chosen. Simulating a model in the TD cost time, whereas one has to do frequent model steps, FD is a better fit.

5.7.5. Linearization

The choice to only assume first-order effect, thus linearizing all EOMs and other behavior, results in a model that does not show higher-order, non-linear effects. This could result in a neglect of higher-order natural frequencies of the bodies. Low- and high-frequency components for Second-order effects occur in frequency ranges not considered in the operability assessment. This high-level operability assessment assumes that the most significant responses are due to first-order effects. These higher-order effects should be considered to get a complete and thorough model for a specific case.

5.7.6. Water Depth

The water depth influences the hydrostatic and dynamic behavior of floating bodies. The water depth of 150 m mainly influences the mooring system of the TLP. As FOW is expected to be located in deep water sites, it marginally affects the vessel's behavior. Different water depths result in different mooring configurations and, thus, different mooring line stiffnesses. Therefore, the current results of the TLP behavior are only applicable to a water depth of 150 m and are not directly scalable to other water depths.

5.7.7. Parametric Variation

The parametric variations made in this research are all subjected to the base case. Some are variations of real-life properties, and others are determined with a percentual variation. In the case of the mooring line stiffness variation, three materials, all suited for mooring a TLP with similar stiffnesses, were considered. Due to having similar stiffnesses, its effect, and difference w.r.t. the base case was minor. If a more extensive range of stiffness variation were chosen, the effect of the mooring line stiffness on the model would have been potentially better outlined.

5.7.8. Building Blocks

All choices made were considered in light of the three main building blocks of the numerical model. When one changes the floater, minor alterations to the model must be made. Depending on the size, one has to check if sufficient vessel floater clearance is in order. If a floater has a different interface height, the tower height has to be compensated to retain the fixed hub height of the WTG. If one is to change the WTG, alterations to the rigging must be made, but the model stays the same on the major parts. As the model is set up in a way that first the vessel is configured, then the WTG is suspended in the crane, and finally, the floater is positioned underneath the tower base, changing the vessel would impact the more severe. However, the post-process of this model can still be conducted in the same way, as most POIs are defined at locations existing on all (crane) vessels, and others are defined with respect to POIs located at the WTG.

6

Conclusions and Recommendations

In this Chapter, the conclusions of this research are presented. The research question: ”What is the influence of the design parameters of a WTG, TLP, and Lifting Configuration on the operability of a floating to floating single lift installation of a 15MW WTG on a TLP with an SSCV?” will be answered. Other findings will be outlined. Furthermore, recommendations for further research will be made.

6.1. Operability study

All operability results show that the model is sensitive to swell-dominated sea states with wave periods larger than 7.8s. For waves with periods longer than 10 s, the maximal operational significant wave height, H_s, is 0.5 m for the most optimal cases. This results in very low operability in these sea states. For wind-dominated sea states, the operation is more suitable. This swell sensitivity is dominated by the natural periods of the WTG pendulum, as those periods lay inside the swell wave range.

The overall governing limit regarding the operability is the nacelle crane-boom clearance. All variations made to the model that widened the static clearance between the two benefited the operability. The second governing limit is the relative Z-Tip motion between the tower and the TLP. This limit was most significant for wave directions for 0°, 135°, and 180°. The Side-Lead was the second governing limit for wave directions 45° and 90°. The reduction in hub height had the most significant average increase of operability for all wave directions, being 17.1%. The nacelle HCG shift improved the operability on average by 14.9%. The boom angle reduction and hub height increase led to a non-operable state. Installing the unaltered version of the IEA 15 MW reference turbine in a single lift is therefore impossible with the used lifting configuration. The variation in TLP design parameters had no significant influence on the operability of the installation.

6.1.1. Vessel Design

In terms of vessel motion, an SSCV is particularly suitable for a floating to floating installation. Its stability, lifting- capacity, and height contribute to having an operability window for the floating installation of FOWTs. The boom radius and slew angle have the most significant effect on the operability. The crane boom radius is leading because of its impact on the nacelle crane boom clearance and the SWL of the Aux Hoist. Slew angle alterations can influence the vessel-induced motions on the RNA+ module. This effect is positive and negative, so limiting parameters that are governing for the one slew angle will become non-governing for other angles. However, other limits can become governing and even more limiting for these other angles than for the first slew angle. As its influence is considerable, for each installation process, it should be accessed. Tugger lines and their angle influence the operability slightly. In wind-dominated sea states, this effect is non-existence. This slight effect is seen for spectra with wave periods of 8 s and up. However, for the average operability, horizontal tugger lines with components in both x- and y-direction have the most effect on the operability.

6.1.2. Floater Design

The floater used in this research did not influence the operability significantly. This was due to the fact that it was very stiff in heave direction, having a natural period of 1.98 s. Therefore, the tower movement mainly governed the relative Z-tip motion between the Tower and TLP. The natural periods for surge and sway of about 27 s are far outside the considered sea states for installation. The responses in this direction show favorable conditions for the installation. Due to its size, the clearance between the vessel and the TLP hull stays sufficient when installing the WTG with a boom radius of 58 m. A larger layout and or spreading of the legs could lead to problems regarding this clearance between the vessel and TLP. However, some variations of the TLP did seem significant firsthand. More extensive or extrapolated alterations to the design could have been made to really see the effect of extensive alterations regarding the operability. Nevertheless, the variations made were in line with a realistic point of view.

6.1.3. Wind Turbine Design

The hub height and HCG of the WTG are deemed to have the most impact on the operability. The rigging for installation depends on those parameters. Also, the total weight of all components could become limiting as few installation vessels are equipped with cranes with the needed lifting height in combination with a sufficient SWL. The new generation of direct drive turbines, whose increased weight is not compensated for with a gearbox, significantly influences the operability. However, this influence is not necessarily negative. It also allows changing the 'standard' rigging configuration and installing the RNA+ module with its hub facing the crane boom.

6.2. Recommendations

This section presents the recommendations for future installation vessels, WTG, and floater designs. Furthermore, recommendations regarding optimizing the parametric sensitivity study will be made. At last, insights and ideas developed during this thesis will be shared.

6.2.1. Parameter variation

The parametric variation in this research is executed with preset variations, and all are compared to the same base case. With the model in place, sensitivity analysis toolboxes such as UQLab [58] could be used to determine the parametric variations. The toolbox provides tools to generate variations of input parameters and analyze their influence on the model responses. With this iterative method, optimal parameter variation combinations can be acquired. This leads to a better implementation of the sensitivity study. This could take significantly more simulation time if all parameters are to be optimized with respect to each other for the most optimal operability configuration. Nevertheless, if set up correctly, this could have an insightful outcome for the input parameters for the model.

6.2.2. Modeling steps

A logical follow-up step is to assess the workability for all parametric variations of this operation to see if the operation is workable for other specific locations and sea states. The workability can be derived with specific wave and weather data, their statistical occurrence, and using the same limits and RAOs as in the operability analysis. It then can be expressed in a percentage per unit of time where the operation is feasible.

For this research, only the free-hanging situation is considered. Also, the other stages in the assembly of the WTG and placement on the foundation could be considered regarding the operability. If a preferred model configuration is found in this FD model, a more detailed and time-consuming TD model can be built to access the installation in a more specific way. Active components and transient effects can then be added. Furthermore, Because the base model is built in UM, the model can be exported to OrcaFlex to conduct this TD analysis.

6.2.3. Vessel Design

With the fast-growing hub heights of current WTGs, the current generation of offshore HLVs has to be upgraded for floating to floating installation practices. Mainly matters to increase their lifting heights and or increase lifting clearances should be contemplated. To limit the influence of the z-tip motion of the WTG module (active), heave compensators could be applied between the position of the upper lifting tool. This could benefit both the WTG module's Z-Tip motion and the nacelle clearance, as the nacelle will move less in vertical direction.

Crane-boom configuration where the lifting point and crane boom construction are not directly located above and behind the lifted WTG could also benefit the operability significantly. Such a configuration could consist of a crane boom (extension) that splits into two crane boom beams containing two separate hoist blocks. Then instead of a spreader bar, the WTG can be directly lifted at the upper lifting tool with these two crane hoist blocks. Furthermore, the nacelle is no longer in danger of coming too close to the crane boom.

6.2.4. Floater Design

As stated before, the TLP used in this research was favorable for the installation process. When designing a floater, one should look at its installed behavior and its behavior in sea states suitable for installation when no WTG is installed. The tendons of the TLP in this research were made of stud-less chains. Up to water depths of 150m, this could be applied. However, synthetic tendons are preferred for most floating wind TLPs, especially in situations with larger water depths. Furthermore, variations with different water depths should be considered, as the water depths influence the mooring configuration and, thus, the behavior of the TLP.

6.2.5. Wind Turbine Design

The development in growth and size of OWTs is out of sync with the growth of installation assets. As installation vessels take years to develop, they can not be expected to grow accordingly in a set time frame. The increase in the capacity of WTGs is mainly caused by doing the same thing but then bigger. Instead of making the current configuration more efficient, the size is often increased. Some WTG developers are now upgrading the rating of their existing WTGs. Nevertheless, this is mainly because the developed generators are more efficient than predicted. The industry should set a limit to the hub height and or blade diameter of future WTGs, and focus on making that set configuration more efficient within its limits. Installation assets could also be developed and optimized for that specific setting, resulting in installing OWTs more efficiently to reach the global goal for more renewable energy. Not only the installation process could benefit from this process but also transport logistics and manufacturers.

6.2.6. Integrated designs

FOW is now assessed in the 'classical' way of fixed offshore wind. Having a foundation, a single 'cylindrical' tower, and one prominent RNA on top. More and more concepts of integrated design are brought to light. Having multiple smaller turbines resulting in the same capacity per floater but lower hub heights and possible installation difficulties. Also, turbines with innovative energy generation where the generator is not located at the nacelle, and therefore having a smaller to no nacelle casing could benefit the installation process. Out-of-the-box ideas, differing from the current benchmark of offshore wind, could innovate the FOW market a lot and bring it to a new level to join fixed wind in its goal to make renewable energy for the future.

6.2.7. Other Ideas

All ideas, remarks, and solutions given above were made from the point of view where the model is subjected to different external environmental conditions and its reaction to those conditions. Instead of looking to counteract these effects of environmental loading on the installation assets themselves, actions countering these environmental impacts could also be assessed. Such as (temporary) (floating) breakwaters could be installed on-site, breaking the waves and limiting their impact on the installation vessel and floater. So instead of limiting the reaction, remove the disturbance's sources.

In conclusion, this study provides valuable insights into the operability of installing FOWT, paving the way for future developments in (floating) renewable energy technologies.

Bibliography

[1] Intergovernmental Panel on Climate Change (IPCC). *Climate Change 2021: The Physical Science Basis Summary for Policymakers*. IPCC, 2021. URL: `https://www.ipcc.ch/report/ar6/wg1/` (visited on 06/06/2022).

[2] P. A. Arias, N. Bellouin, and E. Coppola. *Climate Change 2021: The Physical Science Basis Technical Summary*. Intergovernmental Panel on Climate Change (IPCC), 2021. URL: `https://www.ipcc.ch/report/ar6/wg1/` (visited on 06/06/2022).

[3] United Nations. *Paris Agreement*. 2015. URL: `https://unfccc.int/sites/default/files/english_paris_agreement.pdf` (visited on 06/06/2022).

[4] United Nations. *Glasgow Climate Pact*. 2021. URL: `https://unfccc.int/sites/default/files/resource/cop26_auv_2f_cover_decision.pdf` (visited on 06/06/2022).

[5] Det Norske Veritas. *Energy Transition Outlook 2021 A Global And Regional Forecast To 2050*. DNV, 2022. URL: `https://www.dnv.com/energy-transition-outlook/download.html` (visited on 03/21/2023).

[6] Det Norske Veritas. *Energy Transition Outlook 2021 A Global And Regional Forecast To 2050*. DNV, 2021. URL: `https://eto.dnv.com/2021/about-energy-transition-outlook` (visited on 05/02/2022).

[7] Det Norske Veritas. *Floating Offshore Wind: The Next Five Years*. DNV, 2022. URL: `https://www.dnv.com/focus-areas/floating-offshore-wind/floating-offshore-wind-the-next-five-years.html` (visited on 05/02/2022).

[8] R. James and M. C. Ros. *Floating Offshore Wind: Market and Technology Review*. The Carbon Trust. 2015. URL: `https://www.carbontrust.com/resources/floating-offshore-wind-market-technology-review` (visited on 04/29/2022).

[9] T. Asim, S. Z. Islam, A. Hemmati, and M. S. U. Khalid. "A Review of Recent Advancements in Offshore Wind Turbine Technology". In: *Energies 2022, Vol. 15, Page 579* 15 (2 Jan. 2022), p. 579. ISSN: 1996-1073. DOI: `10.3390/EN15020579`. URL: `https://www.mdpi.com/1996-1073/15/2/579`.

[10] Z. Jiang. "Installation of offshore wind turbines: A technical review". In: *Renewable and Sustainable Energy Reviews* 139 (Apr. 2021). ISSN: 18790690. DOI: `10.1016/J.RSER.2020.110576`.

[11] E. de Vries. *Monopiles beyond XXL, Next generation foundations*. Apr. 2019. URL: `https://issuu.com/navingo/docs/owmag_nov_4_2019` (visited on 05/12/2022).

[12] A. Arapogianni, A. Genachte, R. O. Manzanas, and J. P. Vergara. *Deep Water The next step for offshore wind energy*. EWEA, 2013. URL: `www.ewea.org/report/deep-water` (visited on 06/16/2022).

[13] Wind Europe. *Scotland awards seabed rights for massive amounts of offshore wind, most of it floating | WindEurope*. Jan. 2022. URL: `https://windeurope.org/newsroom/press-releases/scotland-awards-seabed-rights-for-massive-amounts-of-offshore-wind-most-of-it-floating/` (visited on 06/22/2022).

[14] Wind Europe. *France commits to 40 GW offshore wind by 2050 | WindEurope*. 2022. URL: `https://windeurope.org/newsroom/news/france-commits-to-40-gw-offshore-wind-by-2050/` (visited on 06/28/2022).

[15] Rijksoverheid. *Nederland maakt ambitie wind op zee bekend: 70 gigawatt in 2050 | Nieuwsbericht | Rijksoverheid.nl*. Sept. 2022. URL: `https://www.rijksoverheid.nl/actueel/nieuws/2022/09/16/nederland-maakt-ambitie-wind-op-zee-bekend-70-gigawatt-in-2050` (visited on 02/14/2023).

[16] T. Stehly and P. Beiter. *2018 Cost of Wind Energy Review*. National Renewable Energy Laboratory, 2018. NREL/TP-5000-74598. URL: `https://www.nrel.gov/docs/fy20osti/74598.pdf` (visited on 06/21/2022).

[17] E. Barlow, D. T. Öztürk, M. Revie, E. Boulougouris, A. H. Day, and K. Akartunali. “Exploring the impact of innovative developments to the installation process for an offshore wind farm”. In: *Ocean Engineering* 109 (Nov. 2015), pp. 623–634. ISSN: 00298018. DOI: `10.1016/J.OCEANENG.2015.09.047`.

[18] J. Lerche, S. Lindhard, P. Enevoldsen, H. H. Neve, D. E. Møller, E. L. Jacobsen, J. Teizer, and S. Wandahl. “Causes of delay in offshore wind turbine construction projects”. In: *Production Planning & Control* (2022). ISSN: 13665871. DOI: `10.1080/09537287.2022.2026673`.

[19] Wind Europe. *Ports: a key enabler for the floating offshore wind sector*. Sept. 2020. URL: `https://windeurope.org/intelligence-platform/product/ports-a-key-enabler-for-the-floating-offshore-wind-sector/` (visited on 06/21/2022).

[20] A. P. Crowle and P. R. Thies. “Floating offshore wind turbines port requirements for construction”. In: *Proceedings of the Institution of Mechanical Engineers Part M: Journal of Engineering for the Maritime Environment* (2022). ISSN: 20413084. DOI: `10.1177/14750902221078425`.

[21] S. Killoh. *Heerema installs first wind turbine using novel RNA method*. 2022. URL: `https://www.heerema.com/news/heerema-installs-first-wind-turbine-using-novel-rna-method` (visited on 03/11/2023).

[22] The Carbon Trust. *Floating Wind Joint Industry Project Phase III Summary Report*. 2021. URL: `https://www.carbontrust.com/our-work-and-impact/guides-reports-and-tools/floating-wind-joint-industry-project-phase-iii-summary` (visited on 05/19/2022).

[23] F. Olsen and K. Dyre. “Vindeby Off-Shore Wind Farm - Construction and Operation”. In: *Wind Engineering* 17.3 (1993), pp. 120–128. ISSN: 0309524X, 2048402X. URL: `http://www.jstor.org/stable/43749506` (visited on 05/13/2022).

[24] Y. Liu, Y. Fu, L. ling Huang, and K. Zhang. “Reborn and upgrading: Optimum repowering planning for offshore wind farms”. In: *Energy Reports* 8 (Nov. 2022), pp. 5204–5214. ISSN: 2352-4847. DOI: `10.1016/J.EGYR.2022.04.002`.

[25] World Forum Offshore Wind. *Global Offshore Wind Report 2021*. WFO, 2022. URL: `https://wfo-global.org/?jet_download=4814` (visited on 05/19/2022).

[26] *Global Wind Atlas*. URL: `https://globalwindatlas.info/` (visited on 09/06/2022).

[27] *Spinergie*. URL: `spinergie.com` (visited on 09/06/2022).

[28] B. Speer, D. Keyser, and S. Tegen. *Floating Offshore Wind in California: Gross Potential for Jobs and Economic Impacts from Two Future Scenarios Strategic Partnership Project Report*. 2015. URL: `http://www.boem.gov/Pacific-Completed-Studies/.` (visited on 05/19/2022).

[29] E. Uzunoglu and C. G. Soares. “Hydrodynamic design of a free-float capable tension leg platform for a 10 MW wind turbine”. In: *Ocean Engineering* 197 (Feb. 2020). ISSN: 00298018. DOI: `10.1016/J.OCEANENG.2019.106888`.

[30] Global Wind Energy Council. “Floating Offshore Wind-A Global Opportunity”. In: (2022). URL: `https://gwec.net/wp-content/uploads/2022/03/GWEC-Report-Floating-Offshore-Wind-A-Global-Opportunity.pdf` (visited on 06/21/2022).

[31] E. E. Bachynski and T. Moan. “Design considerations for tension leg platform wind turbines”. In: *Marine Structures* 29 (1 Dec. 2012), pp. 89–114. ISSN: 09518339. DOI: `10.1016/J.MARSTRUC.2012.09.001`.

[32] International Energy Agency. *Offshore Wind Outlook 2019*. IEA, 2019. URL: `https://iea.blob.core.windows.net/assets/495ab264-4ddf-4b68-b9c0-514295ff40a7/Offshore_Wind_Outlook_2019.pdf` (visited on 07/21/2022).

[33] E. Gaertner, J. Rinker, L. Sethuraman, F. Zahle, B. Anderson, G. Barter, N. Abbas, F. Meng, P. Bortolotti, W. Skrzypinski, G. Scott, R. Feil, H. Bredmose, K. Dykes, M. Shields, C. Allen, and A. Viselli. “Definition of the IEA Wind 15-Megawatt Offshore Reference Wind Turbine Technical Report”. In: (2020. NREL/TP-5000-75698). URL: `https://www.nrel.gov/docs/fy20osti/75698.pdf` (visited on 05/24/2022).

[34] A. N. Robertson and J. M. Jonkman. “Loads Analysis of Several Offshore Floating Wind Turbine Concepts”. In: (2011). URL: `https://www.nrel.gov/docs/fy12osti/50539.pdf` (visited on 05/24/2022).

[35] S. Bashetty and S. Ozcelik. “Review on Dynamics of Offshore Floating Wind Turbine Platforms”. In: *Energies 2021, Vol. 14, Page 6026* 14 (19 Sept. 2021), p. 6026. ISSN: 1996-1073. DOI: `10.3390/EN14196026`. URL: `https://www.mdpi.com/1996-1073/14/19/6026/htm`.

[36] Det Norske Veritas. *DNVGL-ST-N001 Marine operations and marine warranty*. DNV, 2016. URL: `http://www.dnvgl.com,` (visited on 05/02/2022).

[37] J. M. J. Journée, W. W. Massie, and R. H. M. Huijsmans. *OFFSHORE HYDROMECHANICS Third Edition (2015) Based on Original Lecture Notes (2000) by J M J Journée*. 2015.

[38] S. Schreier. *Floating Structures & Offshore Moorings: System Response*. OE44100 Floating Structures & Offshore Moorings Lecture slides, TU Delft. 2021/2022.

[39] G. Meskers and R. van Dijk. “A Damping Tugger System For Offshore Heavy Lifts”. In: *ASME 2012 31st International Conference on Ocean, Offshore and Arctic Engineering OMAE2012* (2012).

[40] S. Schreier. *Floating Structures & Offshore Moorings: Limiting Sea State & Operability*. OE44100 Floating Structures & Offshore Moorings Lecture slides, TU Delft. 2021/2022.

[41] Det Norske Veritas. *DNV-RP-C205Environmental conditions and environmental loads*. DNV, 2021. URL: `http://www.dnv.com,` (visited on 05/02/2022).

[42] Heerema Marine Contractors. *Heerema Marine Contractors - Sleipnir*. URL: `https://www.heerema.com/heerema-marine-contractors/fleet/sleipnir` (visited on 01/06/2023).

[43] Robert McNeel Associates. *Rhinoceros*. Version 7.0. Dec. 8, 2020. URL: `https://www.rhino3d.com`.

[44] C. Lee, J. Newman, and Massachusetts Institute of Technology. *WAMIT*. Version 7.4. 2020. URL: `https://www.wamit.com`.

[45] R. de Bruin. *DAVE*. Version 1.9.21. 2022. URL: `https://www.open-ocean.org/dave`.

[46] WAMIT inc. *WAMIT USER MANUAL V7.4*. 2022. URL: `https://www.wamit.com/manualupdate/v74_manual.pdf` (visited on 01/15/2023).

[47] Orcina Ltd. *OrcaWave*. Version 11.3d. 2023. URL: `https://www.orcina.com/webhelp/OrcaWave/` (visited on 02/28/2023).

[48] Orcina Ltd. *OrcaFlex*. URL: `https://www.orcina.com/webhelp/OrcaFlex/` (visited on 07/22/2022).

[49] Heerema Marine Contractors. *LiftDyn Validation Based on Model Tests*. 2017.

[50] Dictionary.com. *English Dictionary*. URL: `https://www.dictionary.com/` (visited on 06/22/2022).

[51] J. Halkyard. “Chapter 7 - Floating Offshore Platform Design”. In: *Handbook of Offshore Engineering*. Ed. by S. K. CHAKRABARTI. London: Elsevier, 2005, pp. 419–661. ISBN: 978-0-08-044381-2. DOI: `https://doi.org/10.1016/B978-008044381-2.50010-2`. URL: `https://www.sciencedirect.com/science/article/pii/B9780080443812500102`.

[52] M. K. Al-Solihat and M. Nahon. “Stiffness of slack and taut moorings”. In: *Ships and Offshore Structures* 11 (Oct. 2016), pp. 890–904. DOI: `10.1080/17445302.2015.1089052`.

[53] Heerema Marine Contractors. *Sleipnir Brochure - HMC equipment*. URL: `https://www.heerema.com/heerema-marine-contractors/fleet/sleipnir` (visited on 03/10/2023).

[54] FibreMax. *FibreMax - Cable Configurator*. URL: `https://fibremax.nl/cables/cable-configurator/` (visited on 03/10/2023).

[55] MATLAB. *version 9.2.0 (R2017a)*. Natick, Massachusetts: The MathWorks Inc., 2017.

[56] NS (2023). *Curve intersections*. MATLAB Central File Exchange, 2023. URL: `https://www.mathworks.com/matlabcentral/fileexchange/22441-curve-intersections` (visited on 03/16/2023).

[57] S. Wang, Y. Cao, Q. Fu, and H. Li. “Hydrodynamic performance of a novel semi-submersible platform with nonsymmetrical pontoons”. In: *Ocean Engineering* 110 (2015), pp. 106–115. ISSN: 0029-8018. DOI: `https://doi.org/10.1016/j.oceaneng.2015.10.012`. URL: `https://www.sciencedirect.com/science/article/pii/S0029801815005491`.

[58] S. Marelli, C. Lamas, K. Konakli, C. Mylonas, P. Wiederkehr, and B. Sudret. *UQLab user manual – Sensitivity analysis*. Tech. rep. Report UQLab-V2.0-106. Chair of Risk, Safety and Uncertainty Quantification, ETH Zurich, Switzerland, 2022.

A

A. TLP

A.1. Model Overview

Table A.1: TLP model Overview

Points of Interest

No.	point name	connected to	local position			global position		
			x	y	z	X	Y	Z
1	Global Origin	Earth	0	0	0	0	0	0
2	Line1A_SB	Earth	70.002	1.5	-150	70.002	1.5	-150
3	Line1B_SB	Earth	70.002	-1.5	-150	70.002	-1.5	-150
4	Line2A_SB	Earth	-33.702	61.373	-150	-33.702	61.373	-150
5	Line2B_SB	Earth	-36.3	59.873	-150	-36.3	59.873	-150
6	Line3A_SB	Earth	-36.3	-59.873	-150	-36.3	-59.873	-150
7	Line3B_SB	Earth	-33.702	-61.373	-150	-33.702	-61.373	-150
8	TLP CoG	TLP	0	0	18.5	0	0	-19
9	Line1A_TLP	TLP	38.25	1.5	6	38.25	1.5	-31.5
10	Line2A_TLP	TLP	-17.826	33.875	6	-17.826	33.876	-31.5
11	Line3A_TLP	TLP	-20.424	-32.375	6	-20.424	-32.375	-31.5
12	Line1B_TLP	TLP	38.25	-1.5	6	38.25	-1.5	-31.5
13	Line3B_TLP	TLP	-17.826	-33.875	6	-17.826	-33.875	-31.5
14	Line2B_TLP	TLP	-20.424	32.375	6	-20.424	32.376	-31.5

Inline connectors

No.	connector name	Label	connected to		connector vector			length	E*A	Stiffness	Pretension
			node 1	node 2	X	Y	Z	[m]	[kN]	[kN/m]	[kN]
1	Line1A_part0	User-Defined	9	2	31.752	0	-118.5	122.68	1.44E+06	1.18E+04	7722
2	Line2A_part0	User-Defined	10	4	-15.876	27.498	-118.5	122.68	1.44E+06	1.18E+04	7722
3	Line3A_part0	User-Defined	11	6	-15.876	-27.498	-118.5	122.68	1.44E+06	1.18E+04	7722
4	Line3B_part0	User-Defined	13	7	-15.876	-27.498	-118.5	122.68	1.44E+06	1.18E+04	7722
5	Line2B_part0	User-Defined	14	5	-15.876	27.498	-118.5	122.68	1.44E+06	1.18E+04	7722
6	Line1B_part0	User-Defined	12	3	31.752	0	-118.5	122.68	1.44E+06	1.18E+04	7722

Body information

No.	body name	Mass [mT]	CoG (local)			Radii of Gyration			CoB (local)			Displ. [mT]
			x [m]	y [m]	z [m]	Rxx [m]	Ryy [m]	Rzz [m]	x [m]	y [m]	z [m]	
1	TLP	2826	0	0	18.5	23.96	23.96	22.42	0	0	10	7388

A.2. TLP Mesh comparison

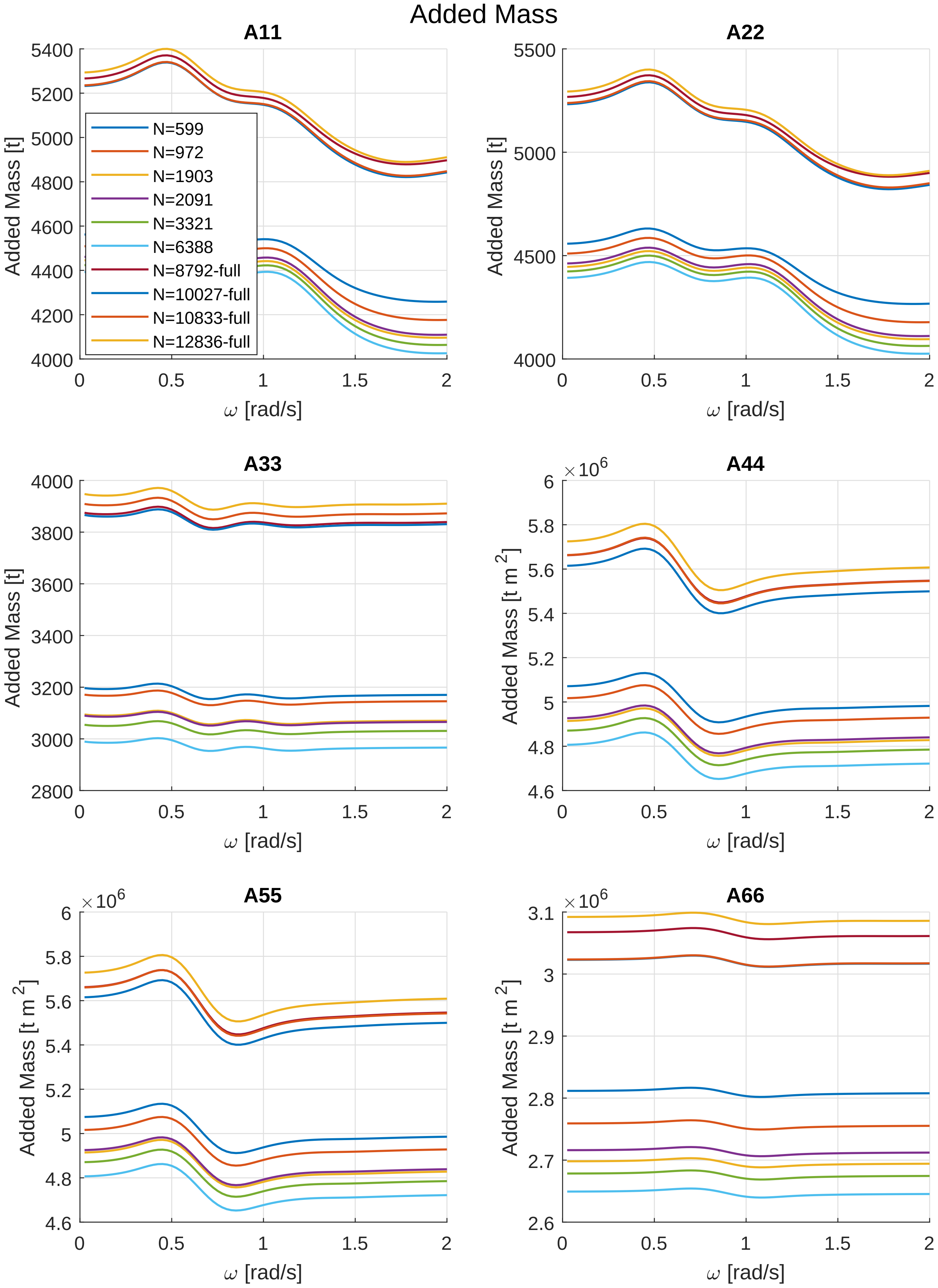

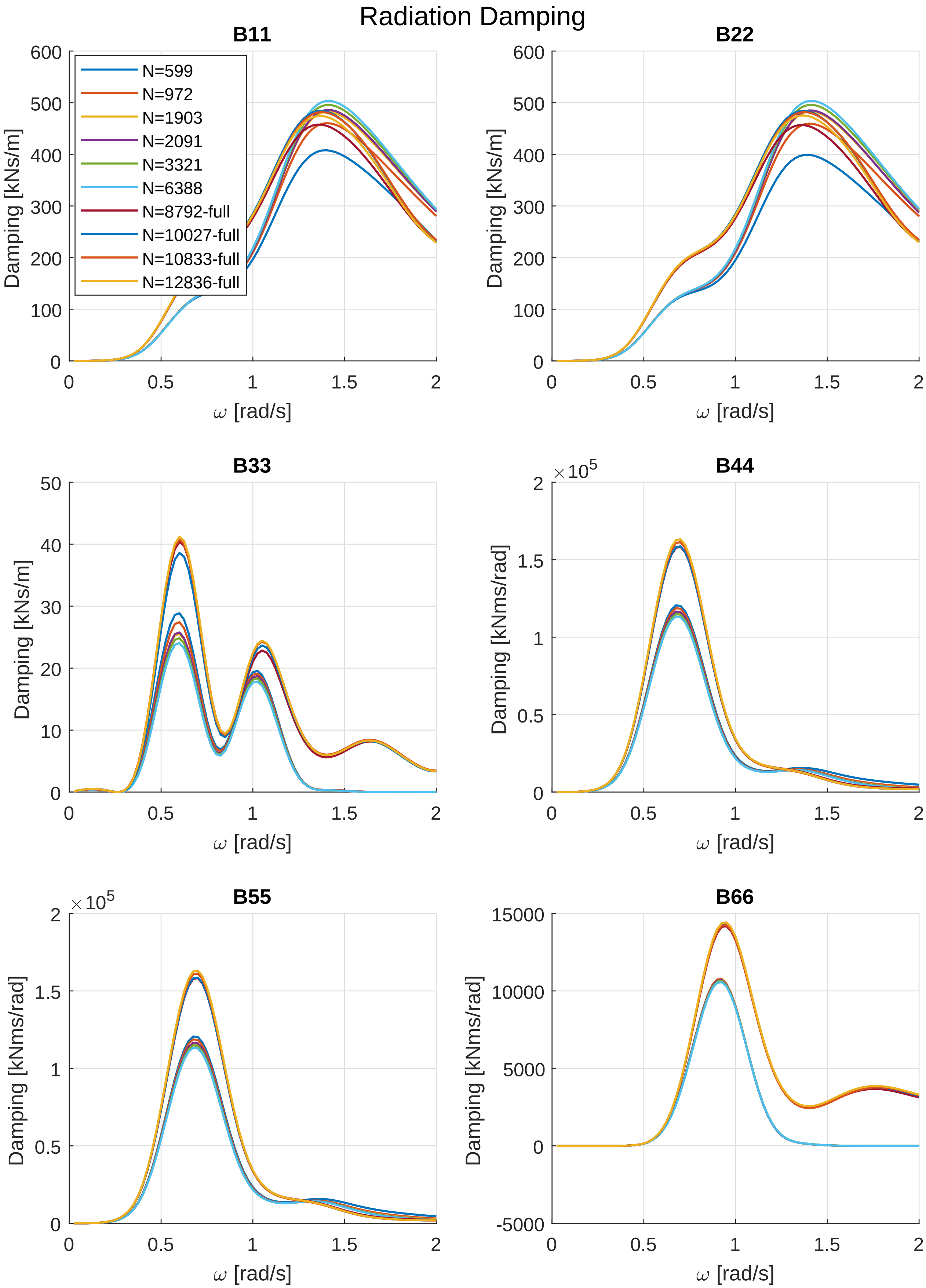
Radiation Damping
B11
B22
B33
B44
B55
B66
N=599
N=972
N=1903
N=2091
N=3321
N=6388
N=8792-full
N=10027-full
N=10833-full
N=12836-full
Damping [kNs/m]
Damping [kNms/rad]
ω [rad/s]
0
0.5
1
1.5
2
100
200
300
400
500
600
10
20
30
40
50
×10^5
5000
10000
15000
-5000

A.3. TLP WAMIT Mesh convergence

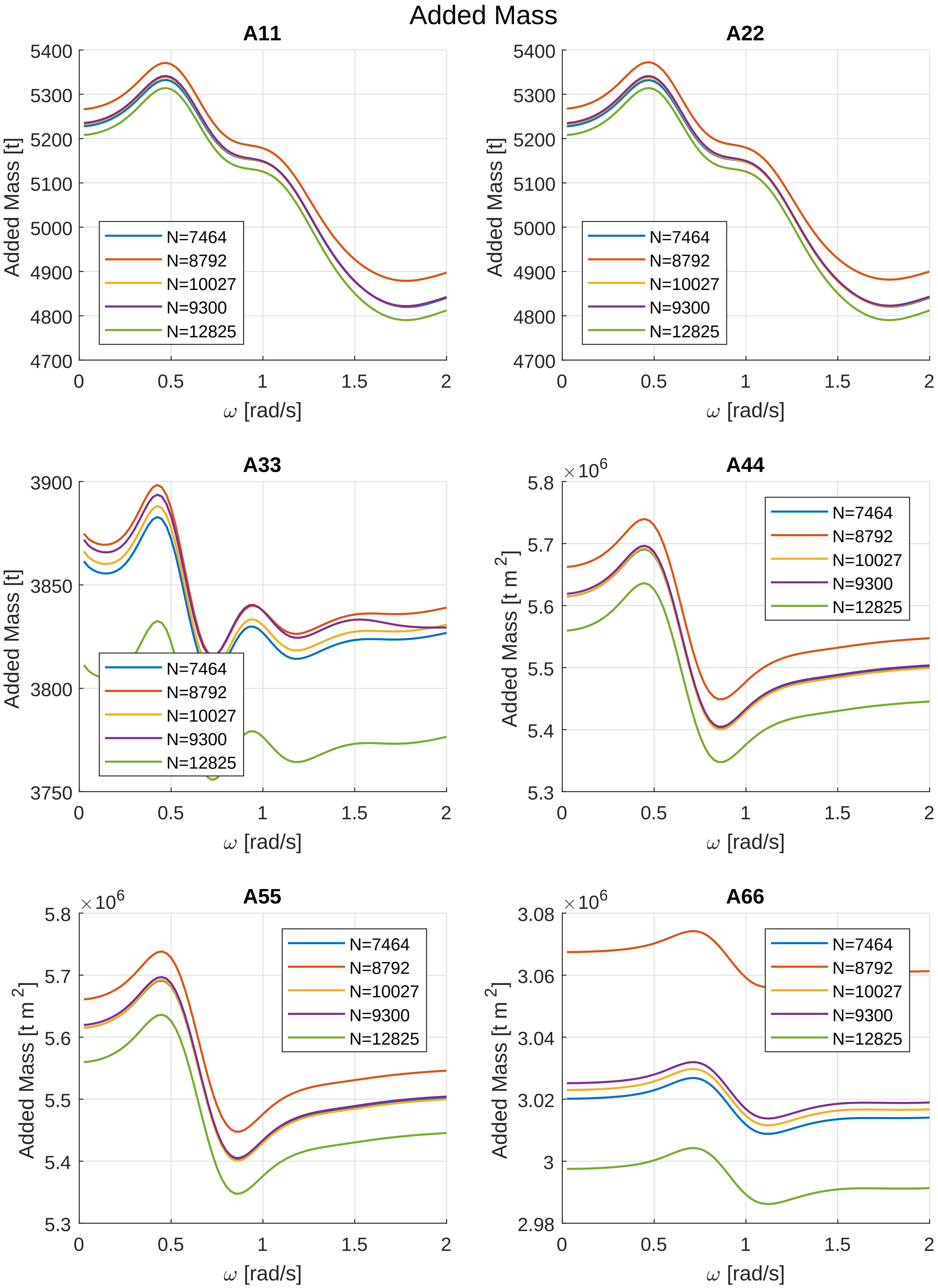

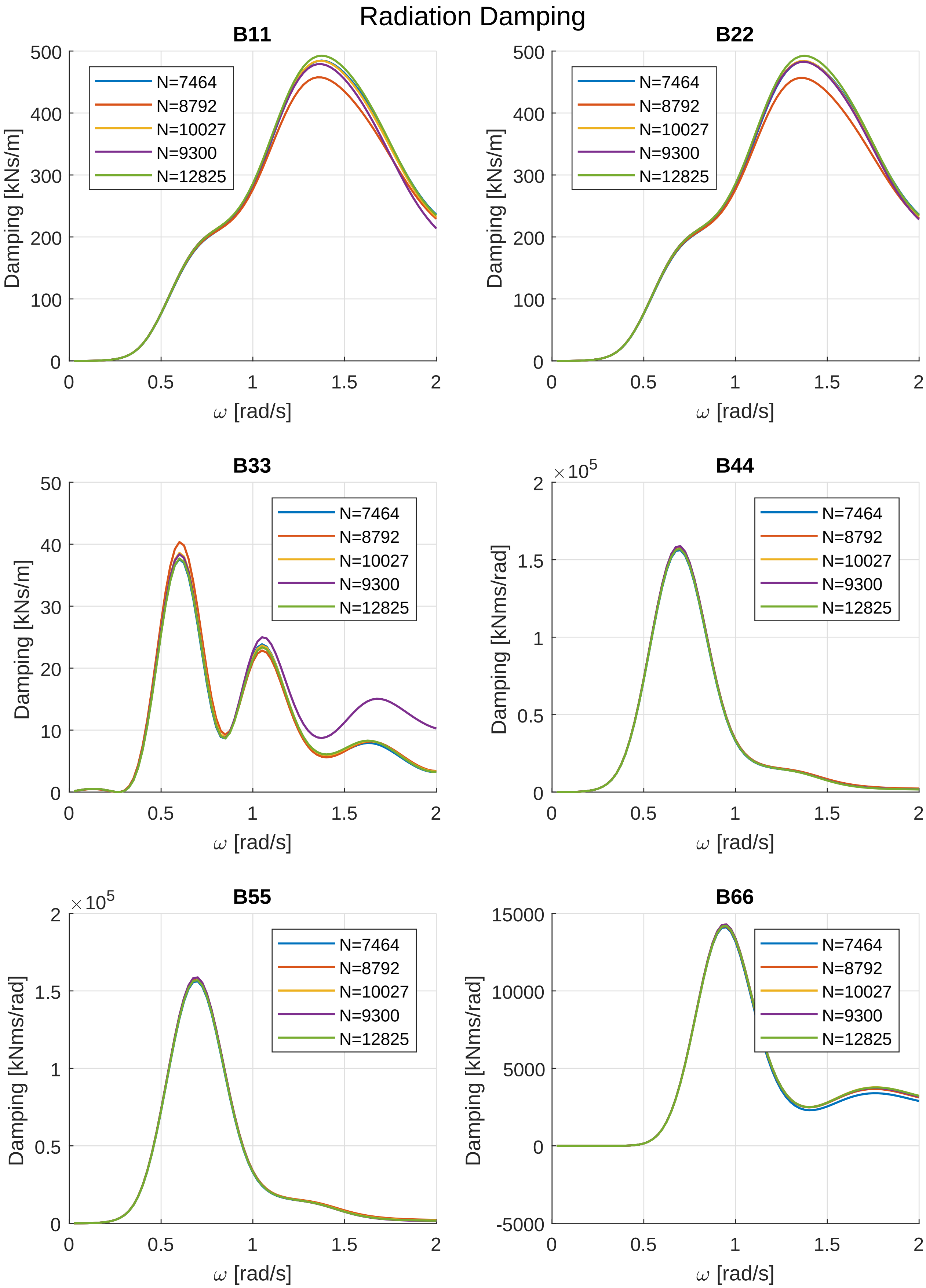
Radiation Damping
B11
B22
B33
B44
B55
B66
N=7464
N=8792
N=10027
N=9300
N=12825
Damping [kNs/m]
Damping [kNms/rad]
ω [rad/s]
0
0.5
1
1.5
2
100
200
300
400
500
10
20
30
40
50
$\times10^5$
5000
10000
15000
-5000

A.4. Final Added Mass TLP

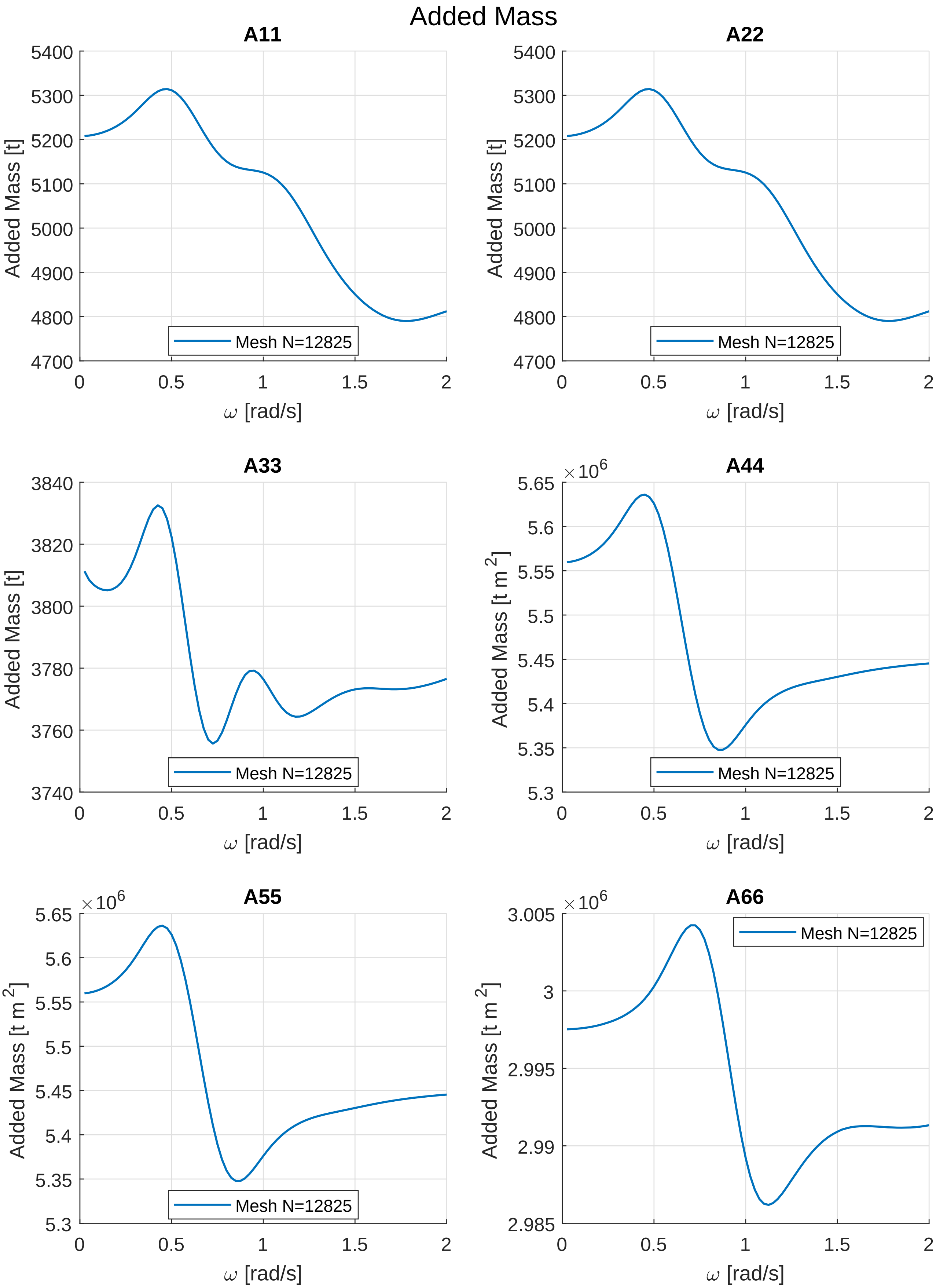

A.5. Final Radiation Damping TLP

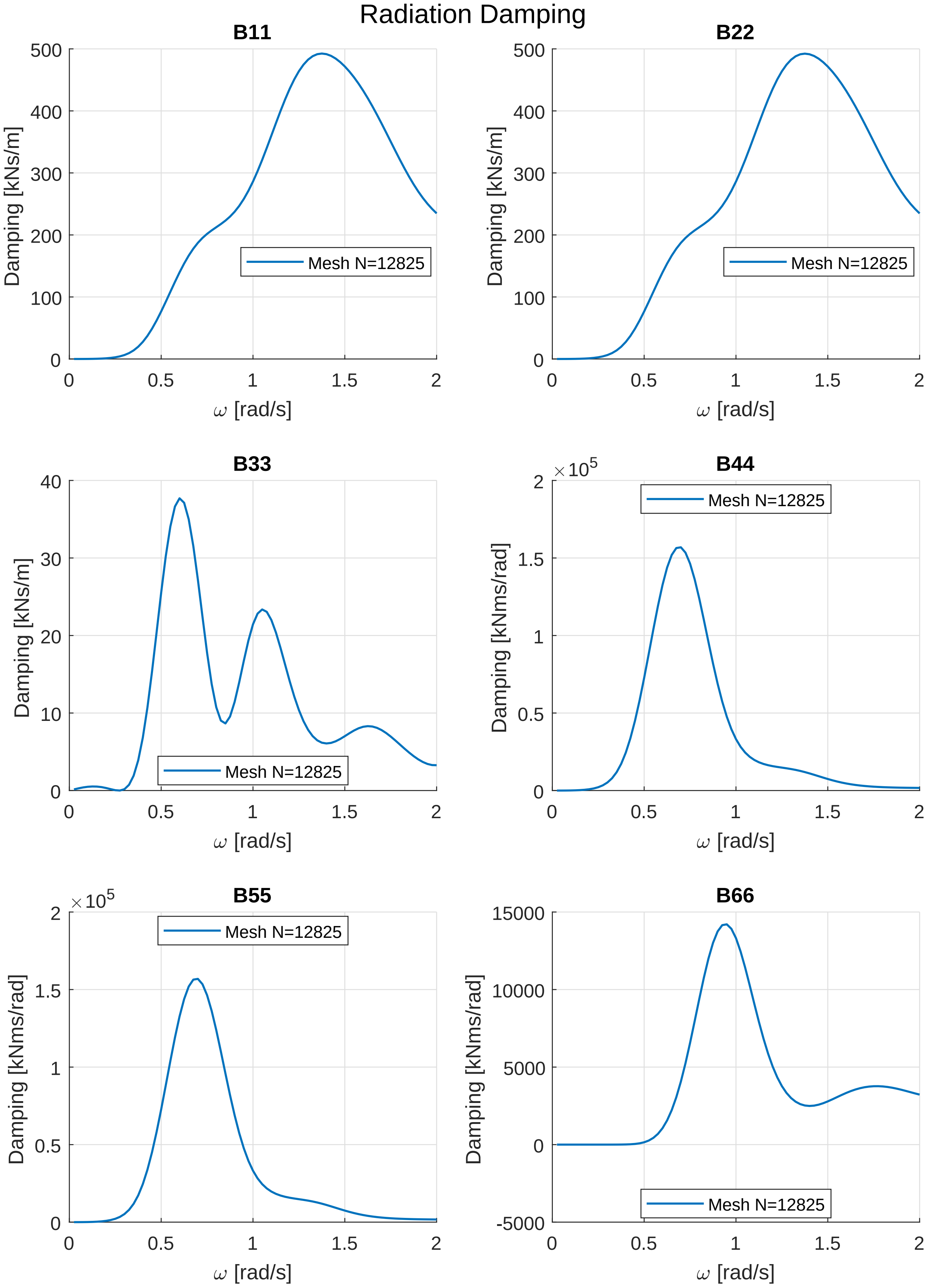

A.6. LiftDyn RAO and Responses for TLP

Comparison of RAOs for 45 deg

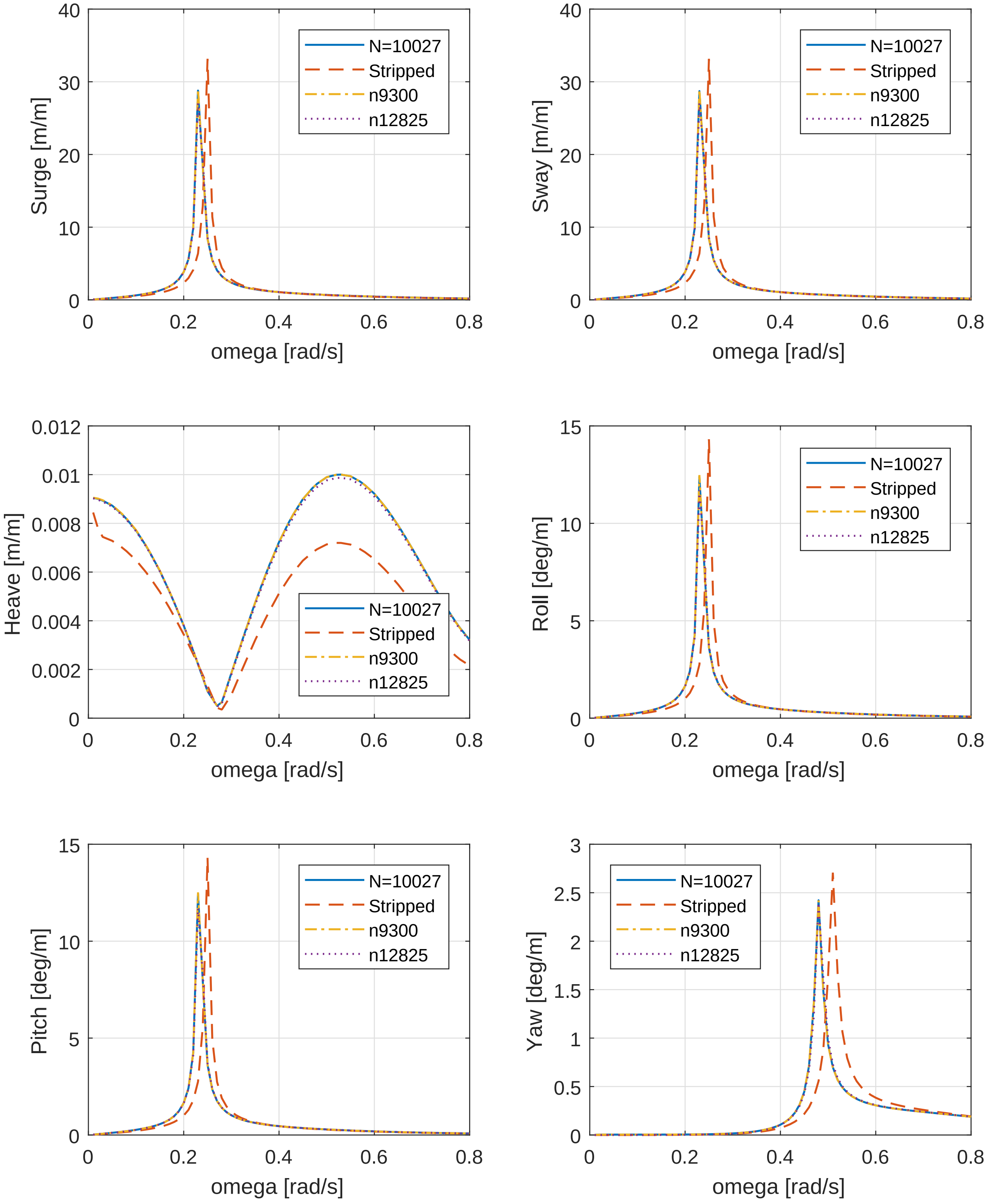

A.7. LiftDyn Responses for TLP

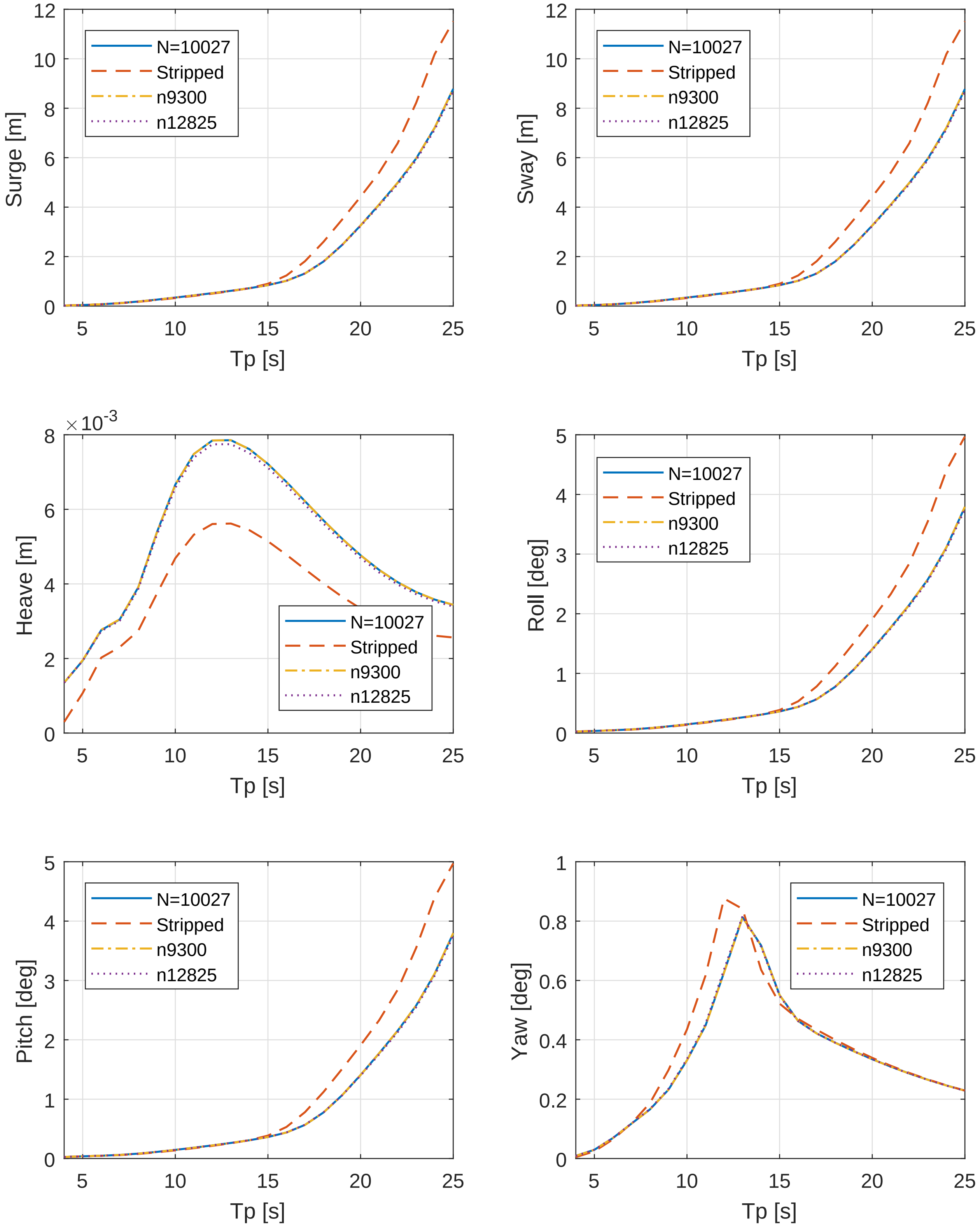

Comparison of responses for 45 deg, Hs = 1m

A.8. WAMIT input

```
model.pot
----------------------------------
Pot file to request frequency range 0.025:0.025:2.0 rad/s and 0:15:180 deg heading
150 waterdepth, <=0 indicates infinite waterdepth
1 1 iRad & iDiff indicating that radiation and diffraction is to be evaluated for all modes
-82  number frequencies minus sign indicates that start and step will be defined
-0.025 0.025  start frequency and frequency step
-24  number of headings minus sign indicates that start and step will be defined
0 15  start heading and heading step
1  single body run: name and position will follow
model2.GDF
0. 0. 0. 0.  position and heading w.r.t. global origin
1 1 1 1 1 1  all modes evaluated
----------------------------------
```

```
model.cfg
----------------------------------
IPOTEN = 1
ILOWHI = 0
IFORCE = 1
PANEL_SIZE = 3
ILOWGDF = 1
ITRIMWL=1
XTRIM= 0 0 0
IRR = 1
IALTFRC = 2
IPERIN= 2
IPEROUT= 2
ISOR=   0
ILOG = 1
ISOLVE= 1
NCPU=3
RAMGBMAX = 6.9
USERID_PATH=C:\WAMITV7
SCRATCH_PATH=C:\Temp
----------------------------------
```

```
model.frc
----------------------------------
Header line of FRC file
1 0 1 0 0 0 0 0 0  {IOPTN(1-9) indicating the required output see Wamit Manual
1.025 {water density}
0 0 -19 {position of CoG with respect to origin of body}
1  {mass matrix with respect to origin of body
2826      0      0      0      0      0
0  2826      0      0      0      0
0      0  2826      0      0      0
0         0         0  1622355         0         0
0         0         0         0  1622355         0
0         0         0         0         0  1420507
```

B

Tower

Table B.1: Tower configuration per segment

Seg	Z max $[m]$	D $[m]$	th $[m]$	r2 $[m]$	r1 $[m]$	H $[m]$	VCG $[m]$	Mass $[t]$	J_{xx} $[tm^2]$	J_{yy} $[tm^2]$	J_{zz} $[tm^2]$	δz $[m]$	J'_{xx} $[tm^2]$	J'_{yy} $[tm^2]$	J'_{zz} $[tm^2]$
1	12	8	0.0395	4.00	3.96	12	6	96.7	1926	1926	1531	42.1	1.73E+05	1.73E+05	1.53E+03
2	24	7.96	0.0365	3.98	3.94	12	18	93.0	1854	1854	1474	30.1	8.63E+04	8.63E+04	1.47E+03
3	36	7.74	0.0338	3.87	3.84	12	30	85.5	1697	1697	1342	18.1	2.98E+04	2.98E+04	1.34E+03
4	48	7.48	0.0322	3.74	3.71	12	42	77.0	1496	1496	1144	6.1	4.38E+03	4.38E+03	1.14E+03
5	60	7.2	0.0307	3.60	3.57	12	54	71.0	1343	1343	984	5.9	3.80E+03	3.80E+03	9.84E+02
6	72	6.84	0.0291	3.42	3.39	12	66	65.2	1200	1200	837	17.9	2.20E+04	2.20E+04	8.37E+02
7	84	6.65	0.0272	3.33	3.30	12	78	58.7	1044	1044	680	29.9	5.34E+04	5.34E+04	6.80E+02
8	96	6.56	0.0240	3.28	3.26	12	90	53.3	932	932	585	41.9	9.45E+04	9.45E+04	5.85E+02
9	108	6.51	0.0208	3.26	3.23	12	102	46.4	805	805	496	53.9	1.36E+05	1.36E+05	4.96E+02
10	112	6.5	0.0240	3.25	3.23	4	110	13.3	88	88	140	61.9	5.11E+04	5.11E+04	1.40E+02
Total						112	48.1	660					6.54E+05	6.54E+05	9.21E+03

C

Combined Model

C.1. Parameter Sets

Table C.1: All variation sets

name	SB boom radius	SB slew angle	tugdamp	Tugger angle	z Offset UpperLFT	Tower mass	NAH mass	NAH cogx	Tower height	Tower vcg	TLP Mass	Tendon angle deg	EA moor
base case	58	180	15	15	7	660	821	5.48	112	48.72	2826	15	1.44E+06
boom radius 50m	50	180	15	15	7	660	821	5.48	112	48.72	2826	15	1.44E+06
boom radius 40m	40	180	15	15	7	660	821	5.48	112	48.72	2826	15	1.44E+06
slew angle 135deg	58	135	15	15	7	660	821	5.48	112	48.72	2826	15	1.44E+06
slew angle 90deg	58	90	15	15	7	660	821	5.48	112	48.72	2826	15	1.44E+06
tugger damp 0	58	180	0	15	7	660	821	5.48	112	48.72	2826	15	1.44E+06
tugger damp 30	58	180	30	15	7	660	821	5.48	112	48.72	2826	15	1.44E+06
tugger angle 0	58	180	15	0	7	660	821	5.48	112	48.72	2826	15	1.44E+06
tugger angle 25	58	180	15	25	7	660	821	5.48	112	48.72	2826	15	1.44E+06
offset liftupper 1m	58	180	15	15	1	660	821	5.48	112	48.72	2826	15	1.44E+06
offset liftupper 14m	58	180	15	15	14	660	821	5.48	112	48.72	2826	15	1.44E+06
tower mass 860	58	180	15	15	7	860	821	5.48	112	48.72	2826	15	1.44E+06
tower mass 1060	58	180	15	15	7	1060	821	5.48	112	48.72	2826	15	1.44E+06
nah mass 620	58	180	15	15	7	660	621	5.48	112	48.72	2826	15	1.44E+06
nah mass 1020	58	180	15	15	7	660	1021	5.48	112	48.72	2826	15	1.44E+06
nah cogx 0m	58	180	15	15	7	660	821	0	112	48.72	2826	15	1.44E+06
nah cogx neg 5 48m	58	180	15	15	7	660	821	-5.48	112	48.72	2826	15	1.44E+06
hub height 130m	58	180	15	15	7	660	821	5.48	102	48.72	2826	15	1.44E+06
hub height 150m	58	180	15	15	7	660	821	5.48	122	48.72	2826	15	1.44E+06
tower vcg 35m	58	180	15	15	7	660	821	5.48	112	35	2826	15	1.44E+06
tower vcg 65m	58	180	15	15	7	660	821	5.48	112	65	2826	15	1.44E+06
tlp mass 2402t	58	180	15	15	7	660	821	5.48	112	48.72	2402	15	1.44E+06
tlp mass 3249t	58	180	15	15	7	660	821	5.48	112	48.72	3250	15	1.44E+06
tendon angle 0deg	58	180	15	15	7	660	821	5.48	112	48.72	2826	0	1.44E+06
tendon angle 20deg	58	180	15	15	7	660	821	5.48	112	48.72	2826	20	1.44E+06
ea moor dyn 772e3	58	180	15	15	7	660	821	5.48	112	48.72	2826	15	7.72E+05
ea moor carbon 178e4	58	180	15	15	7	660	821	5.48	112	48.72	2826	15	1.78E+06

D

Operability per Parameter Variation, all Limits

In this Appendix, the operability curves per parameter for all operability limits presented in Section 5.2 are given for wave direction ranging from 0° to 180° in steps of 45°

D.1. Operability - Base Case

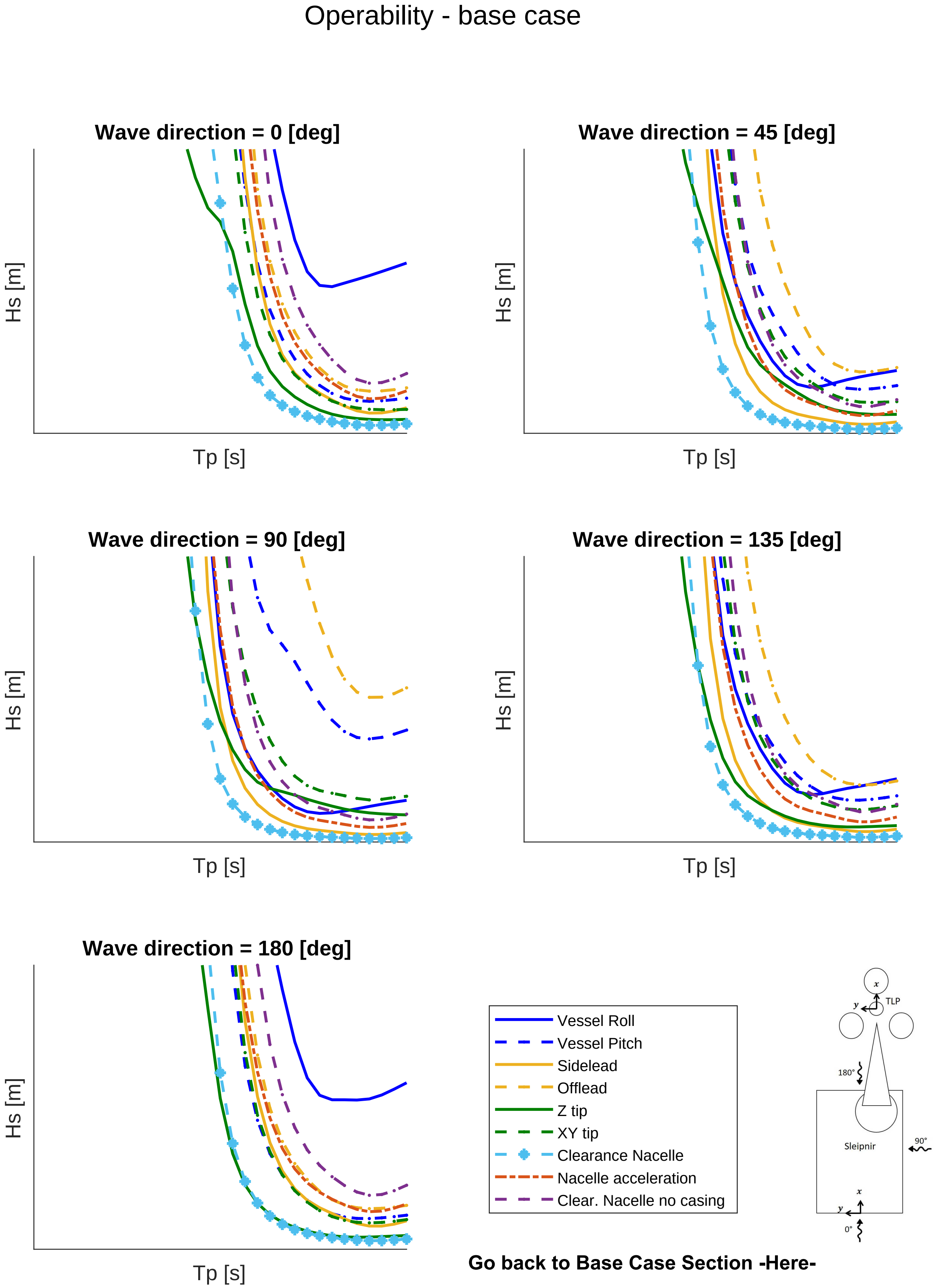

Go back to Base Case Section -Here-

D.2. Operability - Boom radius 50 [m]

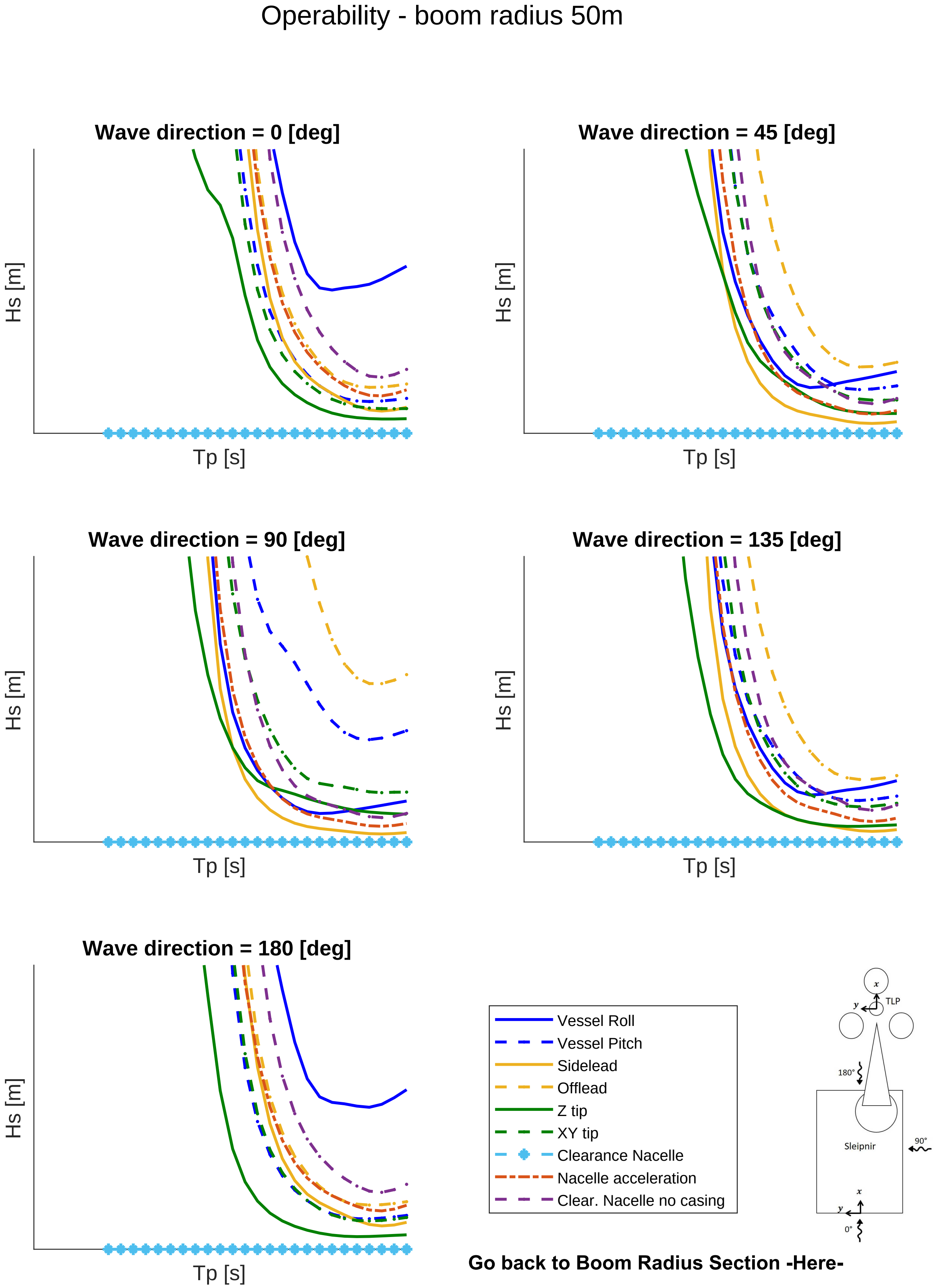

Go back to Boom Radius Section -Here-

See Grouped Operability Boom Radius -Here-

D.3. Operability - Boom radius 40 [m]

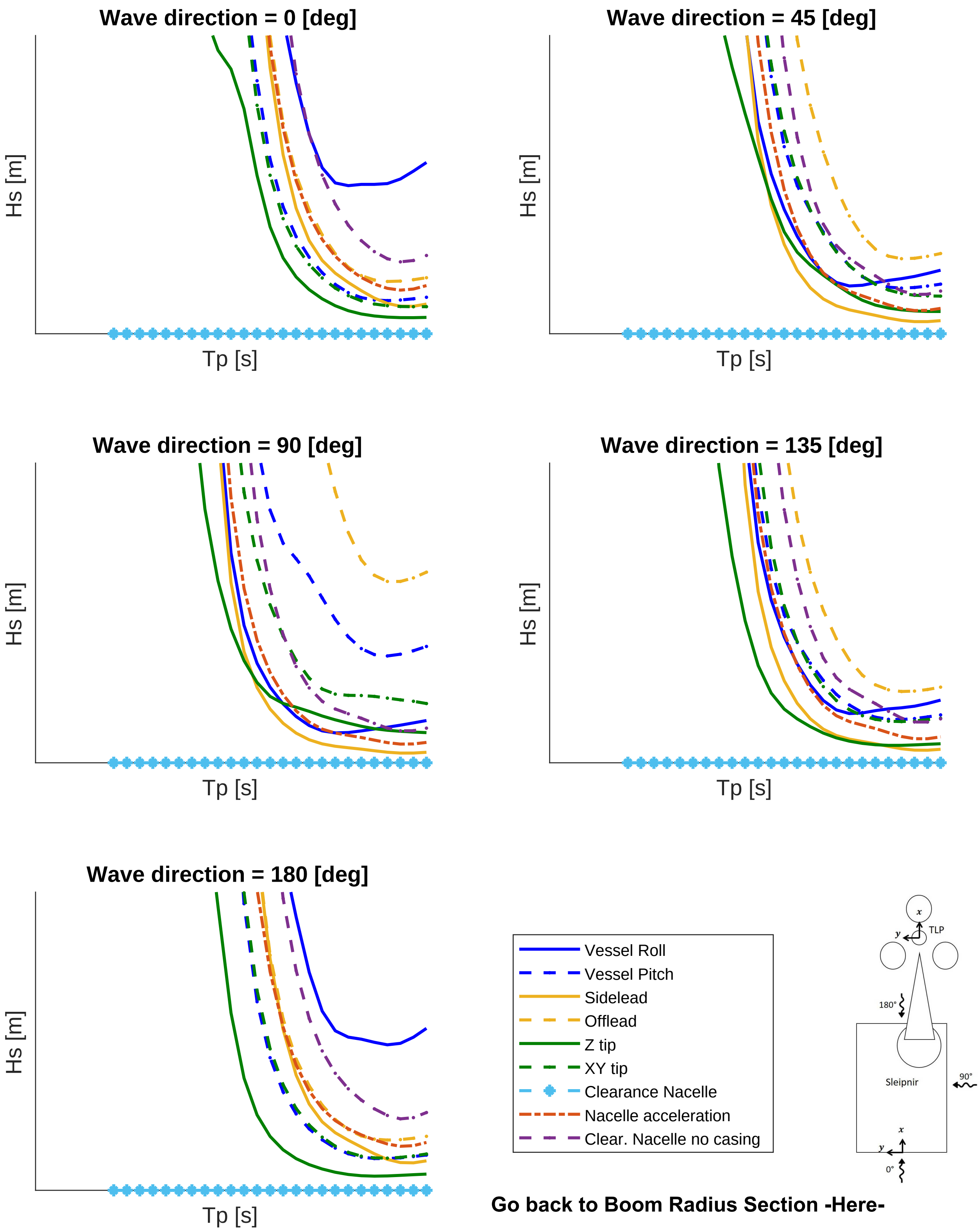

Operability - boom radius 40m

Go back to Boom Radius Section -Here-

See Grouped Operability Boom Radius -Here-

D.4. Operability - Slew Angle 135 [deg]

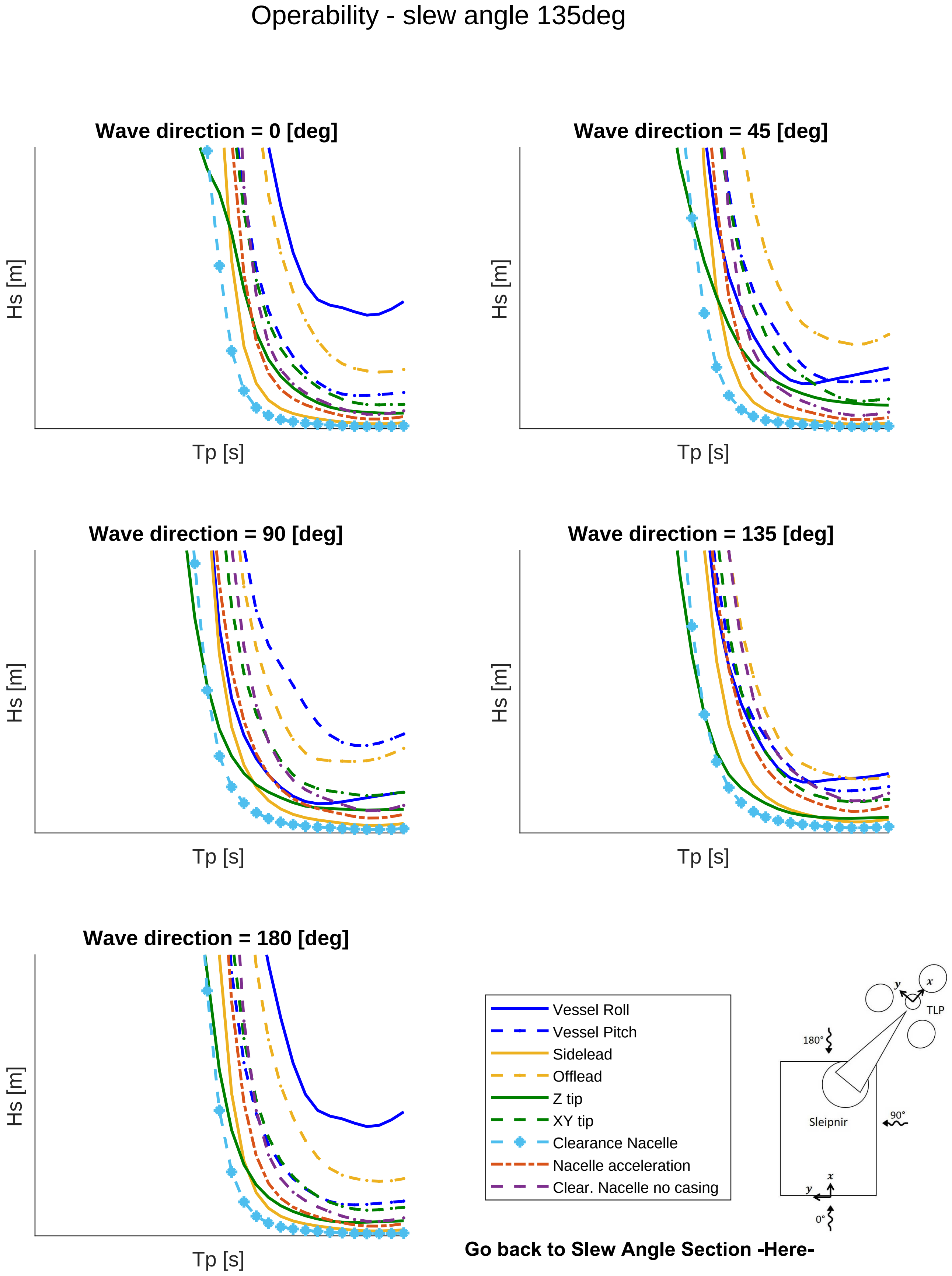

Go back to Slew Angle Section -Here-

See Grouped Operability Slew Angle -Here-

D.5. Operability - Slew Angle 90 [deg]

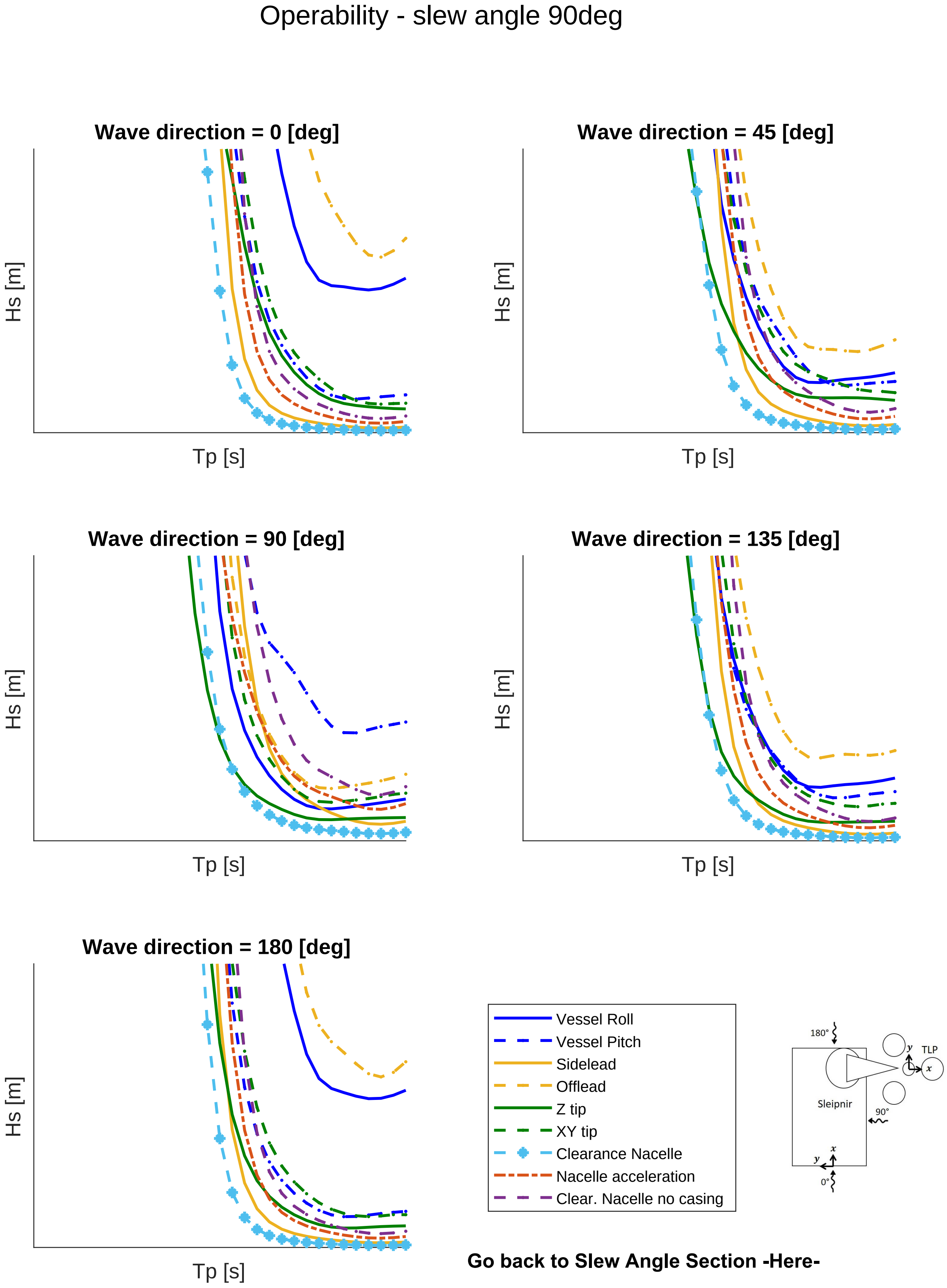
Operability - slew angle 90deg

Wave direction = 0 [deg]

Wave direction = 45 [deg]

Wave direction = 90 [deg]

Wave direction = 135 [deg]

Wave direction = 180 [deg]

Go back to Slew Angle Section -Here-

See Grouped Operability Slew Angle -Here-

D.6. Operability - Tugger Damping 0 [t*s/m]

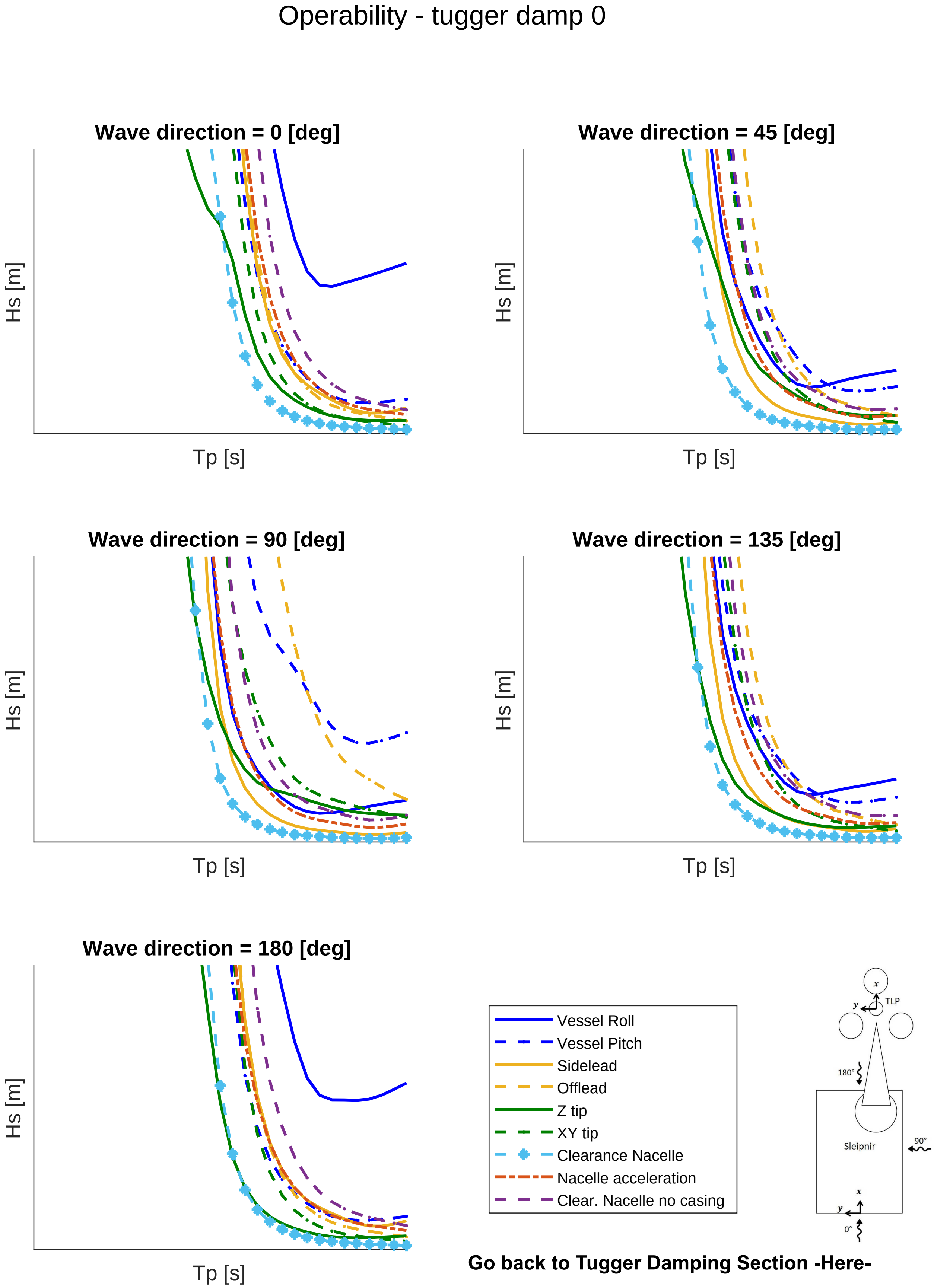

Go back to Tugger Damping Section -Here-

See Grouped Operability Tugger Damping -Here-

D.7. Operability - Tugger Damping 30 [t*s/m]

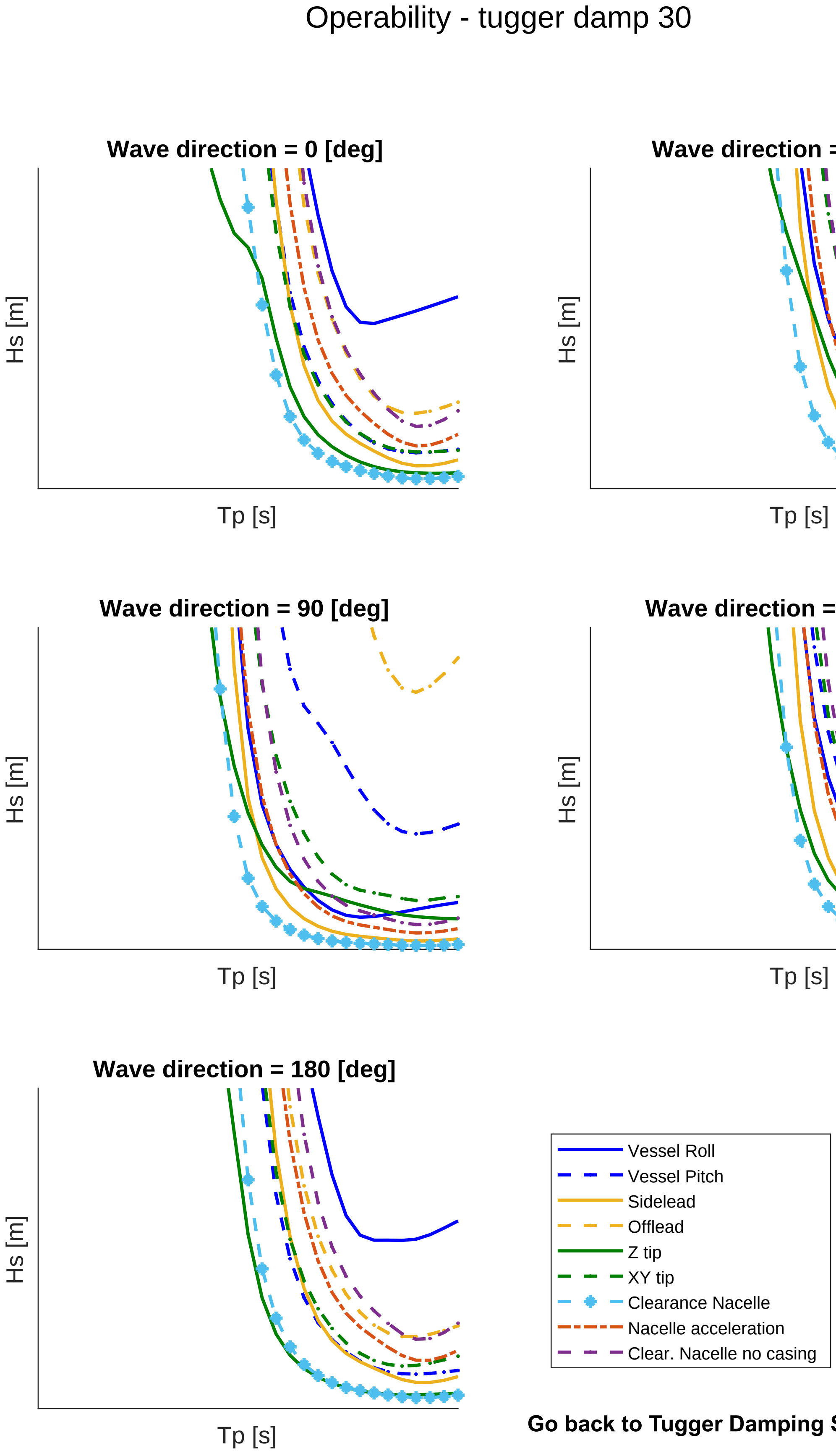

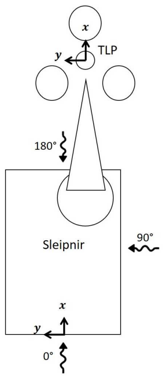

Go back to Tugger Damping Section -Here-

See Grouped Operability Tugger Damping -Here-

D.8. Operability - Tugger Line Angle 0 [deg]

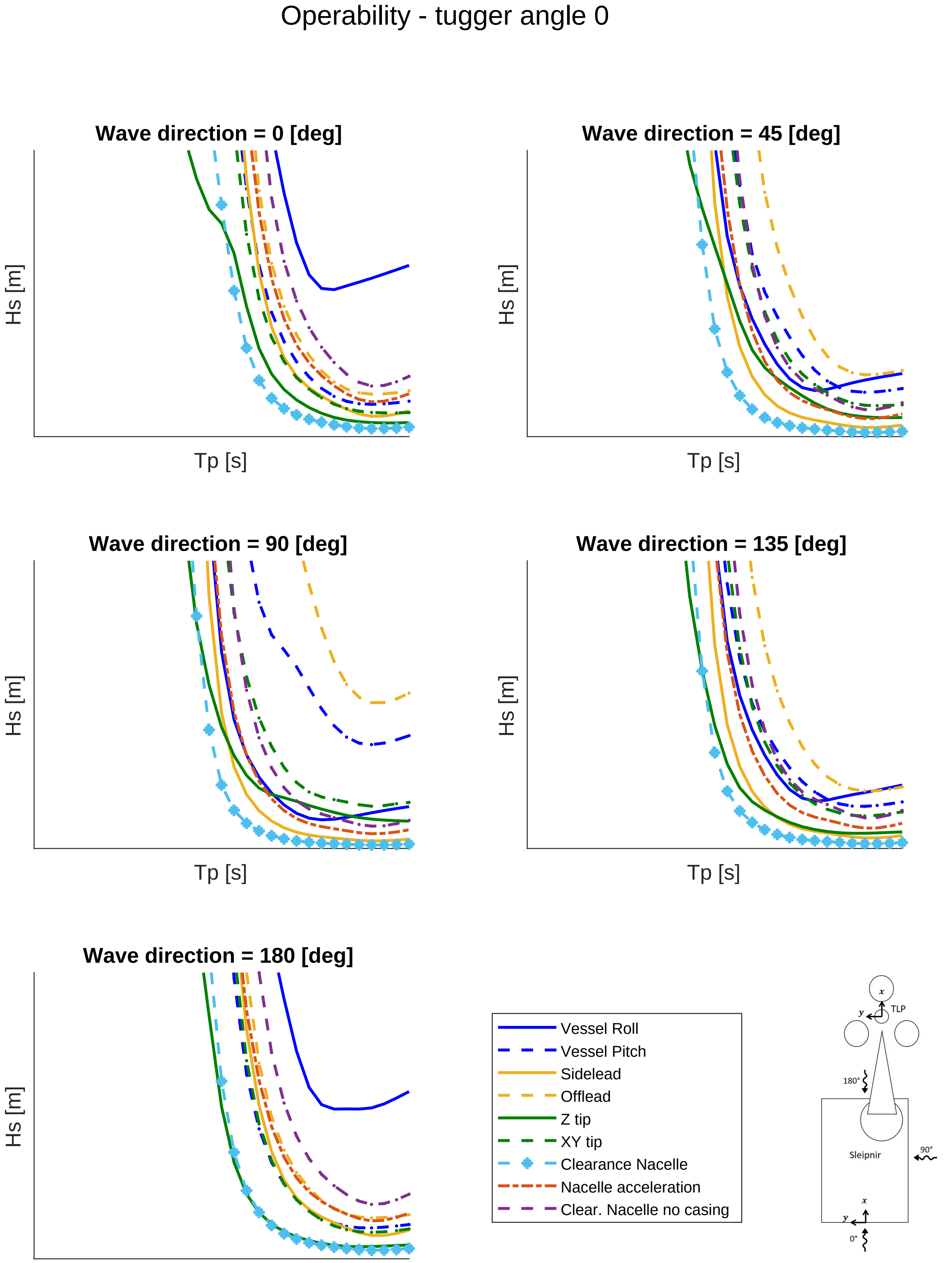

Go back to Tugger Line Angle Section -Here-

See Grouped Operability Tugger Line Angle -Here-

D.9. Operability - Tugger Line Angle -25 [deg]

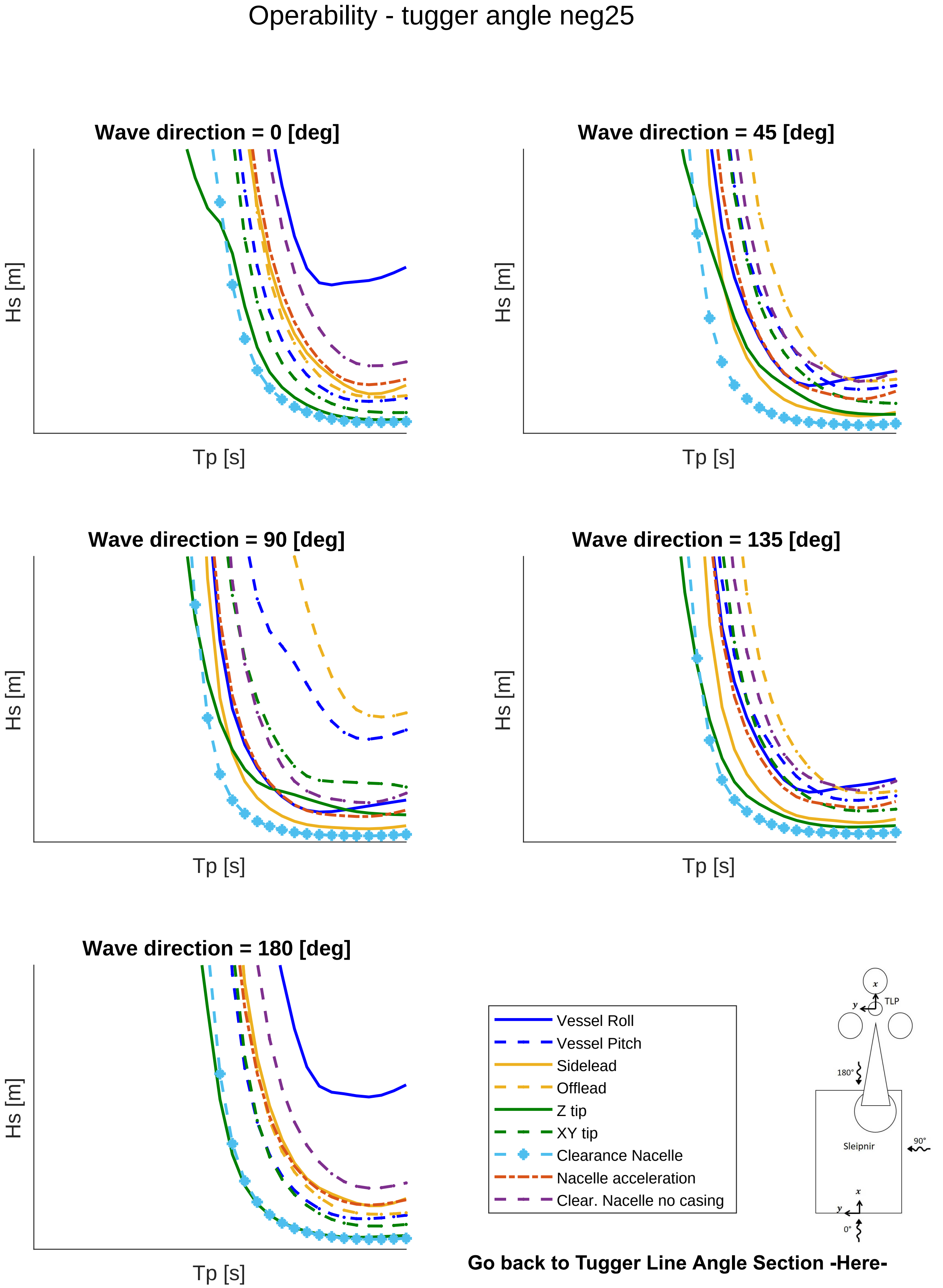

Go back to Tugger Line Angle Section -Here-

See Grouped Operability Tugger Line Angle -Here-

D.10. Operability - Upper Lifting Tool Offset 1 [m]

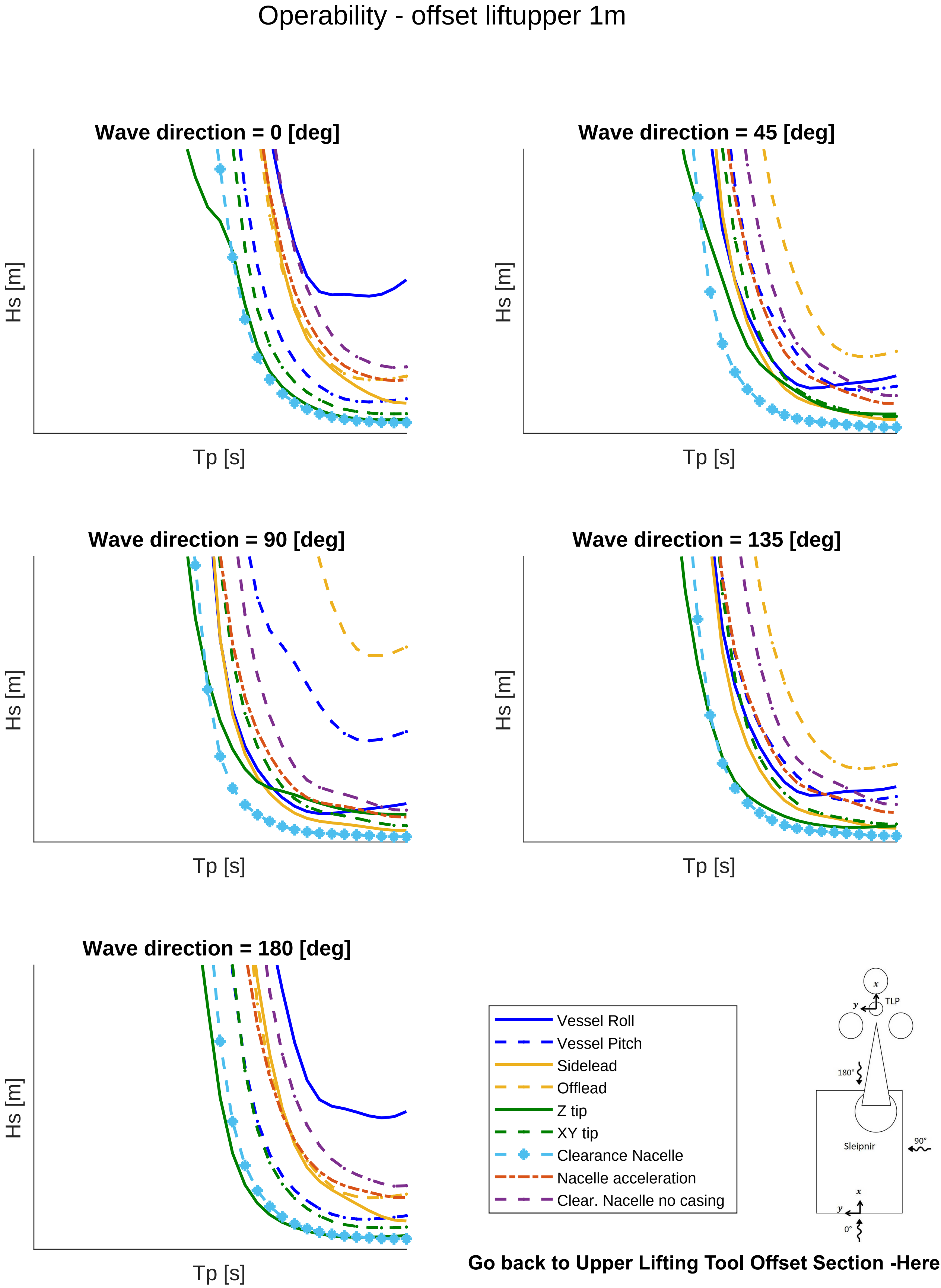

Go back to Upper Lifting Tool Offset Section -Here-

See Grouped Operability Upper Lifting Tool Offset -Here-

D.11. Operability - Upper Lifting Tool Offset 14 [m]

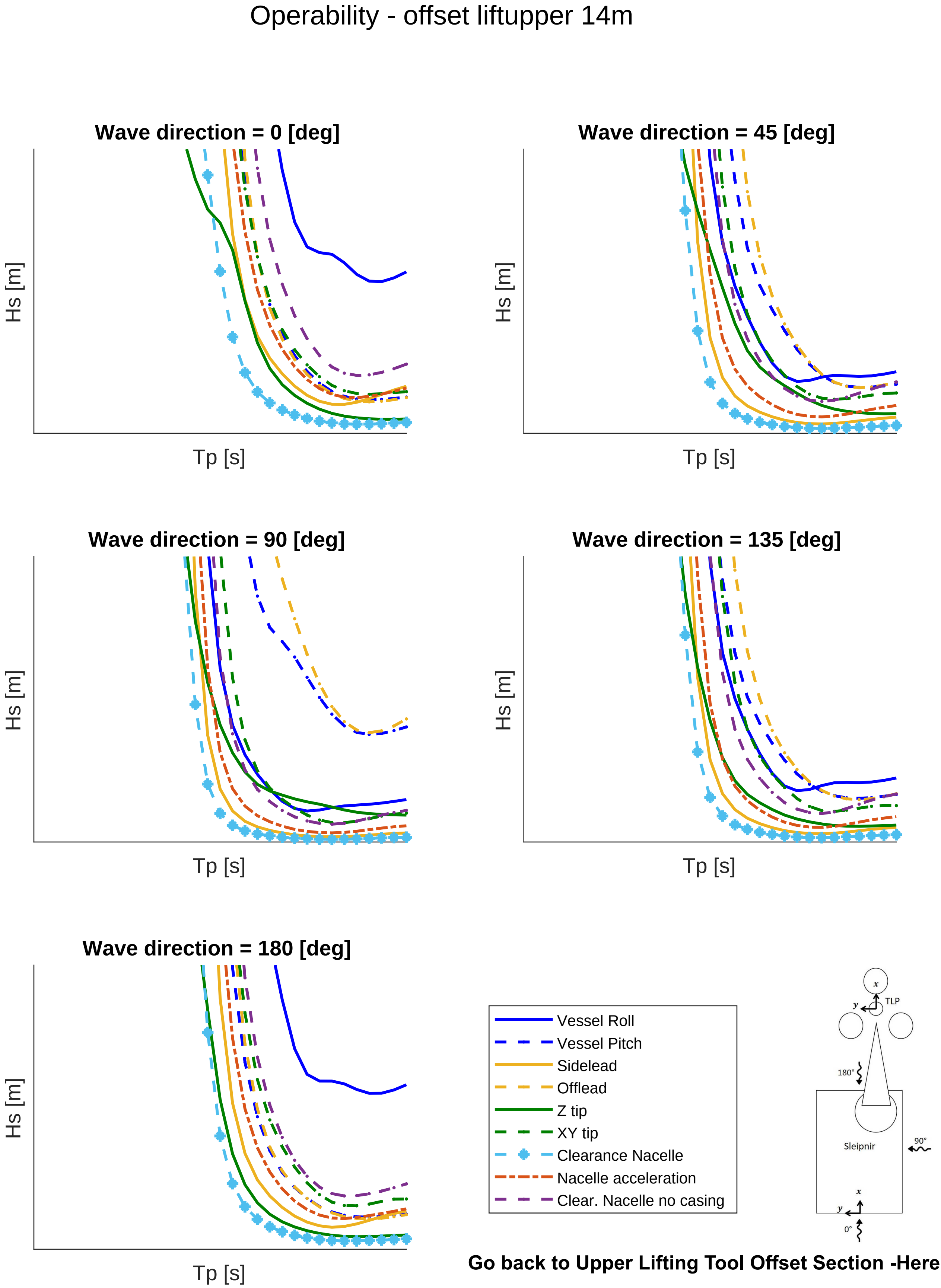

Go back to Upper Lifting Tool Offset Section -Here-

See Grouped Operability Upper Lifting Tool Offset -Here-

D.12. Operability - Tower Mass 860 [t]

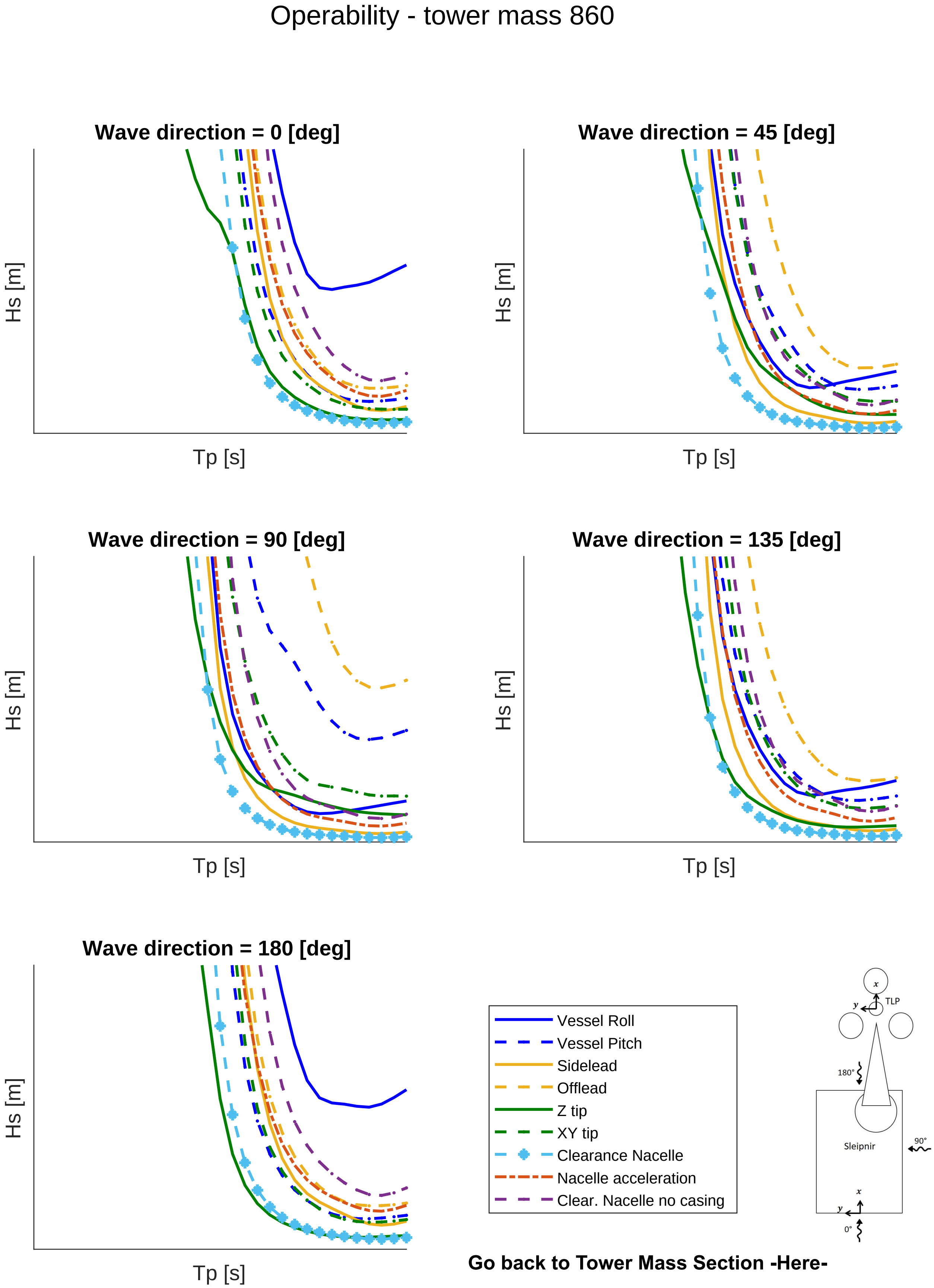

Go back to Tower Mass Section -Here-

See Grouped Operability Tower Mass -Here-

D.13. Operability - Tower Mass 1060 [t]

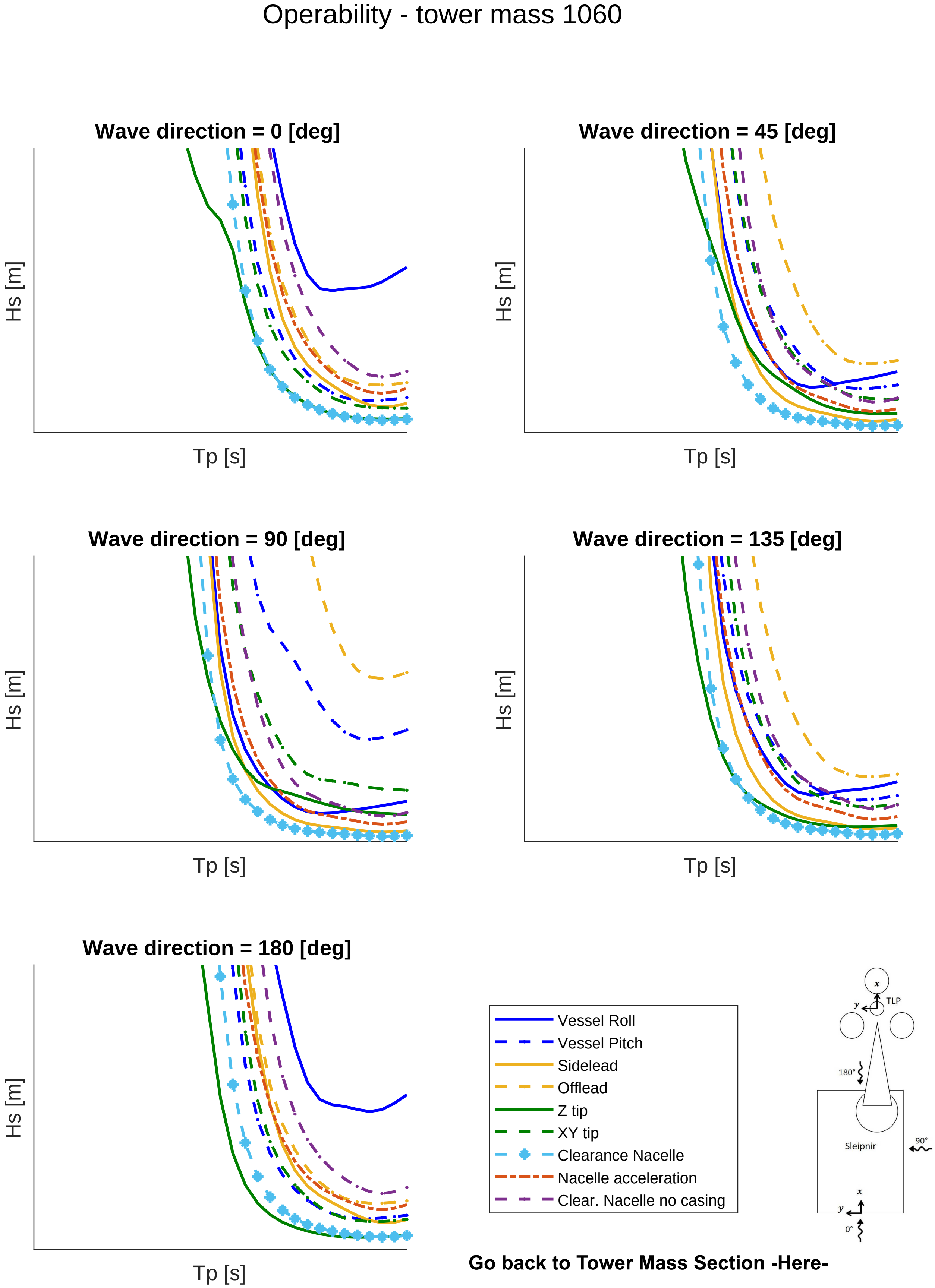

Go back to Tower Mass Section -Here-

See Grouped Operability Tower Mass -Here-

D.14. Operability - Nacelle Mass 620 [t]

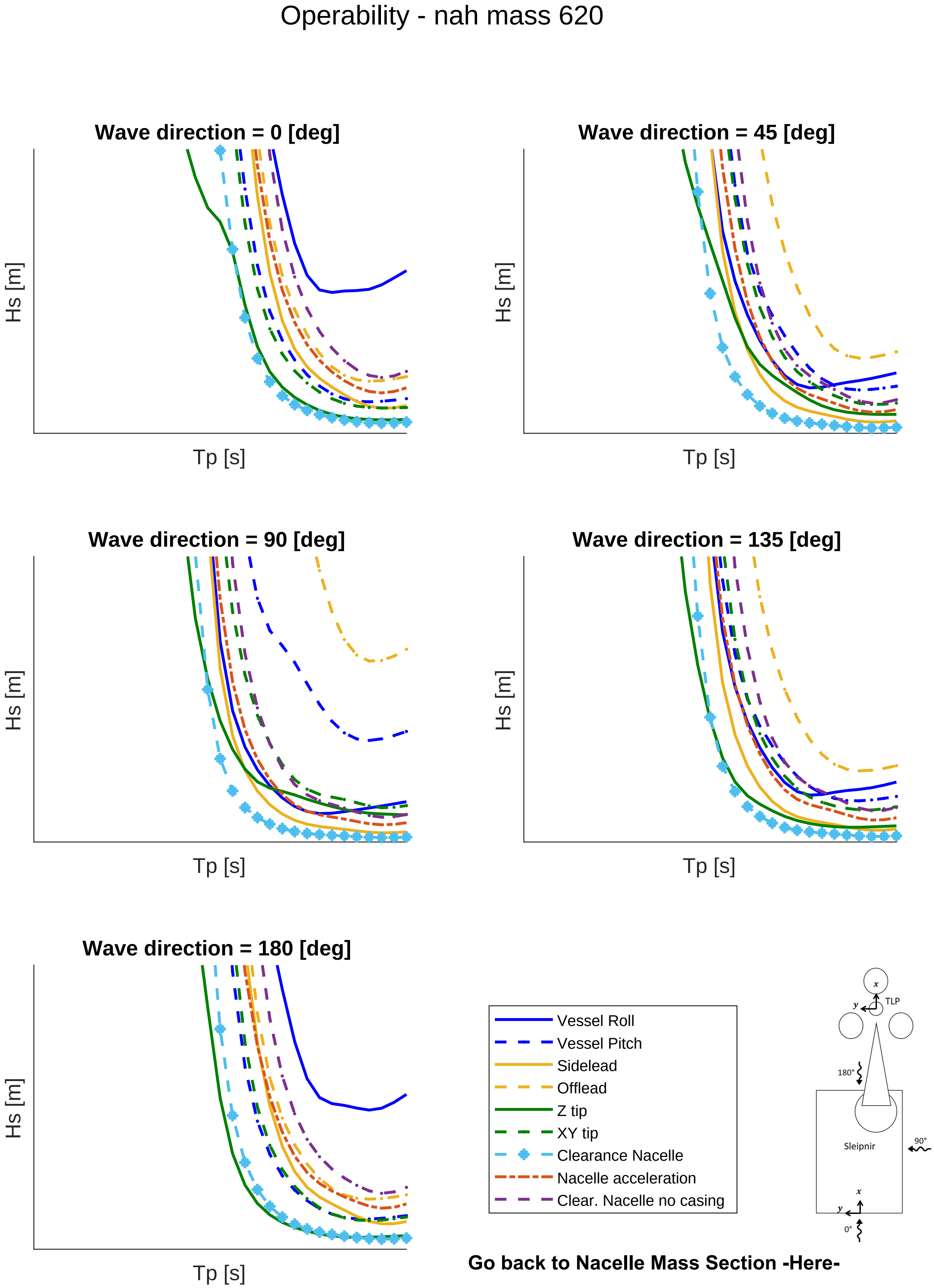

Go back to Nacelle Mass Section -Here-

See Grouped Operability Nacelle Mass -Here-

D.15. Operability - Nacelle Mass 1020 [t]

Operability - nah mass 1020

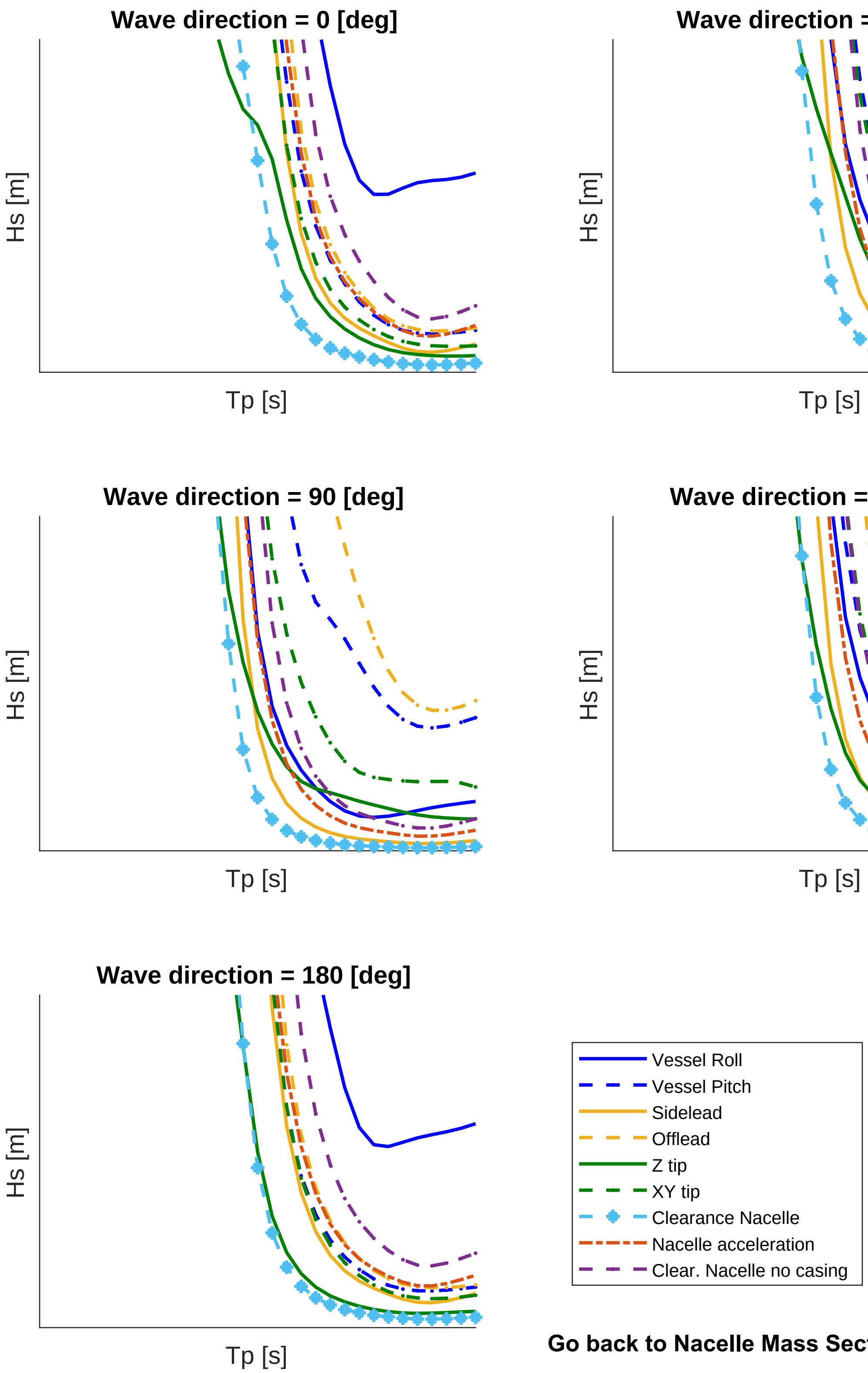

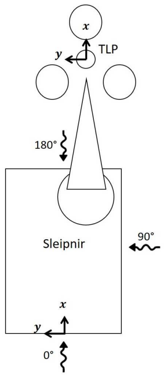

Go back to Nacelle Mass Section -Here-

See Grouped Operability Nacelle Mass -Here-

D.16. Operability - Nacelle HCG 0 [m]

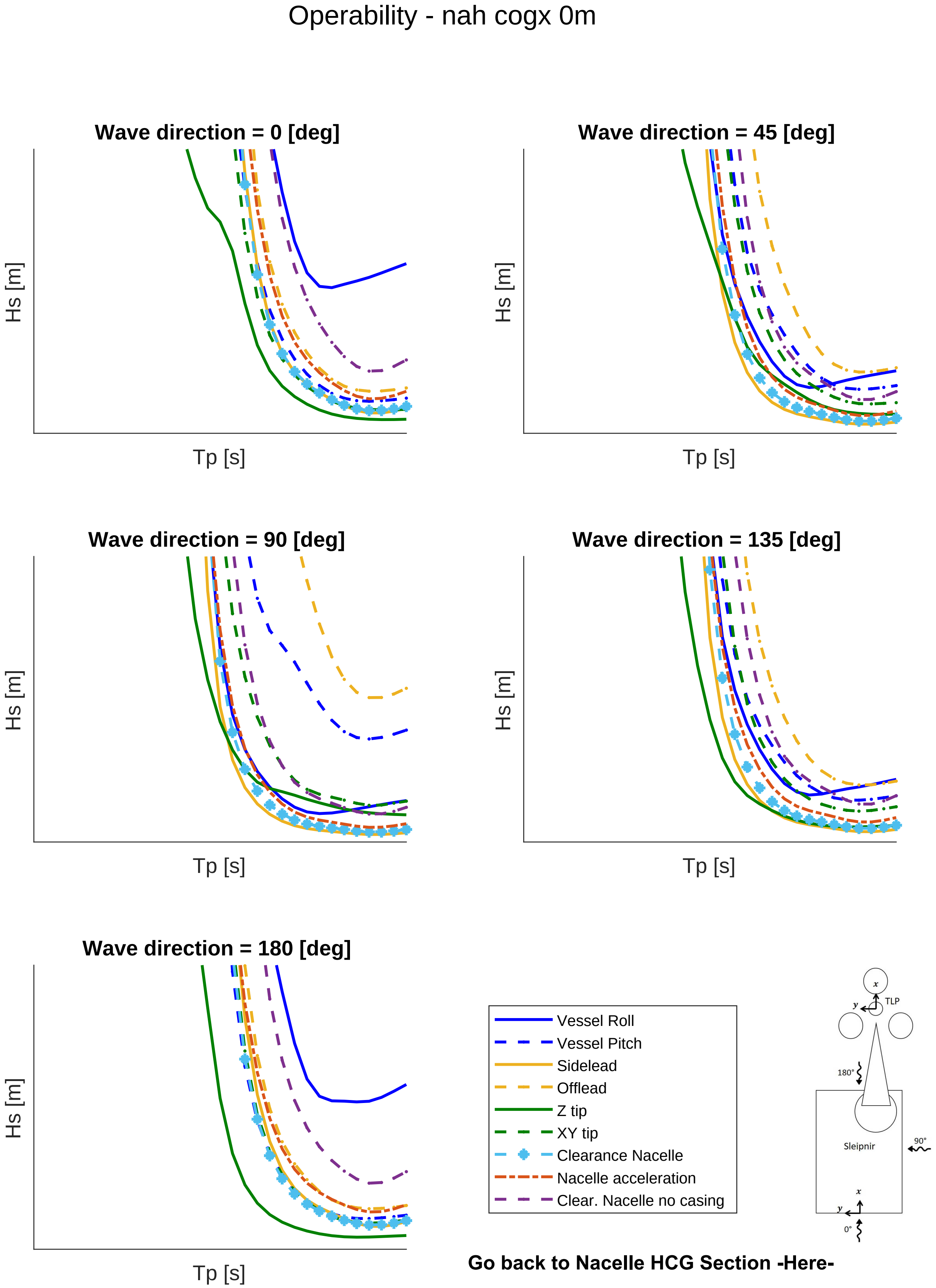

Go back to Nacelle HCG Section -Here-

See Grouped Operability Nacelle HCG -Here-

D.17. Operability - Nacelle HCG 5.48 [m]

Operability - nah cogx neg 5 48m

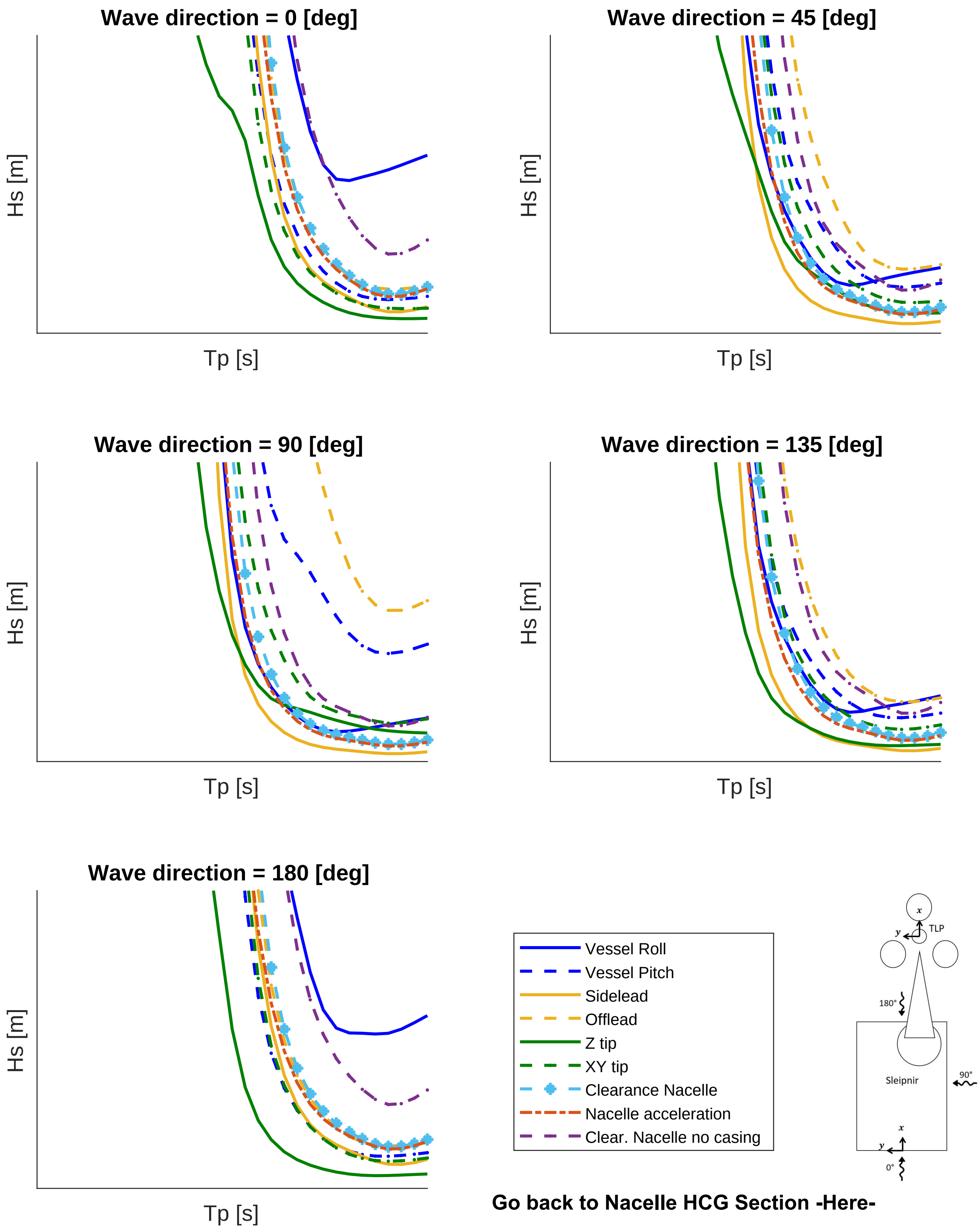

Go back to Nacelle HCG Section -Here-

See Grouped Operability Nacelle HCG -Here-

D.18. Operability - Hub Height 130 [m]

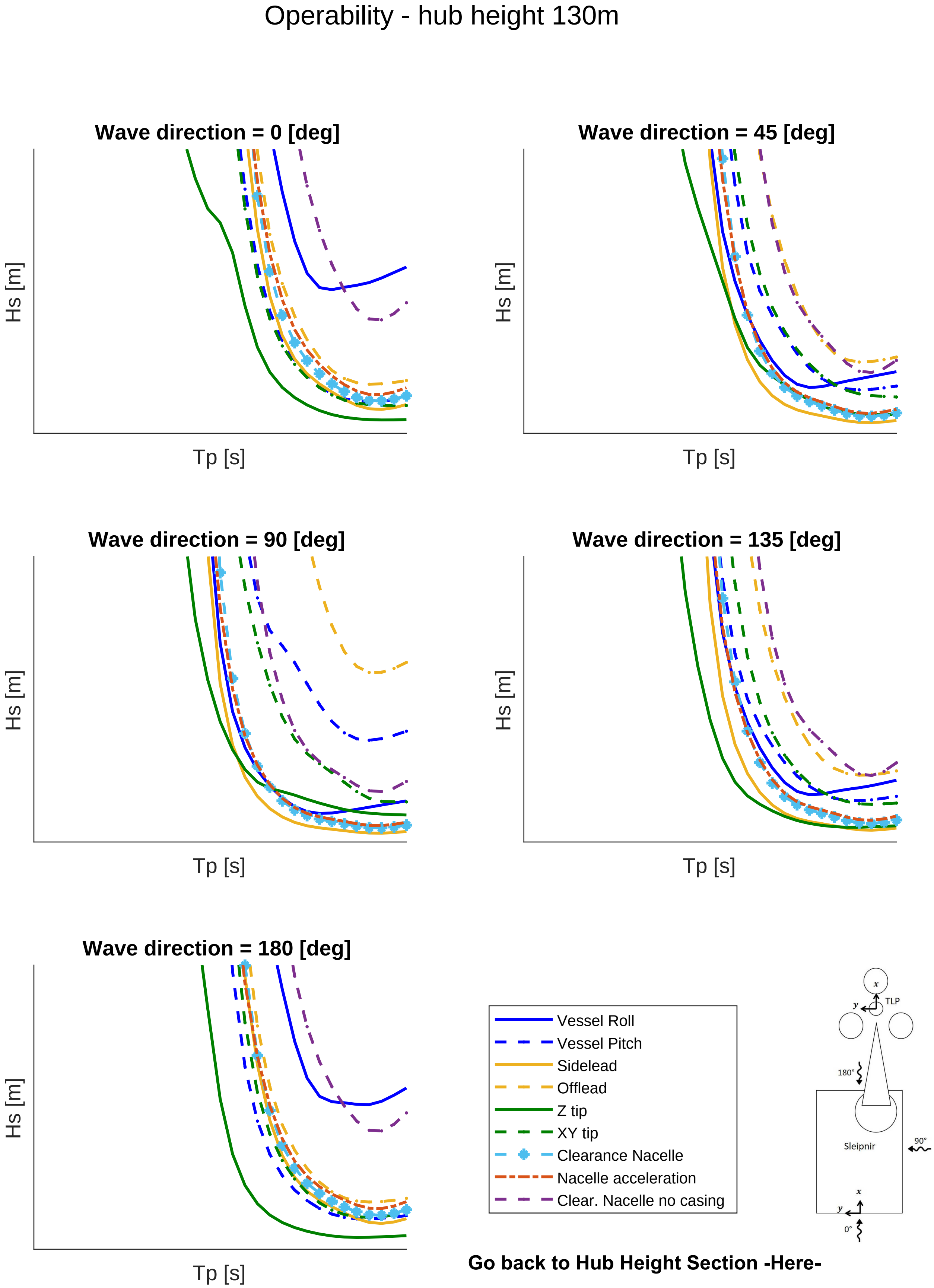

Operability - hub height 130m

Go back to Hub Height Section -Here-

See Grouped Operability Hub Height -Here-

D.19. Operability - Hub Height 150 [m]

Operability - hub height 150m

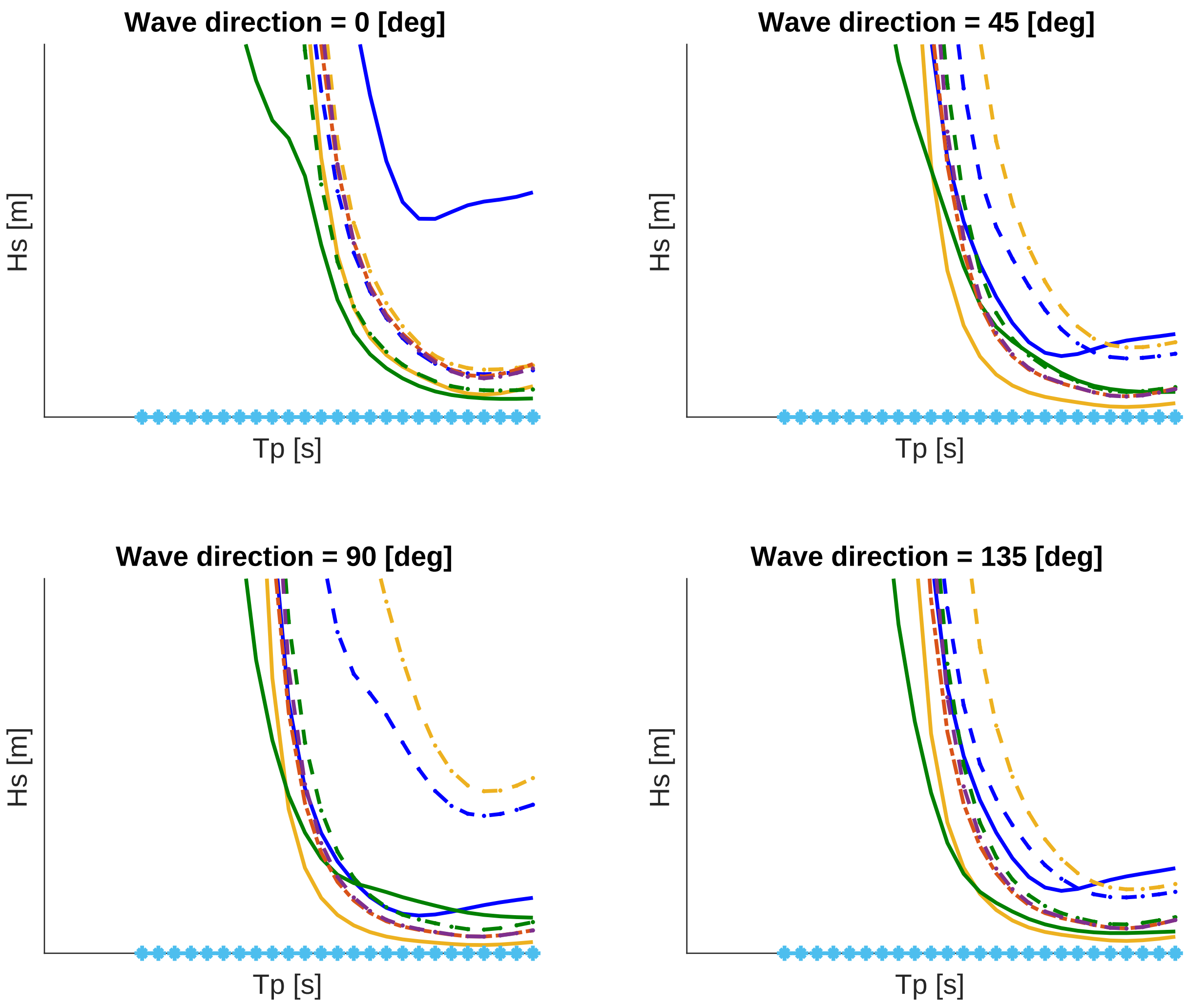

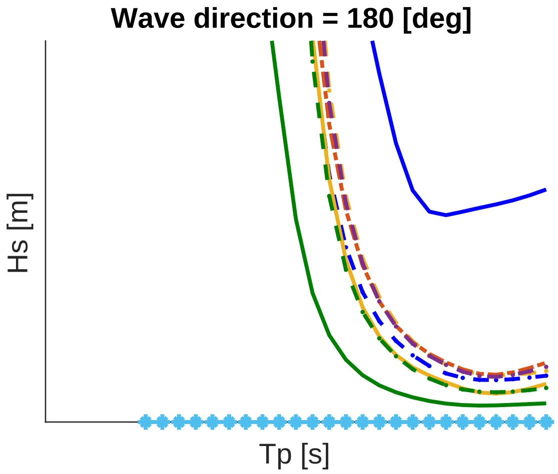

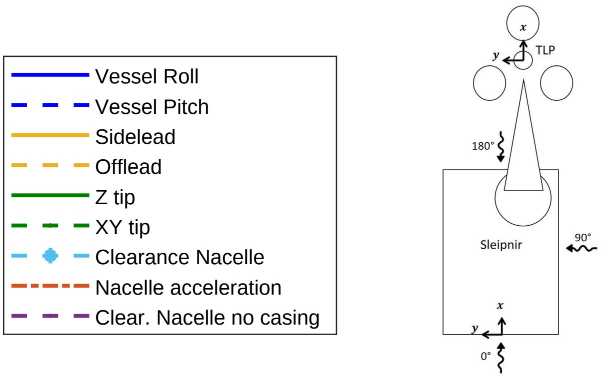

Go back to Hub Height Section -Here-

See Grouped Operability Hub Height -Here-

D.20. Operability - Tower VCG 35 [m]

Operability - tower vcg 35m

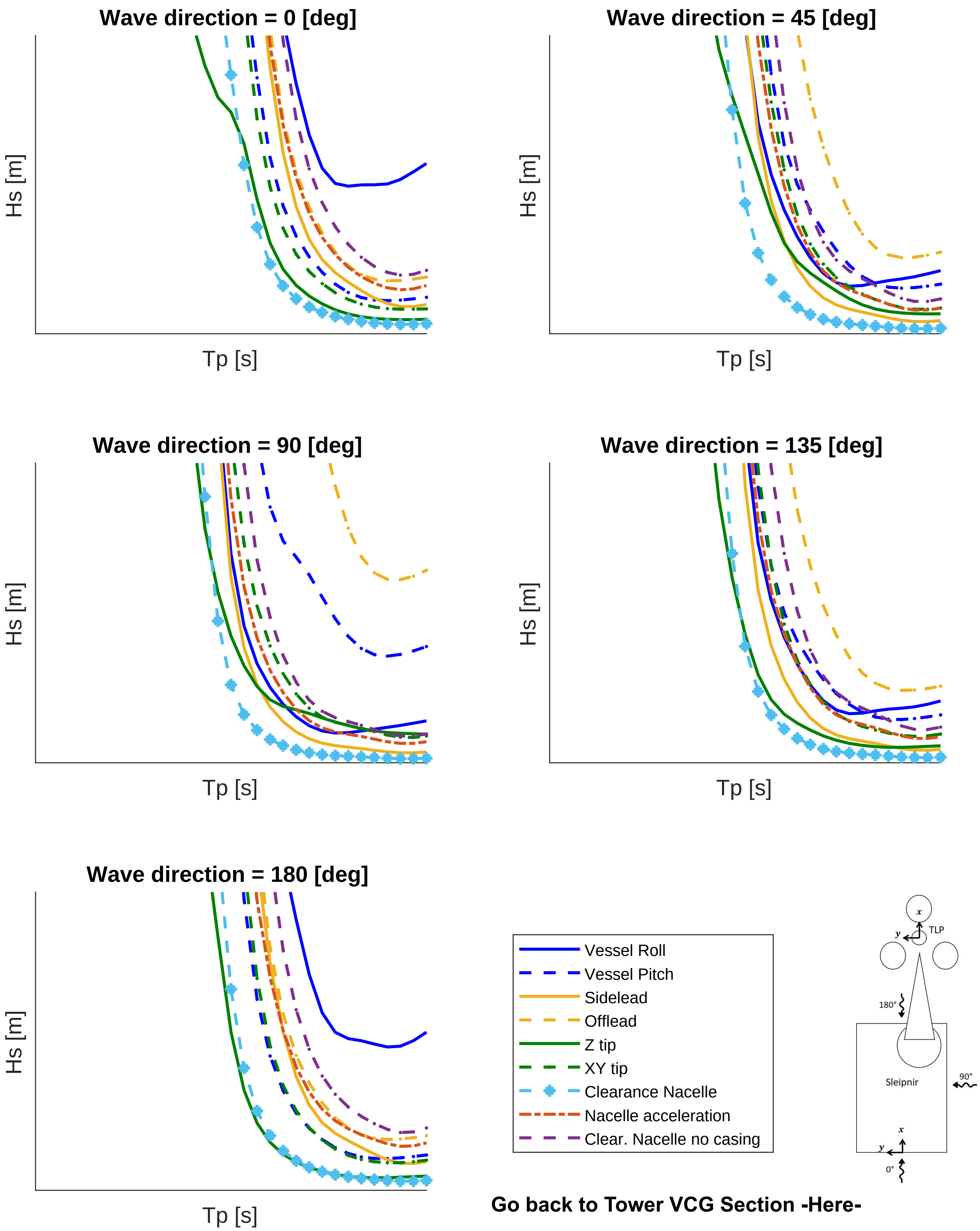

Go back to Tower VCG Section -Here-

See Grouped Operability Tower VCG -Here-

D.21. Operability - Tower VCG 65 [m]

Operability - tower vcg 65m

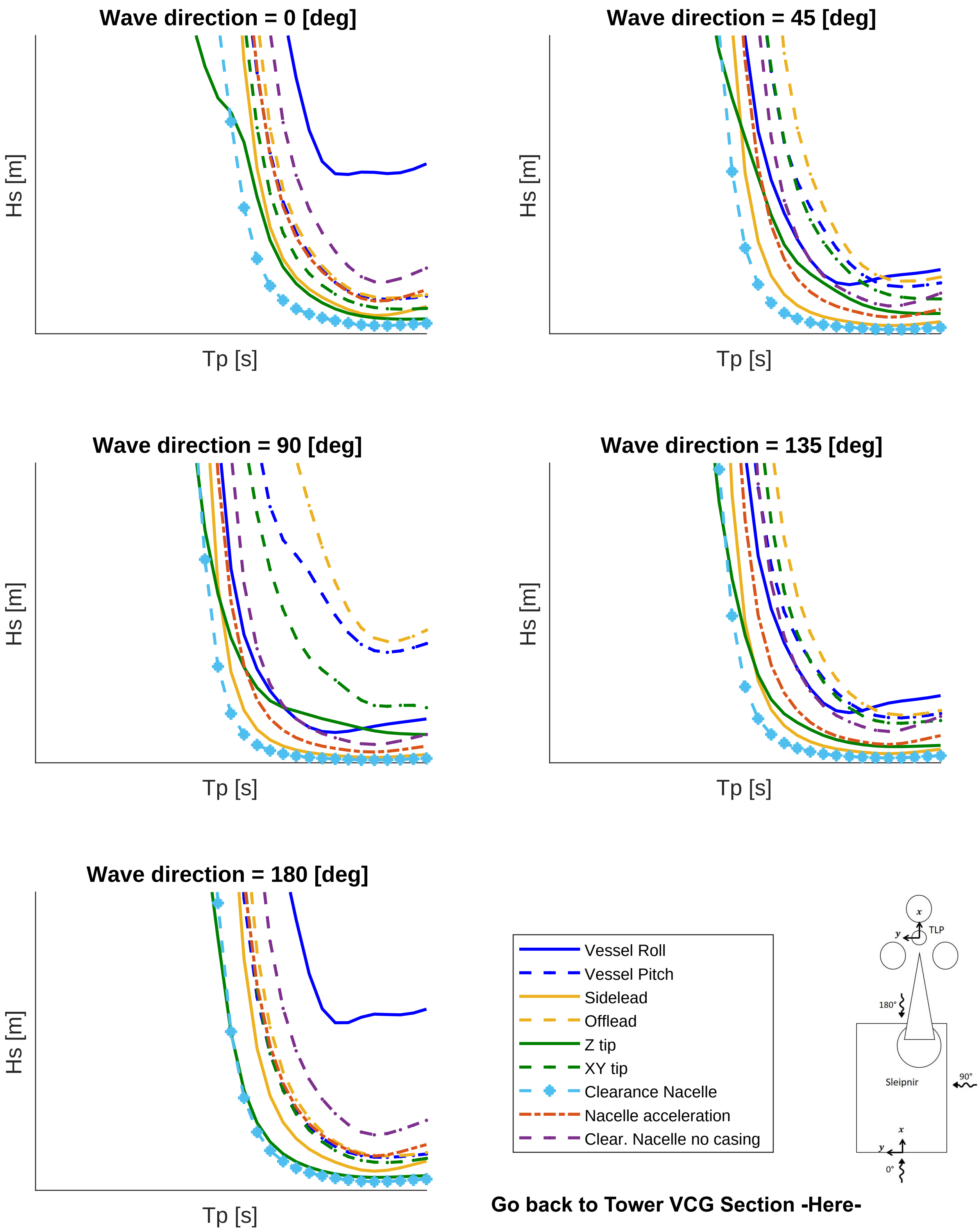

Go back to Tower VCG Section -Here-

See Grouped Operability Tower VCG -Here-

D.22. Operability - TLP Mass 2402 [t]

Operability - tlp mass 2402t

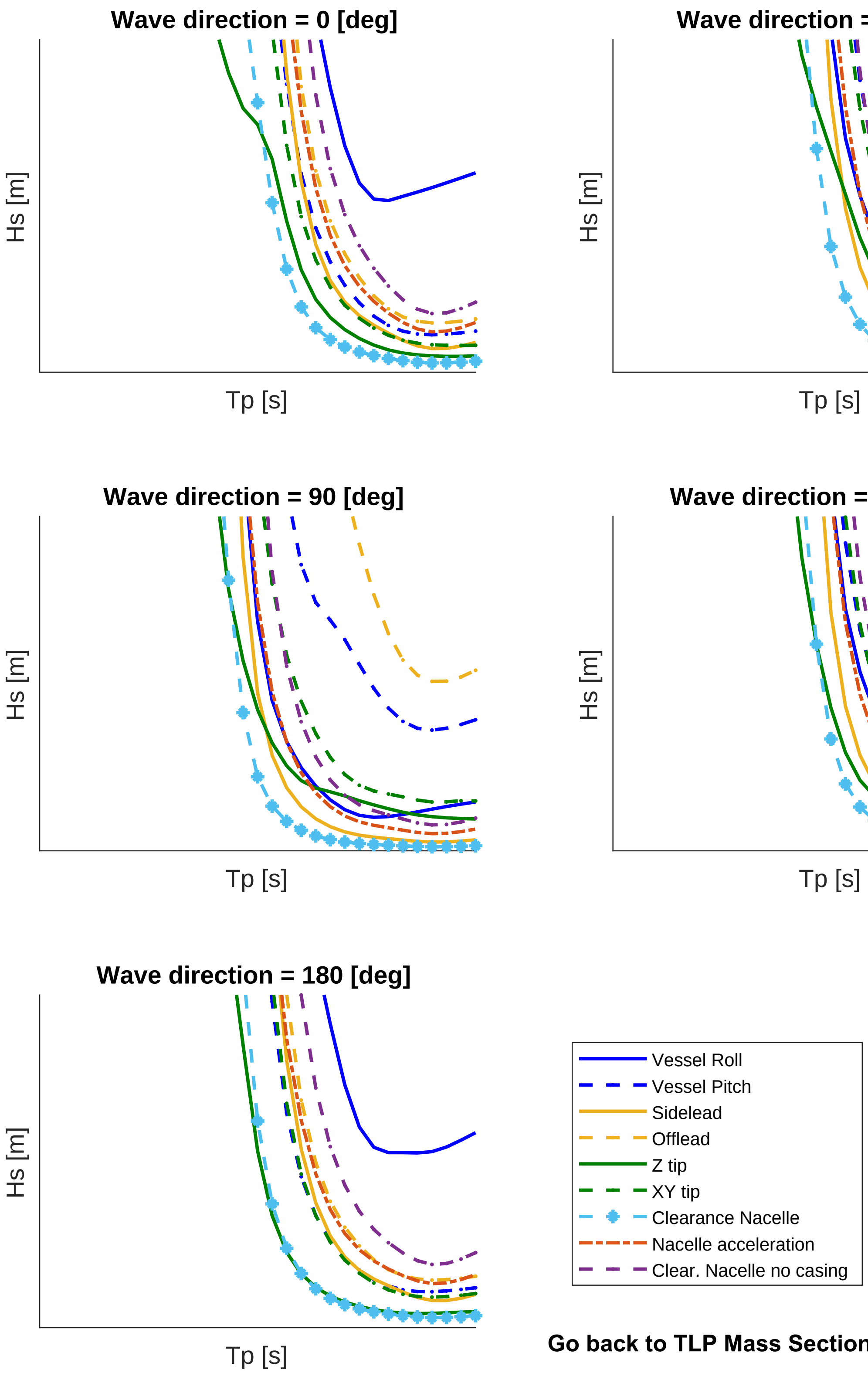

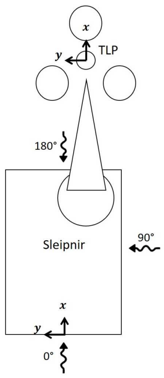

Go back to TLP Mass Section -Here-

See Grouped Operability TLP Mass -Here-

D.23. Operability - TLP Mass 3249 [t]

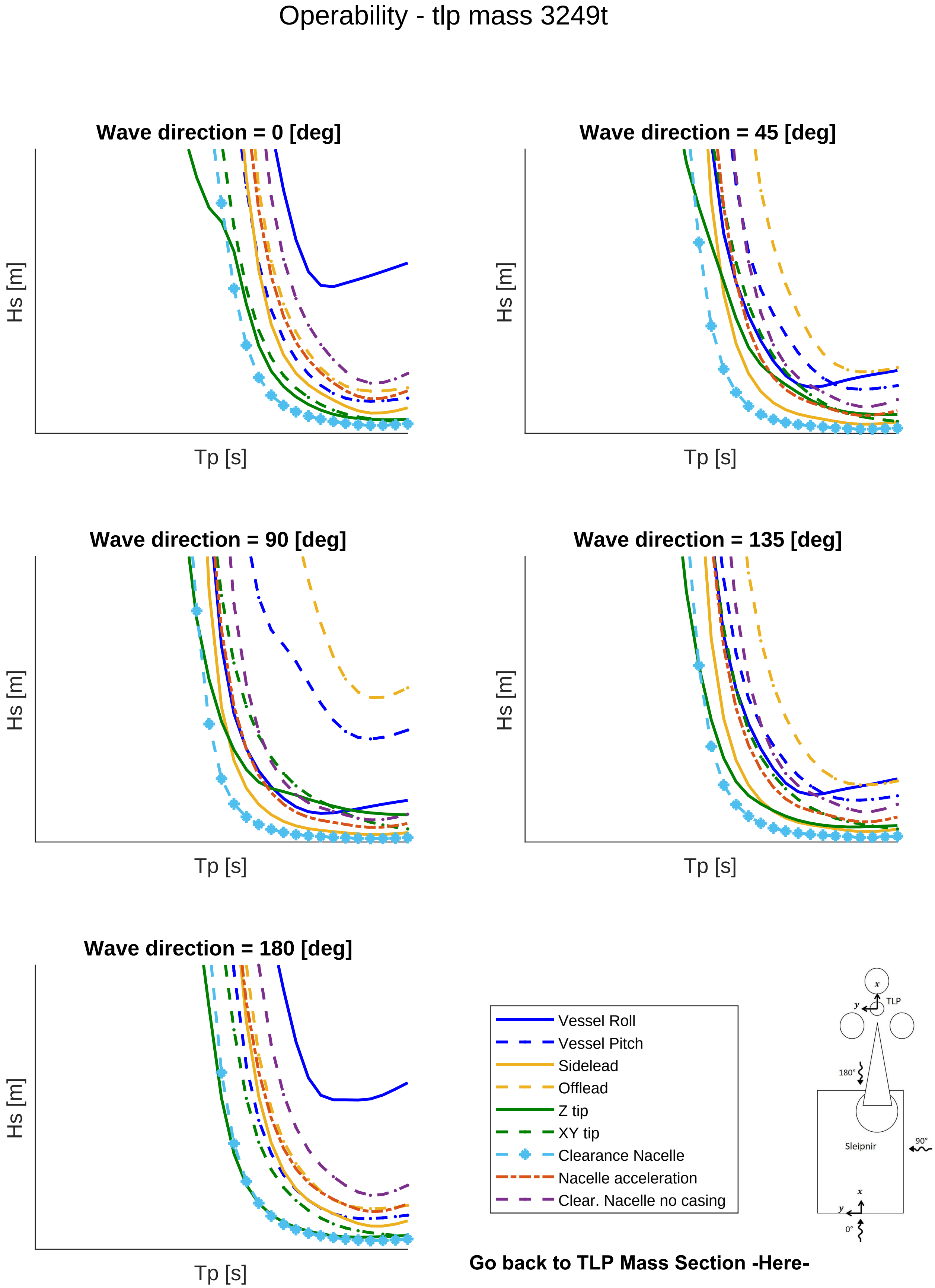

Go back to TLP Mass Section -Here-

See Grouped Operability TLP Mass -Here-

D.24. Operability - Tendon Angle 0 [deg]

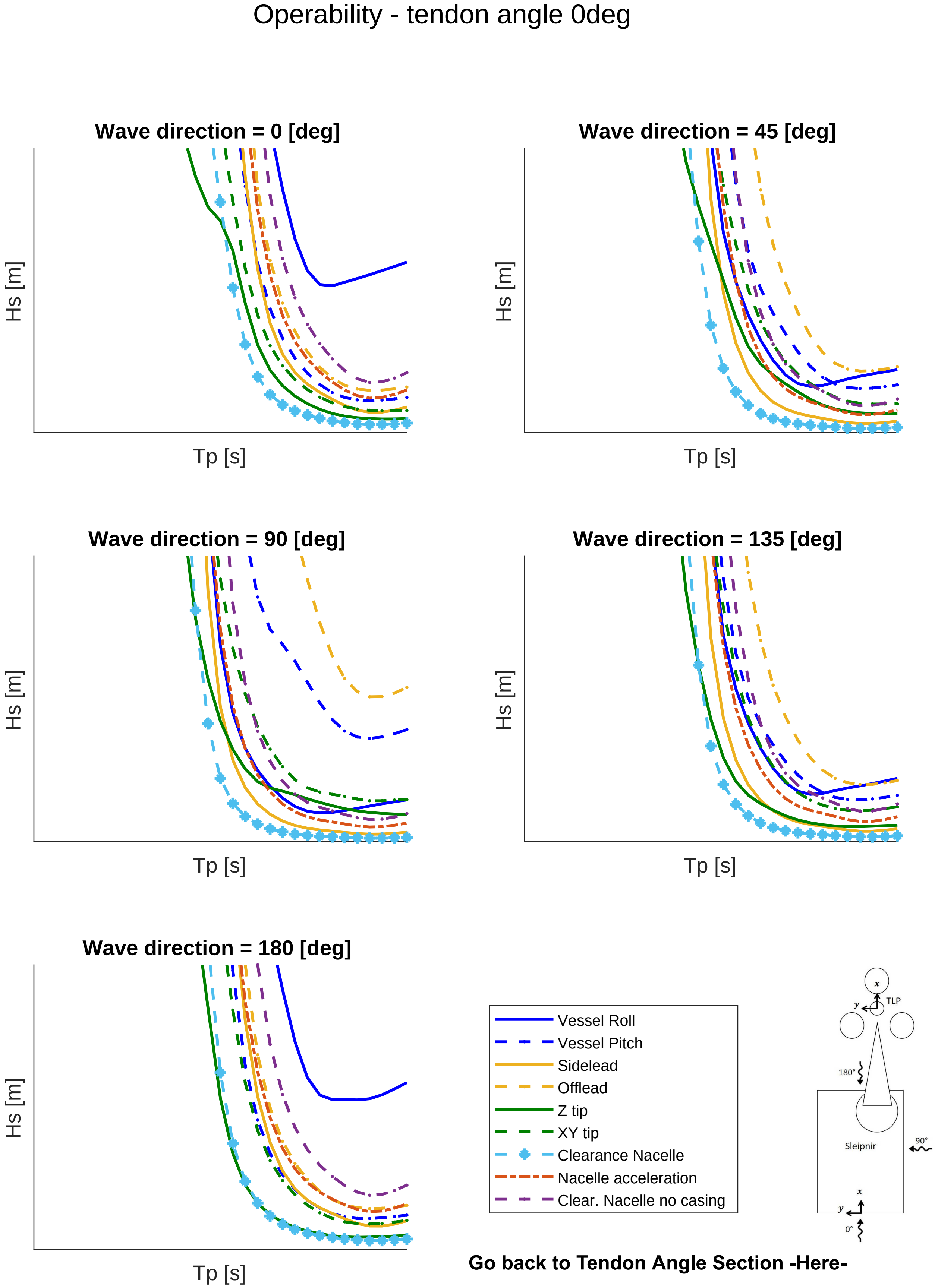

Go back to Tendon Angle Section -Here-

See Grouped Operability Tendon Angle -Here-

D.25. Operability - Tendon Angle 20 [deg]

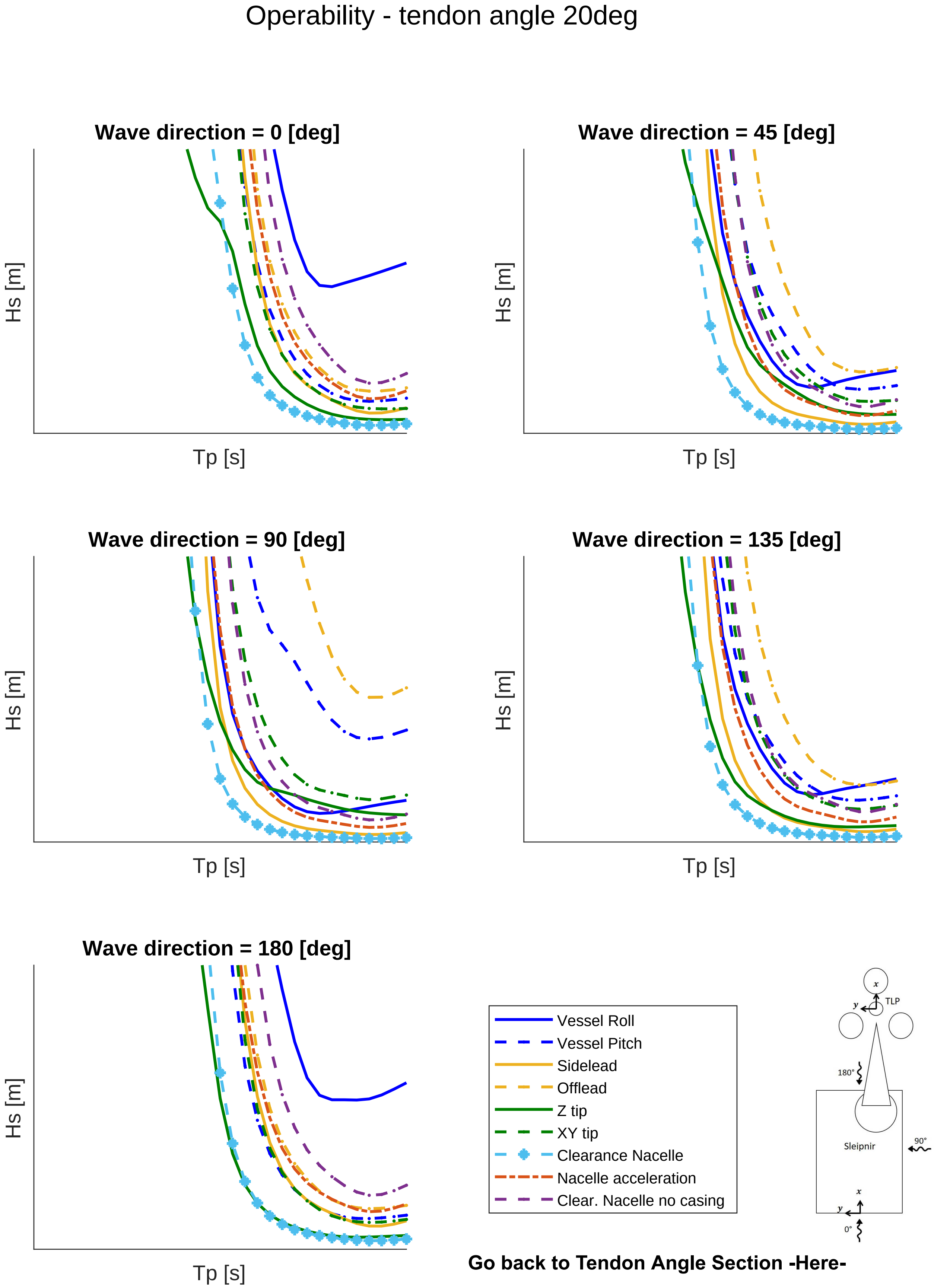

Go back to Tendon Angle Section -Here-

See Grouped Operability Tendon Angle -Here-

D.26. Operability - Mooring Line Stiffness 772e3 [kN]

Operability - ea moor dyn 772e3

Wave direction = 0 [deg]

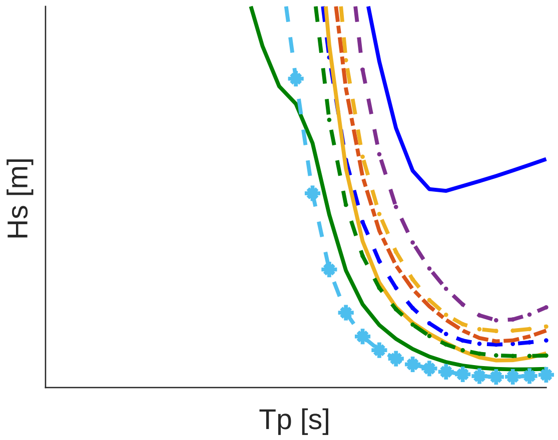

Wave direction = 45 [deg]

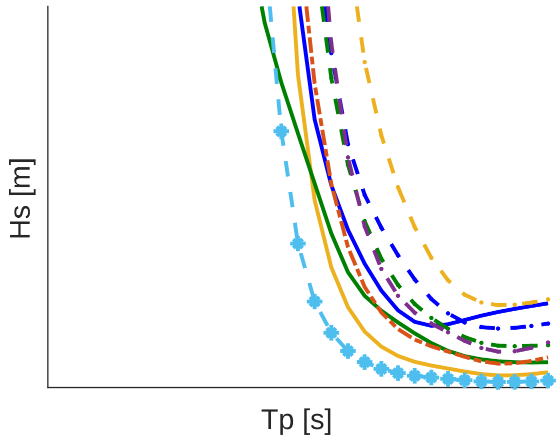

Wave direction = 90 [deg]

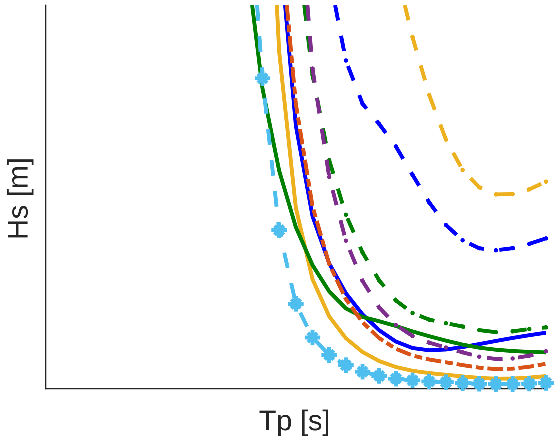

Wave direction = 135 [deg]

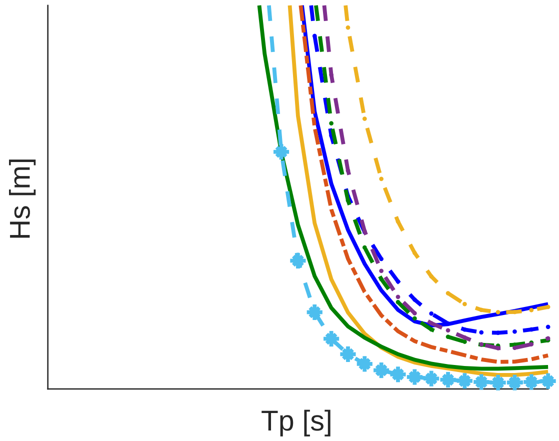

Wave direction = 180 [deg]

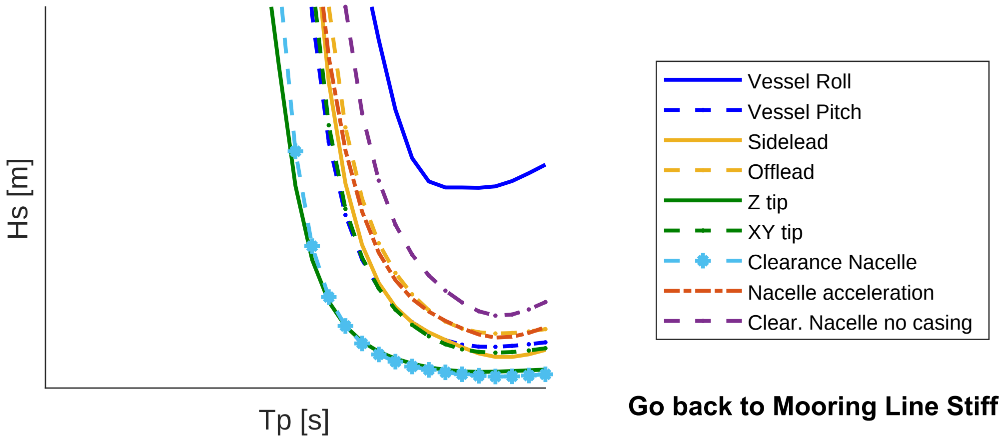

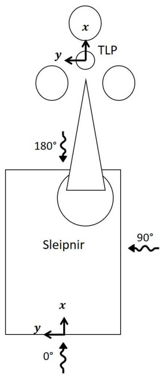

Go back to Mooring Line Stiffness Section -Here-

See Grouped Operability Mooring Line Stiffness -Here-

D.27. Operability - Mooring Line Stiffness 178e4 [kN]

Operability - ea moor carbon 178e4

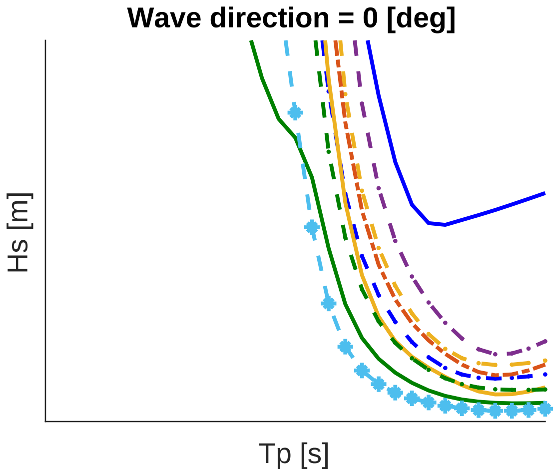
Wave direction = 0 [deg]

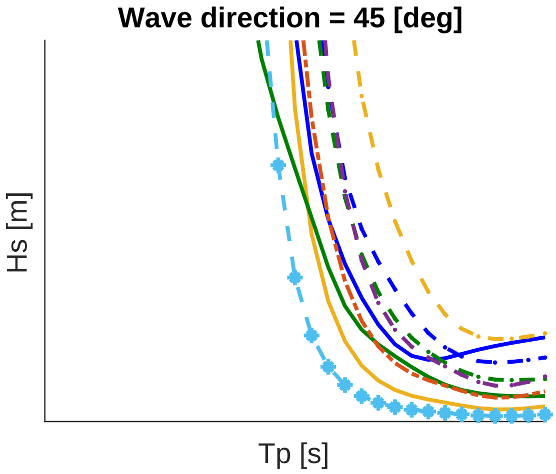
Wave direction = 45 [deg]

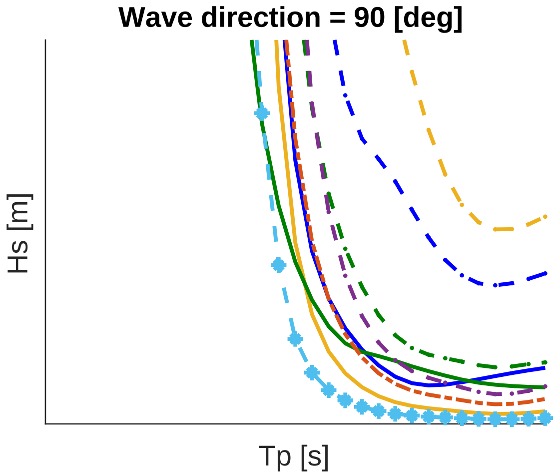
Wave direction = 90 [deg]

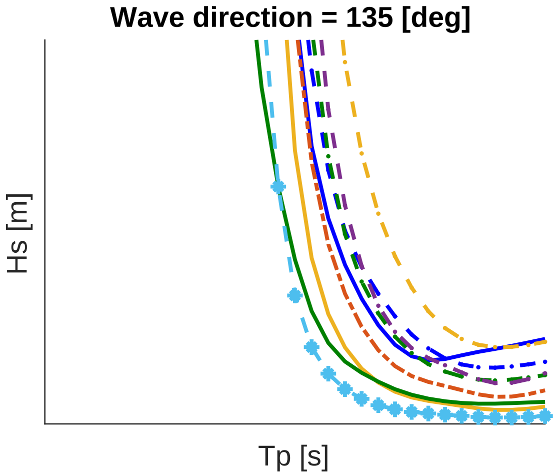
Wave direction = 135 [deg]

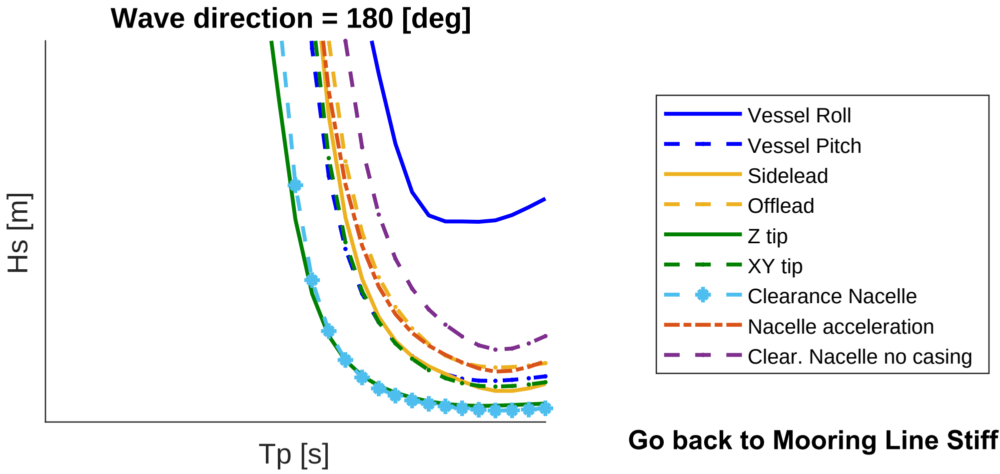
Wave direction = 180 [deg]

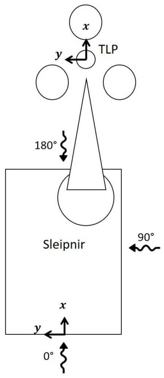

Go back to Mooring Line Stiffness Section -Here-

See Grouped Operability Mooring Line Stiffness -Here-

D.28. Operability - Slew Angle 55 [deg]

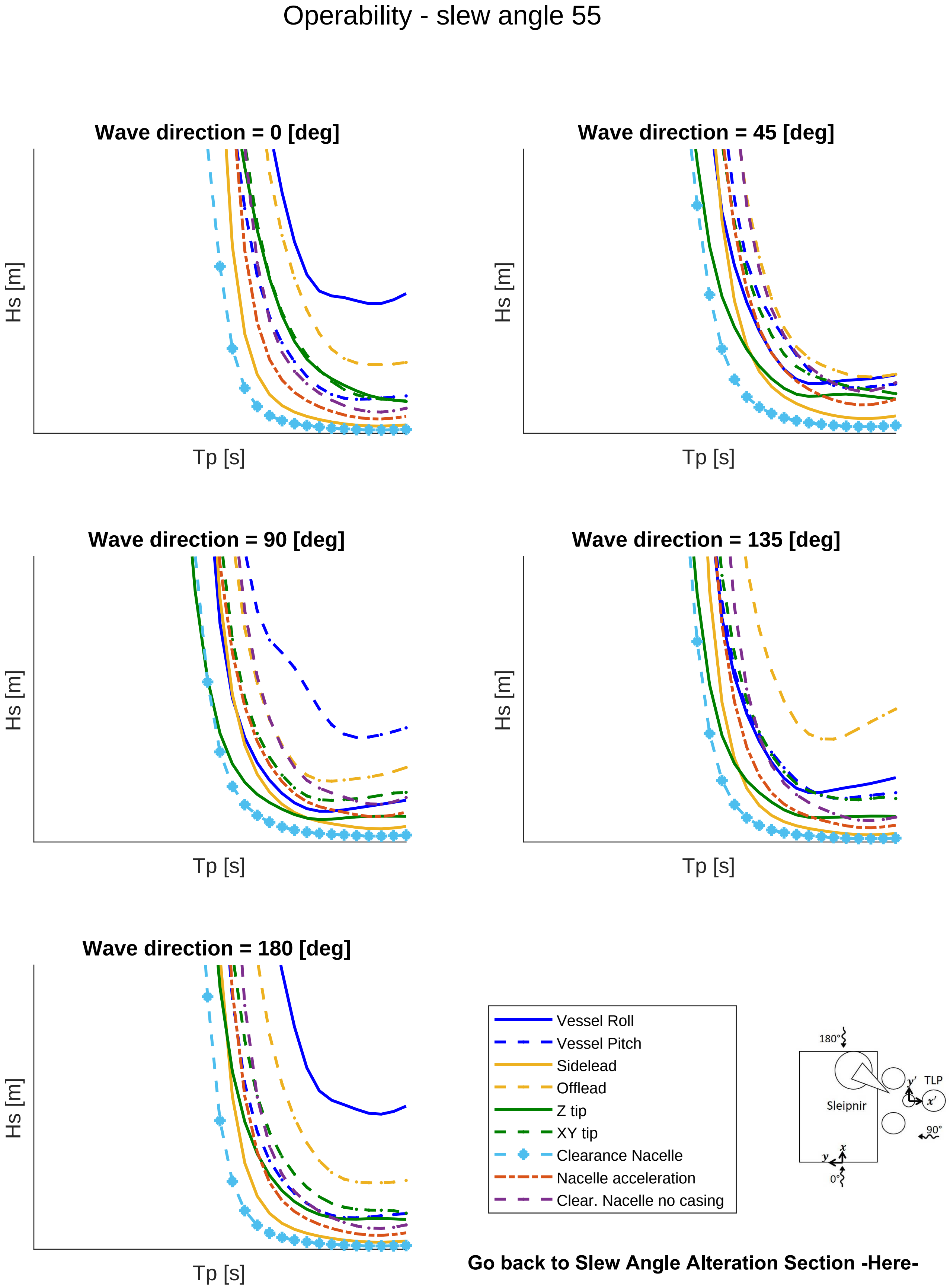

Go back to Slew Angle Alteration Section -Here-

See Grouped Operability Slew Angle Alteration -Here-

D.29. Operability - Slew Angle 217.5 [deg]

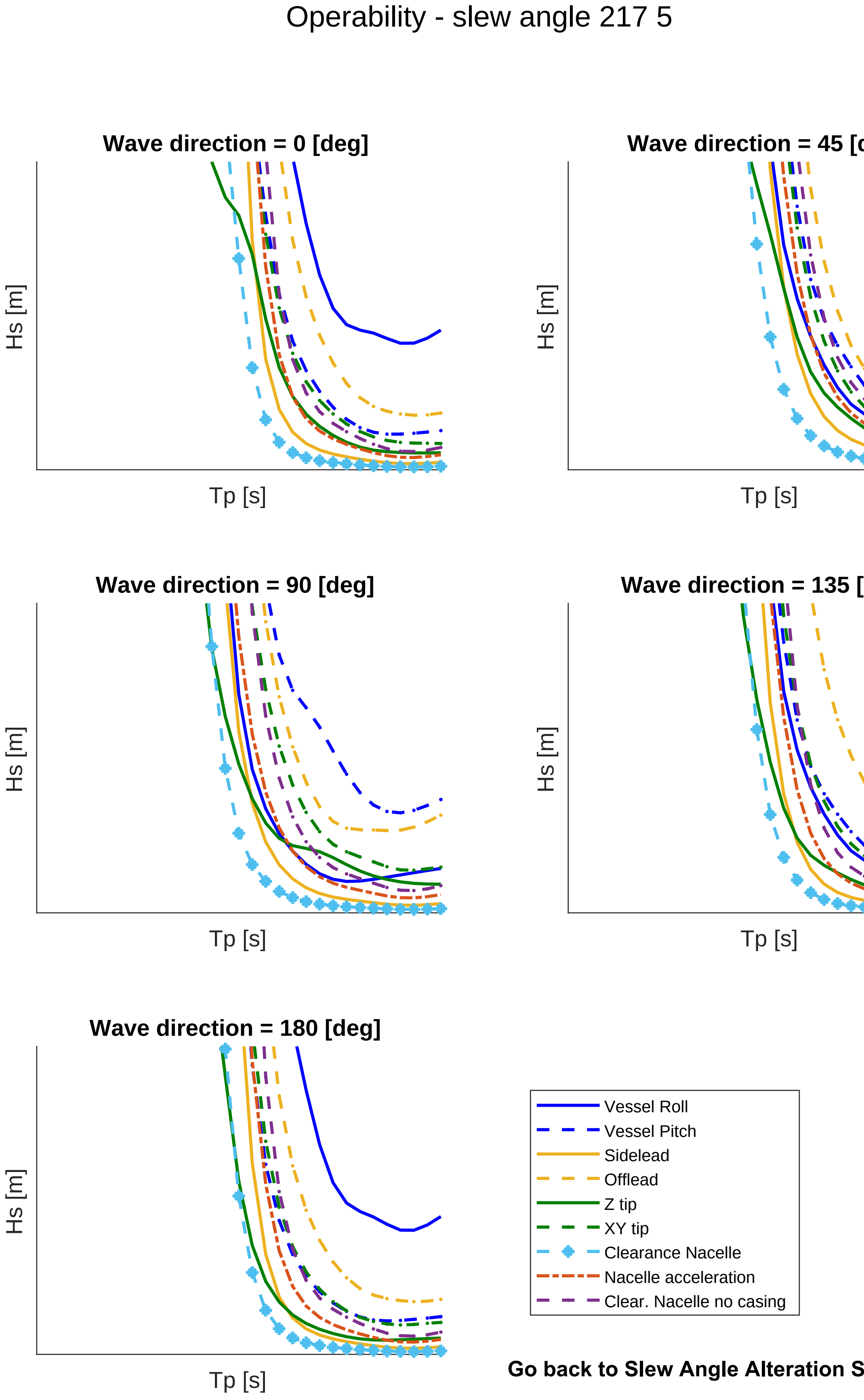

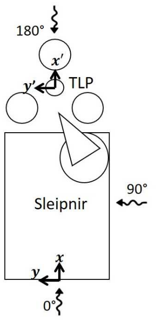

Go back to Slew Angle Alteration Section -Here-

See Grouped Operability Slew Angle Alteration -Here-

D.30. Operability - Rotated RNA+

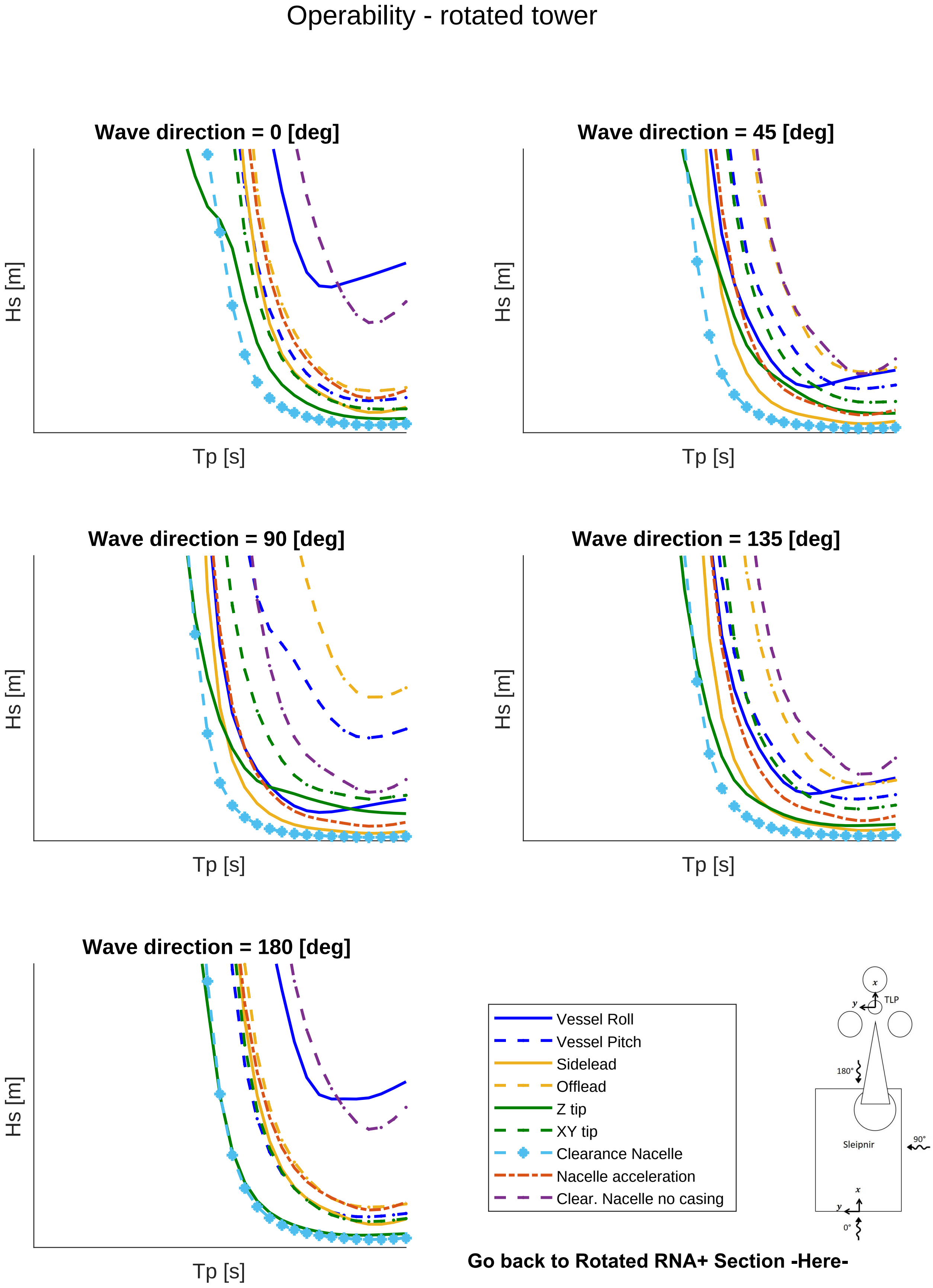

Go back to Rotated RNA+ Section -Here-

See Grouped Operability Rotated RNA+ -Here-

E

Maximum Responses

E.1. 3h SMPM Operability Limits

Table E.1: 3h SMPM values for H_s = $2m$ and $H_S T_p^2$ = 120 ms^2

Parameter	Vessel Roll [deg]	Vessel Pitch [deg]	Sidelead A [deg]	Offlead A [deg]	Z tip [m]	XY tip [m]	Clearance Nacelle [m]	Nacelle acceleration [m/s^2]	Clearance Nacelle 2 [m]
Base case									
Boom radius 50m									
Boom radius 40m									
Slew angle 135deg									
Slew angle 90deg									
Tugger damp 0									
Tugger damp 30									
Tugger angle 0									
Tugger angle neg25									
Offset liftupper 1m									
Offset liftupper 14m									
Tower mass 860t									
Tower mass 1060t									
Nah mass 620t									
Nah mass 1020t									
Nah cogx 0m									
Nah cogx neg 5.48m									
Hub height 130m									
Hub height 150m									
Tower vcg 35m									
Tower vcg 65m									
TLP mass 2402t									
TLP mass 3249t									
Tendon angle 0 deg									
Tendon angle 20 deg									
EA moor dyn 772e3 kN									
EA moor carbon 178e4 kN									

E.2. 3h SMPM All motions

Table E.2: 3h SMPM values for all motions

Parameter	Vessel Roll	Vessel Pitch	Sidelead A	Offlead A	Z tip	XY tip	Clearance Nacelle	Nacelle acceleration	Clearance Nacelle 2	
Base case	Difference relative to Base Case									
Boom radius 50m	-0.59	0.89	-12	-7.9	-4.8	-5.1	-7.2	-11	-7.2	%
Boom radius 40m	-0.79	1.9	-26	-15	-11	-11	-17	-24	-17	%
Slew angle 135deg	-4.8	1.6	71	-24	-9.8	-11	72	69	71	%
Slew angle 90deg	-14	6.8	55	-3.1	-9.6	-12	57	57	56	%
Tugger damp 0	-0.76	7.3	-0.62	142	6.5	142	0.27	-0.15	0.35	%
Tugger damp 30	-0.13	-1.3	0.51	-34	-1.6	-24	0.51	0.46	0.5	%
Tugger angle 0	0.23	-0.15	-0.12	-0.08	-0.15	0.08	-0.2	-0.12	-0.18	%
Tugger angle neg25	-5	1.1	-34	13	1	9.8	-34	-29	-33	%
Offset liftupper 1m	-0.95	1.7	-46	-21	0.66	28	-43	-49	-42	%
Offset liftupper 14m	-0.1	-5	92	35	-3.9	56	68	112	64	%
Tower mass 860t	0.22	0.57	-15	-7.1	0.58	-3.3	-7.4	-12	-7.6	%
Tower mass 1060t	1.1	0.43	-27	-13	0.48	-6.2	-14	-21	-15	%
Nah mass 620t	-1.2	1.2	-24	-18	0.69	-6.9	-16	-21	-16	%
Nah mass 1020t	1.7	-1.7	29	19	-1.2	5.8	19	25	19	%
Nah cogx 0m	0.23	-0.03	-1.2	0.13	-0.62	0.46	-6.1	-1	-4.9	%
Nah cogx neg 5.48m	-0.01	-0.18	-1.3	0.16	-1.3	0.71	-8.1	-2.3	-5.8	%
Hub height 130m	-0.95	1.2	-18	-14	1.3	-16	-8.7	-13	-10	%
Hub height 150m	0.1	-1.9	25	16	-1.9	47	13	21	14	%
Tower vcg 35m	-0.42	1.4	-28	-16	1	0.33	-21	-27	-20	%
Tower vcg 65m	1.3	-2.3	64	24	-1.8	1.6	43	60	42	%
TLP mass 2402t	-0.43	-0.15	-0.07	-0.1	-0.15	2.1	-0.08	-0.07	-0.08	%
TLP mass 3249t	-0.43	-0.15	-0.07	-0.1	-0.15	74	-0.08	-0.07	-0.08	%
Tendon angle 0 deg	-0.43	-0.15	-0.07	-0.1	-0.13	7.7	-0.08	-0.07	-0.08	%
Tendon angle 20 deg	-0.43	-0.15	-0.07	-0.1	-0.17	-3.3	-0.08	-0.07	-0.08	%
EA moor dyn 772e3 kN	-0.43	-0.15	-0.07	-0.1	-0.36	0.21	-0.08	-0.07	-0.08	%
EA moor carbon 178e4 kN	-0.43	-0.15	-0.07	-0.1	-0.11	-0.08	-0.08	-0.07	-0.08	%

F

Grouped Operability per Parameter

F.1. Grouped Operability - Boom Radius

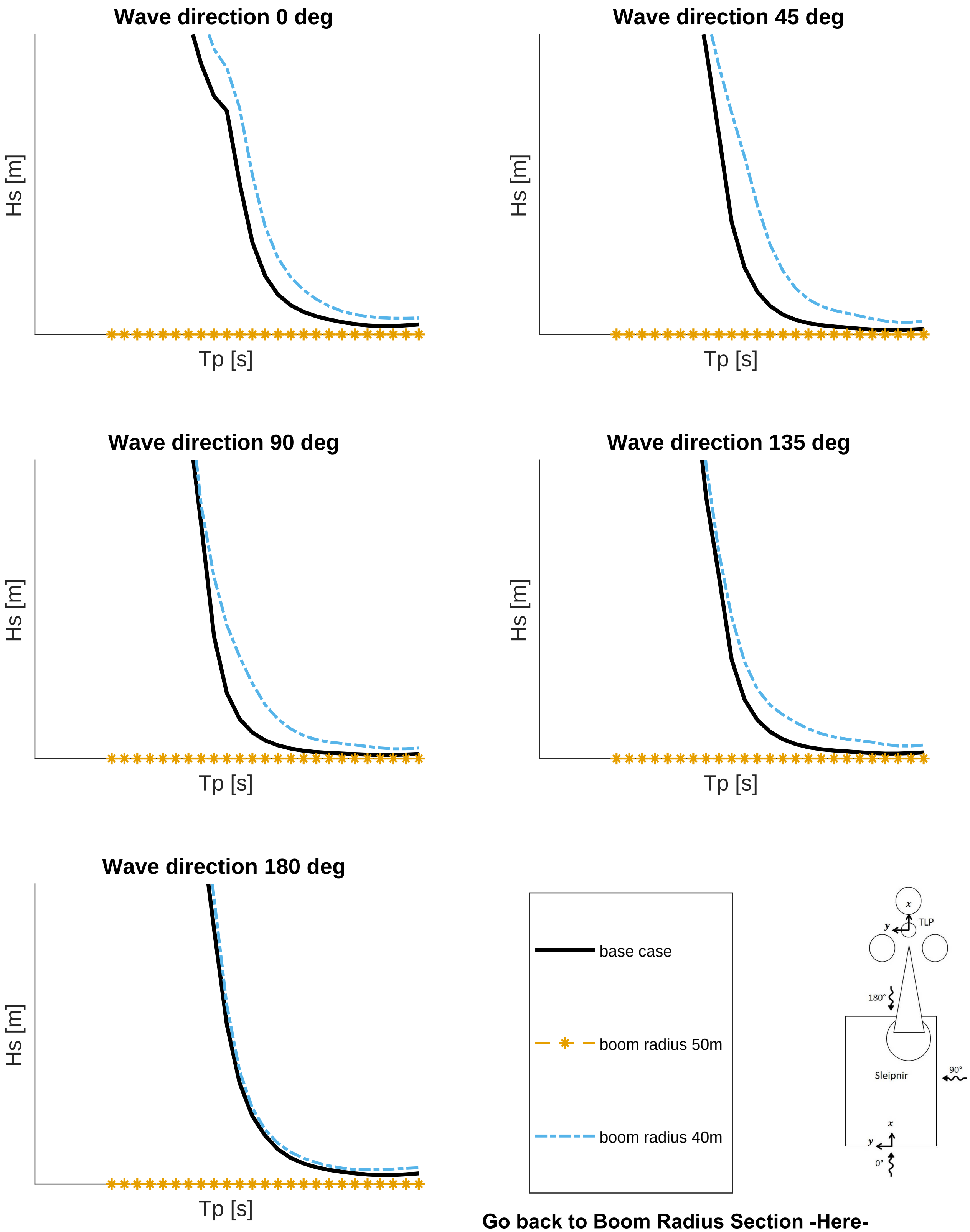
Operability - Boom Radius

Go back to Boom Radius Section -Here-

See Operability Boom radius 50 [m] -Here-

See Operability Boom radius 40 [m] -Here-

F.2. Grouped Operability - Slew Angle

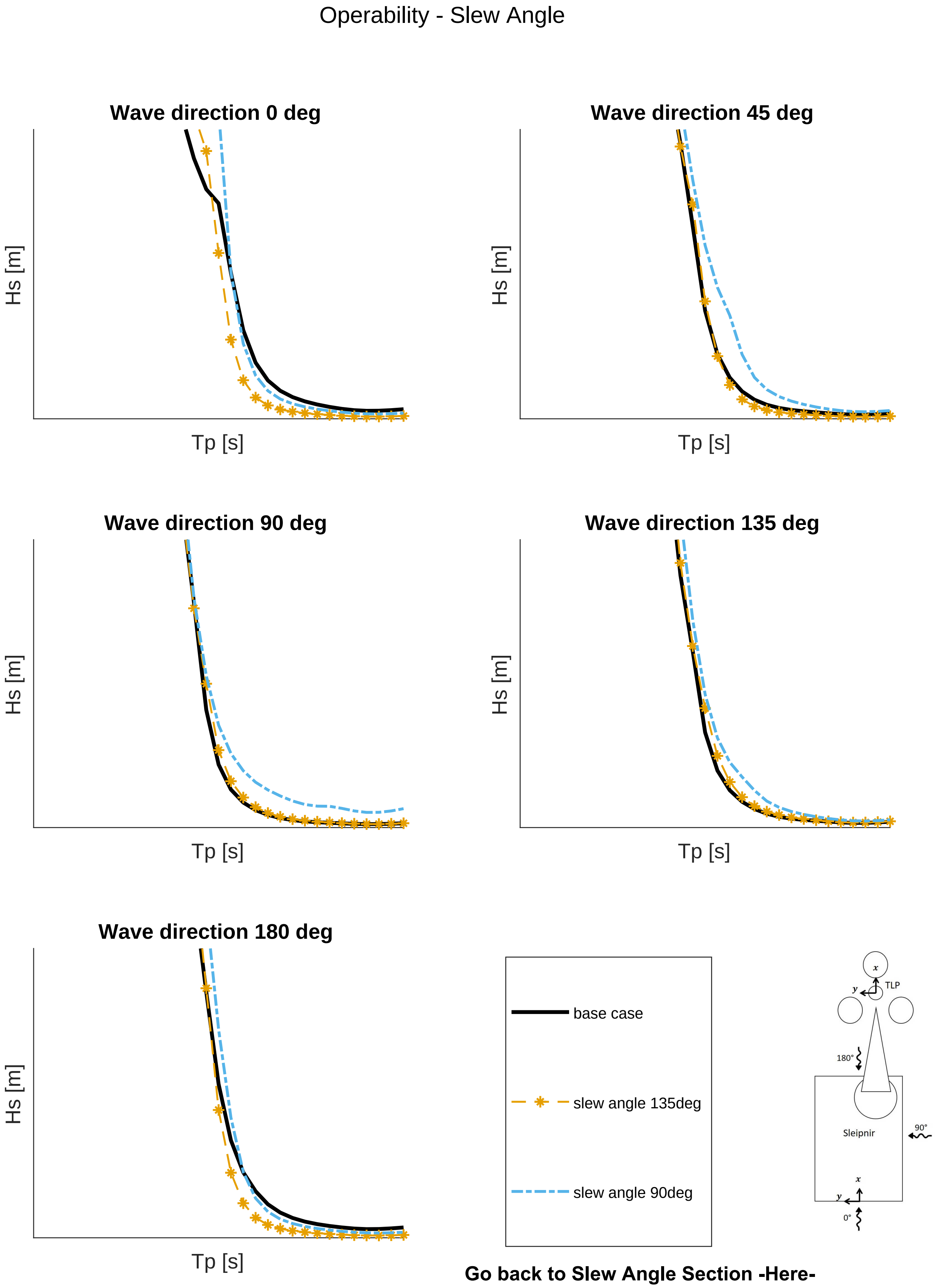

Go back to Slew Angle Section -Here-

See Operability Slew Angle 135 [deg] -Here-

See Operability Slew Angle 90 [deg] -Here-

F.3. Grouped Operability - Tugger Damping

Operability - Tugger Damping

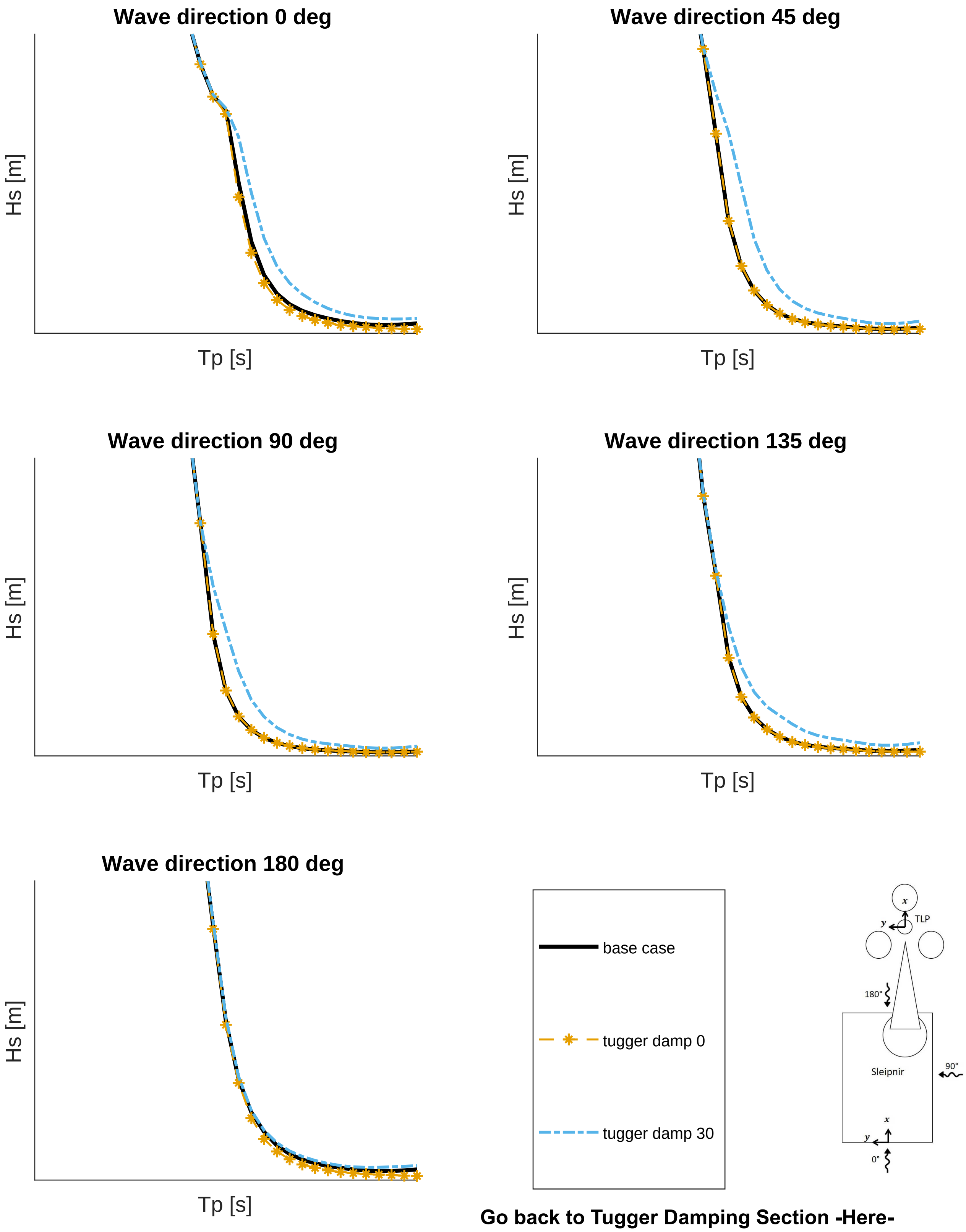

Go back to Tugger Damping Section -Here-

See Operability Tugger Damping 0 [t*s/m] -Here-

See Operability Tugger Damping 30 [t*s/m] -Here-

F.4. Grouped Operability - Tugger Line Angle

Operability - Tugger Line Angle

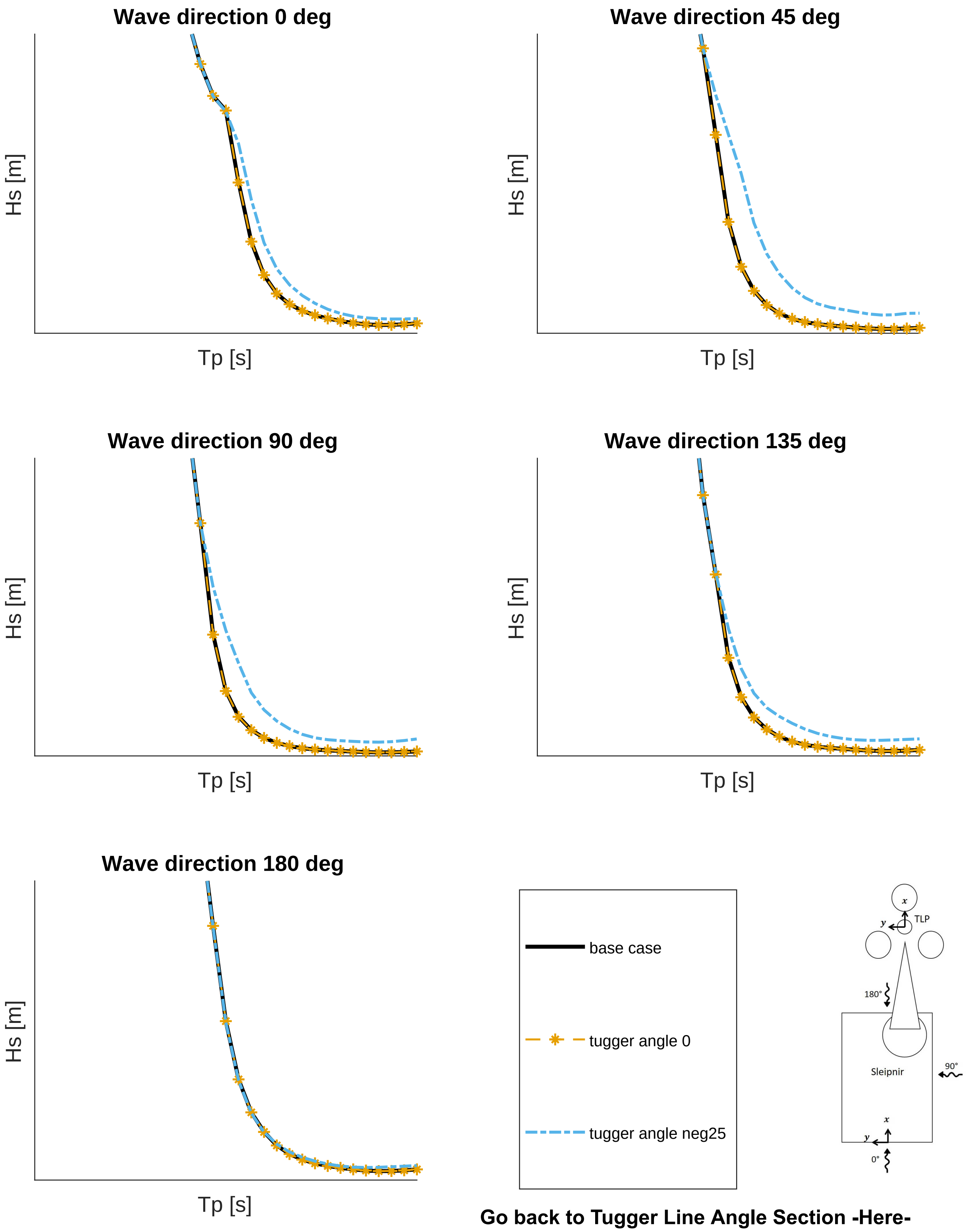

Go back to Tugger Line Angle Section -Here-

See Operability Tugger Line Angle 0 [deg] -Here-

See Operability Tugger Line Angle -25 [deg] -Here-

F.5. Grouped Operability - Upper Lifting Tool Offset

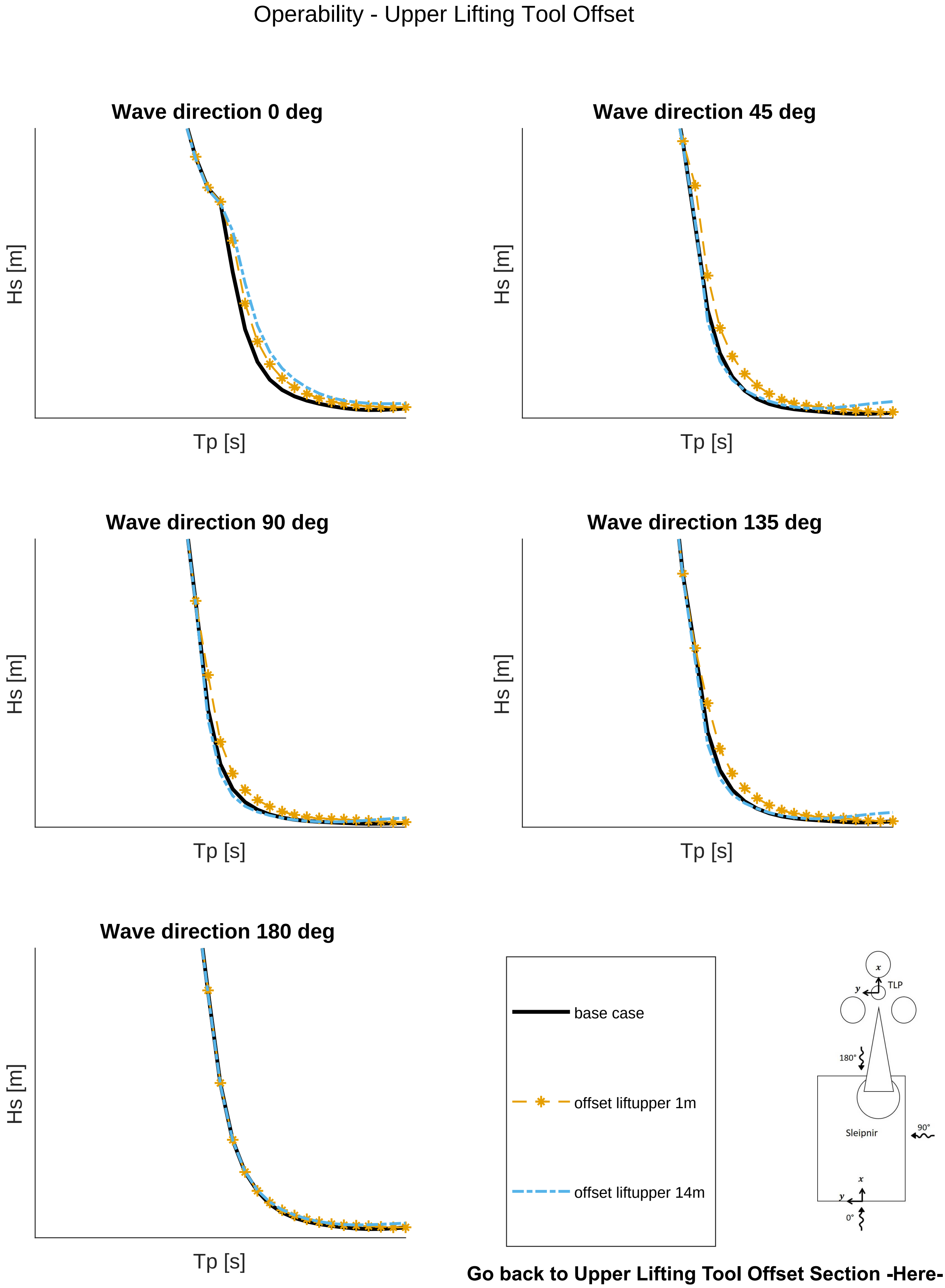

Go back to Upper Lifting Tool Offset Section -Here-

See Operability Upper Lifting Tool Offset 1 [m] -Here-

See Operability Upper Lifting Tool Offset 14 [m] -Here-

F.6. Grouped Operability - Tower Mass

Operability - Tower Mass

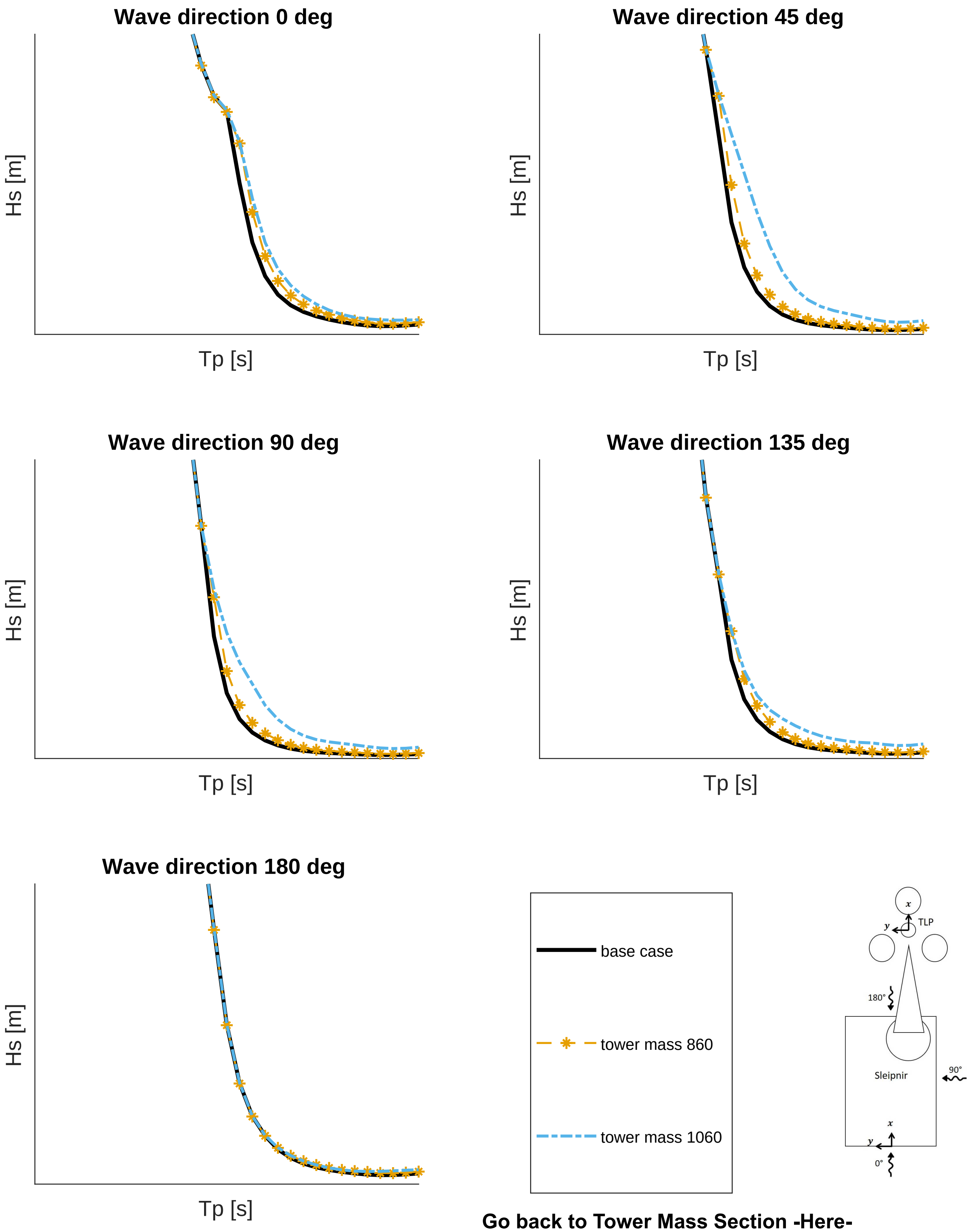

Go back to Tower Mass Section -Here-

See Operability Tower Mass 860 [t] -Here-

See Operability Tower Mass 1060 [t] -Here-

F.7. Grouped Operability - Nacelle Mass

Operability - Nacelle Mass

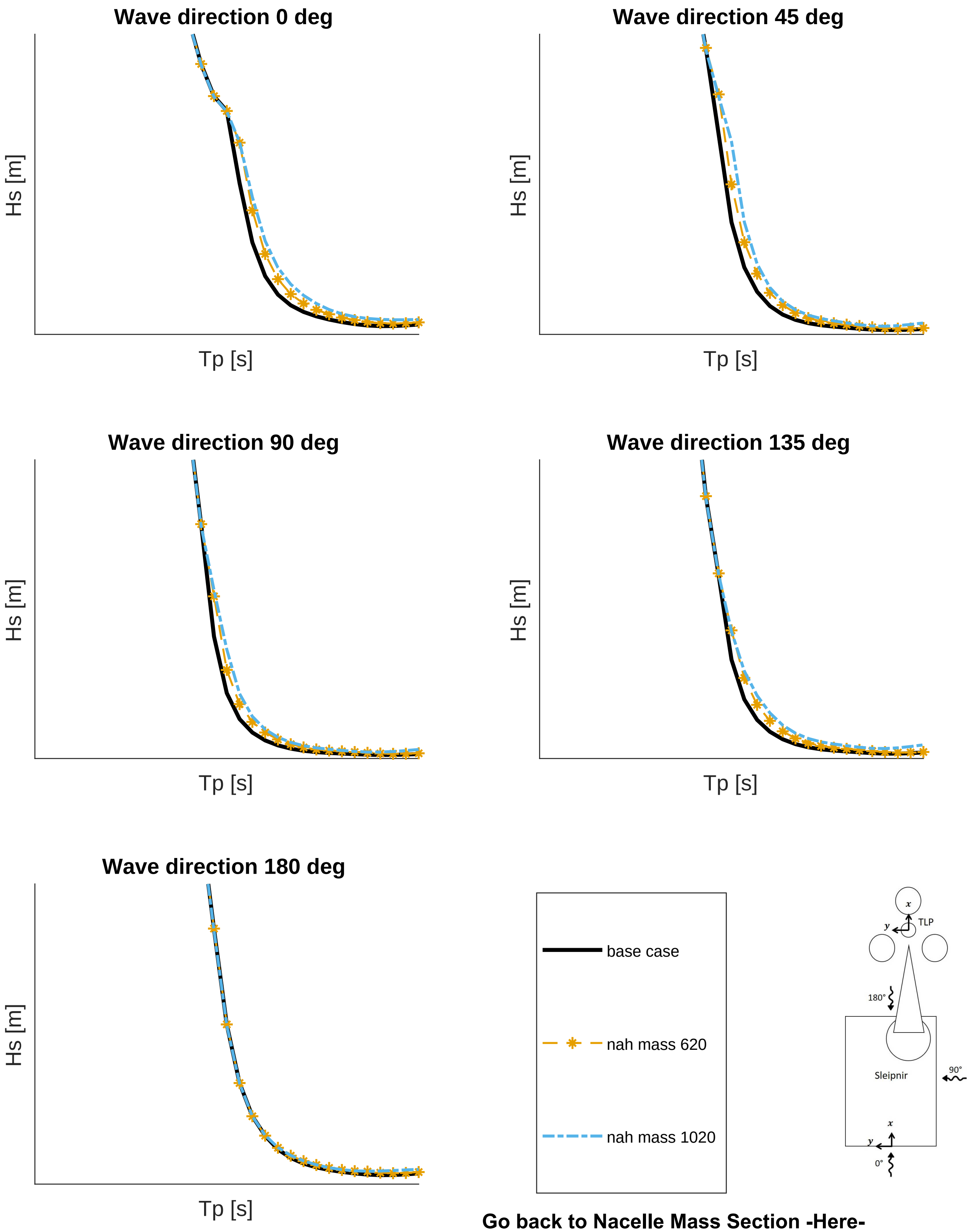

Go back to Nacelle Mass Section -Here-

See Operability Nacelle Mass 620 [t] -Here-

See Operability Nacelle Mass 1020 [t] -Here-

F.8. Grouped Operability - Nacelle HCG

Operability - Nacelle HCG

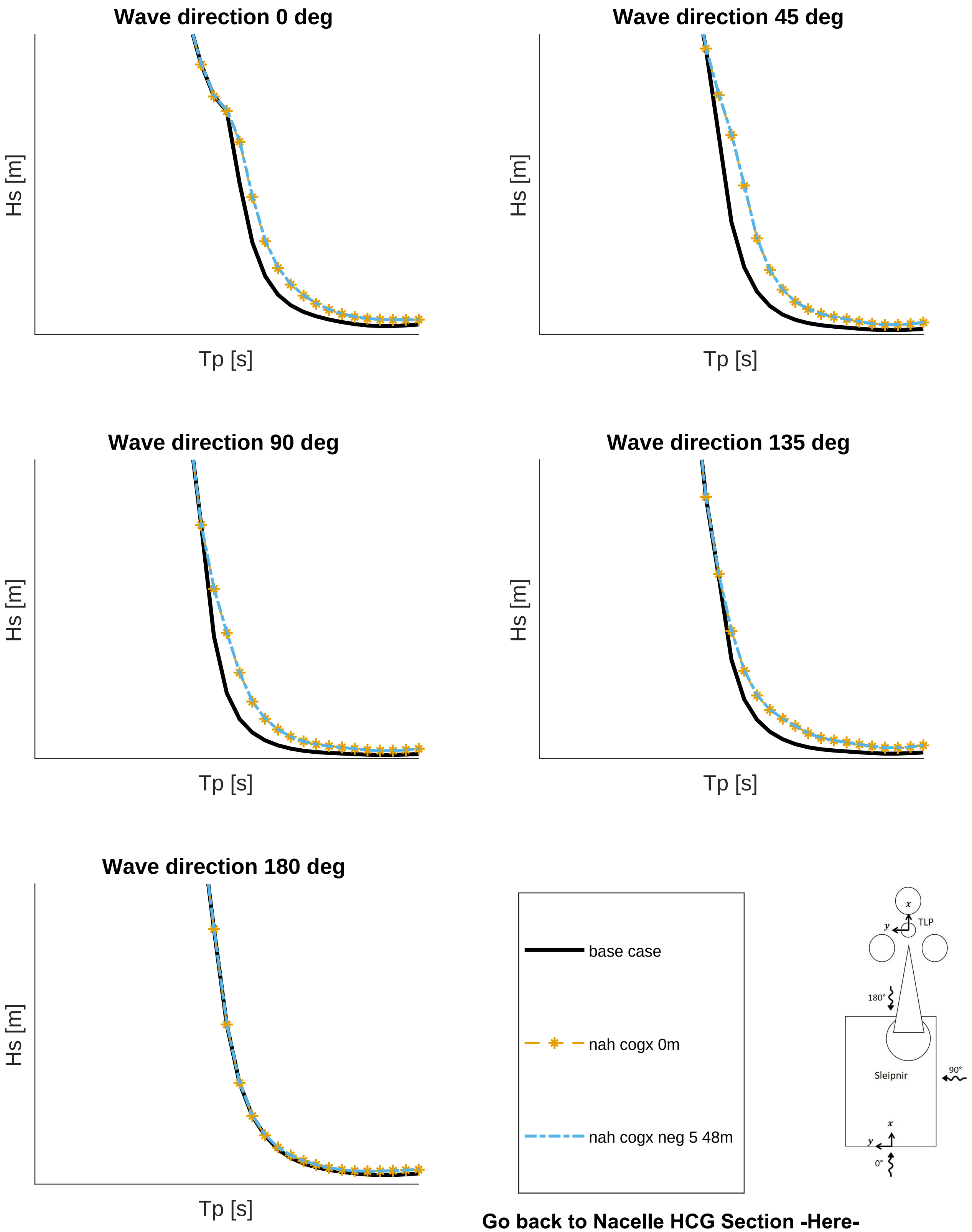

Go back to Nacelle HCG Section -Here-

See Operability Nacelle HCG 0 [m] -Here-

See Operability Nacelle HCG 5.48 [m] -Here-

F.9. Grouped Operability - Hub Height

Operability - Hub Height

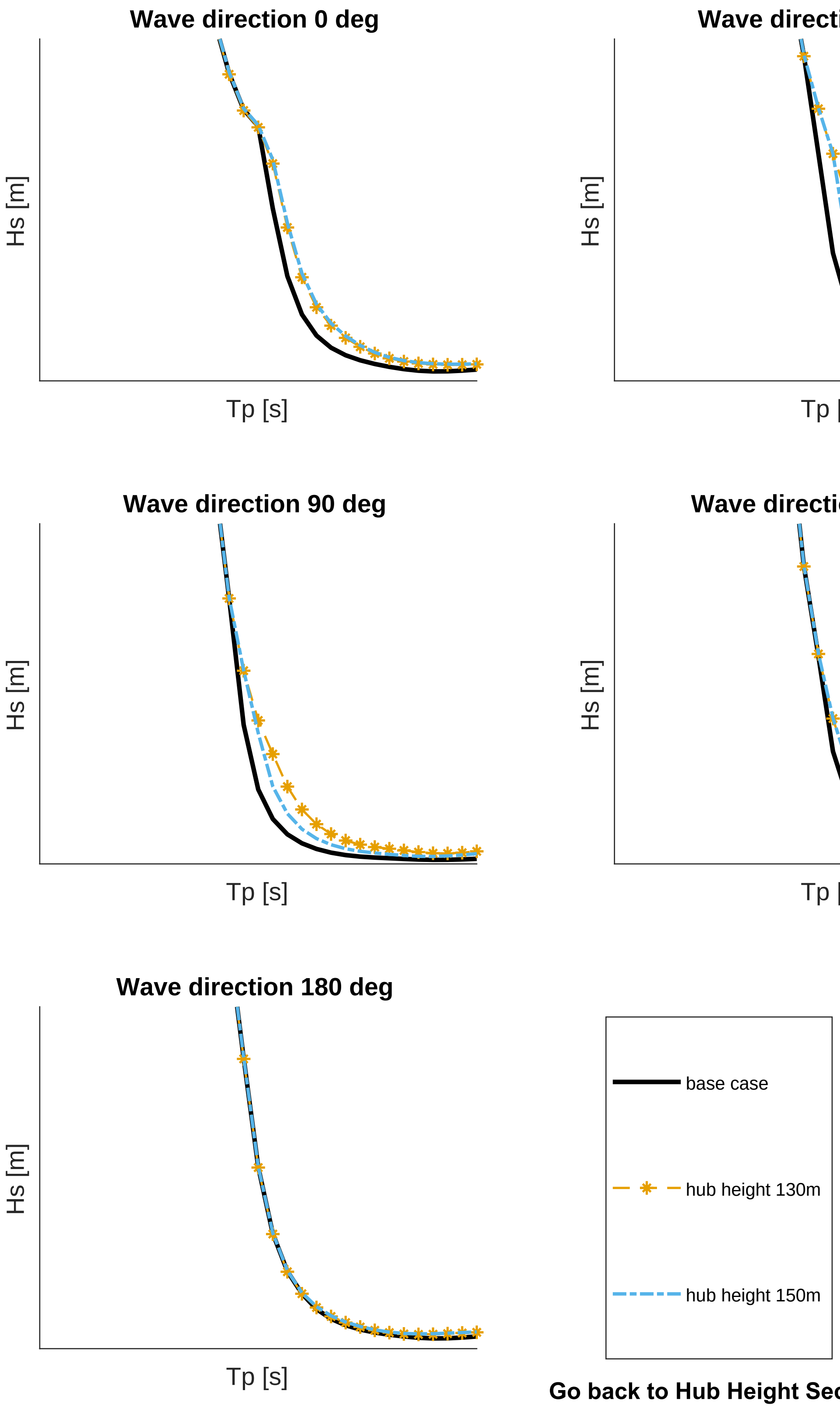

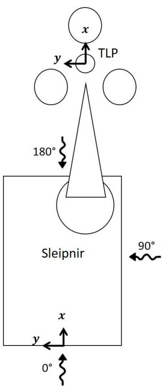

Go back to Hub Height Section -Here-

See Operability Hub Height 130 [m] -Here-

See Operability Hub Height 150 [m] -Here-

F.10. Grouped Operability - Tower VCG

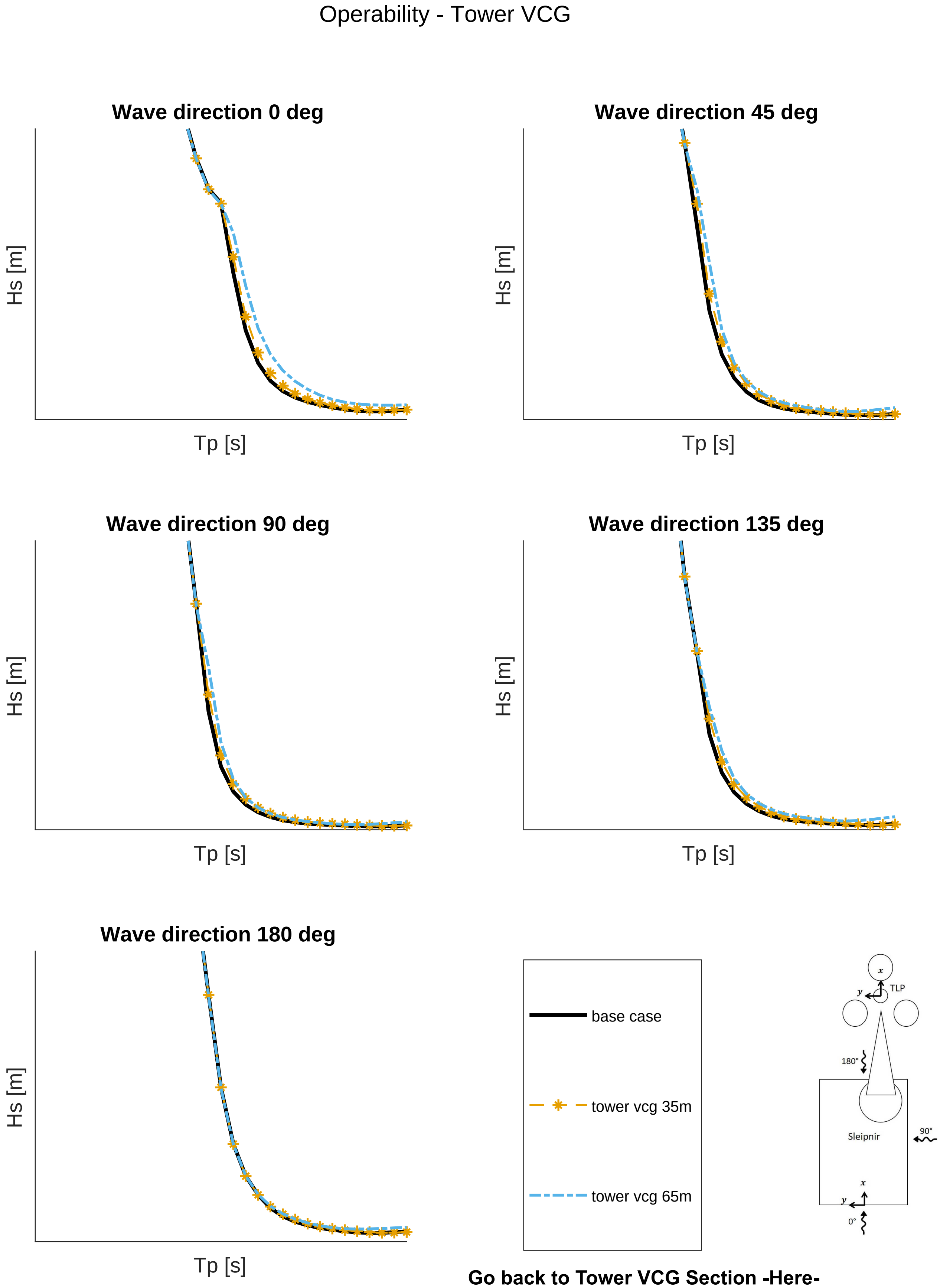

Go back to Tower VCG Section -Here-

See Operability Tower VCG 35 [m] -Here-

See Operability Tower VCG 65 [m] -Here-

F.11. Grouped Operability - TLP Mass

Operability - TLP Mass

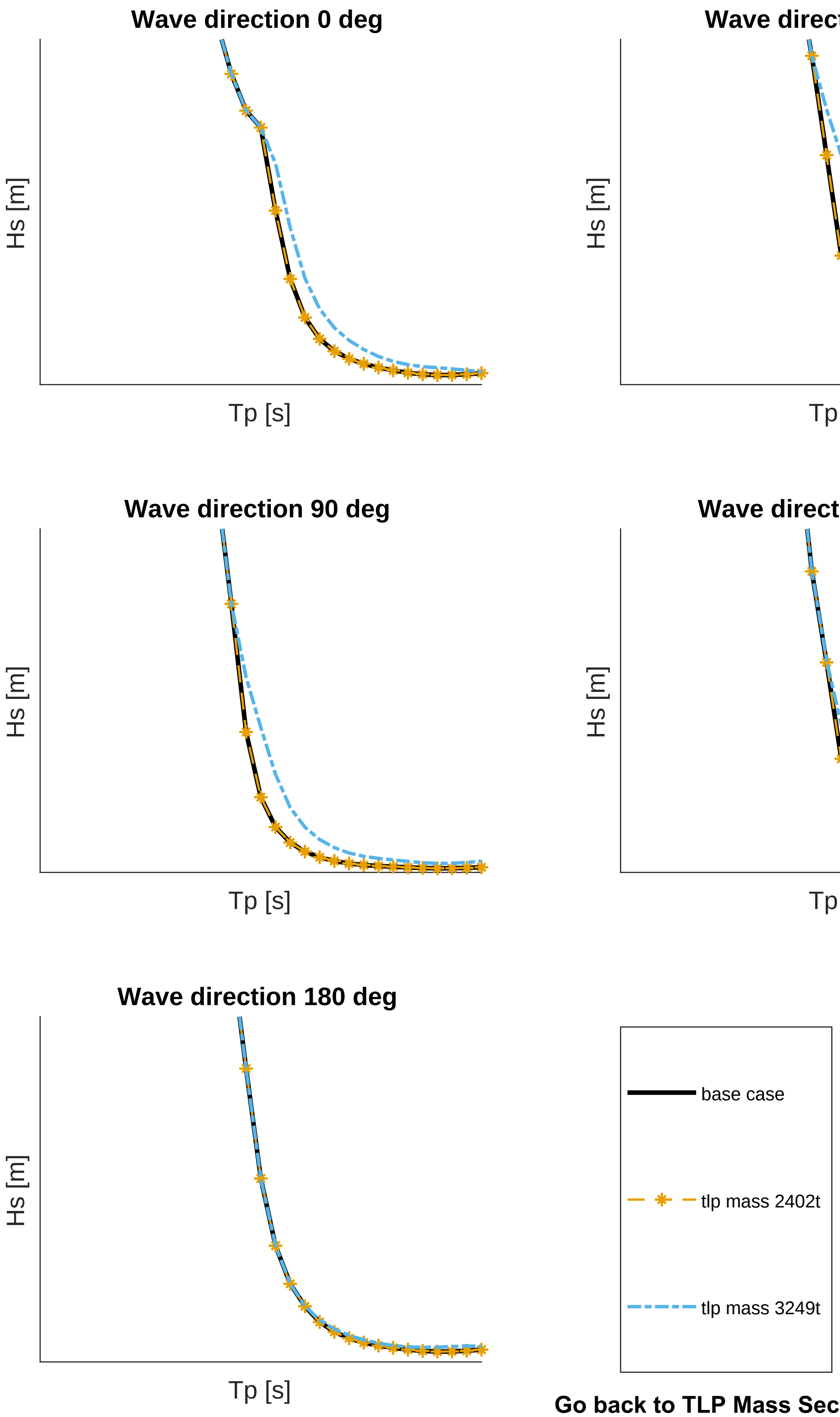

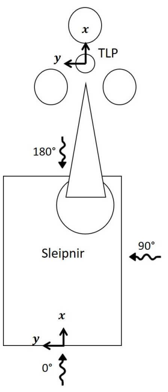

Go back to TLP Mass Section -Here-

See Operability TLP Mass 2402 [t] -Here-

See Operability TLP Mass 3249 [t] -Here-

F.12. Grouped Operability - Tendon Angle

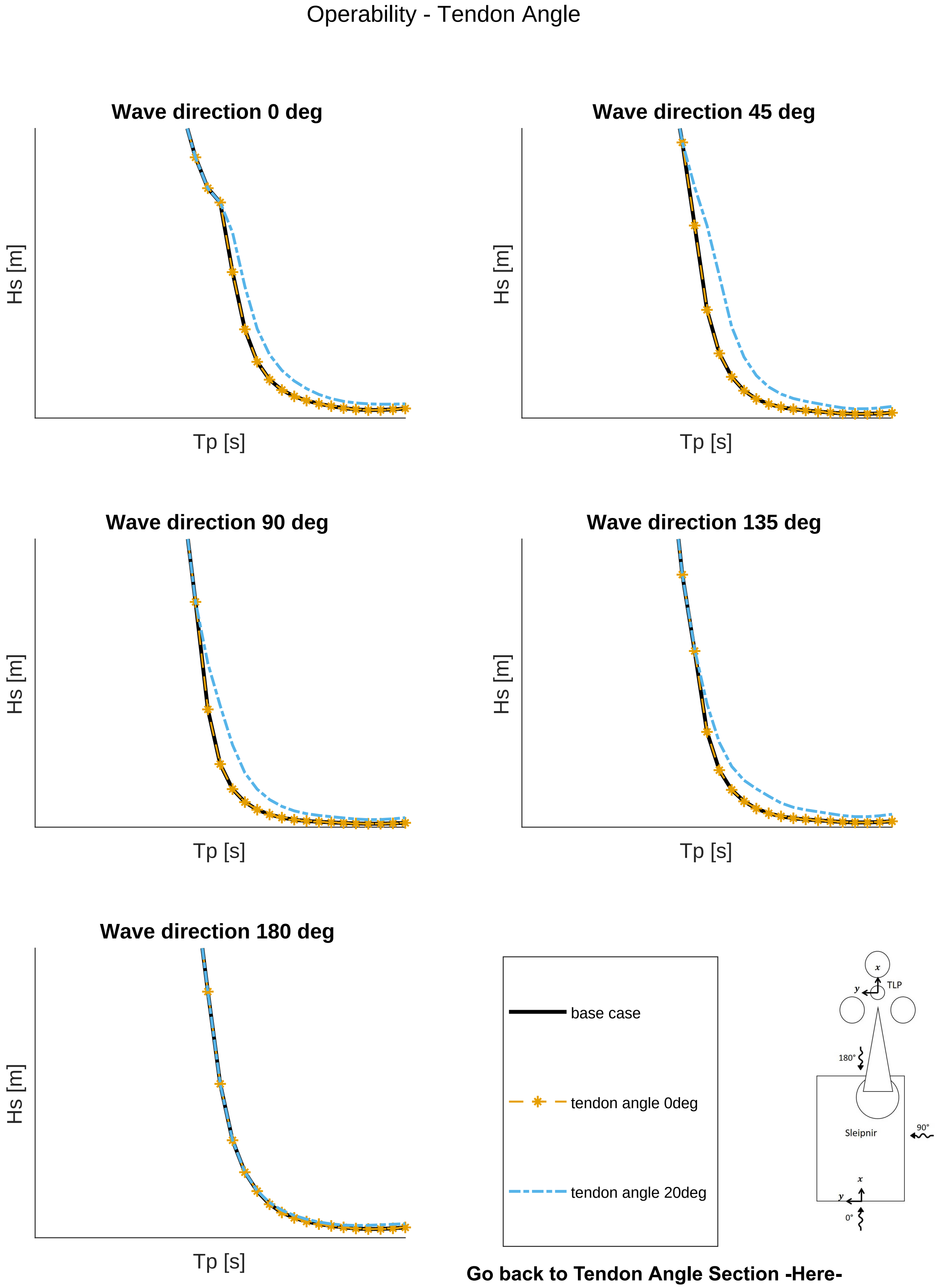

Go back to Tendon Angle Section -Here-

See Operability Tendon Angle 0 [deg] -Here-

See Operability Tendon Angle 20 [deg] -Here-

F.13. Grouped Operability - Mooring Line Stiffness

Operability - Mooring Line Stiffness

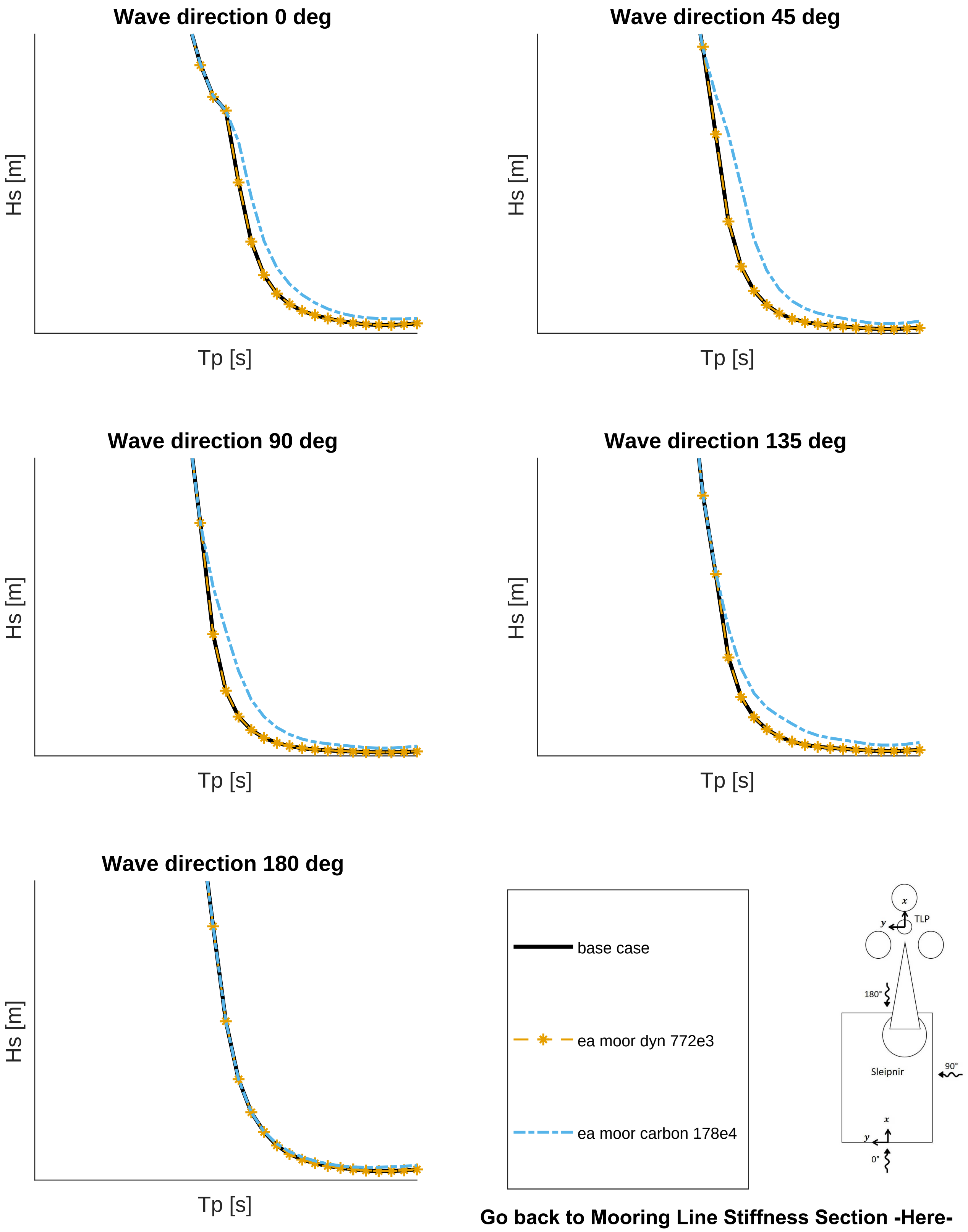

Go back to Mooring Line Stiffness Section -Here-

See Operability Mooring Line Stiffness 772e3 [kN] -Here-

See Operability Mooring Line Stiffness 178e4 [kN] -Here-

F.14. Grouped Operability - Slew Angle Alteration

Operability - Slew Angle Alteration

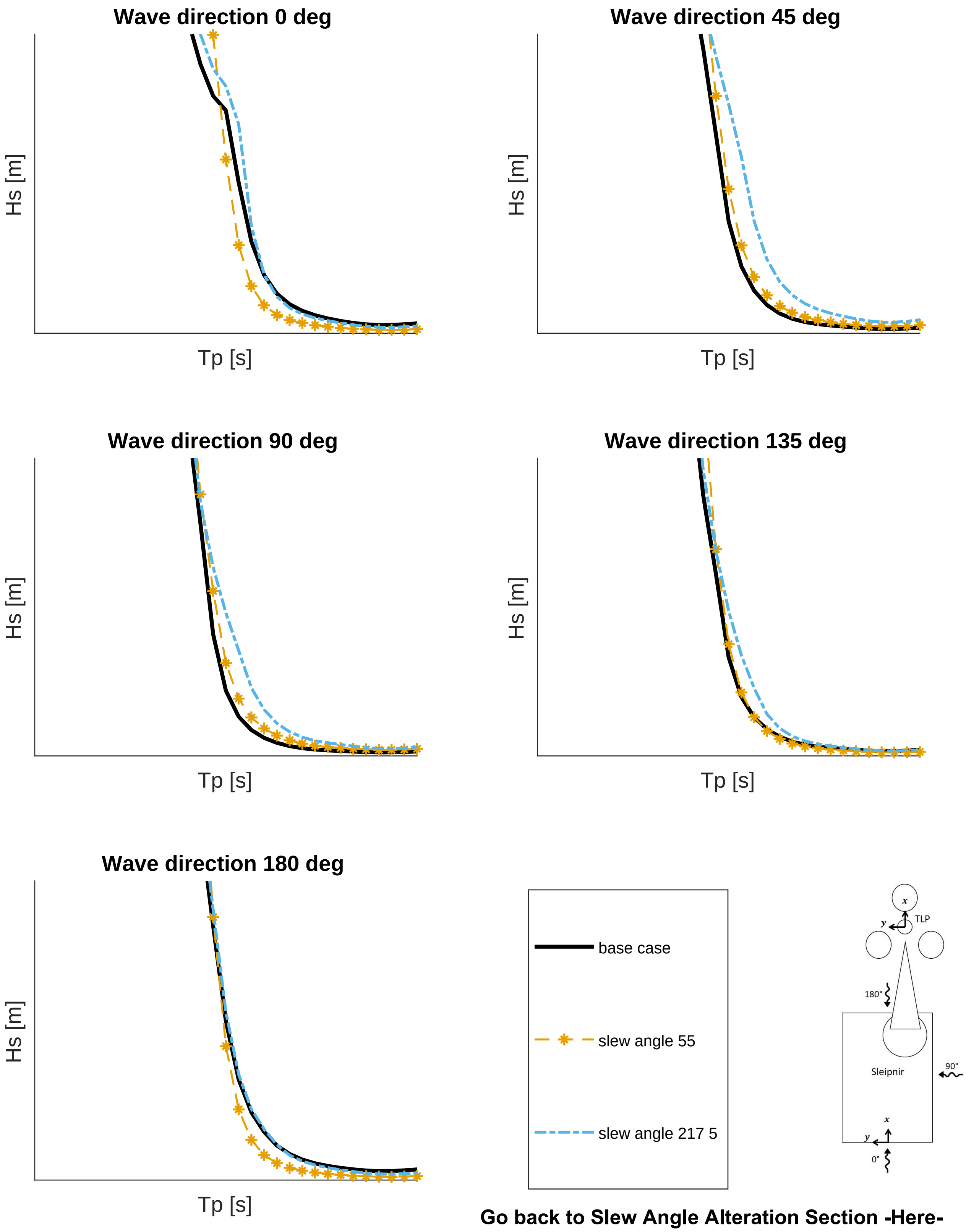

Go back to Slew Angle Alteration Section -Here-

See Operability Slew Angle 55 [deg] -Here-

See Operability Slew Angle 217.5 [deg] -Here-

F.15. Grouped Operability - Rotated RNA+

Operability - Rotated Tower

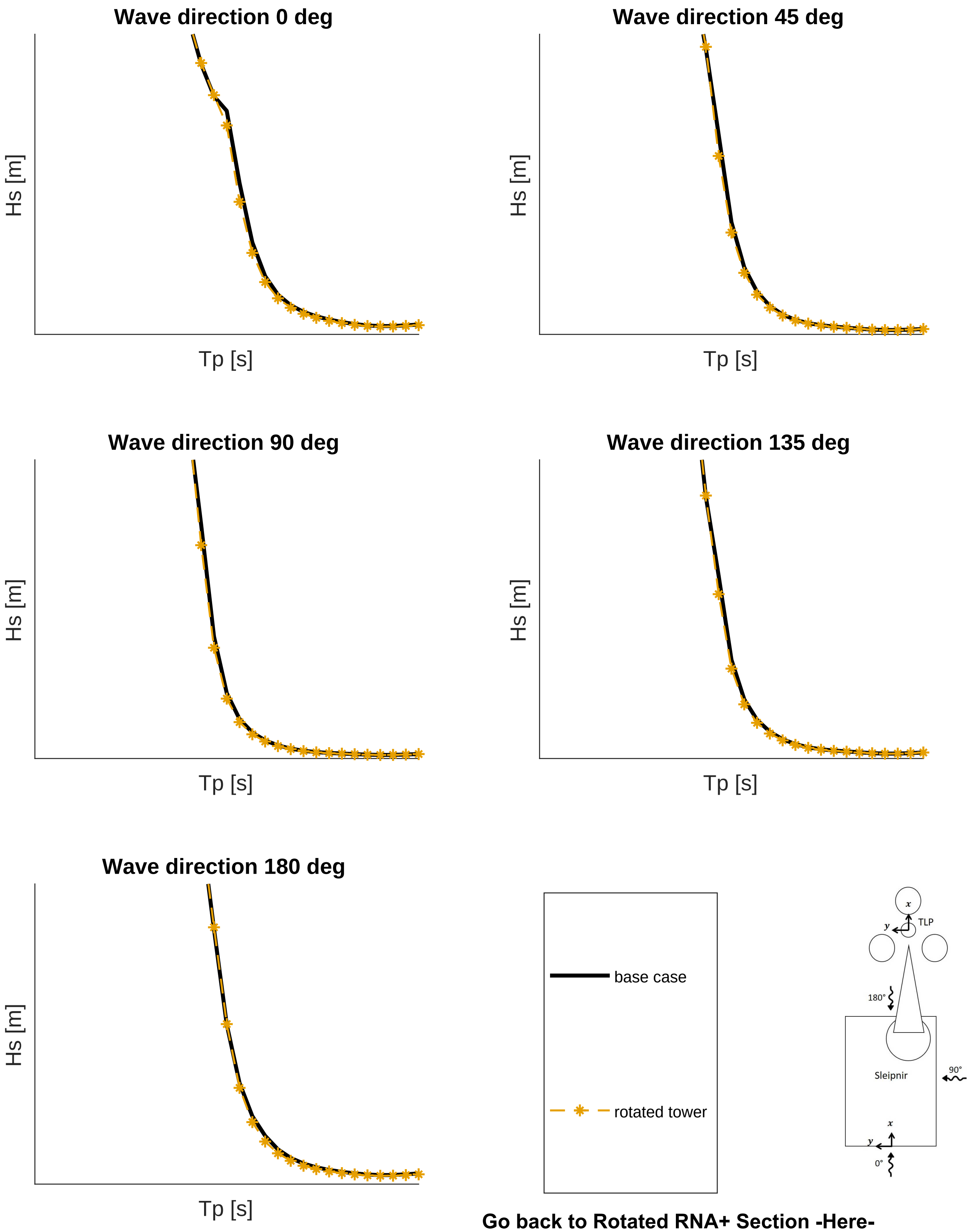

Go back to Rotated RNA+ Section -Here-

See Operability Rotated RNA+ -Here-

G

Workability - Base Case

G.1. Workability - Base Case - US East Coast, January

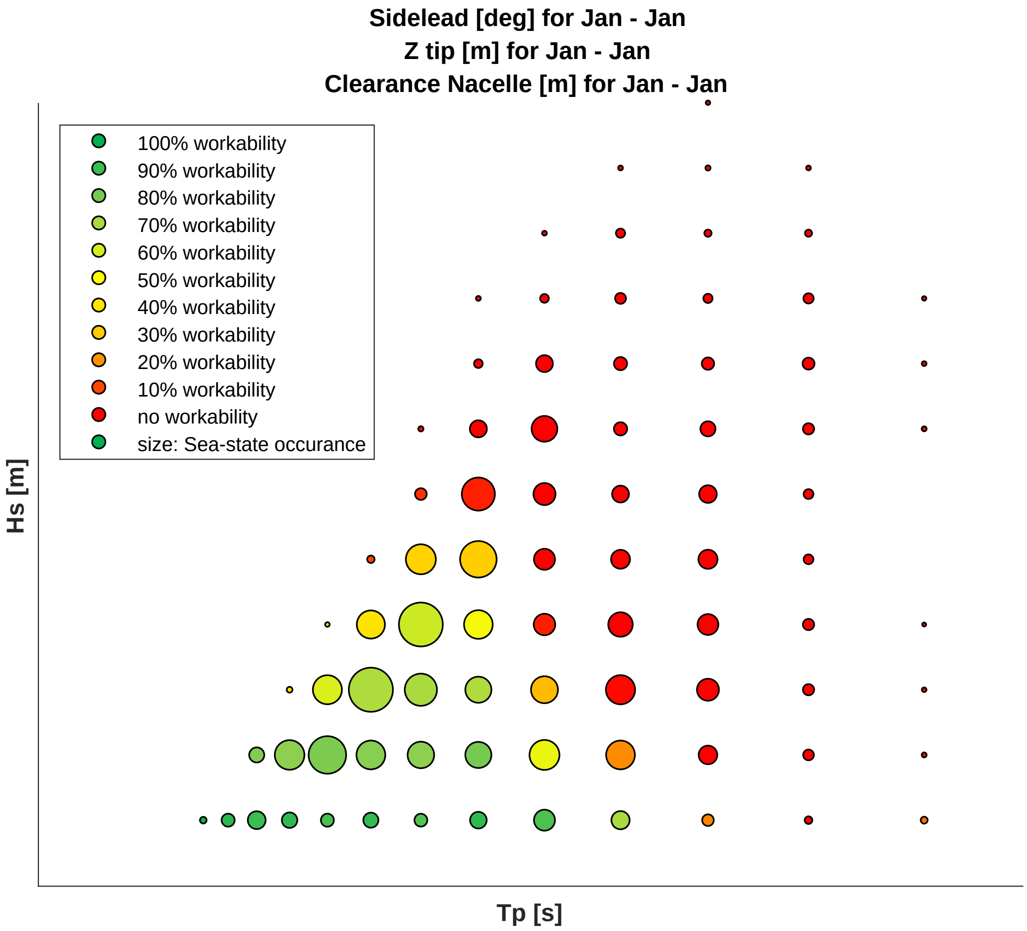

Workability Plot for Combined case based on the governing response per situation for Median heading

Workability for Jan - Jan = %

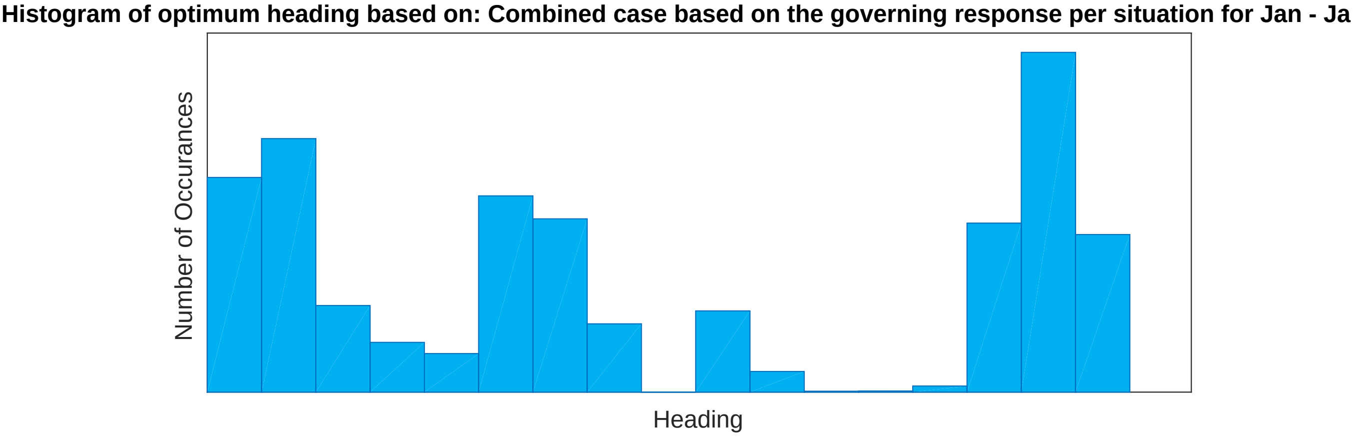
Histogram of optimum heading based on: Combined case based on the governing response per situation for Jan - Ja
Number of Occurances
Heading

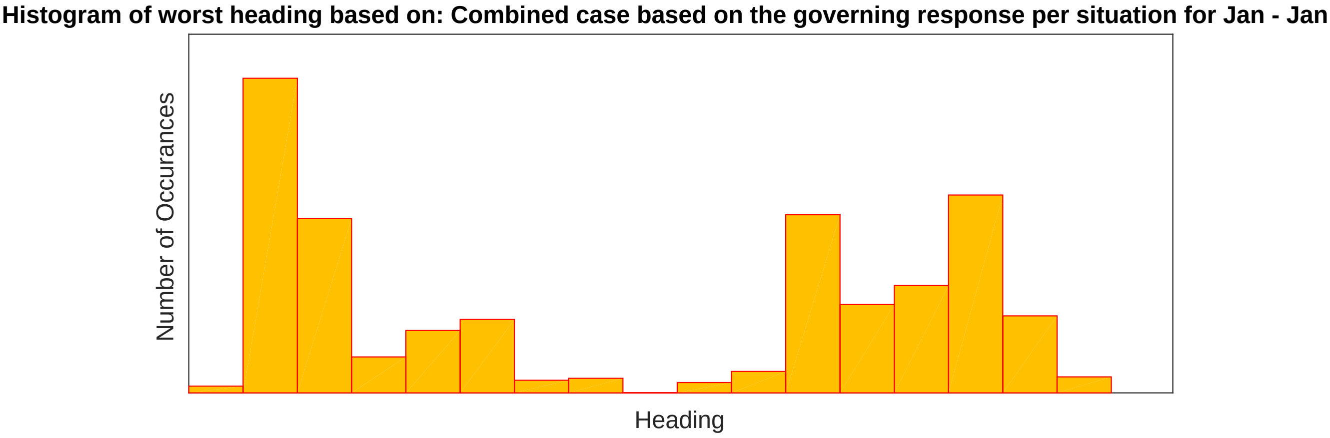
Histogram of worst heading based on: Combined case based on the governing response per situation for Jan - Jan
Number of Occurances
Heading

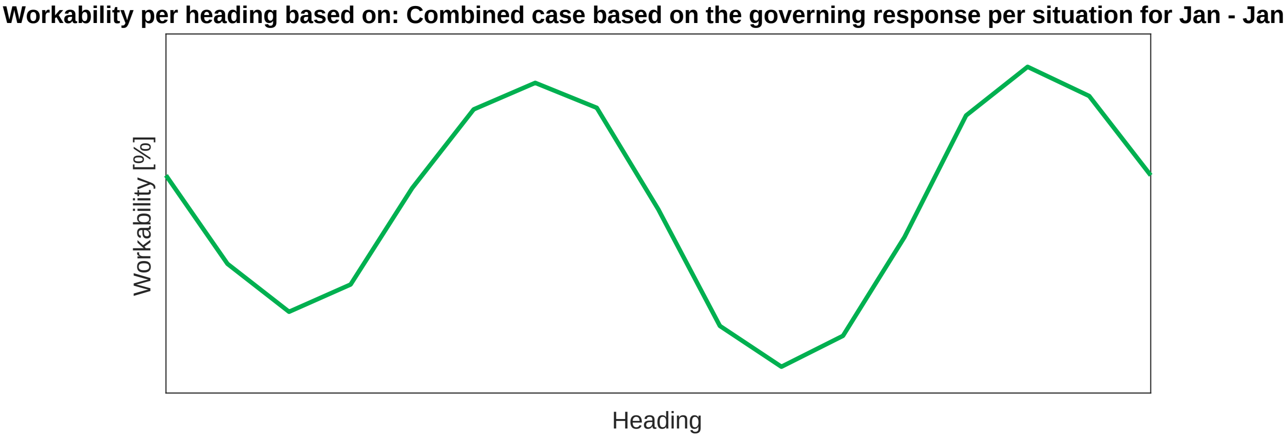
Workability per heading based on: Combined case based on the governing response per situation for Jan - Jan
Workability [%]
Heading

G.2. Workability - Base Case - US East Coast, July

Z tip [m] for Jul - Jul
Clearance Nacelle [m] for Jul - Jul
Sidelead [deg] for Jul - Jul
Z tip [m] for Jul - Jul
Clearance Nacelle [m] for Jul - Jul

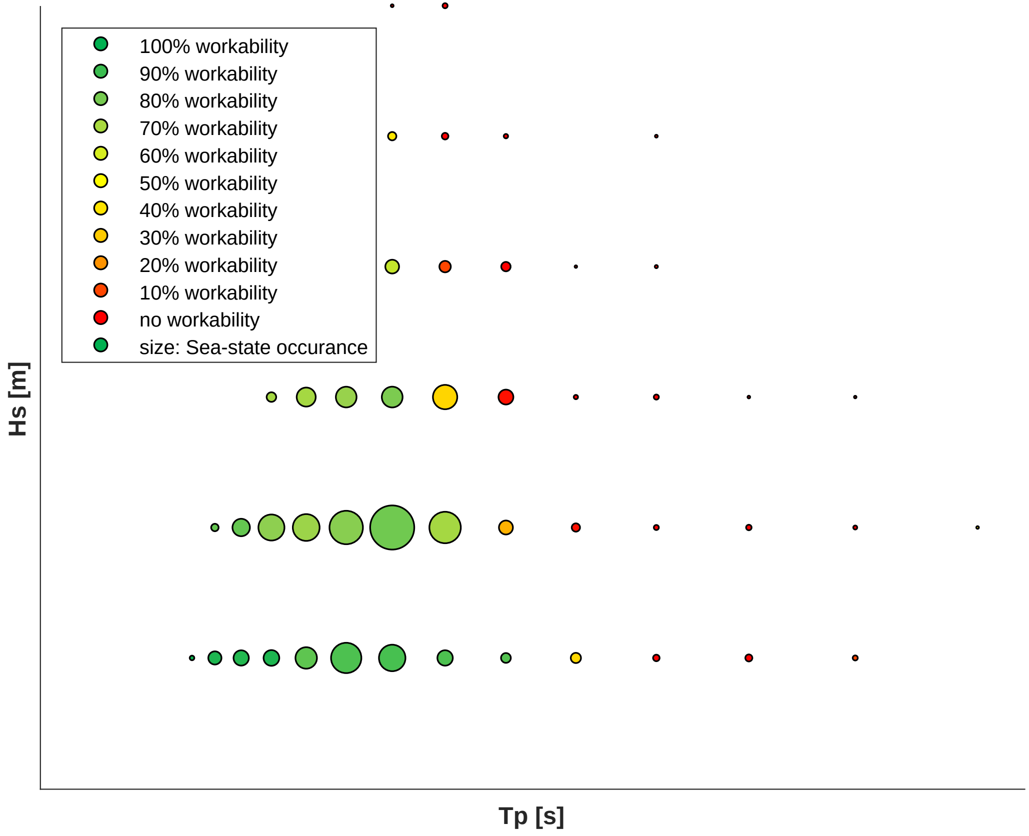

Workability Plot for Combined case based on the governing response per situation for Median heading

Workability for Jul - Jul = %

Histogram of optimum heading based on: Combined case based on the governing response per situation for Jul - Ju

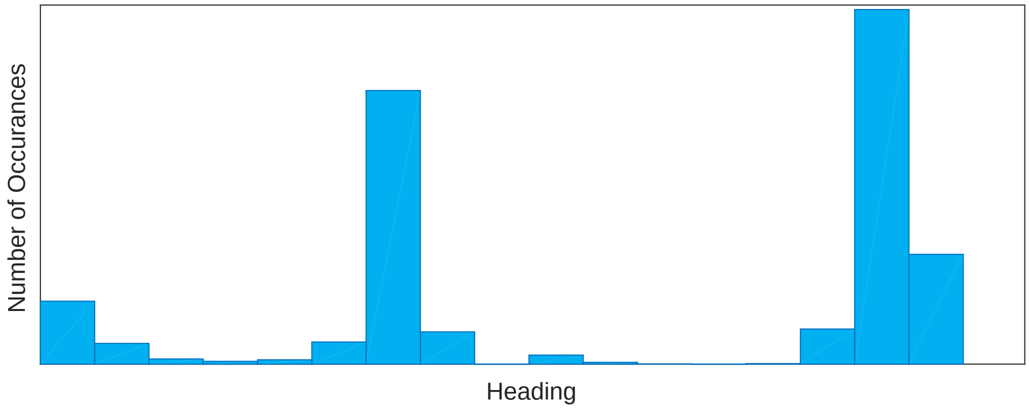

Histogram of worst heading based on: Combined case based on the governing response per situation for Jul - Jul

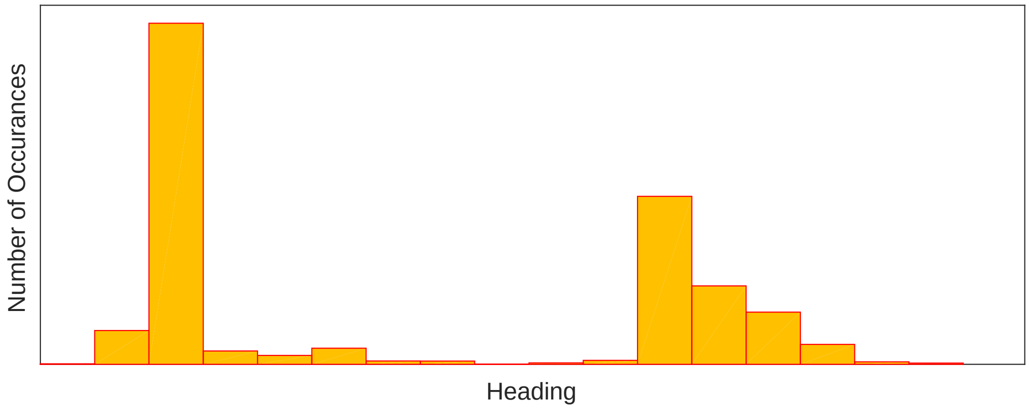

Workability per heading based on: Combined case based on the governing response per situation for Jul - Jul

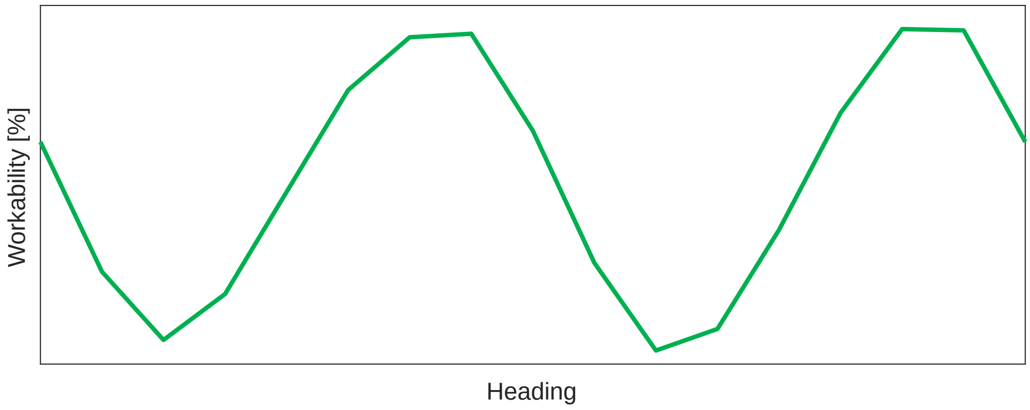

G.3. Workability - Base Case - Baltic Sea, January

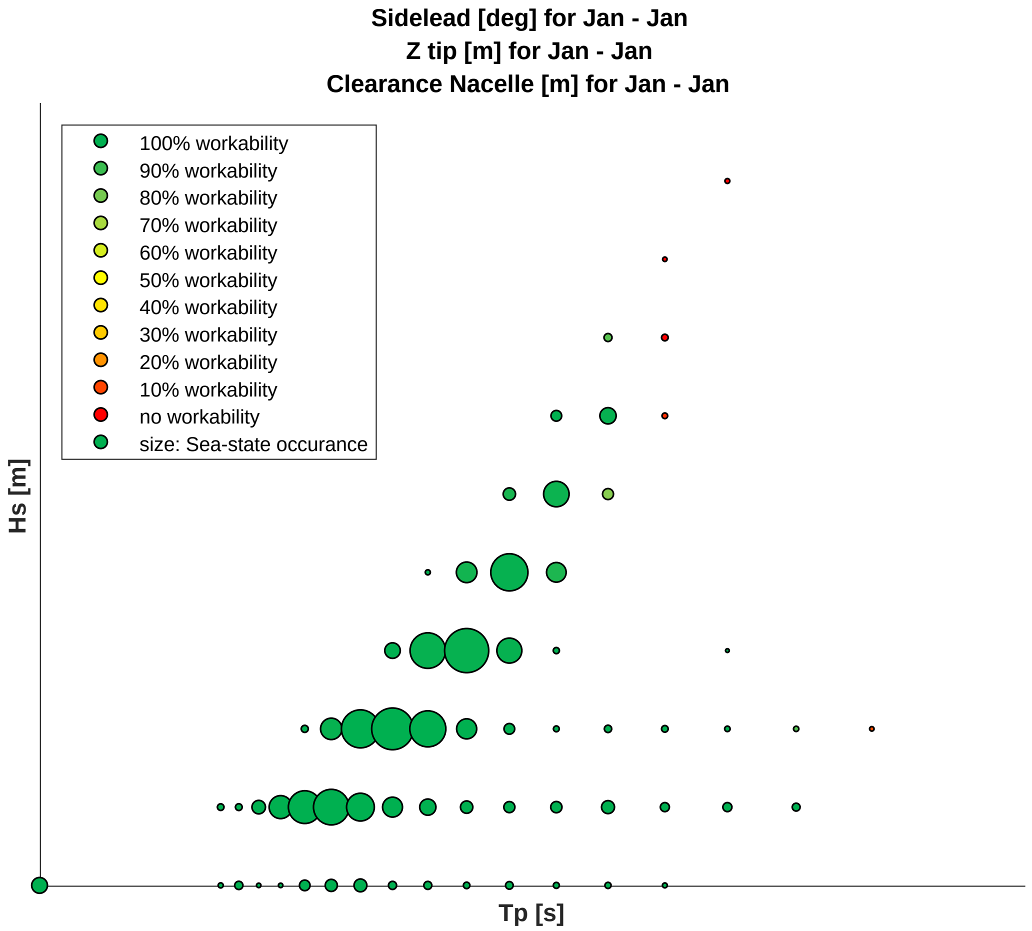

Workability Plot for Combined case based on the governing response per situation for Median heading

Workability for Jan - Jan = %

Histogram of optimum heading based on: Combined case based on the governing response per situation for Jan - Ja

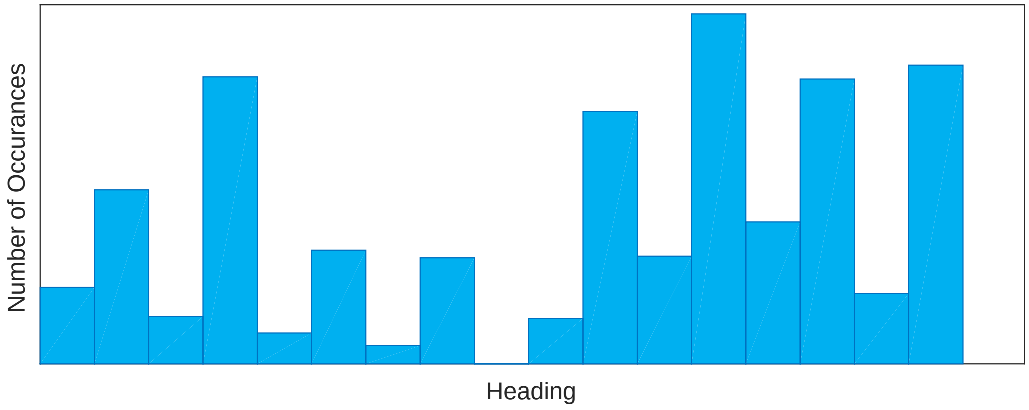

Histogram of worst heading based on: Combined case based on the governing response per situation for Jan - Jan

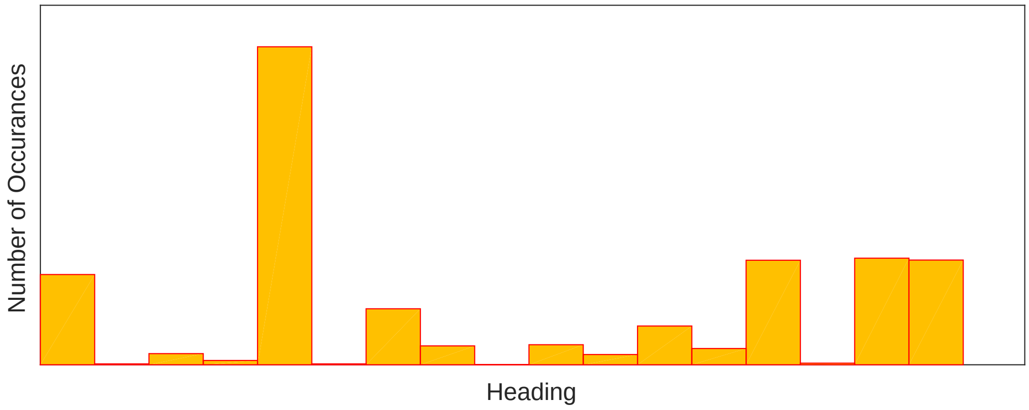

Workability per heading based on: Combined case based on the governing response per situation for Jan - Jan

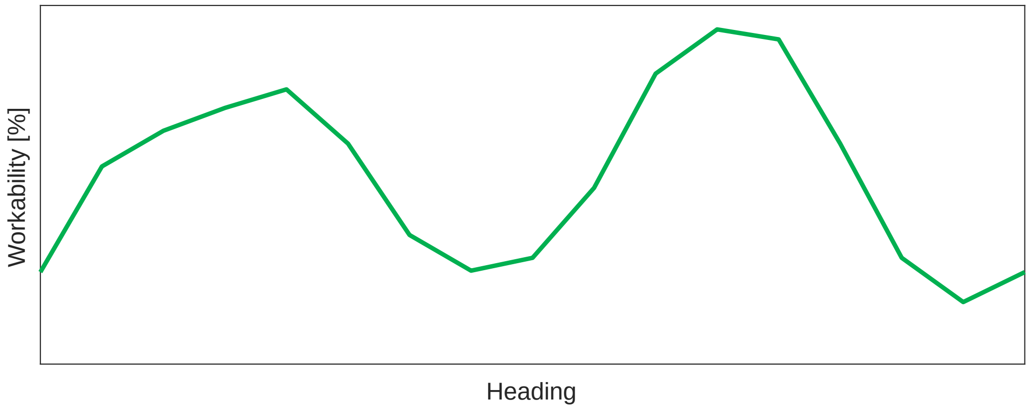

G.4. Workability - Base Case - Baltic Sea, July

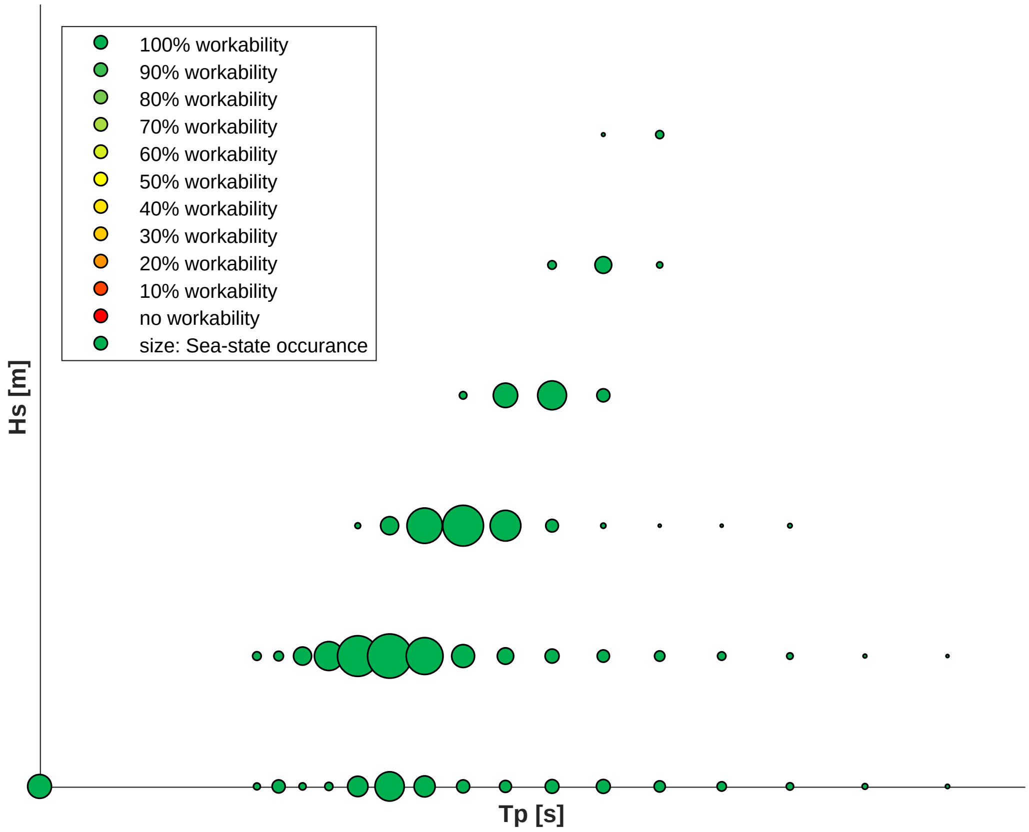
Z tip [m] for Jul - Jul
Clearance Nacelle [m] for Jul - Jul
Sidelead [deg] for Jul - Jul
Z tip [m] for Jul - Jul
Clearance Nacelle [m] for Jul - Jul

Workability Plot for Combined case based on the governing response per situation for Median heading

Workability for Jul - Jul = %

Histogram of optimum heading based on: Combined case based on the governing response per situation for Jul - Ju

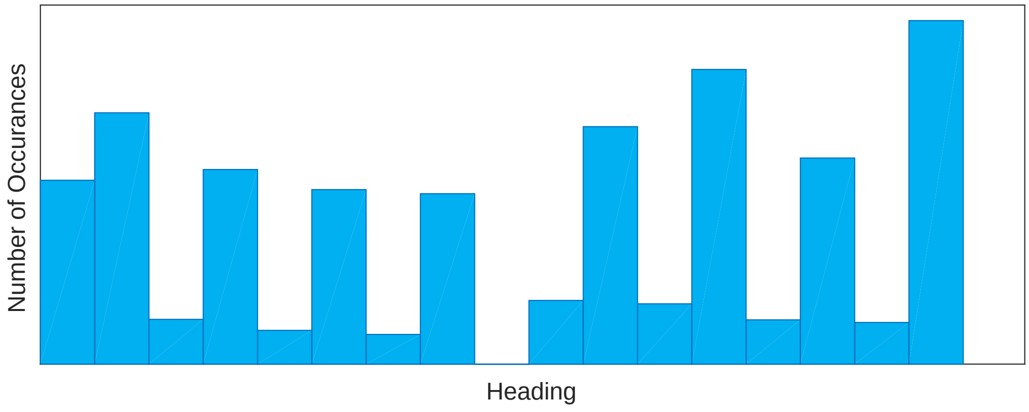

Histogram of worst heading based on: Combined case based on the governing response per situation for Jul - Jul

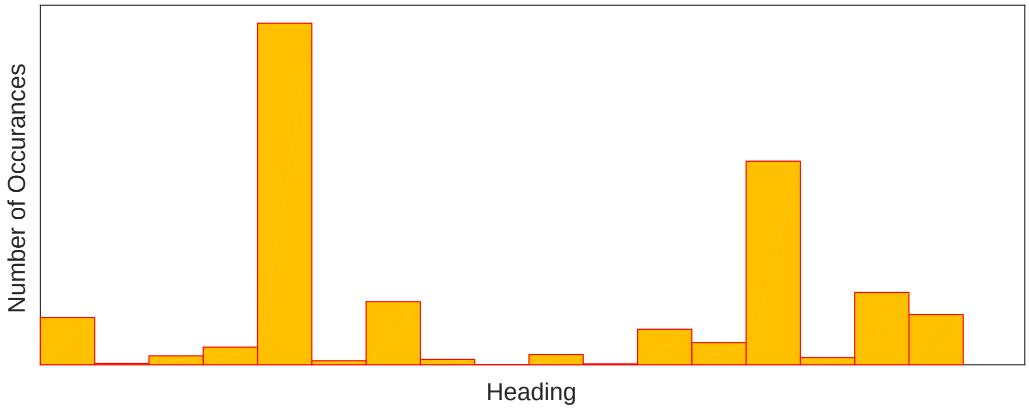

Workability per heading based on: Combined case based on the governing response per situation for Jul - Jul